UNIVERSITÀ DEGLI STUDI DI TRIESTE

XXXII CICLO DEL DOTTORATO DI RICERCA IN FISICA

Performance study of the RICH at COMPASS experiment for hadron identification in SIDIS physics

Settore scientifico-disciplinare: FIS/04

DOTTORANDO
CHANDRADOY CHATTERJEE

COORDINATORE
PROF. FRANCESCO LONGO

SUPERVISORE DI TESI
DR. FULVIO TESSAROTTO

CO-SUPERVISORE DI TESI
DR. SILVIA DALLA TORRE

ANNO ACCADEMICO 2018/2019

UNIVERSITÀ DEGLI STUDI DI TRIESTE

DOCTORAL THESIS

Performance study of the RICH at COMPASS experiment for hadron identification in SIDIS physics

Author:
Chandradoy
CHATTERJEE

Supervisor:
Dr. Fulvio
TESSAROTTO

A thesis submitted in fulfillment of the requirements for the degree of Doctor of Philosophy

in the

Department of Physics

February 10, 2020

Declaration of Authorship

I, Chandradoy CHATTERJEE, declare that this thesis titled, "Performance study of the RICH at COMPASS experiment for hadron identification in SIDIS physics" and the work presented in it are my own. I confirm that:

- This work was done wholly or mainly while in candidature for a research degree at this University.
- Where any part of this thesis has previously been submitted for a degree or any other qualification at this University or any other institution, this has been clearly stated.
- Where I have consulted the published work of others, this is always clearly attributed.
- Where I have quoted from the work of others, the source is always given. With the exception of such quotations, this thesis is entirely my own work.
- I have acknowledged all main sources of help.
- Where the thesis is based on work done by myself jointly with others, I have made clear exactly what was done by others and what I have contributed myself.

Signed: Chandradoy Chatterjee

Date: 10th February, 2020

UNIVERSITÀ DEGLI STUDI DI TRIESTE

Abstract

Faculty Name
Department of Physics

Doctor of Philosophy

Performance study of the RICH at COMPASS experiment for hadron identification in SIDIS physics

by Chandradoy CHATTERJEE

Hadron production in semi-inclusive measurements of deep-inelastic lepton nucleon scattering (SIDIS) is one of the most powerful tools to investigate the hadron structure. Particle IDentification (PID) is essential to study the processes where inclusive DIS is not able to provide all the information. For instance to study the role played by the different flavours in SIDIS processes. In the high momenta regime ($\mathbf{p} \geq 20\ GeV/c$) the Ring Imaging Cherenkov technique is a unique tool to perform hadron identification in a wide momentum range. In particular in the COMPASS experiment at CERN pion-kaon-proton identification is obtained thanks to a $\approx 80\ m^3\ C_4F_{10}$ gaseous radiator focusing RICH capable of $2\sigma\ \pi\ K$ separation up to 50 GeV/c. The COMPASS RICH has 5.6 m^2 of active photon detector (PD) surface, composed of three different detection technologies, MultiAnode PMTs ($\approx 1.4 m^2$) in the central part, gaseous detectors with CsI photocathodes in the peripheral part: Multi-Wire Proportional Chambers ($\approx 2.8\ m^2$) and new photon detectors based on THick Gaseous Electron Multiplers (THGEMs) and Micromegas covering the remaining $\approx 1.4\ m^2$. The first chapters describe SIDIS physics, the COMPASS spectrometer, the principle of PID and COMPASS PDs. Chapter 5, 6 and 7 of this thesis will describe and discuss the work have been done by me. Chapter 5 will elaborate the characterization of both the newly installed detector and the RICH-1 performance. For this purpose a dedicated pion beam data taking was requested to the COMPASS collaboration and a dedicated trigger was implemented. An illustration of the methodology to obtain the the number of photons of the newly installed detector, single photon resolution along with the operating gain and stability will be described together with the main results. Chapter 6 and 7 describe the study of the non uniform RICH-1 response, the procedure for curing it and the results obtained after the final tuning. The analysis of the detector position survey and the corrections of the mirror VUV wall position is described. This thesis presents the technique developed and adopted to extract the refractive index of the radiator from the data, which greatly reduces the contamination from electrons and positrons tracks and the consequently improves the RICH-1 PID performance. PID is obtained both via Cherenkov ring angle based on χ^2 analysis and using the single photon information in an extended likelihood algorithm on a track by track basis. A detailed study of the likelihood algorithm and the consistency with the χ^2 analysis are presented. With the updated RICH-1 detector parameters, the performance figure for COMPASS RICH-1 in terms of PID efficiency and purity is extracted from selected meson decays. The result of this work is also an essential element for the extraction of DIS hadron multiplicities, namely the differential cross section for identified hadron production normalised to the differential inclusive DIS cross section.

Acknowledgements

I thank heartily to my supervisor Fulvio Tessarotto and co supervisor Silvia Dalla Torre. Their constant encouragement has helped me enormously. Their availability to discuss problems, ideas and passing critical judgements of my work led me to understand and improve my research. I am grateful to COMPASS collaboration to allow me to analyse the data for my PhD and to INFN Trieste and University of Trieste for all kind of supports during the period of my work. Thanks to Yuxiang Zhao, Andrea Bressan, Stefano Levorato for their helps, comments and suggestions during my PhD.
Heartiest thanks to Franco Bradamante for introducing me to the world of spin physics and also to Anna Martin.Thanks to all professors who have provided me courses during these three years. Thanks to Gergo Hamar for his help during the first year of my PhD. Thanks to Shuddha Shankar Dasgupta for his effective tips about electronics and lab works. Under the supervision of Stefano Levorato I have worked in the lab and at CERN with complex hardware facilities. I am thankful to him for his suggestions, and guidance. For my lab activities my colleague Triloki has helped me a lot during these days.
I am received large supports from Jan Matoushek, Bakur Parsamyan, Marketa Peskova, Elena Zemlyanichkina. Thanks to Nicolas Pierre for his support with the COMPASS RICH efficiency software. I am grateful to COMPASS collaboration for allowing us to take the pion data for the hybrid characterisation. Thanks to all of our COMPASS colleagues for their enormous help and support for ensuring the quality of the pion data.
Thanks to Triloki, Shuddha and Daniele and of course Fulvio, for their literally sleepless efforts for the removals of the typos-grammatical flaws and many errors. Without them the thesis would have remained unreadable. Thanks to Benigno Gobbo, Piero Ciliberti, Mauro Gregori, Girogio Menon, Livio Rinaldi and Claudio Azzan for their help in many directions.
I am grateful to Shuddha, Triloki, Fulvio and Stefano for the helps I received from them outside the work-life. I am grateful to Matrivani Institute of experimental research and education, Kolkata and Prof. Dr. S.S.Dasgupta.
Endless thanks to Luisa Bacciolo. Thanks to all of my friends, they have always stood by me, cared for me, sent me pictures of cute cats and dogs in social media, went on for endless discussions specially when I was waiting alone for late night buses. I am grateful to everyone of my family, they have constantly supported my parents during my absence. Hearty thanks to Saswati Bhar, Arun Roy and Pramita Roy. Finally, I am grateful to my parents for their endless support, love and trust in me and helping me to always remain optimistic.
I thank everyone working tirelessly for the betterment of human race.

Contents

List of Figures

List of Tables

Chapter 1

The Structure of the nucleon

1.1 Introduction

A complete understanding of the spin structure of the nucleon is not yet achieved. The intriguing interest of understanding the internal structure of the nucleon started from the outcome of the measurement of the anomalous magnetic moment κ_p of the proton made in 1933. It was found that $\kappa_p \simeq 1.79$ μ_B [1], where μ_B is the Bohr proton magneton. This surprising result suggested that the proton is not a Dirac particle, and it has an internal structure. Lepton proton scattering provides a powerful tool to probe into the nucleon structure. At low energies the scattering is dominantly elastic, namely the virtual photon coherently interacts with the proton as a whole. This leads to the global properties of the proton. For instance, the charged radius of proton. However, at higher energies the dominant scattering process is inelastic, where the proton breaks up, and the underlying process is elastic scattering of the lepton with the spin$\frac{1}{2}$ quarks of the proton. Our current understanding is therefore the following, at higher energies the lepton scatters with spin$\frac{1}{2}$ quarks, the quarks interact among themselves by exchange of mass-less spin 1 coloured bosons: gluons. The strong interaction of the partons is described by Quantum Chromodynamics (QCD). The finite size of the proton is responsible for the rapid decrease in the elastic cross-section with energies for lepton-proton scattering process. The idea of this scattering method dates back to 1911. In Rutherford's experiment [2] alpha particles were scattered onto a few atoms thick gold foil, to understand the structure of atoms. The result of this scattering experiment suggested that the positive charge of the atom is concentrated as a point at the centre of the atom. In the 50s the idea to use the high energetic electrons to probe the nucleus structure was developed by Hofstadter [3]. The technological advancements during years allowed physicists to accelerate electrons more and more in order to achieve higher collision energies and hence to probe deeper into the nucleus target. In the late 60s, SLAC and MIT made a joint venture to investigate the electromagnetic structure and interactions of the proton [4, 5]. The elastic lepton-proton differential cross-section can be written as [6]:

$$\frac{d\sigma}{d\Omega} = \frac{\alpha^2}{4E_1^2 \sin^4(\theta/2)} \frac{E_3}{E_1} \Big(\frac{G_E^2 + \tau G_M^2}{1+\tau} \cos^2 \frac{\theta}{2} + 2\tau G_M^2 \sin^2 \frac{\theta}{2} \Big) \qquad (1.1)$$

where E_1 and E_3 are the energy of the initial and final state leptons respectively and θ is the scattered lepton angle. If the 4-momentum squared of the virtual photon is defined as q^2, then $\tau = \frac{Q^2}{4.M_P^2}$,where $Q^2 = -q^2$ and M_P is the mass of the proton. The finite size of the proton is accounted by the introduction of the form factors. The form factors describe the electric charge distribution (G_E) of the proton and the magnetic moment distribution (G_M) within the proton.

The inelastic scattering requires new kinematic variables for full description. As was the case for the elastic scattering, Q^2 is the negative 4-momentum squared. For the fixed target lepton-proton scattering processes the 4-momenta of the incoming and the scattered leptons are explicitly written as P_1=$(E_1, 0, 0, p_1)$, P_3=$(E_3, p_1 \sin\theta, 0, p_1 \cos\theta)$, in the proton rest frame. Then, $Q^2 = -(P_1 - P_3)^2$ $\approx 4E_1E_3 \sin^2\frac{\theta}{2}$. Bjorken introduced [7] the Lorentz invariant kinematic variable (x) to describe the inelastic scattering.

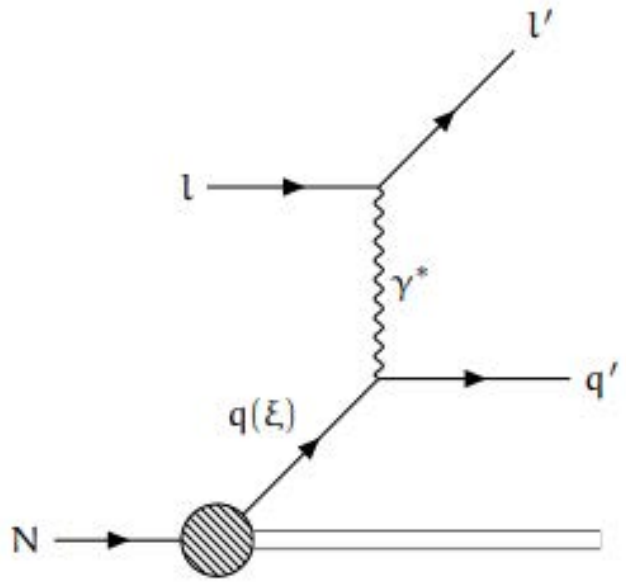

FIGURE 1.1: Feynman Diagram of Deep Inelastic scattering

$$x = \frac{Q^2}{2 \cdot P_2 \cdot q} \tag{1.2}$$

P_2 is the 4-momentum of the proton. In the proton rest frame it can be written as: $(M_P, 0, 0, 0)$. If the unidentified final state has an invariant mass W, then equation 1.2 can be written as

$$x = \frac{Q^2}{Q^2 + W^2 - M_P^2} \tag{1.3}$$

The invariant mass of the final state hadronic system is always greater than the proton rest mass, as the proton is the lightest baryon, therefore for $Q^2 \geq 0$

the equation 1.3 implies $0 \leq x \leq 1$. This new variable has an important physical meaning: it describes the "elasticity " of a scattering process, $x = 1$ corresponding to the elastic process. Another Lorentz invariant variable is used to describe the inelasticity of the process: $y = \frac{P_2 \cdot q}{P_2 \cdot P_1}$. In the proton rest frame $y = \frac{M_P(E_1 - E_3)}{M_P.E_1} = \nu E_1$, where ν is defined as the energy lost by the incoming lepton: $\nu = E_1 - E_3$.

The equation 1.1, known as Rosenbluth formula, can be generalised to the inelastic process. With the newly defined variables the cross-section can be rewritten in terms of the structure functions F_1 and F_2:

$$\frac{d\sigma}{dx.dQ^2} = \frac{4\pi\alpha^2}{Q^4}\Big(\frac{F_2(x,Q^2)}{x}(1 - y - \frac{M_p^2 y^2}{Q^2}) + y^2 F_1(x,Q^2)\Big) \tag{1.4}$$

The structure functions are fundamentally different from the form factors. Their dependence on both x and Q^2 does not allow interpreting these functions as the Fourier transformations of the proton charge or magnetic moment distributions. The first systematic measurements of the structure functions were performed at SLAC: electrons of energies between 7 and 17 GeV impinged on a liquid hydrogen target. A movable magnetic spectrometer was used to measure the scattering angle of the electron and the momentum of the final state electron. The resulted data suggested two interesting points. Firstly, the two structure functions $F_1(x,Q^2)$ and $F_2(x,Q^2)$ are almost independent of Q^2. Secondly, in the deep inelastic scattering region, viz. $Q^2 >$ few GeV^2, the structure functions are not independent. They satisfy the Callan-Gross relation [8]: $F_2(x,Q^2) = 2xF_1(x,Q^2)$. In figure 1.2 we see the experimental determination of the ratios of the structure functions as a function of x. These observations suggest that the virtual photon (γ^*, in figure 1.1) interacts with spin$\frac{1}{2}$ Dirac like particles [9]. If the interaction would have taken place with spin-less particles, the Callan-Gross ratio would have been expected to be zero.

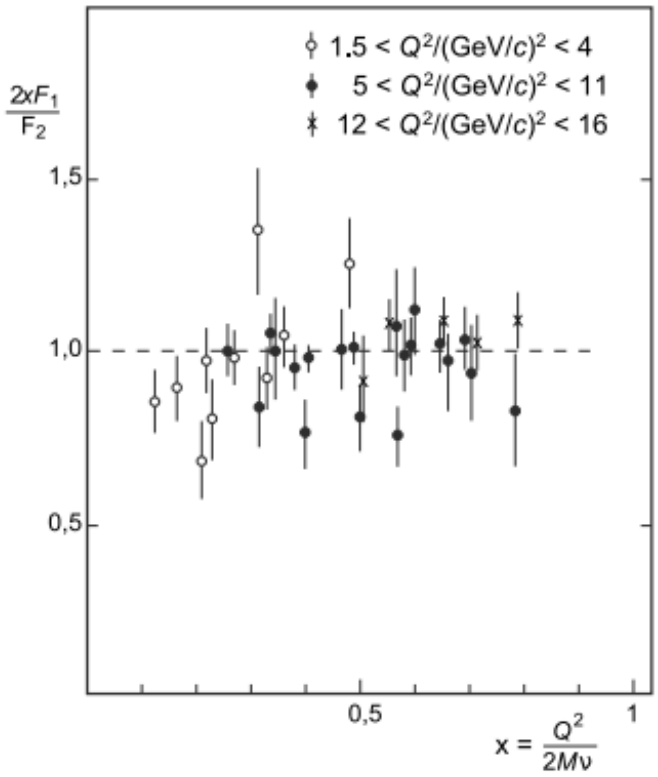

FIGURE 1.2: Measurement of the Callan-Gross ratio as a function of Bjorken x. The data was taken at SLAC.

1.1.1 The quark-parton model

In the 1950s and 60s a set of new particles was discovered. M. Gell-Mann and Y. Neeman showed that these particles can be grouped in octets (mesons and baryons) or decuplets (hyperons) as a representation of a SU(3) symmetry group. Nevertheless, it was hard to believe that all of them were elementary particles and the simplest representation of this group, viz. a triplet was not realised in nature.
Therefore, to describe the "particle zoo" of hadrons in terms of SU(3) representations, Gell-Mann and Zweig [10, 11, 12] proposed that hadrons have substructure with spin$\frac{1}{2}$, point-like charged particles: mesons are bound quark anti-quark systems and baryons are bound three quark systems. Gell-Mann called these 'constituent' particles quarks. This assumption implied attributing strange features to the constituent quarks. Their charges are fractional and they violate the spin-statistics of spin$\frac{1}{2}$ particles. The puzzle was resolved by the introduction of the new quantum number: colour [13].

To describe the results of the SLAC experiment Feynman proposed that the proton has a substructure. He called the substructure elements partons [14], keeping an open possibility to have partons other than quarks. He postulated that in the SLAC experiment the electrons inelastically scattered with point-like charged partons.

By combining the quark model and the parton model one obtains the quark parton model (QPM).

In this model the underlying idea is that the parent proton is in a frame where its energy is very high. In that regime, $E \gg M_P$, the mass can be neglected and the frame is called ***infinite momentum frame***. The four momentum is written conventionally as, $P^\mu = (P, 0_T, P)$, the parent proton has no transverse momentum component. If the parent proton moves in the Z direction with momentum P_z, then the partons will have momentum, $k = \xi \cdot P_z + k_T$. In the frame where $P_z \to \infty$, the transverse momentum of the partons can be ignored. The invariant mass of the struck quark after absorbing the virtual photon of momentum q is :

$$(\xi \cdot P_z + q)^2 = \xi^2 P_z^2 + 2\xi P_z q + q^2 = m_q^2; \tag{1.5}$$

Neglecting quark mass and $\xi^2.P_z^2$, from equation 1.5 we can identify ξ as the kinematic variable x (sometimes written as x_B, named after Bjorken). Physically x describes the fraction of the proton momentum carried by the struck quark. The partons in general will have a momentum distribution. If $f_i(x)$ is the distribution function for a specific flavour i (up,down etc.), then this distribution represents the probability to find a quark of type i with a momentum fraction x of the parent proton in this frame. This distribution is called **parton distribution function**(PDF). According to the QPM, this distribution can be written in the following form [15]:

$$\frac{d^2\sigma}{dQ^2dx} = \sum_i f_i(x) \Big(\frac{d^2\sigma}{dQ^2dx}\Big)_i \tag{1.6}$$

Where the sum is taken over all flavours. The left hand side is the measured deep inelastic scattering cross section, mentioned in equation 1.4. The PDF (f_i) signifies the number density of partons with fractional momentum x of the parent proton.

A field theoretical description was developed to describe the dynamics of the strong interaction in analogy to Quantum ElectroDynamics (QED), known as Quantum ChromoDynamics (QCD). According to QCD in the high x regime the partons are ascribed as the valance quarks. Similar to fluctuations of photons into electron-positron pairs in quantum electrodynamics, quark antiquark pairs can also be generated from the QCD vector bosons fluctuations, the gluons. These pair-produced charged partons are called sea quarks. Unlike photons, gluons have colour charges. The presence of colour helps solving the spin statistics puzzle. From the field theoretical approach, the lepton nucleon interaction cross-section via single photon exchange can be written in the tensor form:

$$d\sigma \sim L^e_{\mu\nu} W^{\mu\nu} \tag{1.7}$$

where $W^{\mu\nu}$ is the hadronic tensor and $L_{\mu\nu}$ is the leptonic tensor. It is known that the tensor can be split into symmetric and anti-symmetric parts, where

for the hadronic tensor, the anti-symmetric part contains the spin information of the target nucleon. At the interaction vertex taking into account that the current is conserved and any parity violating component is not present then the symmetric part can be written in terms of two structure functions [12]:

$$\frac{1}{2M_P}(W^{\mu\nu})_{sym} = W_1\Big(-g^{\mu\nu} + \frac{q^\mu q^\nu}{q^2}\Big) + W_2\frac{1}{M^2}\Big(P^\mu - \frac{P.q}{q^2 q^\mu}\Big)\Big(P^\nu - \frac{P\cdot q}{q^2}q^\nu\Big) \tag{1.8}$$

and the anti-symmetric part is expressed in terms of two new, spin dependent, structure functions:

$$\frac{1}{M_P}(W^{\mu\nu})_{asym}(S,P,q) = \epsilon^{\mu\nu\alpha\beta}q_\alpha\big[M_P S_\beta G_1 + [(P\cdot q)S_\beta - (S\cdot q)P_\beta]\frac{G_2}{M_p}\big] \tag{1.9}$$

the polarisation vector is defined as S^μ. If the cross-section is averaged over the spin states of an unpolarised proton then the anti-symmetric tensor term does not contribute to the cross-section. The unpolarised structure functions (W_1 and W_2) are another representation of the structure function $F_1(x,Q^2)$ and $F_2(x,Q^2)$. If the spin information is not summed over, then the cross-section explicitly depends on the spin dependent structure functions.
The difference of the inclusive cross-sections for the lepton and the target nucleon polarised longitudinally along and opposite to the direction of the lepton beam, is given by:

$$\frac{d^2\Delta\sigma}{dxdQ^2} = \frac{16\pi\alpha y}{Q^4}\left[\left(1 - \frac{y}{2} - \frac{4M^2xy^2}{Q^2}\right)g_1 - \frac{4M^2xy}{2}g_2\right] \tag{1.10}$$

where $\Delta\sigma = \sigma^{\rightarrow}_{\Leftarrow} - \sigma^{\rightarrow}_{\Rightarrow}$ and the two spin dependent structure functions are g_1 and g_2. In the equation the single arrow represents the polarisation of the partons and the reversal of the nuclear spin is indicated with the double arrow. In the QPM the assumption is parton and proton mass are negligible and the electron scatters incoherently with the partons which do not interact among themselves. The structure functions $F_1(x,Q^2)$, $F_2(x,Q^2)$ and $g_1(x,Q^2)$ can be described in QPM. While $g_2(x,Q^2)$ can not be described in the naive parton model, and its value is assumed to be zero. The $g_2(x,Q^2)$ contains information about the quark-gluon interaction [16]. The expression of $g_2(x,Q^2)$ is written in the following way in its twist expansion: $g_2(x,Q^2) = g^{WW}(x,Q^2) + \tilde{g_2}(x,Q^2)$. The term $g^{WW}(x,Q^2)$ is known as the Wandzura-Wikczek term [17]. In the leading twist approximation $g^{WW}(x,Q^2)$ can be fully expressed in terms of $g_1(x,Q^2)$.

1.1.2 Parton model in QCD

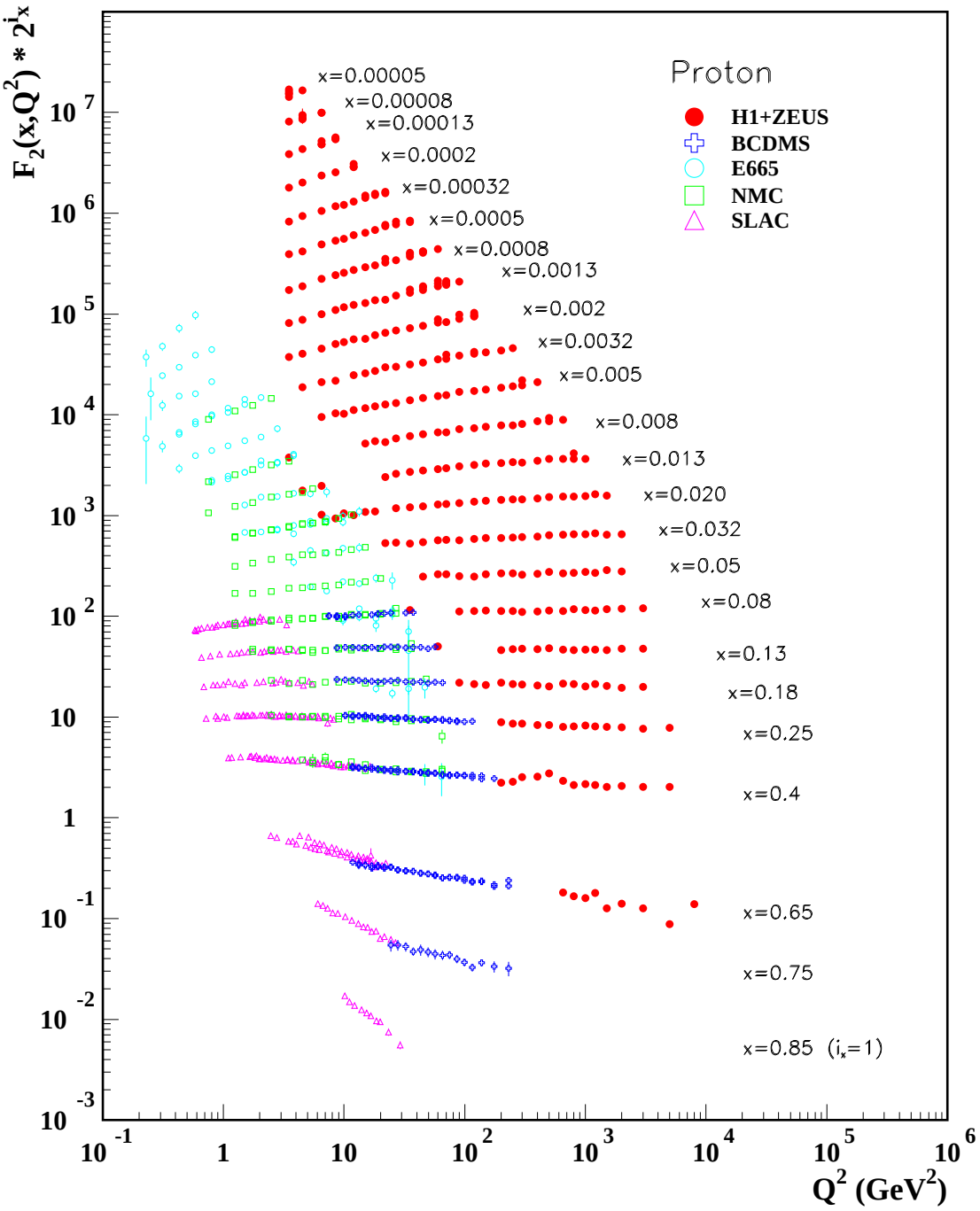

FIGURE 1.3: The structure function F_2^p measured at fixed target experiments using electrons and measured at collider experiments. The measurements are shown with an offset depending on the Bjorken-x bin [18].

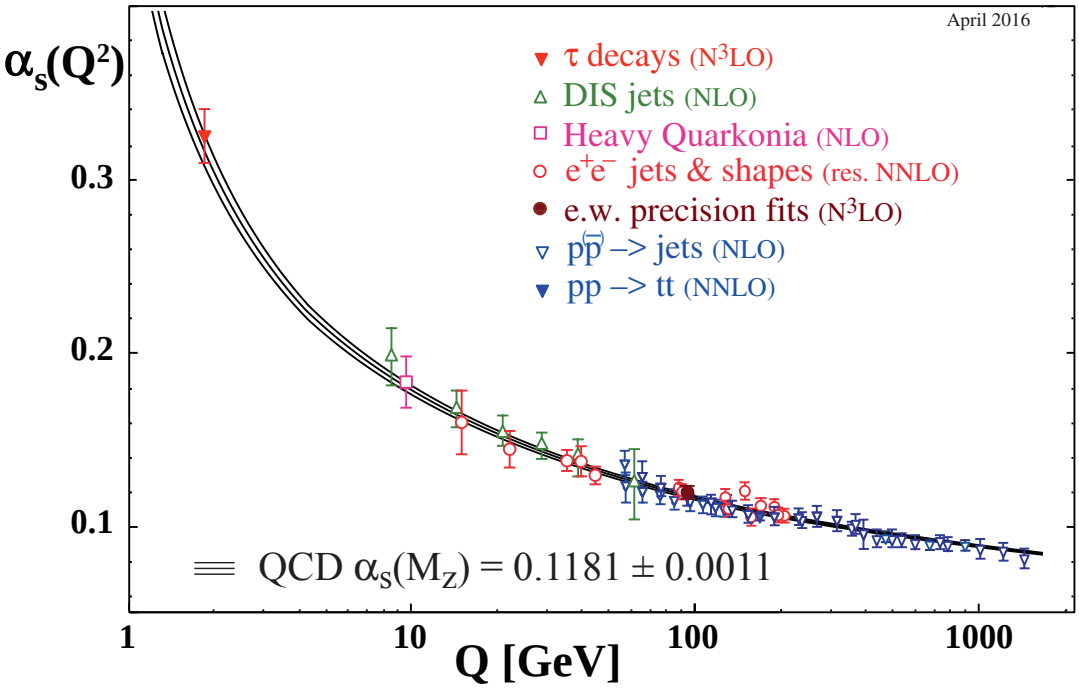

FIGURE 1.4: Evolution of strong coupling constant α_s with Q^2 [18].

Figure 1.3 shows the structure function F_2 as a function of Q^2 for different x ranges. We can see that for $0.01 < x < 0.5$ the measurements extended up to $Q^2 = 2 \times 10^4 GeV^2$ and almost no dependence on Q^2 is observed. In this range we can conclude that the quarks are point-like and the observation is consistent with Bjorken scaling. If the quarks were composite, virtual photons of wavelength ($\lambda \sim hc/ \mid \mathbf{Q} \mid$) comparable to the size of quark, would show deviations from Bjorken scaling. The observed scaling consistency therefore implies that quarks must have radius less than $0.001 fm$ [13, 12, 19].

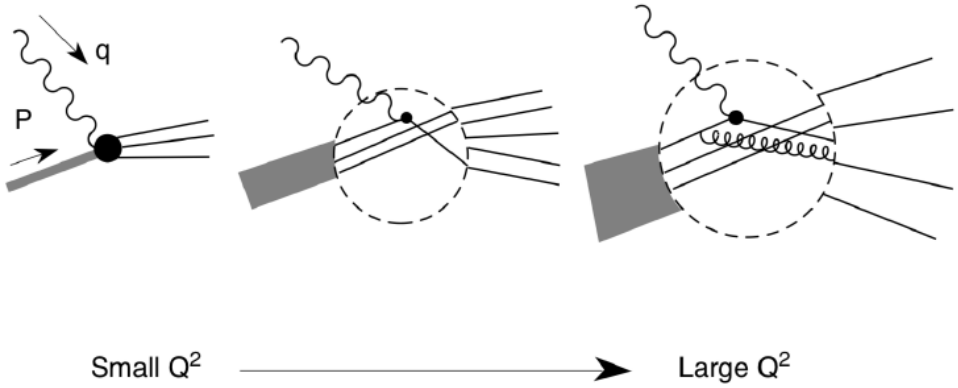

FIGURE 1.5: Resolution of the virtual photon probe at different Q^2, at large Q^2 we become sensitive to the gluon radiation made by the quark.

The QCD predicts a dependence of the strong coupling constant α_s with Q^2, which has been experimentally verified as shown in figure 1.4.

Nevertheless, the data suggests that at very high (low) values of x, the structure functions decreased (increased) with large values of Q^2. Physically we can interpret this observation as follows: at high value of Q^2 there is a presence of large fraction of charged partons with low value of x. This 'scaling violation' is calculable in QCD [20, 13]. At low Q^2 the length scale corresponding to the wavelength of the virtual photon does not allow to resolve any spatial sub-structure. However, at higher value of Q^2 it is possible to resolve the the finer detail. In this case, the deep inelastic scattering is sensitive to the quark radiating virtual gluons, $q \rightarrow qg$ process at small scale. Consequently, at high Q^2 more low x partons are "seen", figure 1.5 depicts the underlying concept.

1.2 Spin dependent deep inelastic scattering

The spin dependent deep inelastic scattering reveals information about the spin orientation of the quarks and gluons inside the proton (or nucleon in general). Contrary to unpolarised DIS spin dependent DIS access information on the polarisation of the partons inside the nucleon. The cross-section in equation 1.10 allows to extract the helicity of the quarks in a longitudinally polarised nucleon. Similarly, we can form another equation with different combination of the g_1 and g_2 for the cross-section of DIS on transversely polarised nucleons [21].

1.3 Semi inclusive deep inelastic scattering

Information obtained from the deep inelastic scattering is limited. The semi inclusive deep inelastic scattering (SIDIS) is a sensitive tool to access quantities like transversity and transverse momentum dependent PDFs, where

Transversity is the probability distribution of transversely polarised quark in a transversely polarised nucleon. Unlike the helicity distribution function, transversity is chirally odd, which restricts its appearance in the handbag diagram of inclusive DIS. To access this observable directly, the chirality must be flipped twice. Therefore hadrons states are needed for both initial and final state. In the SIDIS method a leading hadron is detected in coincidence with the scattered muon. In this framework another invariant variable is defined, representing the fractional energy of the hadrons:

$$z = \frac{\mathbf{P} \cdot \mathbf{p_h}}{\mathbf{P} \cdot \mathbf{q}} = (\frac{E_h}{\nu})_{lab} \tag{1.11}$$

The SIDIS cross-section can be written in the leading order as:

$$\frac{d^3\sigma}{dxdydz} = \frac{8\pi\alpha^2 ME}{Q^4}\left[xy^2 H_1(x, Q^2, z) + (1-y)H_1(x, Q^2, z)\right] \tag{1.12}$$

The structure functions H_1 and H_2 can be interpreted in terms of standard dimensionless F_1 and F_2, according to Mulders and Levelt [22]. The relationship is the following:

$$\begin{aligned} < n_h(x) > F_1(x) &= \int dz H_1(x,z) \\ < n_h(x) > F_2(x) &= \int dz H_2(x,z) \end{aligned} \tag{1.13}$$

$< n_h(x) >$ is the average number of hadrons h produced with Bjorken x.

1.3.1 SIDIS in quark parton model : Factorization

The cross-section of the SIDIS can be realised as a convolution of three independent processes. 1. The soft part $q(x)$s are the PDFs. 2. The hard process σ_q is the cross-section of the absorption of the virtual photon by the quark q and 3. the soft part $D_q^h(z)$, describes the probability that a quark q fragments into a hadron h with fractional energy z. In this factorization ansatz process 1. and 3. are non perturbative and 2. is a perturbative term. The structure function described in equation 1.13 contains the information of the struck quark. The fragmentation function (FF) contains the information on the generation of a hadron type of h from the quark of flavour q. The spin averaged SIDIS cross section can be written at the leading order as:

$$\frac{d^3\sigma}{dxdydz} = \frac{8\pi\alpha^2 ME}{Q^2}\left[\frac{1}{2}y^2 + (1 - y - \frac{y^2\gamma^2}{4})\right] \times \sum_q e_q^2 q(x) D_q^h(z) \tag{1.14}$$

The extraction of FFs can also be done from e^+e^- and hadron-hadron collision. However, the SIDIS allows to access fragmentation function separately for quark and antiquarks along with the parton kinematics. Despite

the fact that the theoretical description of the e^+e^- annihilation has been obtained up to $NNLO$ order and it is so far the cleanest process, without invoking model-dependent algorithms for quark-flavour tagging only limited flavour separation is possible. Kniehl, Kramer and Pötter tested experimentally that the fragmentation function is universal [23]. Different models have been developed to describe how quarks confine together to make a hadron. Lund String model describes the hadron production by creation of $q\bar{q}$ production.The model predicts that in addition to the particle jets formed along the original paths of two separating quarks, there will be a spray of hadrons produced between the jets by the string itself, which is precisely what is observed at colliders. The fragmentation functions extracted from e^+e^- data showed their dependence with Q^2. In figure 1.6 the dependence on Q^2 of the Fragmentation Functions extracted from e^+e^- data is shown.

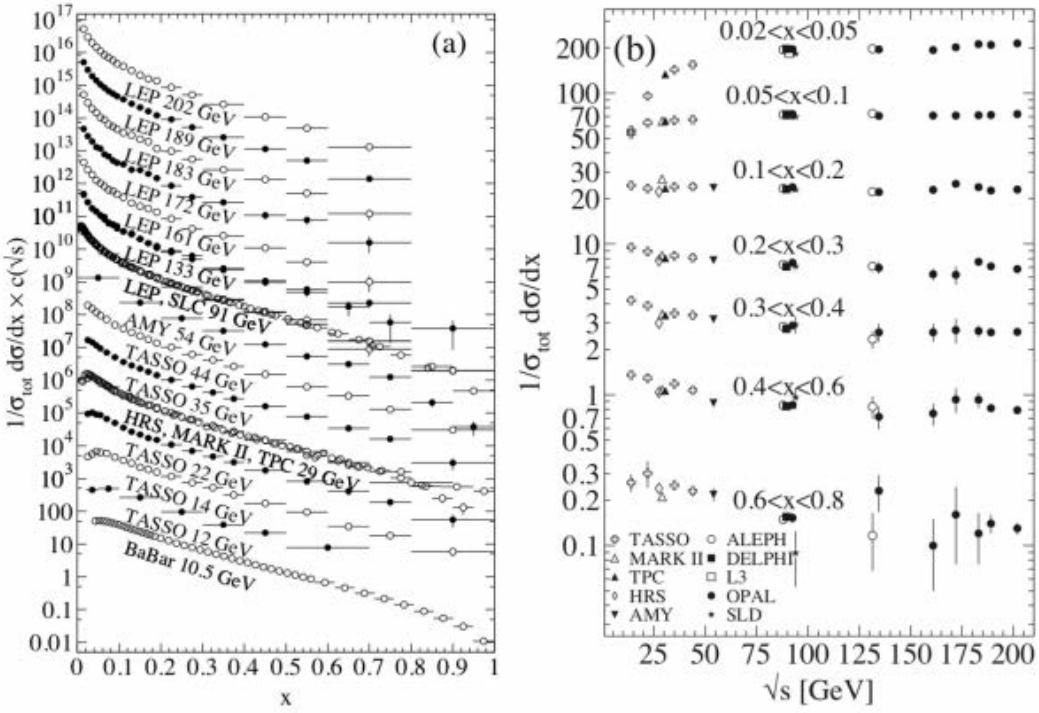

FIGURE 1.6: The e^+e^- fragmentation function for all particles versus x for different $\sqrt{s}$ which has same meaning of Q^2 is shown in the left, in the right the fragmentation function versus $\sqrt{s}$ for different x [18].

This behavior is similar to the PDF one. The Q^2 evolution of the FFs can also be described by the DGLAP [20, 24, 25] evolution equation.

$$\frac{dD_q^h(z,Q^2)}{dlnQ^2} = \frac{\alpha_s(Q^2)}{2\pi}\sum\int_x^1 (P_{qj}(z/\xi,\alpha_s(Q^2))D_q^h(\xi,Q^2))\frac{d\xi}{\xi} \tag{1.15}$$

For each hadron species h, one FF can describe its relation to one quark flavour q. Considering only light quarks, we therefore have 12 FFs for positive and negative hadrons. Aiding to the QCD improved parton model,

isospin symmetry or charge conjugation reduces the number of independent FFs. Based on the fact that quarks are valance or sea, the FFs can be grouped as favoured or unfavoured respectively.

1.3.2 Accessing the Fragmentation Function

The FFs can be accessed by means of hadron multiplicities [26]. Hadron multiplicities is the number of hadrons produced per DIS events [27]. At LO the multiplicities are not complex convolutions of the PDFs and FFs, but simple products weighted by the square of the quark electric charge.

$$\begin{aligned} M^h(x,Q^2,z) &= \frac{d\sigma^{lN\to l'hX}}{d\sigma^{lN\to l'X}dz} = \frac{d\sigma^h/dxdQ^2dz}{d\sigma^{DIS}dxdQ^2dz} \\ M^h(x,Q^2,z) &= \frac{\sum_q e_q^2 q(x,Q^2) D_q^h(z,Q^2)}{\sum_q e_q^2 q(x,Q^2)} \end{aligned} \tag{1.16}$$

By measuring the $M^h(x,Q^2,z)$ for positive and negative identified hadrons one can distinguish bewteen D_q^h and $D_{\bar{q}}^h$ [28].

1.4 Experimental studies of nucleon structure: contribution of the COMPASS Experiment

Pioneering experiments on the spin structure of the nucleon performed in the seventies at SLAC were followed by the EMC experiment at CERN which obtained a surprisingly small value for the singlet axial charge, usually interpreted as the quark spin contribution to the nucleon spin. This observation challenged the naive expectation that the spin of the nucleon is built mainly from valence quark spins. This result triggered extensive studies of the spin structure of the nucleon in polarised lepton nucleon scattering experiments at CERN by the SMC and COMPASS, at SLAC, at DESY and at JLAB as well as in polarised proton–proton collisions at RHIC. The COMPASS Experiment, described in chapter 2, has contributed largely for experimental studies of the nucleon structure. COMPASS performed SIDIS experiments to reveal the details of the quark-gluon structure of the nucleon, in particular the gluon polarisation and the quark transversity distributions. Using the naturally polarised muon beam and longitudinally polarised targets COMPASS has extracted the flavour separated helicity distributions, where n, the double spin asymmetries for hadrons h produced in the current fragmentation region has been extracted as a function of x [29], which is shown in figure 1.7.

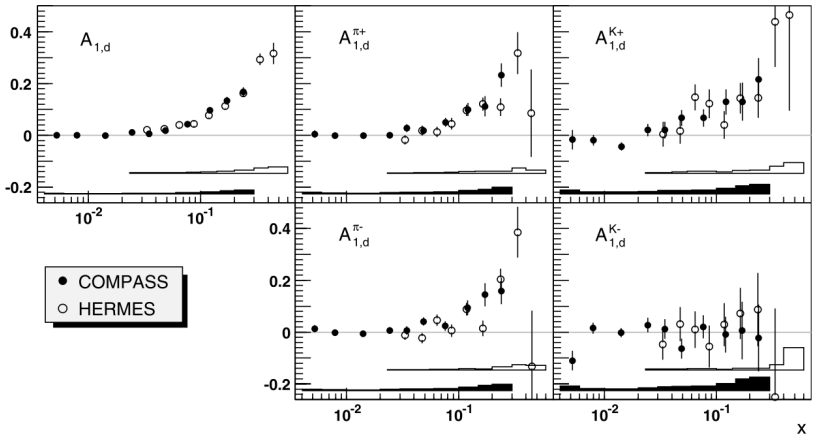

FIGURE 1.7: Comparison of final asymmetries [29] of COMPASS as a function of x with results of HERMES. Bands at bottom of graphs represent systematic uncertainties. Solid markers and bands correspond to COMPASS data. Open markers and bands are taken from the HERMES publication.

These measurements are used in combination with the inclusive asymmetries to evaluate the polarised valence, non-strange sea and strange quark distributions. Figure 1.8 shows the extraction of strange quark spin distribution $x\Delta s(x)$ at $Q^2 = (3GeV/c)^2$ derived from the charged kaon asymmetry $A_{1,d}^{K^+ + K^-}$ using DSS FFs and from $A_{1,d}$.

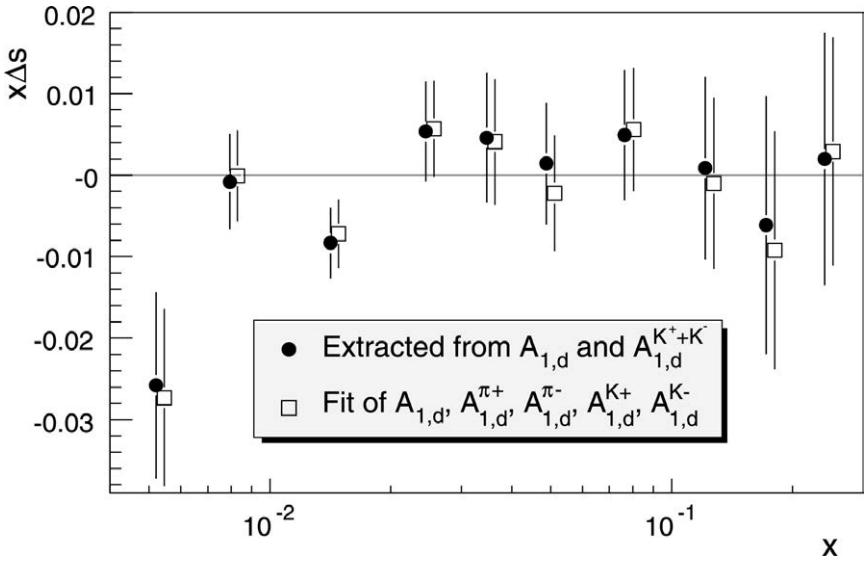

FIGURE 1.8: The strange quark spin distribution $x\Delta s(x)$ at $Q^2 = (3GeV/c)^2$ derived from the charged kaon asymmetry $A_{1,d}^{K^+ + K^-}$ using DSS FFs and from $A_{1,d}$, compared to the result of the corresponding least square fit. The quoted errors are statistical only [29].

Apart from the quarks, the gluon polarisation has been measured assuming the open-charm production is dominated by the photon-gluon-fusion

(PGF) mechanism yielding a $c\bar{c}$ pair which fragments mainly into D mesons and also by high-p_T hadron pair production, where p_T is the transverse momentum of the produced hadron.
The measurement of the $< \Delta g/g >$ by open charm mechanism is much less model dependent compared to high-p_T hadron pair production, and both results has been found compatible to each other [30]. The results of $< \Delta g/g >_x$ extracted from open charm mechanism and its comparison with other method, namely high-p_T hadron pair production, done at COMPASS and elsewhere is shown in figure 1.9.

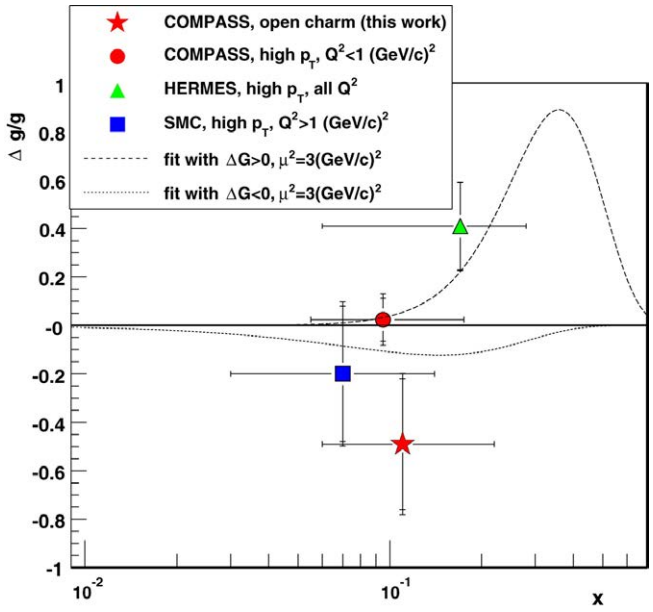

FIGURE 1.9: COMPASS extracted results of $< \Delta g/g >$ in different methods as a function of x and its comparison with different experiments [30].

COMPASS has extracted the Collins and Sivers asymmetries both from transversely polarised proton [31] and transversely polarised deuterium targets [32]. These results are essential ingredients to have a complete understanding of the structure of the nucleon twist two level, where the transverse spin distributions $\Delta_T q(x)$ must be added to the better known spin-average distributions $q(x)$ and to the helicity distributions $\Delta q(x)$. The transversity distribution is difficult to measure in inclusive Deep Inelastic scattering, due to the chiral odd nature of transversity. A convolution of this chirally odd transversity to a chirally odd FF could allow us extract the transversity from a measurable single spin asymmetry. The asymmetry arises due to the combined effect of the $\Delta_T q(x)$ and the chirally odd FF. At leading twist, the existence of such a naively T-odd FF arising from final state interaction effects, was predicted by Collins [33]. Figure 1.10 shows the Collins asymmetries for charged pions (top), charged kaons (middle) and neutral kaons (bottom) on transversely polarised proton as a function of kinematic variables x, z and p_T^h measured by COMPASS.

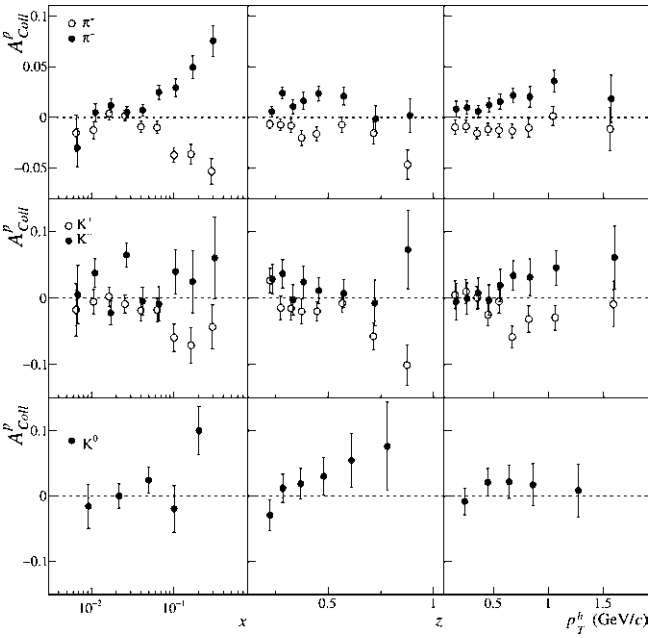

FIGURE 1.10: The Collins asymmetries for charged pions (top), charged kaons (middle) and neutral kaons (bottom) on proton as a function of kinematic variables x, z and p_T^h [31].

The same asymmetry has been studied with transversely polarised ^6LiD target as a function of kinematic variables x, z and p_T^h, the results are shown in figure 1.11.

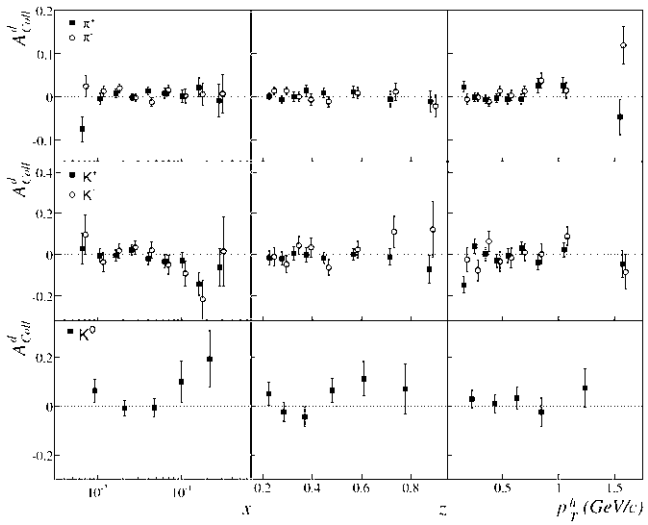

FIGURE 1.11: The Collins asymmetries for charged pions (top), charged kaons (middle) and neutral kaons (bottom) on ^6LiD as a function of kinematic variables x, z and p_T^h [32].

An entirely different mechanism was suggested by Sivers [34] as a possible cause of the transverse spin effects observed in pp scattering. This mechanism could also be responsible for a spin asymmetry in the cross-section

of SIDIS of leptons off transversely polarised nucleons. COMPASS has extracted the Sivers asymmetry as a function of the kinematic variables x, z and p_T^h using transversely polarised proton and transversely polarised ^6LiD target. The results are shown in figures 1.12 and 1.13 respectively.

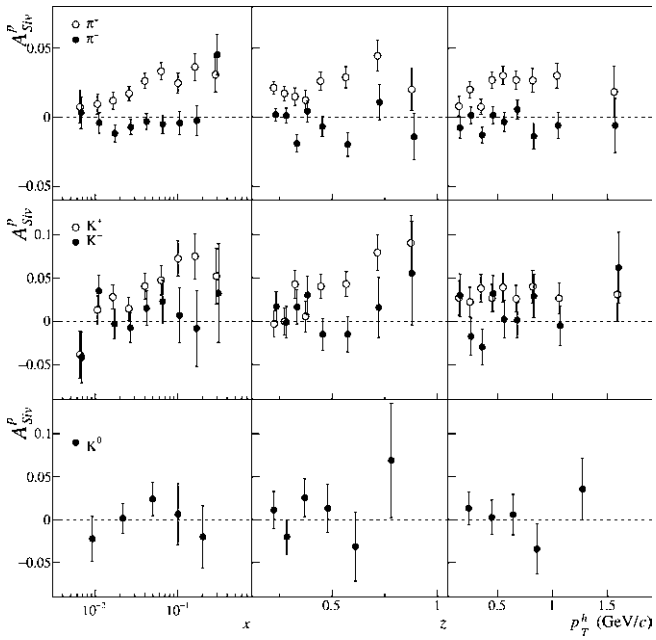

FIGURE 1.12: Sivers asymmetry against x, z and p_T^h for transversely polarised proton data [31].

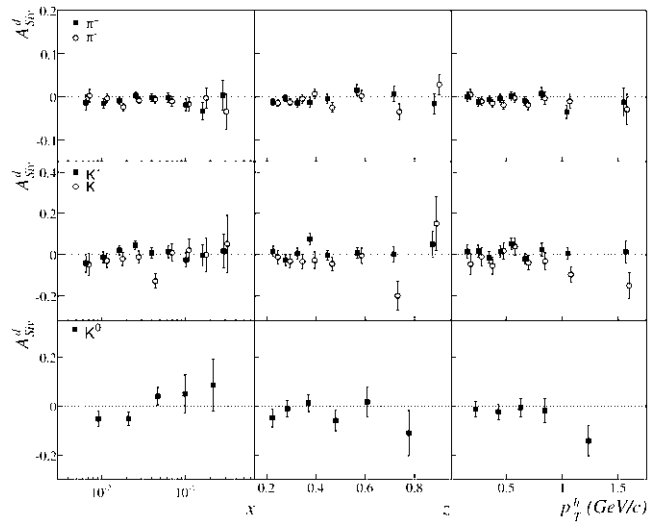

FIGURE 1.13: Sivers asymmetry against x, z and p_T^h for transversely polarised ^6LiD data [32].

The years 2008 and 2009 were dedicated to hadron spectroscopy [35]. Pion and proton beams were bombarded on hydrogen and nuclear targets to explore subtle details of light-meson spectrum. The pion polarisability [36] using Primakoff scattering of pions from heavy nuclei was also studied

in 2009. During the phase-II of COMPASS the transverse and 3D structure of nucleons are studied in detail by means of Deeply Virtual Compton scattering (DVCS), Hard Exclusive Meson Production (HEMP) [37], SIDIS and polarised Drell-Yan (DY) reactions. The first-ever polarised Drell-Yan measurement [38] with a beam of negative pions and a polarised proton target was successfully performed in 2015 and the data taking was resumed in 2018. The years 2016 and 2017 were dedicated to DVCS measurement and simultaneously data on HEMP and SIDIS were collected.
In recent years COMPASS reported results on charged-hadron, pion and kaon multiplicities obtained over a wide kinematic range [39]. Figure 1.14 shows the x-Q^2 range of the selected DIS events in COMPASS experiment. The extracted results for the pion multiplicities as a function of z for 9 different x bins can be seen in figure 1.15 where the positive pions are represented by closed circles and negative pions are represented by open circles. The data shown had been collected by impinging naturally polarised muon beam on an isoscalar target, namely ^6LiD.

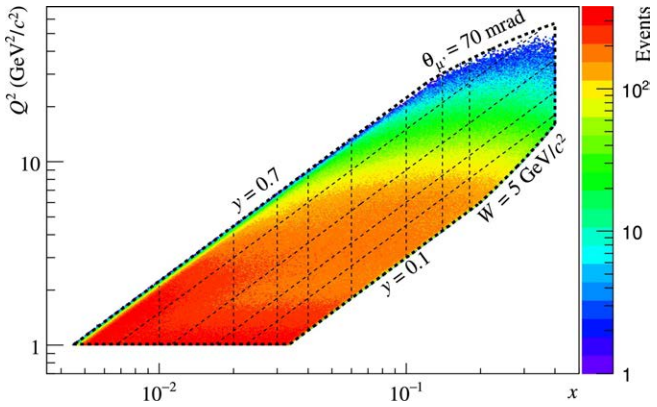

FIGURE 1.14: (x, Q^2) range of the selected DIS sample [39].

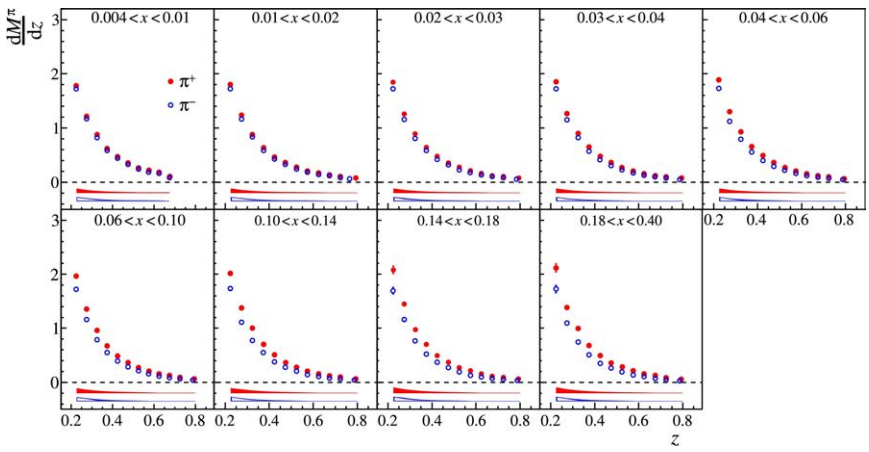

FIGURE 1.15: Positive (closed) and negative (open) pion multiplicities versus z for nine x bins. The bands correspond to the total systematic uncertainties [39].

These results provide important input for phenomenological analyses of FFs. The pion multiplicities were found to be well described both in leading-order (LO) and next-to-leading order (NLO) pQCD, while this was not the case for kaon multiplicities. The region of large z appears to be particularly problematic for kaons, as it was also observed in subsequent analyses of the COMPASS multiplicities. Here, z denotes the fraction of the virtual-photon energy carried by the produced hadron in the target rest frame.
Not only the aforesaid measurements but also COMPASS has published results on the K^- over K^+ multiplicity ratio in the large-z region, i.e. for z > 0.75. Moreover, instead of studying multiplicities for K^- over K^+ separately, their ratio R_K is analysed as in this case most experimental systematic effects cancel. Similarly, the impact of theoretical uncertainties, e.g. scale uncertainties, is largely reduced in the ratio. Also, while pQCD cannot predict values of multiplicities, limits for certain multiplicity ratios can be predicted [40]. The extracted and published result of COMPASS can be seen in figure 1.16.

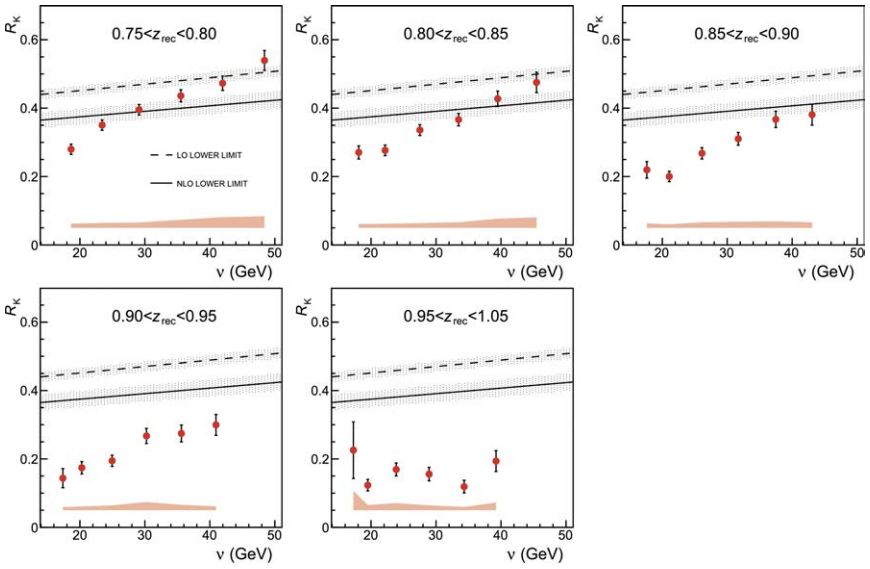

FIGURE 1.16: The K^- over K^+ multiplicity ratio as a function of ν in bins of z, shown for the first bin in x. The systematic uncertainties of the data points are indicated by the shaded band at the bottom of each panel. The shaded bands around the (N)LO lower limits indicate their uncertainties [40].

For 2021 after long shut-down 2, further measurements of SIDIS off transversely polarised deuterons are approved. A rich program of future measurements is proposed by the COMPASS++/AMBER Collaboration, starting with a precise measurement of the proton charge radius [41] in 2022 and 2023.
Similar to the many other studies where the knowledge of the final state hadrons are essential (e.g. flavour seperated helicity distribution, gluon polarisation via open charm mechanism, Collins and Siveres asymmetry, meson spectroscopy etc.) the extraction of the identified hadron multiplicities an efficient particle identification is mandatory. In COMPASS Experiment the particle identification (PID) is done by using the RICH detector, described

in detailed in chapter 3. The current particle identification procedure is depended on a likelihood function, which is based upon the number and distribution of the photons that are detected by the photon detectors of three different technologies mounted on the RICH and the detected photons are associated to a charged particle trajectory. The likelihood values are calculated by comparing the reconstructed Cherenkov angle for each photon with the one expected for different mass hypotheses (π, K, proton), taking the distribution of background photons into account. The mass is assigned to the detected hadron choosing the hypothesis with the maximum likelihood. In order to improve the separation between the different mass hypotheses and thus the sample purity, constraints are imposed on the ratios of the maximum over the other likelihood values. The purity of the identified hadron samples depends on the probabilities of correct identification and misidentification. The true hadron yields N_{true} are obtained by applying an unfolding algorithm to the measured hadron yields N_{meas}:
$N^i_{true} = \sum_j (P)^{-1}_{ij} N^j_{meas}$
The RICH PID matrix P contains as diagonal elements the efficiencies and as off-diagonal elements the misidentification probabilities.

Summarising, the structure of the nucleon can be probed efficiently by deep inelastic scattering. The semi inclusive deep inelastic scattering allows to access further information of the quark distribution inside the proton and also allows us to access the fragmentation function, which is a universal quantity describing the hadronisation of the quarks.
In the kinematic range of the COMPASS Experiment at CERN SPS, SIDIS measurements allow to extract pion, proton and kaon multiplicities, the kaon ones allow to gain insight the hadronisation of the s and $\bar{s}$ quark too.
COMPASS has taken data in 2016 and 2017 with an unpolarised proton target, the identified pions and kaons allow us to measure the pion and kaon multiplicities and to access the related fragmentation functions. The pions are copiously produced compared to the kaon, therefore, efficient separation between pion and kaon is mandatory for the measurement of multiplicities of identified hadrons. An efficient particle identification is thus mandatory. The core of the particle identification is based on a likelihood function, which is based upon the number and distribution of photons that are detected by the photon detectors of the RICH and the photons are associated to a charged particle trajectory. Therefore the efficient performance of the COMPASS RICH photon detection system is uncompromising.

Chapter 2

The COMPASS experiment at CERN

2.1 Introduction

COMPASS [42, 43] is a high-energy physics experiment, collaborated by 200 physicists from 13 countries and 25 institutions, at the Super Proton Synchrotron (SPS) of CERN in Geneva, Switzerland aimed to study the hadron structure and perform hadron spectroscopy using high intensity muon and hadron beams. It consists a two stage spectrometer, the stages being determined by two spectrometer magnets. Both stages are equipped with many layers of trackers, electromagnetic and hadronic calorimeters, muon identification systems. The first stage of the spectrometer hosts a $3.3m$ long gaseous Ring Imaging Cherenkov counter for hadron identification. The layout of the spectrometer is presented in figure 2.1.

2.2 Spectrometer for SIDIS physics

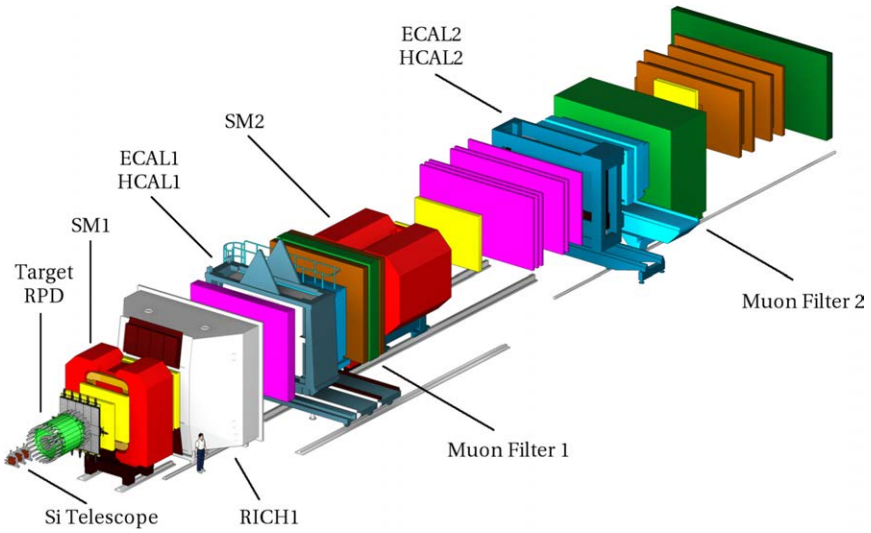

FIGURE 2.1: Layout of the COMPASS spectrometer

2.2.1 Beam

The lepton nucleon scattering program at high $\sqrt{s}$ provides more information about the structure of the nucleon. COMPASS uses muon beams with momenta of 100, 160 and 190 GeV/c, produced from the decay of the pions, and hence naturally polarised. The schematic of the CERN M2 beam-line is shown in figure 2.2.

A detailed description of the M2 beam line can be found elsewhere [44, 45]. Currently SPS beam can be tuned to have positive beam of muons upto 190 GeV/c or high intensity hadron beams (mainly proton and pion, positive and negative) up to 280 GeV/c. Negative muon beams are available with lower intensity. Low-energy tertiary electron beams are used for calibration purposes. Fully computer controlled systems provide a relatively easy and fast way to change the beam modes.

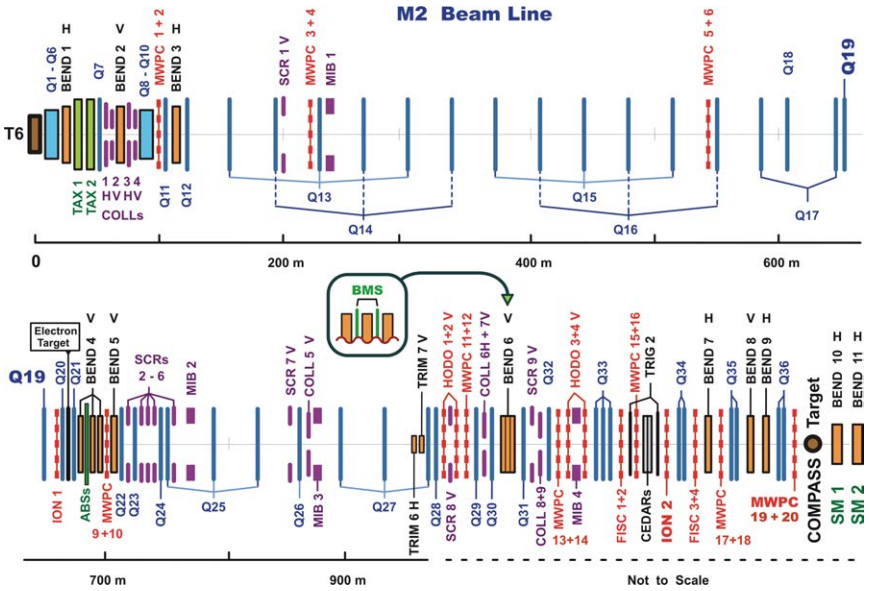

FIGURE 2.2: Schematic view of the CERN M2 beam line. Taken from [43]

Proton beam of nominal flux 1.2×10^{13} per SPS cycle during 4.8 s long spills at momentum 400 GeV/c are extracted from CERN SPS, to generate muon beam with intensities and momentum required for COMPASS. The proton beam is impinged on a 500 mm Beryllium target (T6 target) and generated pions are selected using 6 acceptance quadrupoles and 3 dipoles. The pions have momenta within $\pm 10\%$ around the nominal momenta 225 GeV/c. They are also within a geometrical acceptance of 3 μsr. The pion flux has a 3.6% contamination from kaons. The pions are allowed to travel 650 m channel of regularly alternating focusing and defocusing quadrupoles. At this phase the pions are decayed into muons and neutrinos. The parity violating decay of pions ensures that the muons are naturally polarised. However, the muons are then filtered by focusing and the hadrons are absorbed by 9 motorised modules of 1.1 m long Beryllium. Beryllium is a low Z material. Hence, the multiple scattering will be much less compared to high density

materials. The absorbers are inside the apertures of three dipole magnets in series providing a 4.8 *mrad* of deflection by each. A fourth dipole adding another 9.6 *mrad* of deflection, resulting a total of 24 *mrad* of deflection, in order to obtain a good momentum separation. The accepted muon beams are cleaned and momentum is selected by two horizontal and three vertical magnetic collimators. Furthermore,these skimming muons are allowed to pass another 250 m long FODO channel.Before getting impinged to the COMPASS target the muons are finally bent by three 5 m long dipole magnets, surrounded by 4 hodoscopes and 2 scintillating fibers planes for momentum measurement. The muon momentum is chosen to be around $90 - 94\%$ of the hadron momentum, in order to provide best compromise between flux and polarisation. The schematics of the beam monitoring station is given in figure 2.3

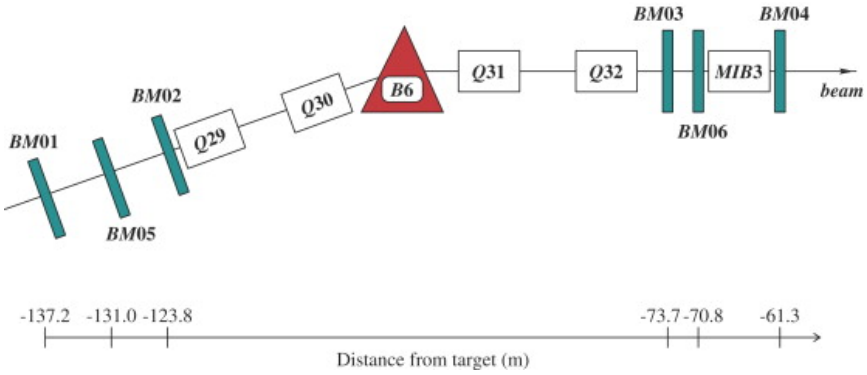

FIGURE 2.3: Schematic of Beam Monitoring Station

The polarisation of the muon decaying from a hadron h at the hadron rest frame can be expressed in terms of ratio of the muon and the hadron energy.

$$P_{\mu^{\pm}} = \mp \frac{m_{\pi}^2 + (1 - 2\frac{E_{\pi}}{E_{\mu}})m_{\mu}^2}{m_{\pi}^2 - m_{\mu}^2} \tag{2.1}$$

The definition of the symbols are the following:

- E_{μ} = Energy of muon.
- E_{π} = Energy of pion.
- m_{π} = Mass of pion.
- m_{μ} = Mass of muon.

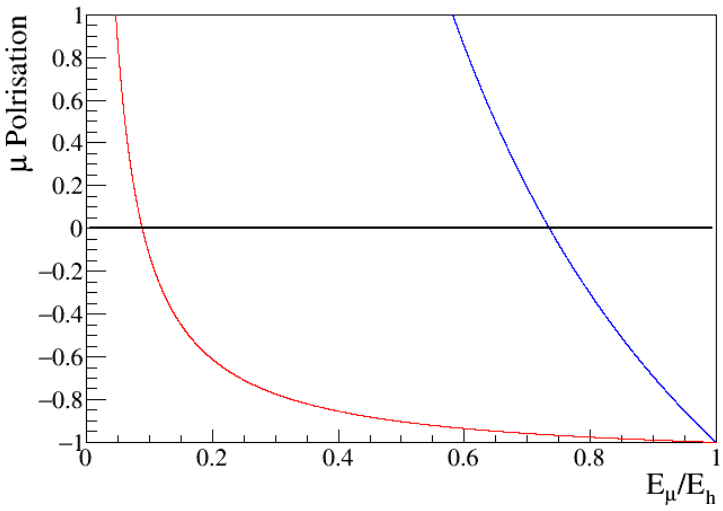

FIGURE 2.4: Polarisation of muons versus energy ratio of muon and the parent hadron. The red curve corresponds to the kaons and the blue curve corresponds to the pions decayed into muons.

In figure 2.4 we see the dependency of the muon polarisation with the ratio of the E_μ / E_h. The blue line corresponds for the pions and the red lines corresponds to the kaons decayed into muons. High positive muon polarisation is obtained for $E_\mu / E_\pi \sim 0.6$ and high negative muon polarization is obtained for $E_\mu / E_\pi \sim 1$. In the first case the muons generated from the kaon decays are polarised in the opposite direction with respect to the pion ones. This condition degrades the muon polarisation. The best option is to take situation similar to $E_\mu / E_h \sim 1$. The statistical factor of merit allows COMPASS to use the muons with momentum 160 GeV/c coming from decaying pions of momentum 172 GeV/c shown in figure 2.5.

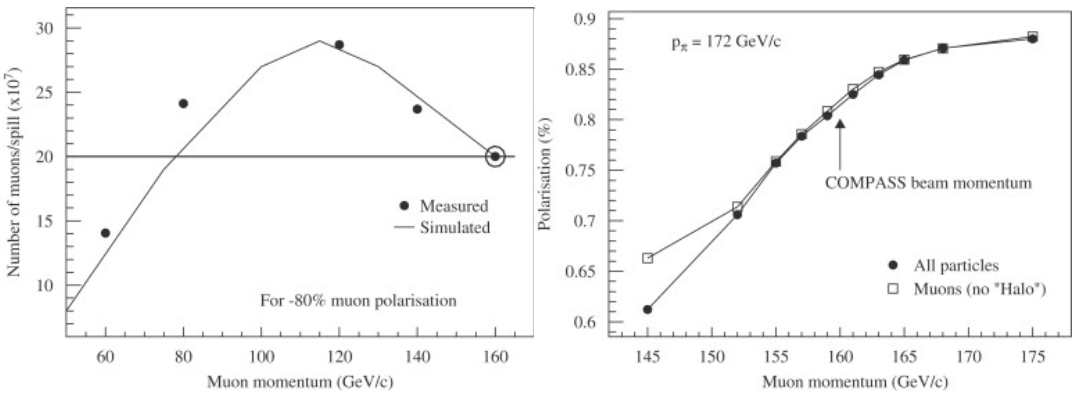

FIGURE 2.5: Left: The dependency of the beam flux with muon momentum. Right: The dependency of muon polarisation with muon momentum. Taken from [42]

2.2.2 Target

To extract the transverse momentum dependent parton distribution functions, COMPASS has mostly used a large polarised target, which is unique in the world. The description of the polarised target can be found elsewhere [46, 47]. For 2016 and 2017 a 2.5 m long liquid hydrogen target was used for the DVCS program [48] complemented by a large proton recoil detector (CAMERA) around the target. The spectrometer is being used to extract the GPDs and quantities related to unpolarised SIDIS physics. The schematic of the target and the upstream visualisation of the CAMERA are shown in figure 2.6. The inner ring of the CAMERA consists of 24 scintillators around the target, each connected with light guides to two photomultiplier tubes (PMT). The outer ring is built around the inner ring and it consists of 24 scintillators and PMTs as well.

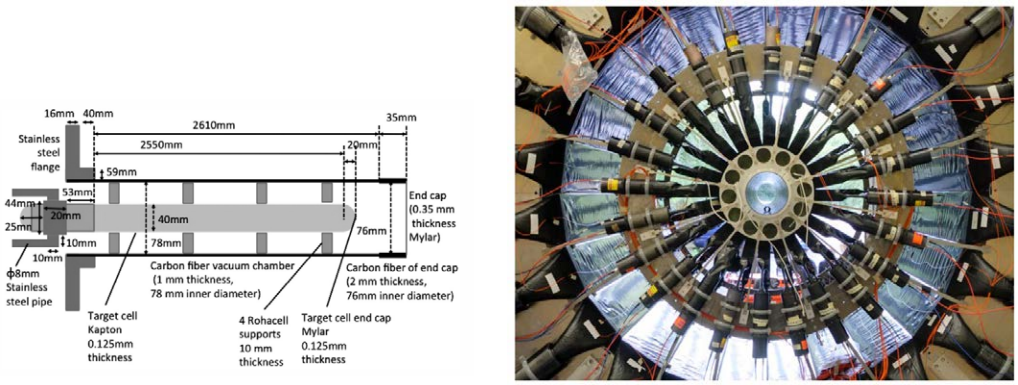

FIGURE 2.6: Left: The schematic figure for the target. Right: Upstream visualisation of the CAMERA

2.2.3 Magnets of the spectrometer

The two dipole magnets define the stages of the spectrometer. SM1 is the magnet used for measuring momentum of the tracks in the large angle spectrometer (LAS) region. Its average integrated magnetic field is $1Tm$. The bending is done in the horizontal plane.
The second dipole magnet SM2 defines the Small Angle spectrometer (SAS). It has a higher bending power than SM1: $4.4Tm$, hence allowing more accurate determination of the momentum of high momentum tracks.

2.2.4 Tracking

More than 300 active planes serve the COMPASS tracking purpose [49]. COMPASS has a pioneering history of using GEMs and Micromegas(MM) in a working experiment. Several families of detector technologies are used for COMPASS tracking. The tracking detectors can be mainly classified into three types, based on the size of their active area. Namely, very small, small and large area trackers. Throughout the 50 m long spectrometer hall, many

tracking stations comprises these detectors. Each station contains several layers of detectors of same type, located approximately at the same z coordinate (recall, positive z is the beam direction, downstream). A charged trajectory is measured in several transverse projection to the beam direction to reduce ambiguities. Near the beam, the detector requirements are stricter: capability to stand high flux, good timing and spatial resolutions are key demands. Requirements are more relaxed for detectors, which are stationed far from the beam. These drive the three aforesaid classifications.

Very Small area Trackers

These trackers cover the radial distance up to 2.5-3 cm near the beam region. The high beam flux in the region, up to 10^5 s^{-1} mm^2 requires, excellent time and space resolution. SciFis, silicon micro-strips and pixelised GEM and pixelised MMs are used in this region. The SciFi detectors consist of several staggered layers of scintillating fibers, allowing large overlap and good detection efficiency. A column of fibres lined up in the beam direction is read out by one channel of a multi-anode photomultiplier tube. In each station, at least a X- and a Y-plane are used. For some stations also a U-plane is added, typically inclined by 45^o. The scintillating fibers have a diameter of 0.5 mm or 1 mm. Hits associated to a muon track are correlated by time information too as only spatial correlation can lead to ambiguities due to high particle rates.

Beside the SciFis the silicon strip detectors are used for improving the space resolution of the incoming muon beam. Figure 2.7 shows a COMPASS silicon tracker. The silicon trackers consist of n-type wafers with 5×7 cm^2 active area. The signals are read out from both sides. One side has 1024 strips and the other has 1280 strips. They are orthogonal to each other allowing to measure muon signatures in the X and Y planes. One detector station is made of two such detectors back to back. The nearby station is inclined by 5^o, to provide U and V coordinates. The detectors are operated at around 130K, to reduced noise and improve time and space resolutions. They provide excellent space resolution of 4-6 μm and also time resolution of 2.5 ns.

Small Area Trackers

The small area trackers region includes MPGD based detectors, GEMs and Micromegas trackers. GEMs [50, 51] are gaseous electron multipliers consisting of a thin composite sheet with two metal layers separated by a thin insulator, and pierced by a regular matrix of open channels. Micromegas (MICRO MEsh GAseous Structure) [52, 53] are gaseous detectors based on a simple geometry with planar electrodes. It is a new generation of reliable and cheap detectors able to cope with very high-particle intensities. It consists of a conversion gap in which charged particles liberate ionisation electrons and of a thin amplification gap. Figure 2.8 shows the operating principle of the Micromegas and the GEM detectors.

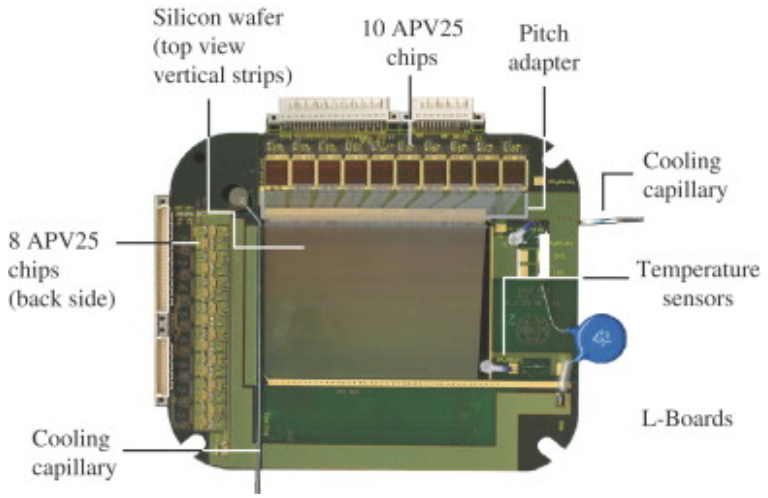

FIGURE 2.7: A Silicon tracking detector for the COMPASS Experiment

11 GEM stations, each consisting of 2 layers with 2D strip readout and having $31 \times 31 cm^2$ of active area are used [54, 55]. GEMs have low material budgets, 0.4% X_0 and provide 12 ns and 70 μm time and space resolution respectively. They are equipped with a central zone of 5 cm of diameter which can be made insensitive for normal data taking.
From the target to the SM1, the COMPASS spectrometer hosts 12 micromegas detectors [56, 57]. The detectors of this region are exposed to a high flux of low energy electromagnetic showers, which is not screened by SM1 and to the influence of the fringe field of SM1. The detectors have an active area of $40 \times 40\ cm^2$ and are readout via 1024 strips. The typical gas mixture which is used is $Ne : C_2H_6 : CF_4$ 80 : 10 : 10. COMPASS MMs provide an efficiency $\sim 96\% - 98\%$, 5 ns of time resolution and 90 μm of space resolution.

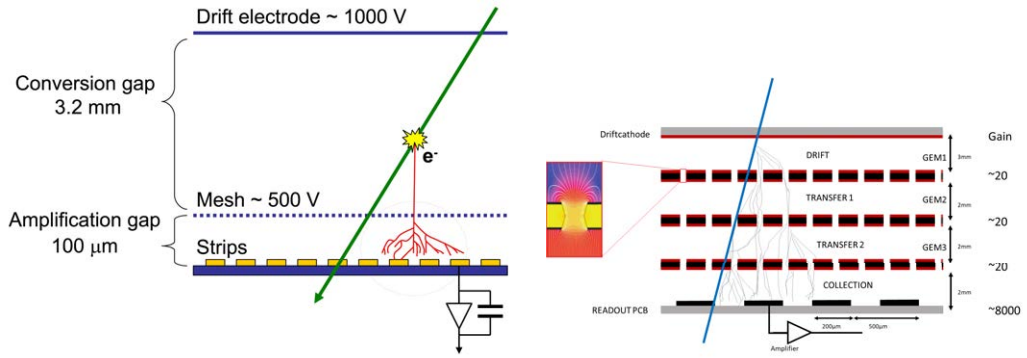

FIGURE 2.8: Working principle of Micromegas and Gas Electron Multiplier(GEM) detectors

Large Area Tracker

The large area trackers are the outermost tracking planes. The reduced flux in the outermost regions allows to reduce the constraints on detector requirements, in terms of radiation hardness, rate capability etc.

The tracking is mainly based on MWPC chambers. A total of 34 wire layers corresponding to 25000 detector channels are installed and are operational. COMPASS has three types of acting MWPCs. Type-A, Type-A^* and Type-B. Type A and A^* MWPCs have a dimension of $178 \times 120\ cm^2$, where Type A has X-,U- and V-plane. There are also Y-plane in A^* MWPCs, Type B has $178 \times 90\ cm^2$ of active area. The spatial resolution is 1.6 mm for these detectors.

The drift chambers are advanced derivative of the technique implemented in MWPC technology. In this technique, the drift time of the avalanche to the anode wire is measured to improve the spatial resolution. The cathode and the potential wires are kept at -1700V and the anode wires are at 0 V. The potential wires are used to form the electric field inside of the detector. In order to solve left-right ambiguities, two drift cells are staggered with shifted wires The detector is filled with a gas mixture of Ar, CF_4 and C_2H_6 or CO_2. Each drift chamber has an insensitive zone in the centre for the passage of the beam in order to avoid the high counting rate. One station consists of several layers of drift cells, whereby two layers are used for each projection.They are staggered to measure all four projections. The U- and V- planes are inclined between 10^o-30^o, providing a spatial resolution between 110-170 μm.
Straw tube detectors are very large area detectors made of straw drift tubes. Each tube is similar to a small drift cell. Several of these tubes are glued together to form a detector plane. In order to avoid left-right ambiguities, again a second staggered layer is added. This forms one straw tube detector. In total 12440 straw tubes were assembled into 15 detectors. Each detector had an active area of about 9 m^2 with a central dead zone of $20 \times 20\ cm^2$. In order to measure three projections of a particle trajectory, one station consists of three detectors, X-, Y-plane and one with inclined by 10^o with respect to the vertical ones. The average resolution is $\sim 200\ \mu m$.

2.2.5 Particle Identification

In COMPASS, the hadron identification is done by a gaseous Ring Imaging Cherenkov detector [58, 59], located in the first stage of the spectrometer and discussed in detail in the following chapter. The working principle of the RICH and a schematic of it is shown in figure 2.9.

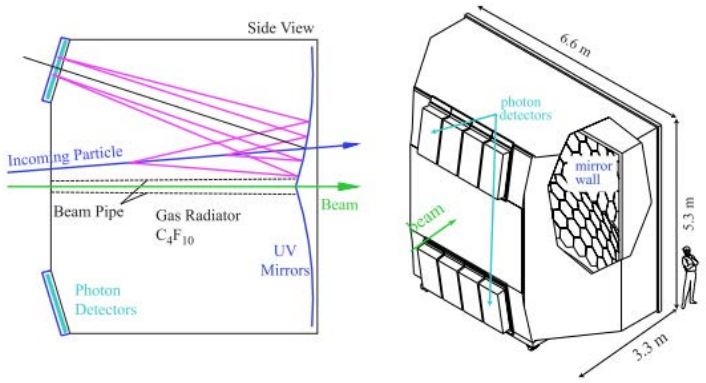

FIGURE 2.9: Left: Schematic slice view of the RICH from the side, the particle can be seen emitting photons and reflected back by the mirror to the detection plane. Right: The Schematic of the RICH

2.2.6 Muon Identification

The muon identification is done by two detector systems: one in LAS, and one in the SAS part. They consists in a set of tracking detectors before and after a hadron absorber. The absorber absorbs the hadron and hence allows to separate the muons from the hadrons. The muon stations are located at the very end of each spectrometer stage.

In the first stage they are called muon wall-1 and composed of 8 mini drift tubes, for particle detection. These tubes are grouped into two parts separated by a 60 cm thick iron absorber. Each half has two planes to measure the X-projection and two planes for the Y-projection. For both absorbers there is a hole to match the acceptance.

In the second stage the muon identification is done by using trackers before 2.4 m long concrete absorber and two stations of muon wall2 after the absorber together with three MWPCs. These two stations contain six planes of X-, Y- and two planes inclined by 15^o. These tubes are made of stainless steel with inner diameter of 29 mm, with gold coated tungsten anode wire of diameter 50 μm. They are operated in $Ar : CH_4$ gax mixture. Two other absorbers are present in the second spectrometer stage. These absorbers are located at the end of the spectrometer in front of the trigger hodoscopes and consist of iron.

2.2.7 Calorimeters

The COMPASS experiment is equipped with electromagnetic and hadronic calorimeters in both stages of the spectrometer. In each stage the electromagnetic calorimeter is upstream of the hadronic calorimeters. The electromagnetic and hadronic calorimeters in LAS and SAS are called ECAL1,HCAL1 and ECAL2, HCAL2 respectively. The hadronic calorimeters are sampling calorimeters. Namely, the materials for the generation of the hadronic shower

and the generation of scintillation by the particles of the shower are different. On the other hand, the electromagnetic calorimeters are mostly homogeneous, which means the same material is used for the electromagnetic shower and scintillation. It is extremely important for the DVCS physics to detect hard photons in the final state. To extend the coverage at large angles in 2016-2017 run, COMPASS has installed another electromagnetic calorimeter downstream to the proton recoil detector of the target, called ECAL0.

Electromagnetic Calorimeters

The ECAL0 is made of sampling 'shashlik' structure. Each of them consists of a lead/scintilator stack and the generated photons are readout by Multipixel Avalanche PhotoDiode(MAPD) as photon detector with ultrahigh pixel density, (up to 15K pixels per mm^2) [60].

The ECAL1 and ECAL2 are made of lead glass, where the electromagnetic shower is generated inside the lead glass. The electrons and positrons from a shower emit Cherenkov light on their way through the glass. The amount of the Cherenkov light is proportional to the energy deposited in each counter. Each block of lead glass is viewed at one end by a PMT which measures the intensity of the light emitted at the counter. The ECAL1 is composed of lead glass of three different sizes: Centrally, 576 blocks of $38.2 \times 38.2\ mm^2$, intermediate region with 580 blocks of $75 \times 75\ mm^2$ and the external most region with 320 modules $143 \times 143\ mm^2$. The ECAL2 is made of 2972 modules(64×48). The energy resolution is ECAL2 is $5.5\%/\sqrt{E} \oplus 1.5\%$ and the space resolution is $6\ mm/\sqrt{E} \oplus 0.5\ mm$.

Hadronic Calorimeters

The hadronic calorimeters of COMPASS are built out of several modules and each module has a modular structure. They are made of alternating layers of iron and scintillators. The iron plates generates the hadron shower and the scintillators detects the shower.Hadron showers are larger in size compared to the electromagnetic showers and the dimensions of the hadronic calorimeters are larger than the electromagnetic calorimeter ones.

Each module of HCAL1 is composed of 40 layers of iron and scintillators plates, 20 mm and 5 mm thick, respectively, amounting to 4.8 nuclear interaction length. The HCAL2 is a matrix of 22×10 modules. Most of them consists of 36 steel plates of 25 mm thickness and inter-leaved with 5 mm thick scintillators. The overall thickness is 5 nuclear interaction length for the pions and 7 nuclear interaction length for the proton. The parameterised energy resolutions are:

- HCAL1 $\sigma/E = 59.4\%/\sqrt{E} \oplus 7.6\%$ for pions
- HCAL2 $\sigma/E = 65\%/\sqrt{E} \oplus 5\%$ for s

2.2.8 Trigger

COMPASS records the data event by event. This requires a trigger system to start the readout process. In figure 2.10 we can see an example of detectors for the triggering with muon beams. For the physics programs with muon beam the trigger system is mostly based on the signals from the scattered muons [61]. A veto system, energy deposition in the HCALs and signals from the hodoscopes are used in the trigger decision. The system is made of several hodoscopes composed of scintillator strips. To obtain a trigger signal a special coincidence of signals is required, which is obtained from at least two hodoscopes, which are at different positions in the spectrometer and at least one of them is behind an absorber allowing only muons to pass.

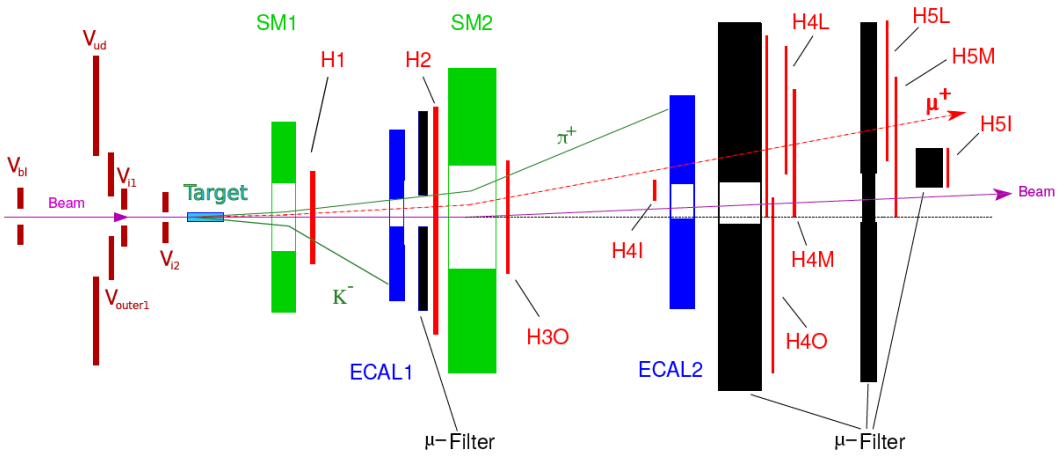

FIGURE 2.10: Example of compass trigger setup, for physics with muon beams.

For the hodoscopes based triggers two methods are used:

- Target pointing method
- Energy loss method

To cover different kinematic regions COMPASS has five different trigger systems. Namely, inner trigger(IT), ladder trigger(LT), middle trigger(MT), outer trigger(OT) and LAS trigger(LAST).

Target pointing method

Events with $Q^2 >\sim 0.5\ (GeV/c^2)^2$ are mainly triggered by the scattered muon information only. The spectrometer magnets deflect the charged particles in the horizontal plane of the spectrometer hall. In the vertical plane the angle of the muon is preserved. Therefore the angle can be measured and

only muons coming from the target will be accepted. A pair of hodoscope stations with horizontal strips are used for this triggering method. Considering all possibilities of coincidence combinations of the signals coming from the two hodoscopes a matrix is formed. The final trigger decision is made from pixels which corresponds to interaction inside the target region. These are the diagonal elements of the coincidence matrix. Using the central strips, the position of the interaction cannot be determined. This results in a singularity in the matrix. This principle is used in LAST, OT and MT.

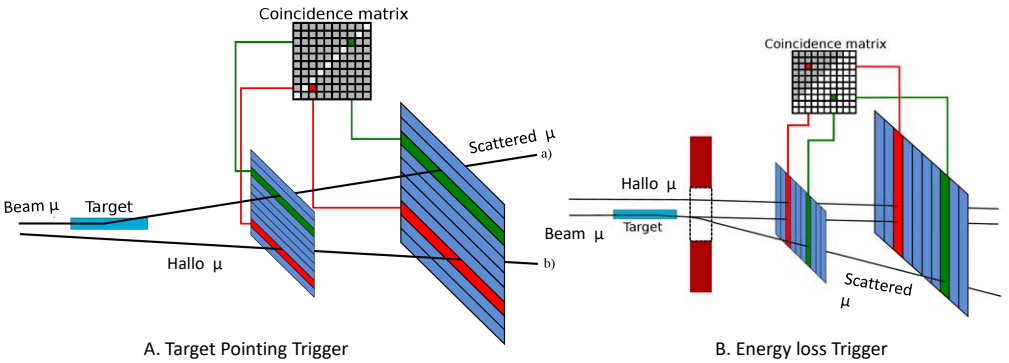

FIGURE 2.11: Left: Target pointing trigger, Right: Energy loss trigger

Energy loss Trigger

The previous method is only applicable to events, where the scattering angle sufficiently large. For quasi-real real photon regime (low Q^2) a different method is applied. Instead of horizontal scintillators, vertical scintillators are used and the deflection in the magnet is taken into account. This bending actually filters out cases where no interaction took place from cases where the energy loss resulted from the interaction providing larger bending. In this case also all possible coincidences are taken in a matrix form, the accepted pixels in the matrix are not diagonal but form a region, due to different possibilities of scattering angles at different energies. The rejected pixels point to events with minimal energy loss. This method is adopted in IT, MT and LT. In figure 2.11 we can see the two different mechanisms. On the left, the target pointing trigger setup and on the right the energy loss trigger set up.

Veto

Another important component of COMPASS triggering is the Veto trigger. The muon beam for COMPASS comes with a halo of sizable divergence and intensity. Without interaction inside the target, the halo may result in trigger

signals. The veto system in front of the target reduces the effect significantly. It is composed of five scintillator hodoscope stations with a central hole for the beam. To veto the halo COMPASS has two large hodoscopes stations and other three hodoscopes veto the part of the beam outside the target region. The final veto signal is an OR of all the signals. The advantage of vetoing is to reduce unwanted trigger signals and hence to reduce processing of unwanted events by the data acquisition system, reducing the dead time. On the other hand, a coincidence of the veto and the trigger signal introduces a dead time.

Calorimeter trigger

This trigger is the only COMPASS trigger for the muon physics programme which does not trigger on muons, rather it triggers on the energy deposition of particles in the calorimeters. This trigger can be used to extend the kinematic range of the system towards large photon virtualities and to trigger on muons outside the acceptance of he hodoscopes. To distinguish between the muons and the hadrons, the energy threshold is set higher than the energy deposited by the muons on passing through the calorimeter. The muons deposit minimal ionization energy in the calorimeter. In order to form a "semi-inclusive" trigger, hodoscope trigger is made in coincidence with Calorimeter trigger signal. The Calorimeter trigger threshold is high enough to suppress 90% of the clusters produced by the single muons.

2.2.9 Data Acquisition and reconstruction

The data acquisition system of COMPASS [62] is responsible for the collection of the data from COMPASS spectrometer. The logical steps can be seen in figure 2.12. It has several layers. The layer closest to the detectors is the Front End Electronics (FEE), which captures signals directly from the detectors and digitises them by means of Analog to Sampling Digital Converters (SADCs) or Time to Digital Converters (TDCs), depending on the type of the detector. There are around 300K channels coming from this first layer. The data is readout by CATCH (COMPASS Accumulate, Transfer and Control Hardware) or GeSiCA (GEM and Silicon Control and Acquisition) and Gandalf concentrator modules, based on VME standard and grouped into sub-events, which are read out, assembled and buffered by modern FPGA (Field Programmable Gate Array) based cards. The data taking is synchronised to the Trigger Control System (TCS) [63]. The trigger signals from the TCS are transferred to all FEE via CATCH. At the beginning CATCH initialises all the FEE, the GeSiCA is similar but the name suggests that it has been optimised for GEMs and Silicons and also used by the RICH-1 gaseous PDs. The data is then transferred to the FPGA based special multiplexers and then via a FPGA/Multiplexers switch it is connected to the 8 Readout Buffer (ROB) PCs (maximum throughput 160 MB/s), where they are stored in 512

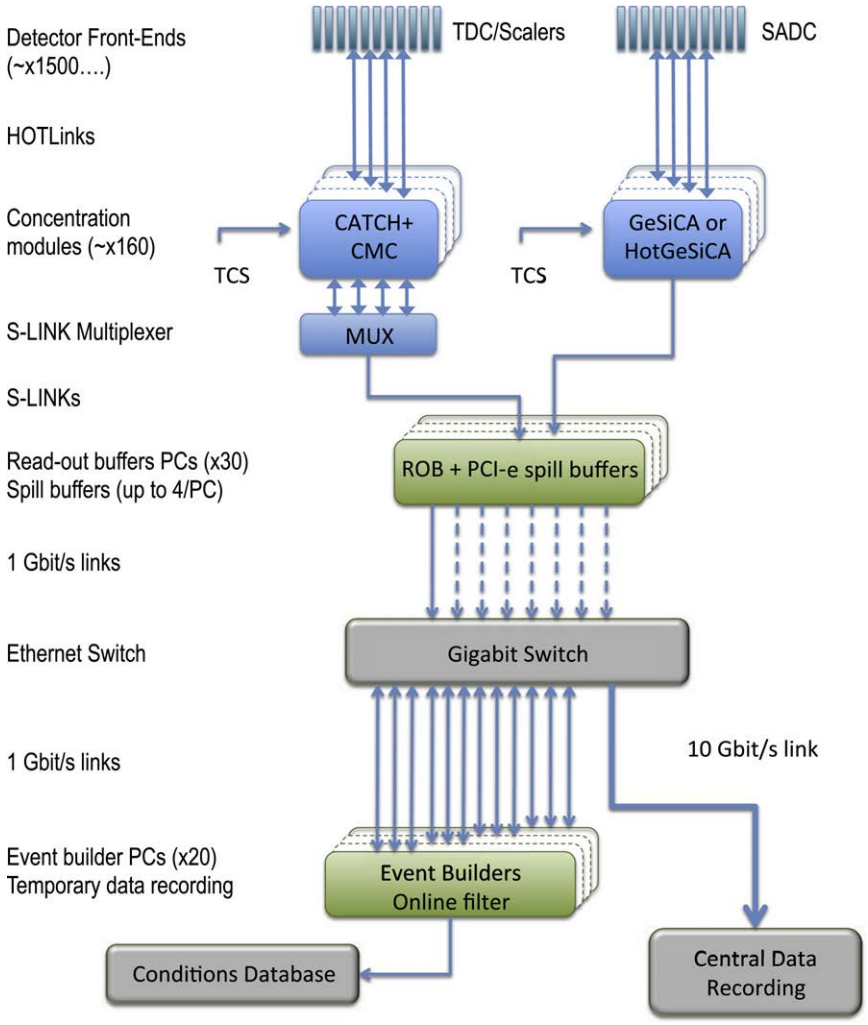

FIGURE 2.12: Logic diagram of the COMPASS DAQ

MB spill buffer cards. For further processing, the information of each subevent in the ROB which do not contain the full information from all detectors, are transferred via three Gigabit Ethernet switches to the event builder (EB) computers. The events are built by 12 event builders and are then written to multiple 1 GB large files (chunks) labeled by the run number and their consecutive chunk number. Eventually, the data are transferred to the CERN central data recording facility (CASTOR).

Chapter 3

Particle Identification techniques

3.1 Introduction

Visual detection techniques (bubble chambers, nuclear emulsion, streamer chambers), which provided a direct image of particle tracks and therefore allowed physicists to perform a complete kinematical reconstruction of events and hence doing particle identification, were extremely important in past days experiments. It was not only limited to charged tracks by accurately calculating the charge and momentum of the tracks but also, the missing momentum allowed to detect the neutral particles from these images. However, these techniques had serious limitations. They had limited rate capability, triggerability and event reconstruction was highly time-consuming. For instance, roughly speaking in 7 TeV LHC, the inelastic proton-proton collision cross-section is ~ 60 $mbarn$, therefore at nominal luminosity of 10^{34} $cm^{-2}s^{-1}$ the event rate is $10^{34} \times 60 \times 10^{-3} \times 10^{-24} = 6 \times 10^{8}$ s^{-1} [64]. It can therefore be realised that in current day high energy physics experiments of comparable rates these techniques can not be adopted. However, demand of fast efficient particle identification has triggered the development of new techniques. These modern particle identification techniques are suitable to cope with the current requirements [65, 66].

Subatomic particles can currently be identified or separated by means of their mass and electrical charge. The mass of the particles can not be measured directly. In order to determine it we need at least two of these three correlated quantities: momentum, kinetic energy and velocity to be measured. If we assume the particle is long lived, practically we can utilise the relativistic mass relationship.

$$m = \frac{p}{c\beta\gamma} \tag{3.1}$$

where all the symbols are carrying usual meaning. In presence of a static magnetic field the curvature of the charged track provides the charge and momentum value. The velocity term can be obtained by many ways: by measuring the time of flight (TOF) of the charged track over a constant distance, ionization energy loss, detection of Cherenkov radiation, and direction of transition radiation. By propagating errors in equation 3.1 we get,

$$\left(\frac{dm}{m}\right)^2 = \left(\gamma^2 \frac{d\beta}{\beta}\right)^2 + \left(\frac{dp}{p}\right)^2 \tag{3.2}$$

From equation 3.2 to estimate the mass precisely, we need a very good determination of momentum and velocity. If we assume that determination of momentum is precise enough to ignore the second term in equation 3.2, we see that we are led by the accuracy in the velocity determination. On top of that, this term is coupled with an additional factor of γ^2, which forces us to be more uncompromising in the accuracy of velocity determination at a higher momentum. If we assume that two particles with mass m_1 and m_2 possess same momenta p, then from equation 3.1 we can write,

$$m_1^2 - m_2^2 = p^2 \frac{\Delta\beta(\beta_1 + \beta_2)}{c^2(\beta_1.\beta_2)^2} \tag{3.3}$$

Where, $\Delta\beta = \left|\beta_1 - \beta_2\right|$. Assuming that $\beta_1, \beta_2 \sim \beta$ we can rewrite 3.3 as;

$$\frac{\Delta\beta}{\beta} = \frac{(m_1^2 - m_2^2).c^2}{2p^2}. \tag{3.4}$$

Figure 3.1 shows how dramatically the beta resolution becomes important with momentum. In an experiment like COMPASS, where we need to do pion kaon separation above $40GeV/c$, we need beta resolution of the order of 10^{-5}.

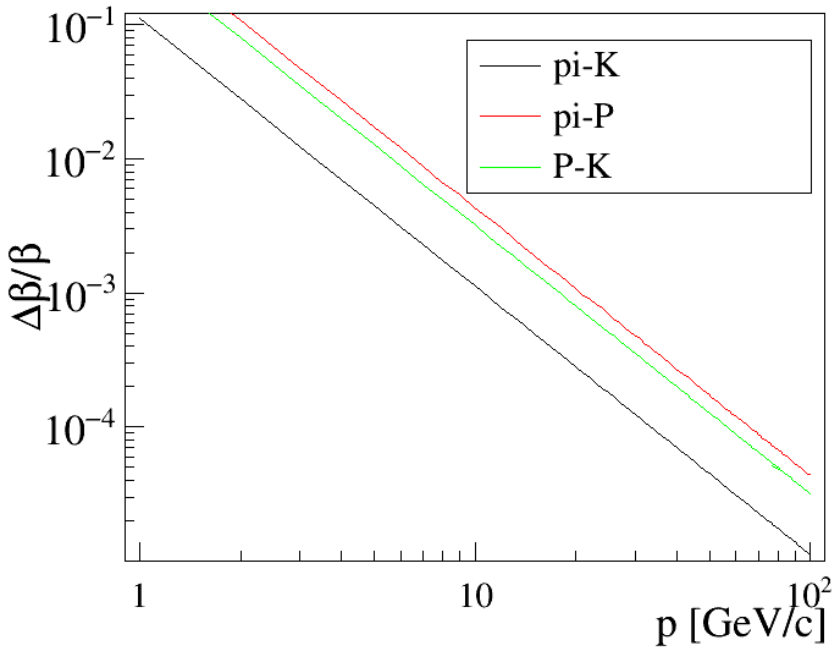

FIGURE 3.1: Beta Resolution versus momentum

3.2 Underlying Physics of Cherenkov radiation

Cherenkov radiation is named after Pavel Cherenkov, who first observed that if a charged particle is moving uniformly in a dielectric medium of refractive

index n, with a velocity $v(v = \beta.c)$ faster than the local phase velocity c/n of the light, then the charged particle radiates electromagnetic radiation in a peculiar way: the photons are emitted at an angle θ_C with respect to the trajectory of the charged particle in that medium and this angle follows the relationship

$$\cos\theta_C = \frac{1}{n\beta}. \tag{3.5}$$

Cherenkov first obtained this equation in 1934, and this characteristic angle θ_c is called Cherenkov angle [67]. Frank and Tamm [68] came with a detail theoretical description of this observation. The quantum mechanical description of Cherenkov equation predicts additional term $\frac{h}{\lambda.p}\frac{n^2-1}{2n^2}$in equation 3.5. However, we neglect this additional term in the rest of the discussion, by Cherenkov angle now on we consider only the classical Cherenkov angle relationship. In literature detailed description of Cherenkov equation can be found [65, 69].

Qualitatively the underlying mechanism is as follows: suppose a charged track is passing through a dielectric with relatively slow speed, then the molecules in the vicinity of the track will become polarised due to the effective field of the charged track. In figure 3.2 near the point P the atoms are polarised and the approximate spherical shape of those atoms are distorted. When the track moves to the point P', the atoms near P will relax back to the original position and shape, due to the transient nature of this polarization state. This polarised atom will be enacting like an elementary diople. But the relatively slow track will ensure the electric fields near the vicinity are exactly symmetric. Owing to the symmetry, there will be no field present in the far region from the track and therefore no radiation. The symmetry is both in azimuth and along the axis [70, 69].

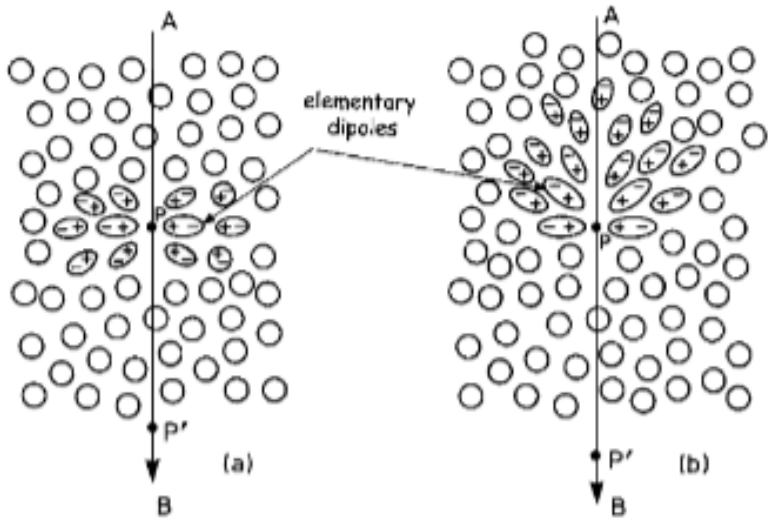

FIGURE 3.2: Polarisation of the medium due to passage of charged tracks at different speed. Left, slower than the speed of light in that medium. Right, faster than the speed of light in that medium. [65]

However, when the track is moving at a speed comparable to the speed of light in that medium, the picture is quite different. First, the symmetry is broken. Although the azimuth is still symmetric but along the axis the symmetry is not preserved. Therefore, along the axis the dipole will be apparent at a distance, which is much larger than the atomic dimension. Such a field will be momentarily set up by the track at each element along the track in turn, each element then radiating a brief electromagnetic pulse. Second, the radiation will be spread over a band of frequencies corresponding to the various Fourier components of this pulse. Generally speaking, the wavelets will destructively interfere, so that at a distant point no resultant field intensity is detected. However, if the speed of the charged particle crosses the phase velocity of light in that medium, the interference becomes constructive, in other words, all wavelets from the tracks will be in phase, leading to a nonzero field intensity at a large distance.

From Huygens's construction figure 3.3 ,we can see that the radiation will be emitted at a particular angle along the track, which is the famous relation mentioned in equation 3.5 and owing to the symmetry in the azimuth, each elemental section will be circular if projected on a plane transverse to the direction of the charged track with different radii depending on the distance from the plane.

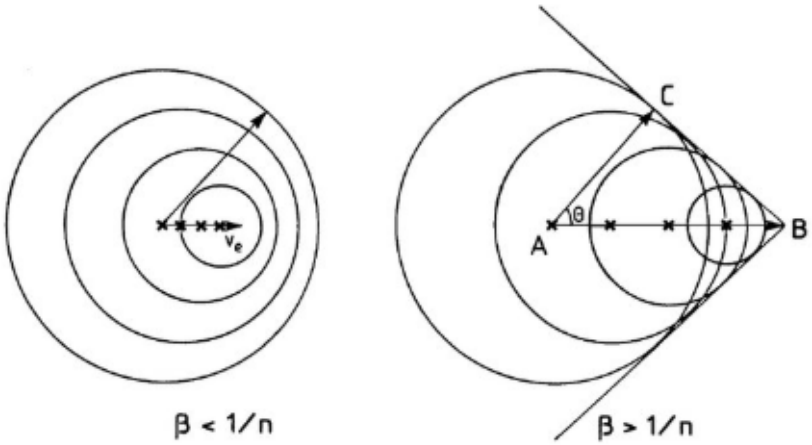

FIGURE 3.3: Huygens's construction of Cherenkov radiation [65]

3.2.1 Theory of Ring Imaging Cherenkov detector

To start with basic equations of the Cherenkov radiation which are adopted in constructing, monitoring and tuning the Ring Imaging Cherenkov techniques, let us go back again to fundamental mechanism of the electromagnetic radiations of a charged particle, moving relativistically. If we try to write the Bessel function of the relativistic charged particle moving in a isotropic

dielectric (Appendix: A), we can find out the constant term in the Bessel function is dictated as follows:

$$\lambda_p^2 = \frac{\omega^2}{v^2} - \frac{\omega^2}{c^2}\epsilon(\omega) = \frac{\omega^2}{v^2}[1 - \beta^2\epsilon(\omega)] \tag{3.6}$$

The electromagnetic wave frequency (ω) produced by the charged particle while moving, $\epsilon(\omega)$ is the dielectric constant of the media. From equation 3.6 we see, when the condition $v > \frac{c}{\sqrt{\epsilon(\omega)}}$ is satisfied, λ_P turns imaginary. The description of the energy loss per unit length by a relativistic charged particle traversing a dielectric, with these two assumptions 1. $\lambda_p = -i|\lambda_p|$ and 2. $v > \frac{c}{\sqrt{\epsilon(\omega)}}$ becomes:

$$\frac{dE}{dx} = \left(\frac{Ze}{c}\right)^2 \int_{\epsilon(\omega)>(1/\beta^2)} \omega\left(1 - \frac{1}{\beta^2\epsilon(\omega)}\right)d\omega \tag{3.7}$$

This equation can be realised in a double differential equation, which is the famous Frank and Tamm Formula [68, 71] which states differential energy radiation per unit path length of a charged particle moving with a speed greater than the speed of light in that medium:

$$\frac{d^2E}{dxd\omega} = \left(\frac{Ze}{c}\right)^2 \omega\left(1 - \frac{1}{\beta^2 n^2(\omega)}\right) \tag{3.8}$$

The term $n(\omega)$ is the refractive index of the medium. The expression of number for photons produced by the charged particle can also be extracted from equation 3.8, writing the refractive index as the function of radiated photon wavelength ($v\lambda = c/n(\lambda)$). The expression is:

$$N = 2\pi.LZ^2\alpha \int_{\beta.n>1} \left(1 - \left(\frac{\beta_{th}(\lambda)}{\beta}\right)^2\right)\frac{d\lambda}{\lambda^2} \tag{3.9}$$

In this equation, $\beta_{th}(\lambda)$ is a consequence of the fact that $\cos\theta_C \leq 1$, hence $\beta_{th} = 1/n(\lambda)$. The number of emitted photons depends on the range of the integrated photon wavelengths. We can write the expression for the number of emitted photons which will be more or less constant per unit length (in cm) and per unit energy (in eV).

$$N \sim 370Z^2\left(1 - \frac{1}{n^2}\right) \tag{3.10}$$

This expression represents the mean of the Poisson distribution in the number of photons, owing to the inherent statistical nature.

The measurement of the Cherenkov angle θ_C, provides a way to measure the velocity of the particle, provided the refractive index and momentum is

known. Starting from the Cherenkov equation, we can write

$$\begin{aligned} \cos\theta_C &= \frac{1}{n\beta}; \\ \beta = \frac{p}{E} &= \frac{p}{\sqrt{p^2+m^2}} \\ \cos\theta_C &= \frac{\sqrt{p^2+m^2}}{n.p}; \\ m^2 &= p^2.\left(n^2\cos^2\theta_C - 1\right) \end{aligned} \tag{3.11}$$

If the errors in estimating θ_C coming from different sources are denoted as $\Delta\theta_j$, then the uncertainty in the measured angle is added in quadrature and the relationship is obtained as:

$$\sigma^2_{\theta_C} = \sum_j \Delta\theta_j^2 \tag{3.12}$$

In order to optimise the performance of the RICH in the higher momentum region, where the difference in the Cherenkov angle of two different particles becomes smaller and smaller, the minimization of these errors is mandatory. The error in the velocity determination is:

$$(\frac{\sigma_\beta}{\beta})^2 = (\tan\theta_C\sigma_{\theta_C})^2 + (\frac{\sigma_n}{n})^2 \tag{3.13}$$

The term $\frac{\sigma_n}{n}$ contains all the uncertainties associated to the determination of the refractive index. This error contribution has irreducible parts which are related to the evolution of refractive index with temperature and pressure and dependence of refractive index with photon wavelength. The first component can be estimated by extracting refractive index at different temperature and pressure values and interpolating over a longer period. This error may have different components depending on the experimental situations. In the COMPASS experiment the refractive index is determined from the data, to monitor the performance and status of RICH. This I will discuss in detail later, that physics background can lead to wrong estimation of refractive index. Nevertheless, in the RICH technique, mass is the physical parameter computed from the measured velocity, momentum and knowledge of refractive index for particle identification. For light gases due to technical reason, the refractive index is labelled as $n-1$, which is in the unit of ppm (10^{-6}). Starting from the Cherenkov equation and ignoring all terms contributing significantly lower than a ppm, the error ascribed to the mass determination goes as follows:

$$\left(\frac{\sigma_{m^2}}{m^2}\right)^2 = \left(2m^2\frac{\sigma p}{p}\right)^2 + \left(p^2\frac{2\theta_C\sigma_{\theta_C}}{(n-1)-1}\right)^2 + \left([2p^2-(p\theta_C)^2]\frac{\sigma_{(n-1)}}{[(n-1)-1]^2}\right)^2 \tag{3.14}$$

This equation shows that with increasing momentum the mass resolution deteriorates. In the higher momentum region the ring diameter is larger, therefore the associated error increases. Once tuned the error in the refractive index is negligible, if it is within few ppm. Each photon is an estimation of the squared mass in principle. However, if the estimation is performed using the ring, the associated error in the theta is reduced by a factor of $\sqrt{(N)}$, where N is the number of photons in the ring, in case of negligible background.

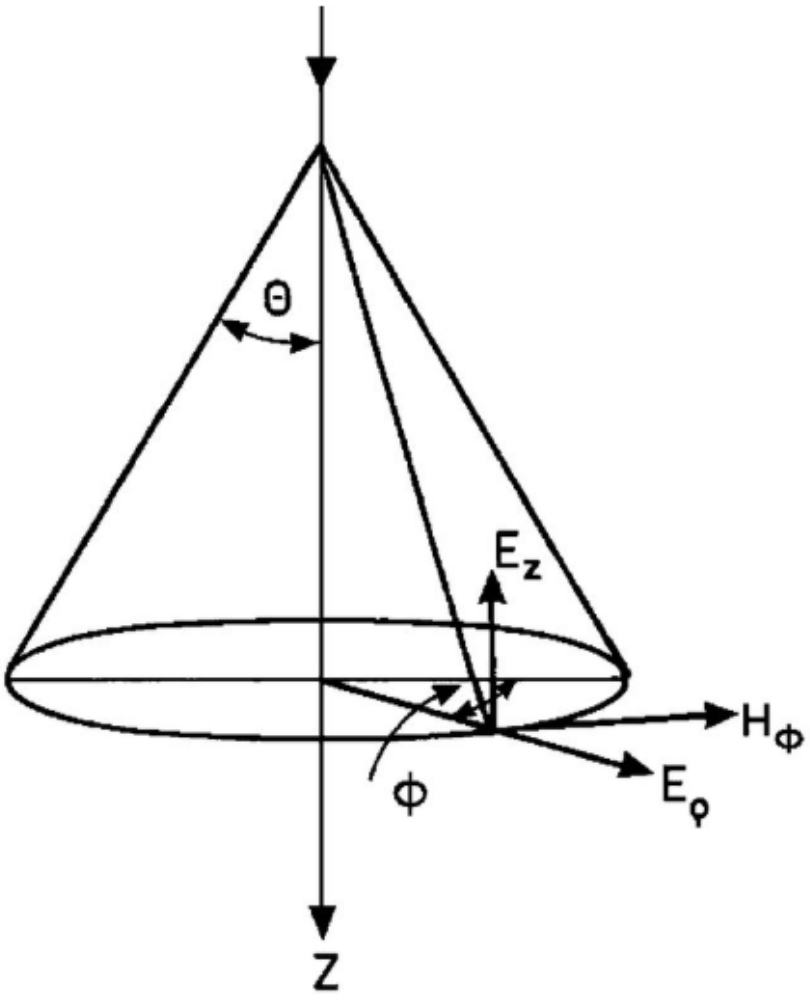

FIGURE 3.4: The polarization of the Cherenkov angle [65]

As the photons are linearly polarised (a detailed derivation can be found in appendix A), the electric field vector lies in the plane defined by the particle direction and the direction of photon propagation. The medium has to be fully isotropic to polarised light and an estimation has to be made for the reflection losses at the medium interfaces. Generally speaking, the Cherenkov photons are emitted in frequency ranges where the refractive index is approximately constant. Which ensures that it is away from the absorption band. The expression for the number of photons N for a given radiator length L is

given by;

$$\begin{aligned} N &= N_0 L \sin^2\theta_c \\ N_0 &= \frac{2\pi\alpha}{\hbar}\int \epsilon.QE.T.R.dE \end{aligned} \tag{3.15}$$

The term QE represents the quantum efficiency of the photon detector, T is the total transmission coefficient of the radiator and the windows, R is the reflectivity of the mirror and ϵ is the efficiency of the single electron detection. The integration is done between the limits, defined by the photoionisation threshold as lower edge to the medium transparency as upper edge. The higher the N_0 the better the detector. It is called the figure of merit (FOM) of a Cherenkov detector.
At saturation, where $\beta \rightarrow 1$, θ turns to be asymptotic. At this point the Cherenkov angle is maximum. The maximum number of photons is therefore given by $N_{max} = N_0 L \sin^2\theta_{max}$. At a given angle ($\theta$) the fractional number of Cherenkov photons is:

$$\frac{N}{N_{max}} = \frac{\sin^2\theta}{\sin^2\theta_{max}} \tag{3.16}$$

From equation 3.16 we see that each ring with its number of photon and ring angle can provide an estimate of the FOM of the RICH detector. The equation is therefore given by:

$$\begin{aligned} N_{max} &= \frac{N_0 L}{\gamma_t^2} \\ \frac{N\gamma_t^2}{N_0 L} &= \frac{\sin^2\theta}{\sin^2\theta_{max}} \\ \frac{Nn^2}{L(n^2-1)}\frac{\sin^2\theta}{sin^2\theta_{max}} &= N_0 \\ where: \gamma_t^2 &= \frac{n^2}{(n^2-1)} \end{aligned} \tag{3.17}$$

From equation 3.4 we can write the upper momentum limit $p_{up_{1,2}}$ for separating two particles with masses $m_1 m_2$, given the FOM N_0, the length of the radiator L and refractive index n:

$$\begin{aligned} \tan\theta\Delta\theta &= \frac{\Delta m^2}{2p_{up_{1,2}}^2} \\ p_{up_{1,2}} &= \left(\frac{\Delta m^2\sqrt{N}}{2n_\sigma\sigma_\theta n\tan\theta}\right)^{1/2} \\ p_{up_{1,2}} &= \left(\frac{\Delta m^2\sqrt{N_0 L}}{2n_\sigma\sigma_\theta n\tan\theta}\right)^{1/2} \end{aligned} \tag{3.18}$$

The physics requirements of the experiment fix the needed n_σ on the desired

particle separation power and the allowed contamination level. Equation 3.18 shows that the upper PID momentum limit can be increased by increasing the FOM N_0 and/or decreasing the σ_θ.

3.2.2 Image formation

The idea to identify mass of charged particles by exploiting the directional properties of the Cherenkov radiation was conceived by Roberts [72]. The Cherenkov radiation is emitted in an isotropic dielectric medium, chosen according to needed range of the particle identification. The detected photons can be used for particle identification in the form of a ring recognised by pattern recognition. Experiments like E605, DELPHI [73], OMEGA [74], SLD, HERA-B [75], HERMES [76], CLEO, BaBar [77], LHCb [78, 79] etc. have used RICH with pattern recognition methods. In the imaging technique the photons can either be detected by focusing on the detector surface by a spherical or a parabolic mirror, or without any focusing technique. The latter, called proximity focusing technique, will not be discussed here. Detailed information can be found elsewhere [80, 81]. The basic ideas behind the focusing RICH for the imaging technique and its evolution can be found elsewhere [82, 83].
The optimal design of a Cherenkov imaging counter must take into account the photon detector technology. This is crucial to reduce the losses in the number of detectable Cherenkov photons. The design of single photon detectors in different direction has played an important role in the success of the Cherenkov imaging counters. Vacuum based detectors, gaseous detectors, solid state detectors and hybridisation of different techniques have been adopted in different Cherenkov imagine detectors [83, 84, 85, 86, 87].
During the years continuous improvements were generated by advancements in the photon detector technologies. Recent experiments are equipped with RICHes which are capable of detecting photons in the visible range. These detectors are based on vacuum photon sensors. Despite many advantages of the vacuum based photon detectors, gaseous detectors are superior when operation in high magnetic field is needed, when covering large area active photon detection surface at lower cost and efficiently is mandatory. CsI film based photon detectors are the options to detect photons in the vacuum ultra violet (VUV) domain. CsI has the highest Quantum efficiency in the VUV domain compare to other alkali halides. It is however extremely hydroscopic. The QE deteriorates with H_2O contamination. CsI allows stable operation up to integrated charge values of the order of 1 $\mu C/mm^2$ [88, 89, 90, 91, 92, 93]. A search for alternative photocathode in the VUV region is ongoing. Hydrogenated nanodiamonds exhibit robustness and large QE in the VUV domain [94, 95]. A collaborative research is ongoing at INFN Trieste and University of Bari to couple hydrogenated nanodiamond with THGEMs for VUV single photon detection. I have actively taken part in the R&D activity related to this research [96, 97].

3.3 An Example: COMPASS RICH-1

Some basic construction characteristics of COMPASS RICH-1, which is the topic of this thesis is discussed in this chapter. It is a RICH with 3 m long C_4F_{10} radiator [98], 21 m^2 VUV reflective mirror [99] system and 5.6 m^2 active detector surface. COMPASS RICH-1 is capable of identifying pions, kaons and protons up to 55 GeV/c. As mentioned in chapter 2, RICH-1 sits in the first stage of the spectrometer.

3.3.1 RICH Vessel and the radiator gas

An aluminium structure enclosed by Al plates is used as the RICH vessel. It has a length of 3 m, a width of 6 m and it is 5 m high. Figure 3.5 shows the RICH vessel during transportation. The hydro-static pressure of the radiator gas are held by the front and rear windows, which are built with minimum material budget due to their presence in the spectrometer acceptance. A total of 2% X_0 is spent by sandwiching layer of foam in between two Al foils. In the central part, near the beam region, it is 0.6% X_0.

FIGURE 3.5: The transportation of RICH vessel in the 888 spectrometer hall at CERN.

A cylindrical pipe of 100 mm diameter on nominal beam axis had been installed to shadow the Cherenkov photons generated by the beam particles. This pipe is filled with helium to reduce the material budget. The 330 cm long C_4F_{10} radiator corresponds to $\sim 10\%X_0$, which would be unacceptable in the beam region. In 2012 the original 120 μm thick stainless steel pipe was replaced by 4 layers of metalised BoPET (25 μm BoPET + 0.2 μm Al). The contribution to the total material budget by the new pipe for beam particles

is 0.08%X_0 along with 0.06% from the helium. The beam pipe can be seen in figure 3.6

FIGURE 3.6: Beam Pipe inside the RICH [100]

3.3.2 The focusing mirrors

COMPASS PID is based on focusing RICH technique. A 21 m^2 VUV mirror wall has been produced to focalise the Cherenkov photons onto the photon detector plane [99]. The photon detectors are stationed above and below the acceptance region. Their surface is a rough approximation of the focal plane. The mirror wall is divided into two spherical surfaces of 6.6 m radius about the horizontal plane containing the center of the beam pipe. This arrangement results in a geometrical aberration of 0.32 $mrad$ for images produced by small incidence angle of the particles and can be larger for particles with large incident angle. The two surfaces have a mosaic formation composed of a total of 116 spherical mirror units: 68 regular hexagons with 522 mm long diagonal and 48 of six different size, to avoid saw-teeth patterns on the surface borders. The external side of the mirror wall with the mirror holding mechanics can be seen in figure 3.8. The wall can be seen in figure 3.7 during the alignment procedure. The clearance left between adjacent mirrors results in a 4% loss of reflecting surface. The reflecting layer is an 80 nm thick Al deposited on a 7 mm thick borosilicate glass substrate and covered by a 30 nm thick MgF_2 protective layer the layers have been deposited with a controlled

and tuned procedure, including: very good vacuum (10^{-7} $mbar$), high deposition rate(2-4nm/s) and rapid rotation of the mirror. Thanks to the CERN reflectometer facility, it was possible to give feedback to the manufacturer.

A strict quality control for the validation has been imposed on the production of the mirrors: the radius of curvature $R = 6600\ mm \pm 1\%$, the reflectance $r > 80\%$ in between $160 - 200\ nm$ photon wavelength range, the "spot diameter" d, which is defined as the diameter of the beam-spot at the focal plane $< 3.5\ mm$. A total of 126 mirror units were produced at IMMA, including 10 spare units. The radius of curvature and the spot diameter D has been characterised individually. The average radius o curvature is $R_{av} = 6606 \pm 20\ mm$ and $D_{av} = 1.65 \pm 0.45\ mm$. The roughness has been measured on a sampling basis. The achieved mirror reflectance is good with a mean value of 83-87% at 160-200 nm. Repeated measurements of the reflectance after 1 and 2 years permanence in RICH vessel indicate, after the expected short term degradation, stable reflectance values above 165 nm.

The hexagons were divided into two sets depending on their R values below or above the R_{av}. The best mirrors (R nearest to the nominals) were used in the central region, where the number of tracks is larger compared to the peripheries. These mirrors will mostly focalise the photons onto the MAPMTs.

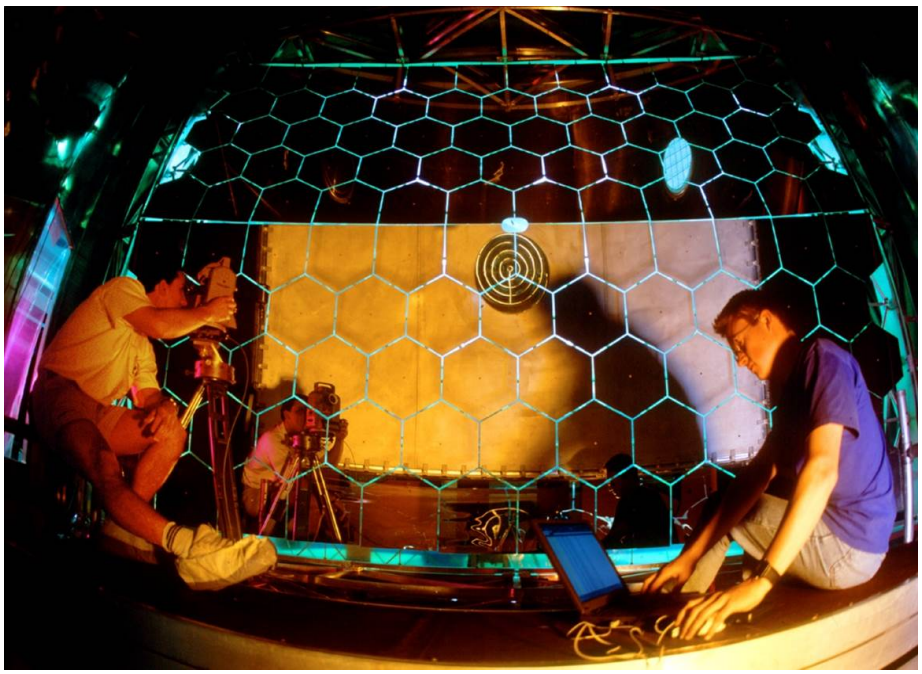

FIGURE 3.7: Delicate mirror alignment procedure

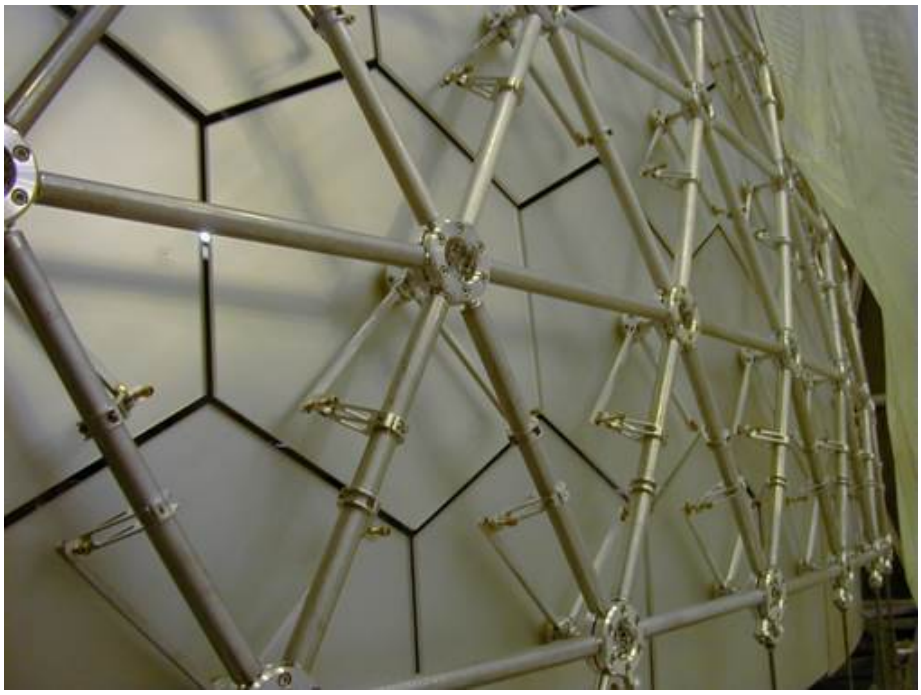

FIGURE 3.8: The mechanics of the mirror

3.3.3 CLAM System

If the adjacent mirrors are not well aligned then the image of a reflected object will be inconsistent. Thus, any discontinuity in the image of a rectangular grid of continuous lines corresponds to a relative mirror misalignment. The figure 3.9 shows the principal CLAM alignment. CLAM system is based on this simple idea. The basic hardware components include four digital cameras for the monitoring of four different segments of the mirror wall, a regular grid of retroreflective strips illuminated by light emitting diodes. The two LEDs are placed close to each camera. All the parts of the system were properly chosen to achieve resolution of mirror misalignment of 0.1 *mrad* [101].

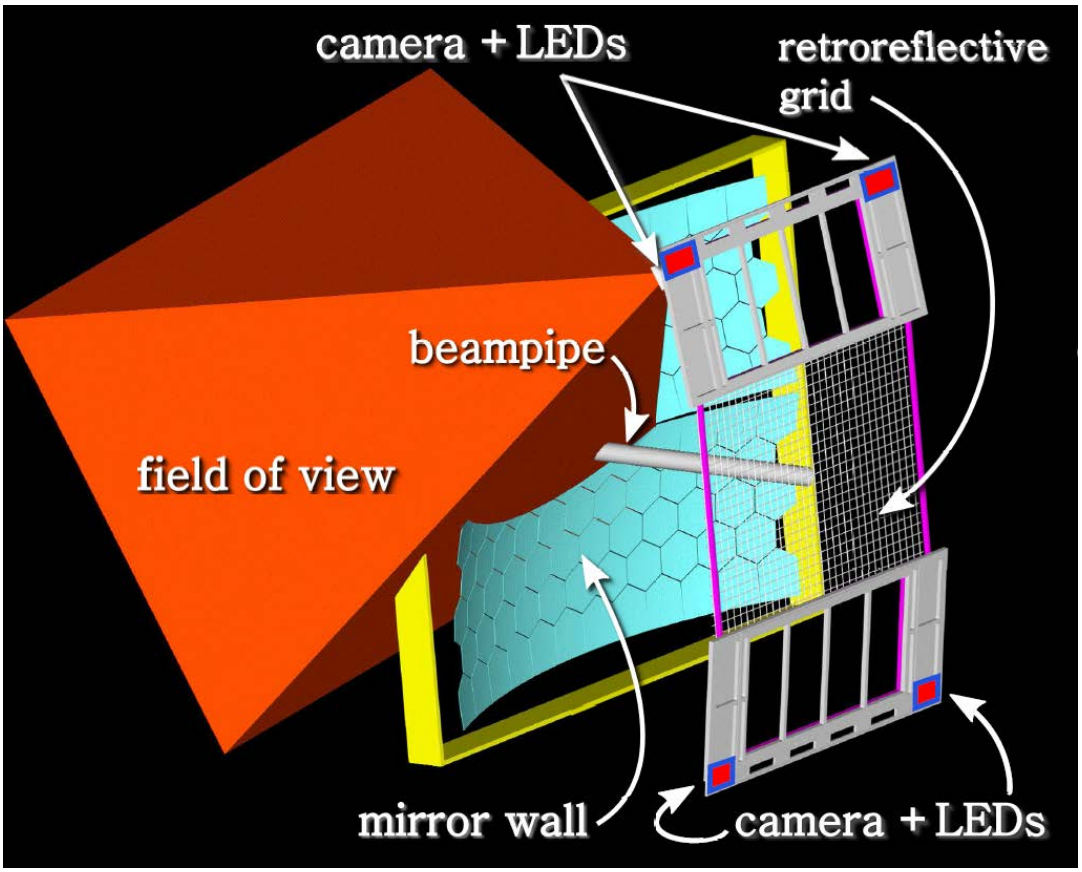

FIGURE 3.9: Principal of CLAM alignment [101].

3.4 Data Analysis Package

COMPASS has multi-layer data analysis packages. They are listed in the following:

- DDD : Daq Data Decoding
- CORAL : COmpass Reconstruction and ALignment software package
- PHAST : PHysics Analysis Software Tools
- COMGeant : COMpaass Geant Monte Carlo simulation program based on Geant 3.21
- TGeant : a Monte Carlo simulation program based on Geant4.
- Time dependent inputs, like calibration and slow control data, are stored in a MySQL DataBase

Here I will give very brief description of CORAL, which I have used mainly for studying the RICH performance for 2016 SIDIS physics.

- CORAL: CORAL is mainly used for alignment and reconstruction of the data. It is an object oriented program (written in C++), with modular architecture. CORAL can process both raw data as well as data produced by the Monte Carlo simulation software of COMPASS (COMGeant) The most relevant tasks performed by CORAL can be listed as the following:
  - The decoding of all the data in order to extract the address of the fired channels (hits), the signal amplitudes and the time information.
  - The reconstruction of the particle trajectories (tracking), the momentum analysis of the charged particles, and the reconstruction of the interaction and decay vertices.
  - The identification of the muons, using the information from the muon detectors.
  - The RICH reconstruction and hadron PID, using the information from RICH-1.
  - The analysis of the response of the hadronic and electromagnetic calorimeters.

3.5 RICHONE

RICHONE is the part of the COMPASS software package CORAL, for RICH reconstruction, characterization and analysis [102, 103, 104]. CORAL is the COmpass Reconstruction and ALignment software package. A brief description of some important tasks performed by the RICH reconstruction software, RICHONE, is as follows: CORAL loops over the events. After reconstruction of the beam and the tracks, the reconstruction of the RICH-1 data is performed. After this the reconstruction related to the calorimeters are done. An option file is read by the RICHONE, the required options and initial values are stored in this option file.

3.5.1 The main functionalities of the RICHONE

RICHONE is a package performing both the standard PID and several accessory tasks, including tuning and calibrations. At the very beginning of the RICH reconstruction, the type of the data fed to the RICHONE is clearly mentioned. There can be many possibilities: raw, simulated or gFiles : which is a special file with only RICH information. Inside the code a monitoring function is available to set the type of data to be analysed by the RICHONE and to set the options accordingly, which are read from the option files. In order to associate the photons emitted by the particle with the particle, RICHONE needs:

- In CORAL a particle trajectory is defined giving its helix (position, direction and momentum). To reconstruct a trajectory inside RICH-1, a

helix is computed at the RICH-1 entrance window; the trajectory is extrapolated inside the RICH-1 volume, taking into account the fringe field of the spectrometer magnet, located about 3 m upstream of RICH-1.

- information recorded by the photon detectors of the RICH-1 and which is decoded by the data acquisition decoder and transformed in the lab system.

The decoded information is called digits. In case of our RICH reconstruction software they are composed of some physical coordinates and signal amplitudes. The execution of the software can be summarised as successful completion of four important steps. They are executed in different classes with many routines and subroutines of the RICHONE code A brief description of the classes is made in appendix C with their key functionalities. The four important steps in the RICHONE are the following:

1. The tracks information is read with the aid of the other parts of the CORAL software by the RICHONE, where the interesting parameters for PID, tuning and characterisation are recorded. They are the momentum multiplied with charge, position and direction of the tracks at the RICH entrance and the exit plane.

2. The photon hits are measured by the RICH-1 PDs, together with either their time information for the MAPMTs or three signal amplitudes for the gaseous detectors. The hit time information is used for out-of-time photon rejection. Whereas, the hit amplitudes are used to reduce background both from the out-of-time photons and electronic noise. For the gaseous detectors, a pad is selected only if the signal amplitude is larger than 8 ADC channels and the three signal samples (A_0,A_1,A_2) is having the following relationship: $A_0 < A_1 < A_2$.

3. Based on the fact that, the converted photons may induce charge over more than one adjacent pads, a clustering algorithm is implemented. In this algorithm, pads of the highest signal amplitude is searched. After having found the pad with highest signal size, the adjacent pads are included in the cluster if the signal amplitude of that is less than a percentage of the highest signal amplitude (60% along the wire-plane direction and 30% along the transverse direction). The impact position (cluster) is then evaluated as the mean of the hit positions, weighted with their pulse height. The average cluster multiplicity is 1.1. For the MAPMT the clustering is not adopted as the probability to have correlated hits in adjacent pads is negligible.

4. For each of these clusters the photon trajectory is reconstructed. This reconstruction is based on the cluster coordinate and the photon emission point. Thanks to the focusing RICH technique, the photon emission point is assumed to be the mid-point of the trajectory inside the RICH volume. After the photons have been reconstructed they are associated

to the particles. Only after this association, the rings are reconstructed and the likelihoods (LH) are computed. For the ring recognition the ring angle are scaled to the UV refractive index.

A simple flow-chart is shown in figure 3.10 illustrating the structure of the code.

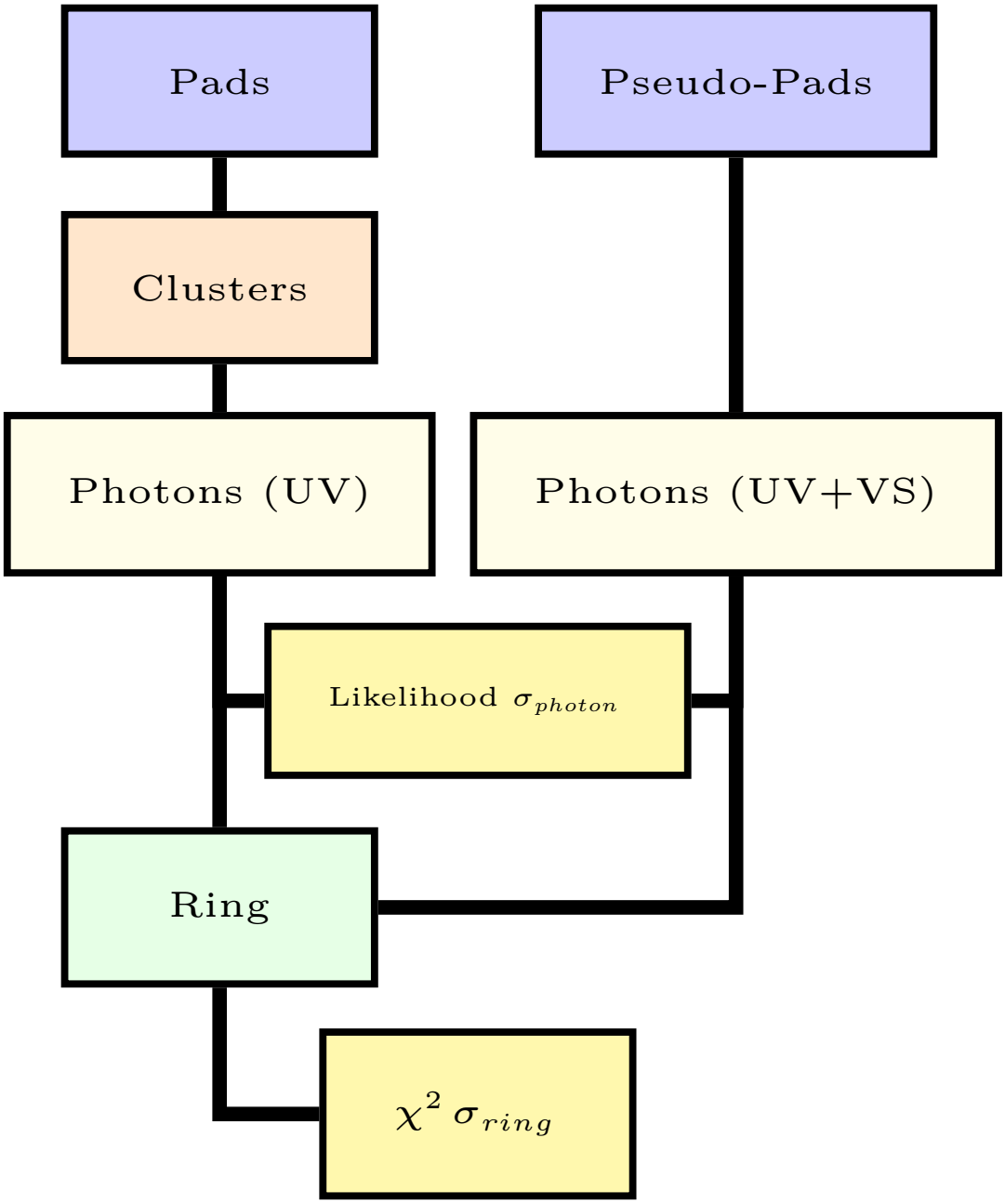

FIGURE 3.10: A simple flowchart for the RICHONE software

A detailed understanding of the entire software is mandatory for the tuning and adding relevant modification needed during the characterisation of the RICH.

Chapter 4

Single Photon Detection in COMPASS RICH-1

4.1 Introduction

In this chapter a brief description of the COMPASS photon detectors is presented. COMPASS RICH-1 has photon detectors of two kinds: MAPMT based detectors and gaseous detectors. Originally the photon detectors (PDs) were only MWPC based. In 2006, the central PDs were upgraded to MAPMT based detectors. For several physics measurements, for instance measurement of absolute cross-sections of particular hadron species production, where the knowledge of the values of the particle identification efficiencies is needed, the stability of these efficiencies is important for accurately measuring the physics quantities. In case of significant fluctuations in the efficiency the corresponding contribution to the systematic error will be critical. The efficiencies depend on the kinematic phase pace but their stability over the entire phase space is essential. This can only be achieved by achieving high efficiency and stability of the Cherenkov photon detectors for both signal detection and background rejection. Vacuum based MAPMT detectors are extremely effective in this regard, thanks to their stable operation, large gain, high QE and fast response. For these reasons COMPASS RICH-1 has been equipped with the MAPMT system in the central region. Nevertheless, where RICH detectors are embedded in a magnetic field or very large photon detection areas need to be covered at an affordable cost, gaseous detectors are the only choice. COMPASS RICH-1 is a nice example. A large surface of $\sim 5.6\ m^2$ was initially covered with MWPC based single photon detectors. Despite of 20 years of successful operations, MWPCs are not free from their technological limitations which affect the stability of the RICH response. To avoid the electrical instabilities due to occasional discharges the MWPCs are compelled to operate at low gain. Consequently, the electronic readout threshold is critical both for the single photoelectron detection efficiency and the noise suppression. Therefore, achievement of high stability is very difficult. The main motivation of the upgrade was to replace the critical MWPCs with new photon detectors which exhibit large gain and better stability in time. Efficient detection of signal of the Cherenkov photons also depends on the time window opened for the signal selection. The minimisation of the time resolution of the signal rise time is therefore another important parameter. After

an eight-year long dedicated R&D for the development of MPGD based single photon detectors for RICH application, in 2016 COMPASS RICH-1 was upgraded with THGEM-MM based hybrid PDs replacing four critical MWPCs. An important element of the upgrade is the reduction of the ion back flow (IBF). This reduction increases the lifetime of the CsI photocathodes and hence the longevity of the PDs. The new detectors are expected to show similar response in terms of number of detected photons per ring and similar or better single photon resolution with respect to the operational MWPCs. In my PhD period I have analysed the data collected by all types of photon detectors of COMPASS RICH-1. The figure 4.1 shows the detectors on the RICH, where we identify the blue panels as the MAPMTs, the green panels are the newly installed hybrids and the yellow ones are the MWPCs. The scheme of the figure is not in scale and Jura is in the left and Saléve is in the right hand side of the figure.

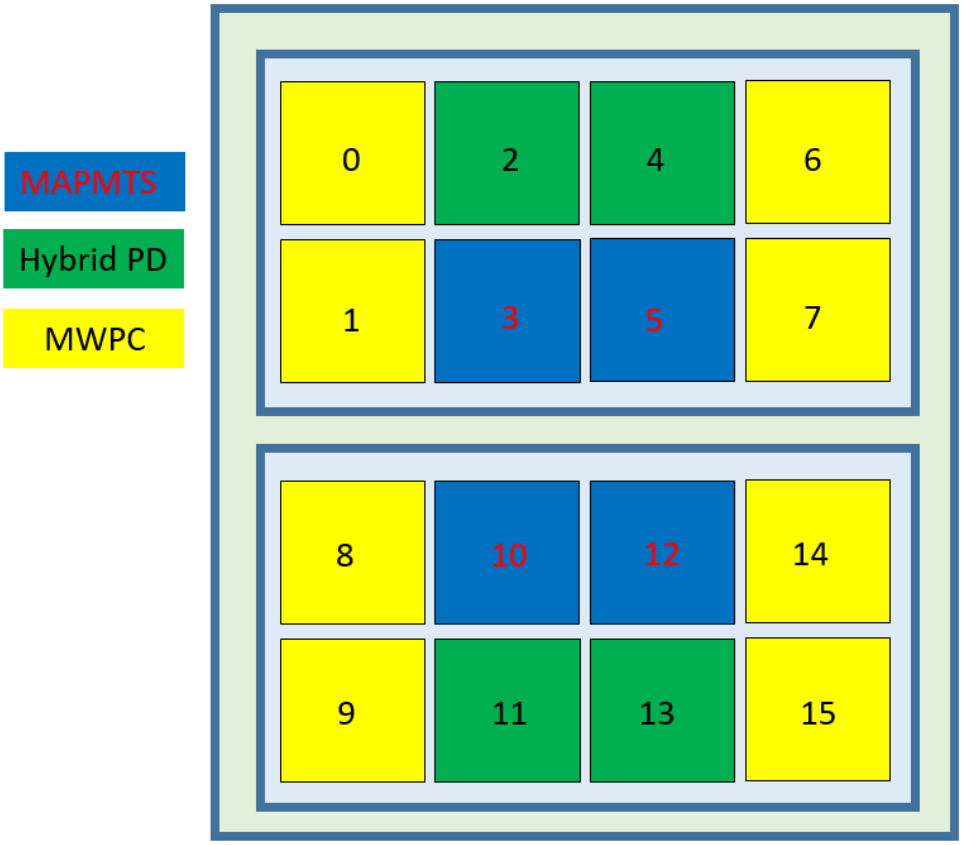

FIGURE 4.1: The detector nomenclature used in our analysis. The scheme is not in scale.

4.2 Multi-anode Photomultipliers

In chapter 3 section 3.3 we have mentioned that the central part of the COMPASS RICH is equipped with the MAPMTs. These covers 25% of the photon

detection surface due to the fact that the central photon detection area (25% of the active surface) is highly populated by uncorrelated background images with rates up to 1 MHz per channel. Thus a very good resolution of the measured Cherenkov angle is needed to push the limit of the hadron identification towards higher momenta. In 2006, the region was upgraded with fast photon detection system based on on Multi-Anode PhotoMultiplier Tubes (MAPMTs). The individual MAPMT is coupled with a telescope of fused silica lenses to enlarge the effective detection area. The lens telescope system together with MAPMTs is shown in figure 4.2. The MAPMTs are mounted in soft iron boxes, they act as magnetic shield against the 200 G residual magnetic field of the open H-shaped spectrometer magnet placed a few metres upstream of the RICH-1 detector. The iron boxes also house the voltage divider boards, which distribute the appropriate voltage to the MAPMT electrodes and transfer the anode signals to the front-end stage. The MAPMTs are intrinsically fast and sub nanosecond devices. These MAPMTs are read out via a digital system based on highly sensitive amplifier-discriminators and high resolution Time to Digital Converters (TDCs). The lens system has been designed such that:

- the photon wavelength domain is extended to the UV range, thanks to the MAPMT UV extended windows, that allow to convert photons down to 200 nm wavelength, and to the choice of telescopes made by fused silica lenses.

- the telescopes coupled to each MAPMT have large demagnification parameter. Therefore, it possible to get a surface ratio between the entrance window of each telescope and the photo-cathode larger than 7. This feature, coupled to an accurate arrangement of the MAPMT and lens mechanical supports, allows both to save on the number of MAPMTs required, and to obtain a dead zone fraction of 2% only.

- to fulfill the COMPASS requirements, namely, high detection efficiency for the single photoelectrons, sub nano second time resolution in achieving a minimised background rate due to uncorrelated events as well as to exploit the MAPMT time resolution fully, and high rate capabilities; a read-out system is used which provides a highly sensitive front-end stage.

The MAPMTs are manufactured by Hamamatsu, they have 16 anode channels and bi-alkali photo-cathode and UV extended glass window. The MAPMTs are characterised by large gains ($\sim 10^6$ at 800 V), fast transit time (~ 10 ns) and fast anode signal rise time(< 1 ns) [105, 106]. They have a custom voltage divider circuit. The MAPMTs are composed of 12 dynode stages. The typical spectrum of a MAPMT is shown in figure 4.3. It consists of three components. The tail of the pedestal signal distribution can be seen at very low amplitudes. Two signal peaks are following the pedestal signal. The high amplitude component corresponds to signals where the photo-electron is amplified by the full 12 dynode chain.

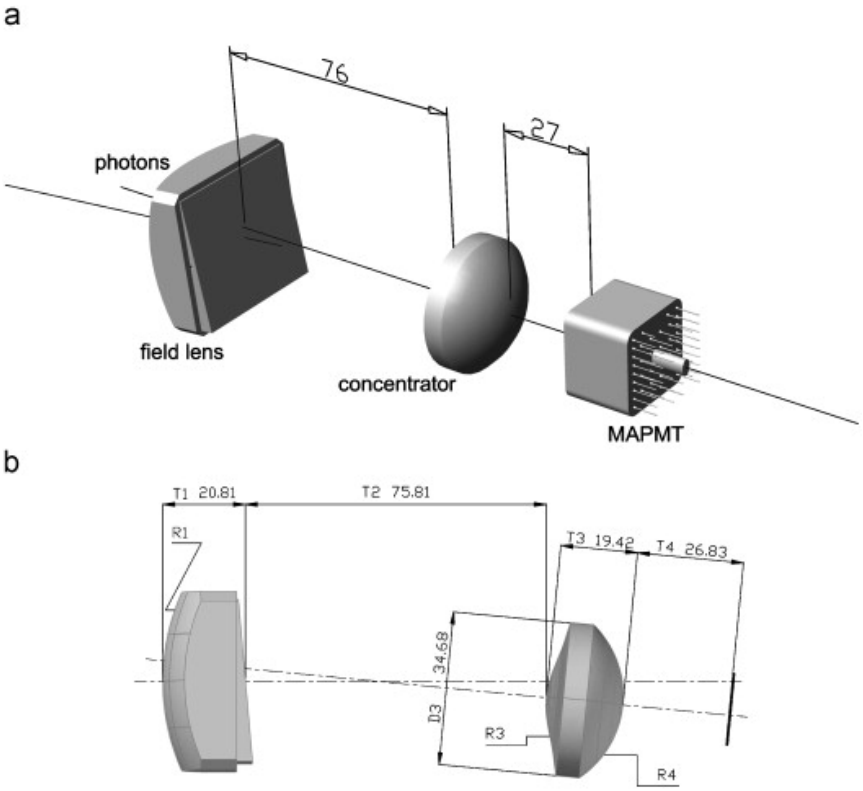

FIGURE 4.2: The mechanical drawing showing the MAPMTs and the lens system

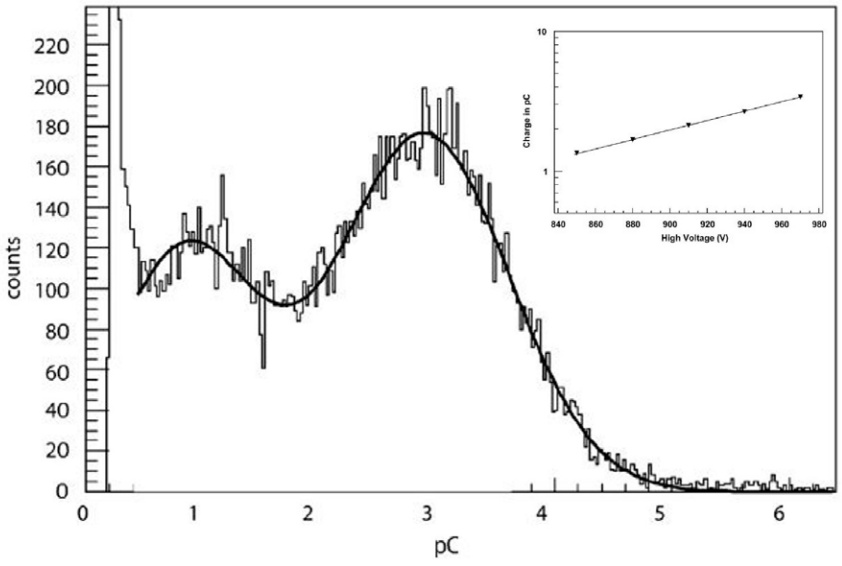

FIGURE 4.3: A typical spectrum of the MAPMTs

This has a typical mean amplitude value of 4×10^6 at 900 V. The low amplitude spectrum is due to photo-electrons escaping one of the dynodes, this peak has a typical mean of 8×10^5 at the same voltage. For each MAPMT, the voltage is adjusted to obtain mean values as similar as possible to the typical values indicated above. COMPASS RICH-1 central photo-detection

system is composed of 576 MAPMTs divided into 4 panels. The panels are identified as cathode 3, 5, 10, 12 from viewpoint of COMPASS coordinate system.

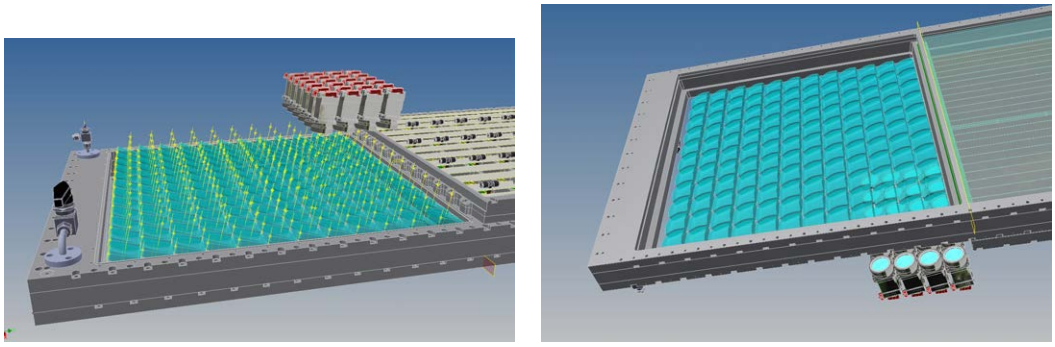

FIGURE 4.4: CAD diagram of the MAPMT and the lens system from up and down view

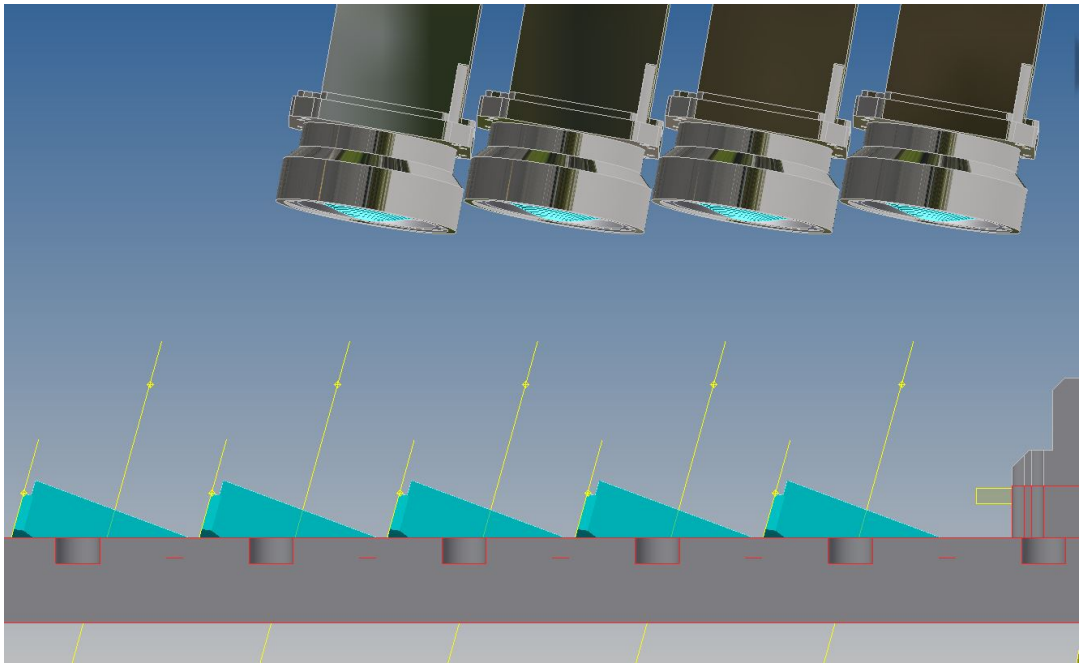

FIGURE 4.5: MAPMTs and the optical lens system

The light is concentrated to the MAPMT by a two-lens telescope system preserving the position information. The design of the lens telescope [107] has been performed using ZEMAX 8 [108]. Top and bottom view of the lens system can be seen in figure 4.4. Photons with wavelength in the range between 200 &700 *nm* are transmitted with a wide angular acceptance. The system provides an image demagnification of a factor 7.3 in area with minimal distortion and complies with the space limitations at the detector (11.5 *cm* total length). Another constraint from the COMPASS spectrometer is that the MAPMT has to be oriented at an angle with respect to the telescope entrance axis to be compatible with the existing MWPCs that remain

as peripheral photon detectors: the telescope has to be a non-axial system. Therefore to match these requirements the optics has been designed from the basic scheme of HeraB [75] with a major modification. In COMPASS RICH-1 a plano-convex field lens with a wedge element is placed at the focal length of the mirror, where the wedge ensures the non axial architecture. This field lens is followed by a biconvex concentrator with one aspherical surface. The describing equation is as follows [109, 105]:

$$z = \frac{\rho^2/R}{1+\sqrt{1-(\rho/R)^2}} + \alpha\rho^4 \tag{4.1}$$

where z is the coordinate along the lens axis and ρ is the distance from the axis; the parameters defining the surface are the radius of curvature R and the aspherical 4^{th} order coefficient α. The close view of the CAD drawings of the MAPMTs are shown in figure 4.5 and 4.6 where the inclination of the telescope system and the optics are seen. Different architectures have been studied and optimised condition has been implemented as the optics of the MAPMTs. The lens production and mounting quality have been strictly controlled. Each lens and each telescope have been tested by custom set up employing Hartmann method. Hartmann method is a classical non-interferometric method to test the optical system. The lenses were tested by placing a mask of regular array of holes, placed at the pupil of the optical system to be tested. A parallel beam illuminates the optical system through the mask.The image of the spots corresponding to the holes is collected at a defocusing position. The shape of the wave front can be deduced from the spot image: the aberrations of the optical system can be determined, comparing the reconstructed wave-front with the ideal one.To measure accurately the position of the spots, the defocusing and the separation of the holes have to be quite large to avoid overlapping spot images [110, 111, 112]

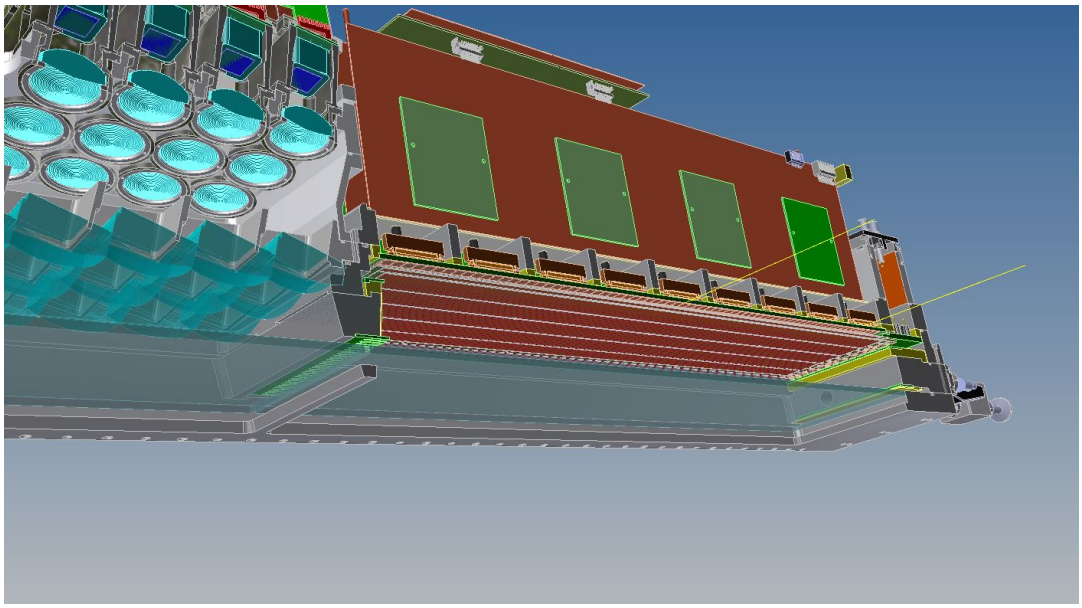

FIGURE 4.6: The Concentrator close to the MAPMTs and the lens is visble in the CAD drawing.

Another important aspect is to reduce the reflectance of the lens system. A single layer MgF_2 coating is effective in most of the wavelength range and its application is a standard procedure. A single 75 nm layer is chosen to reduce the reflectance at 300 nm. A careful mechanical design of the lens support frames, shown in figure 4.9 is allowed to reduce the dead areas below 2% of the surface.

Electronics

The read-out system for the MAPMTs is based on the MAD4 preamplifier discriminator and the high resolution dead time free F1 TDC [113]. A schematic is shown is figure 4.7. The availability of space for the electronics is constrained by the spectrometer, different layers of trackers are stationed just in front of the RICH-1. The entire system has been mounted in an extreme compact format, as close as possible to the photomultipliers. The read-out system is free from cable connections in order to minimise the electrical noise, and to maximise robustness. Figures 4.8 and 4.9 show the CAD diagram of the compactness of the holding frames and the electronics cards.

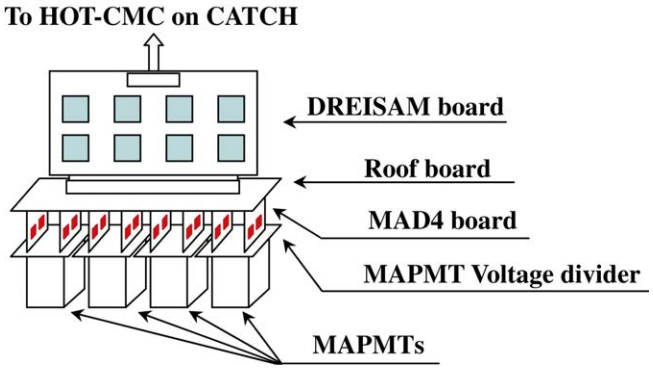

FIGURE 4.7: The electronics readout scheme of the MAPMTs

The MAPMT voltage divider which is shown in figure 4.7 has two connectors, where the MAD4 boards populated with the MAD4 chips are directly plugged in. The differential output signals of eight MAD4 discriminator boards are fed via the intermediate Roof board to the digital read-out board, the Digital RICH ElectronIc SAMpling (DREISAM) board[114]. A original picture can be seen in figure 4.10. The Roof board acts also as mechanical fixation of the read-out electronic boards, and it distributes the Low Voltage (LV) power and the threshold settings to the MAD4 chips [115, 116].

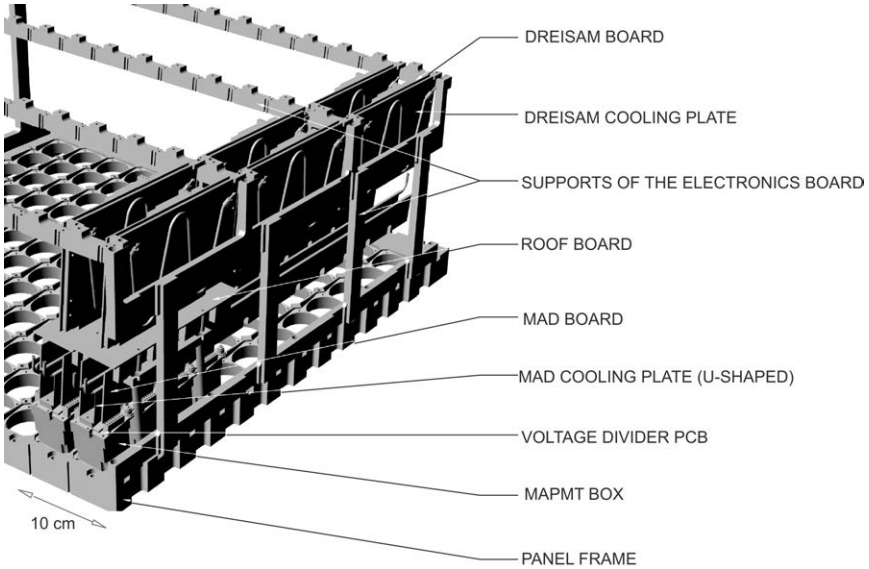

FIGURE 4.8: CAD diagram of the holding frame of the MAPMTs

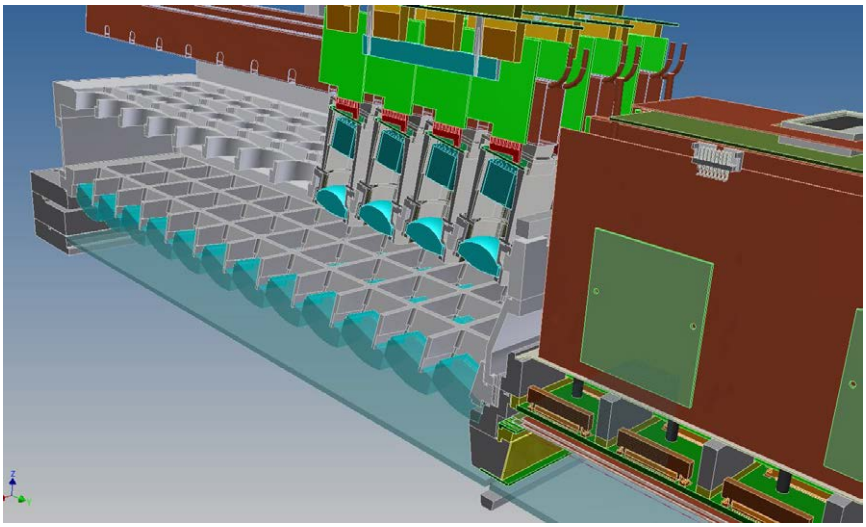

FIGURE 4.9: CAD diagram of the holding frame of the MAPMTs

Optical links are used to transfer the digital data from the DRIESAM boards to the read-out boards. The HOT-CMC mounted on the CATCH boards is located in a VME crate at a few metres distance from the detector. Then the data is transferred to the COMPASS data acquisition system. The HOT-CMC board has been specifically developed for this project, while the CATCH board is standard in the COMPASS data acquisition system.

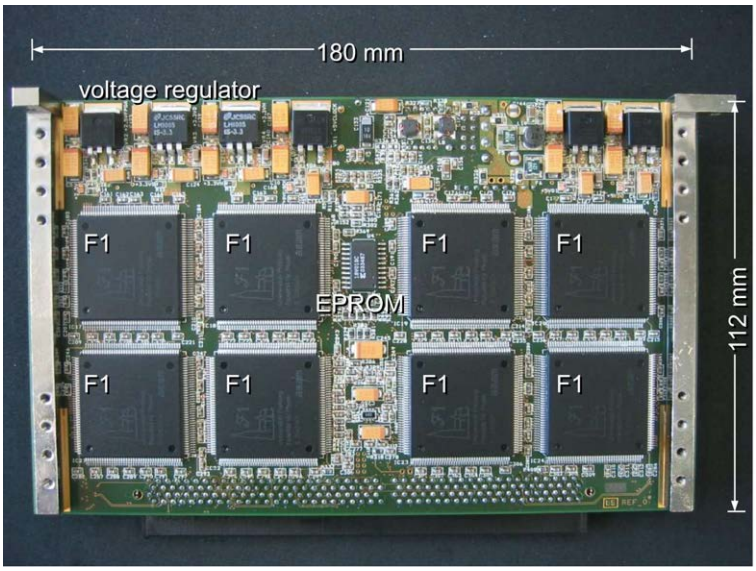

FIGURE 4.10: DREISAM board of the MAPMTs

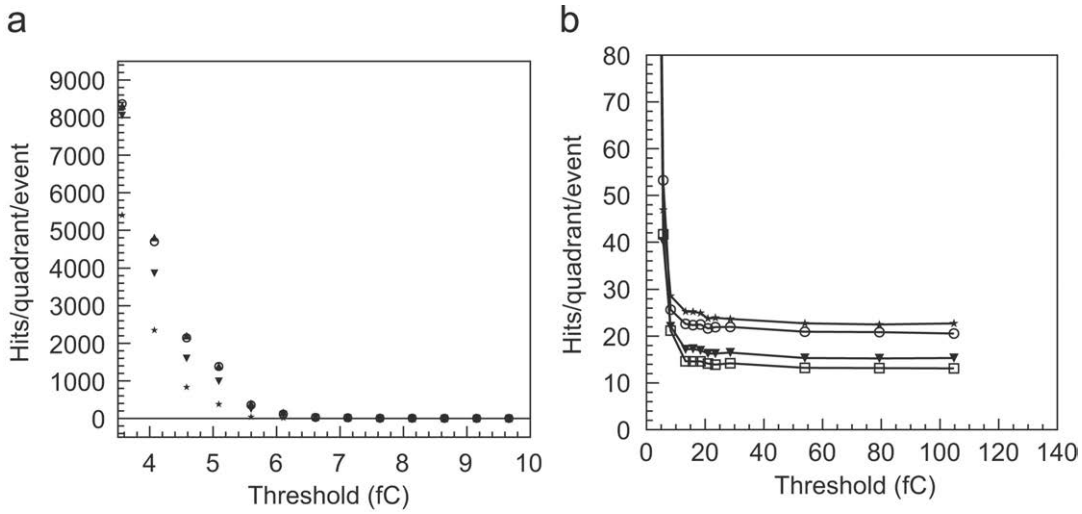

FIGURE 4.11: Threshold scan of MAPMT signals

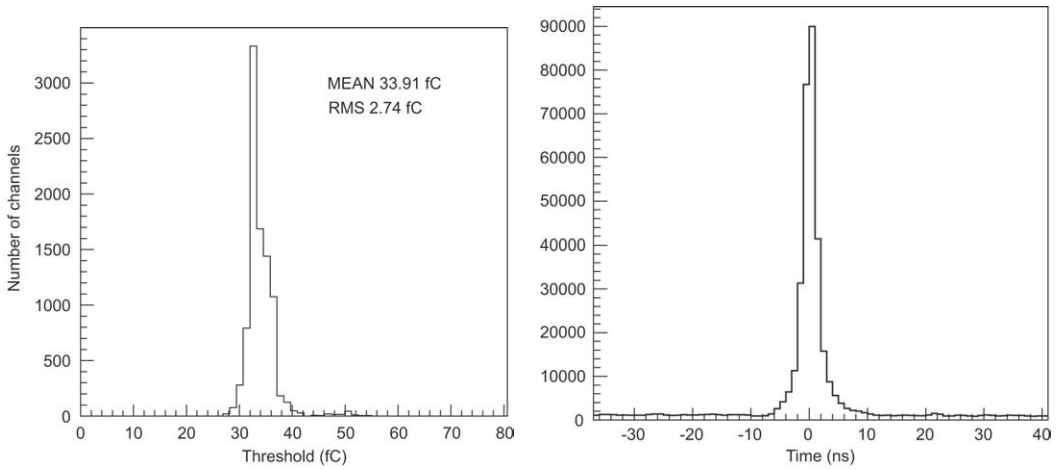

FIGURE 4.12: Threshold distribution and typical time distribution of the MAPMT signals

The threshold scan and the time distribution of the MAPMT signals are shown in figure 4.11 and 4.12 respectively. In the left panel of the figure 4.11 we see the threshold scans for MAPMT photon detectors for each of the four quadrants in the threshold range 3.5 to 10 fC and in the right panel we see the same scan over a broad range of 5 to 105 fC. It is clear that already with a threshold level of 7 fC the number of hits per quadrant is very low. This threshold value can be extended furthermore with no effect on the number on background signal which stay in the average value of (25/(144x16)) per event namely approx 1% of background photon hits coming from the MAPMT system.
The low background level resulting whe the detector is operated with beam is clearly seen in the right panel of figure 4.12, where the peak in the time distribution of Cherenkov photon events can be easily appreciated over the low background outside the -10 to $+10$ ns time window. A more stringent cut

on the time window for Cherenkonv ring reconstruction at software reconstruction helps improving the detector response in rejecting the background hits. This essentially enhances the background separation of physics events (see figure 4.13). Furthermore the four quadrants behave in a very similar way concerning the noise threshold level as clearly seen in the left panel of figure 4.12 where the threshold distribution for the 9216 MAPMT channels is plot. This allows in fact to guarantee a uniform and homogeneous response of the all 4 quadrants.

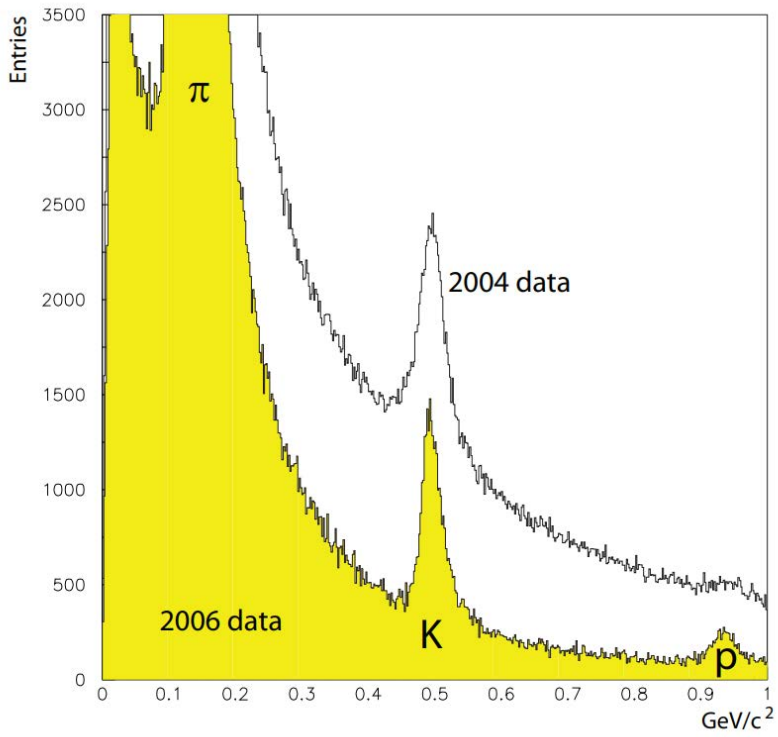

FIGURE 4.13: Mass spectra obtained combining the momentum measured by the COMPASS spectrometer and the RICH information, before (2004 data) in white and after in yellow the RICH upgrade (2006 data). The pion, the kaon peak and the proton peak are visible. The strong background suppression is evident

4.3 Gaseous Photon Detectors: MWPC and MPGD based

4.3.1 MWPC based gaseous photon detectors

MWPCs are used in the peripheral regions of COMPASS RICH-1 as single photon detector[117]. Eight MWPCs are in use four of them are hosted in Saléve side(2 up and 2 down) and 4 in Jura side (2 up and 2 down). MWPCs are a set of thin, parallel and equally spaced anode wires, symmetrically

sandwiched between two cathode planes. For proper operation, the gap (l) is normally three or four times larger than the wire spacing (s). The electrons generated in the gas volume due to ionization drift toward the high field region following the opposite direction of the field lines. Near to the anode wires an avalanche multiplication occurs. MWPCs can be used as photon detectors. The schematic can be seen in figure 4.14. The gaseous photon detector with a solid state photo-converter have been developed by the CERN-RD26 collaboration [92, 93]. The MWPC is coupled with a cathode plane consisting in a PCB segmented into pads and coated with CsI film with the following parameters; 2 mm for each anode-cathode gap, anode wires with diameter = 20 μm and pitch = 4 mm, cathode wires with diameter = 100 μm and pitch = 2 mm. From the construction of all the PD component to the assembly strict mechanical tolerances have been imposed. The MWPCs are operated in pure methane.

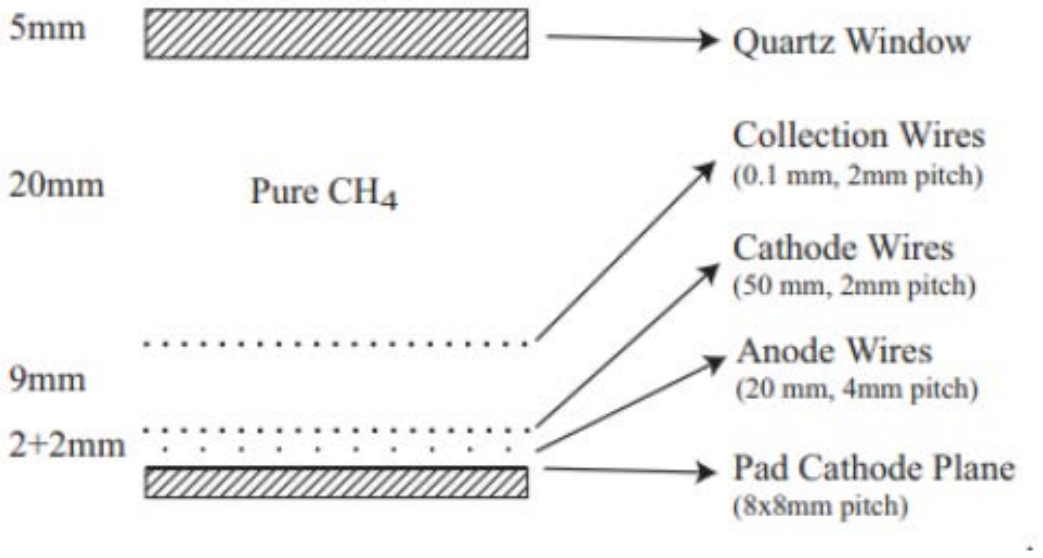

FIGURE 4.14: Schematic of the MWPC based photon detectors for COMPASS RICH-1

CsI has non-negligible quantum efficiency below 210 nm. Good quality quartz windows ensure the effective range of photon detection down to $160 - 210$ nm. The QE of the CsI photo-cathodes depends on the substrate and production procedure: both have been optimised in the context of the RD26 development. Presently, QE as high as about 28% at 170 nm is routinely obtained employing the plants and procedure developed at CERN. Figure 4.15 shows the deposition of the CsI film on the readout pad of the COMPASS MWPCs. Figure 4.16 shows the readout pads after CsI deposition and the endeavours made to protect it from contamination.

The effective QE obtained in a gaseous detector depends on the gas used and the electric field at the photocathode surface. If the photoelectron scatters off elastically a gas molecule the back-scattering probability is high and

part of the photoelectrons impinge back on the photocathode where they are absorbed. Therefore, the effective QE is reduced. The characteristics of the gas molecules and the value of the electric field accelerating the photoelectrons determine the elastic scattering rate and thus the effective QE. Both parameters have been studied in the context of RD26 and newly explored recently. The response in different gas atmospheres has also been reproduced by simulations. At atmospheric pressure, the effective quantum efficiency increases very steeply up to electric field values of about 1000 V/cm. At higher field values, the increase rate versus field is reduced, even if it remains non-negligible. The highest quantum efficiency is obtained in pure methane or in methane-argon mixtures, provided that the methane fraction is high ($> 40\%$).

MWPCs have a basic structure for all applications. For COMPASS RICH-1 the MWPCs are equipped with reflective photocathodes. This solution is preferred over the semitransparent photocathodes because the reflective photocathodes result in a larger photoconversion rate. In fact, the semitransparent photocathodes require the application of a thin metallic film; which absorbs photons to keep the entrance window at a fixed potential. As the probability of the conversion is highest at the entrance surface of the photoconverter hence the probability of photoelectron absorption is lower in a reflective photocathode. Moreover, the thickness of the coating layer is not critical in the reflective configuration and this fact opens the way to the realization of large surface detectors. The detectors have been operating for more than 15 years. The performance and experience of the CsI coating have been studied in detail [118].

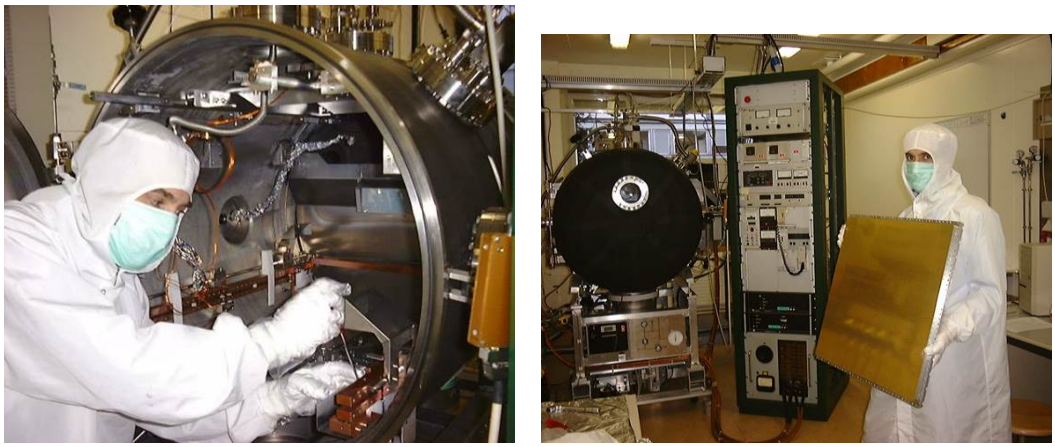

FIGURE 4.15: CsI deposition on the MWPC readout pads at CERN

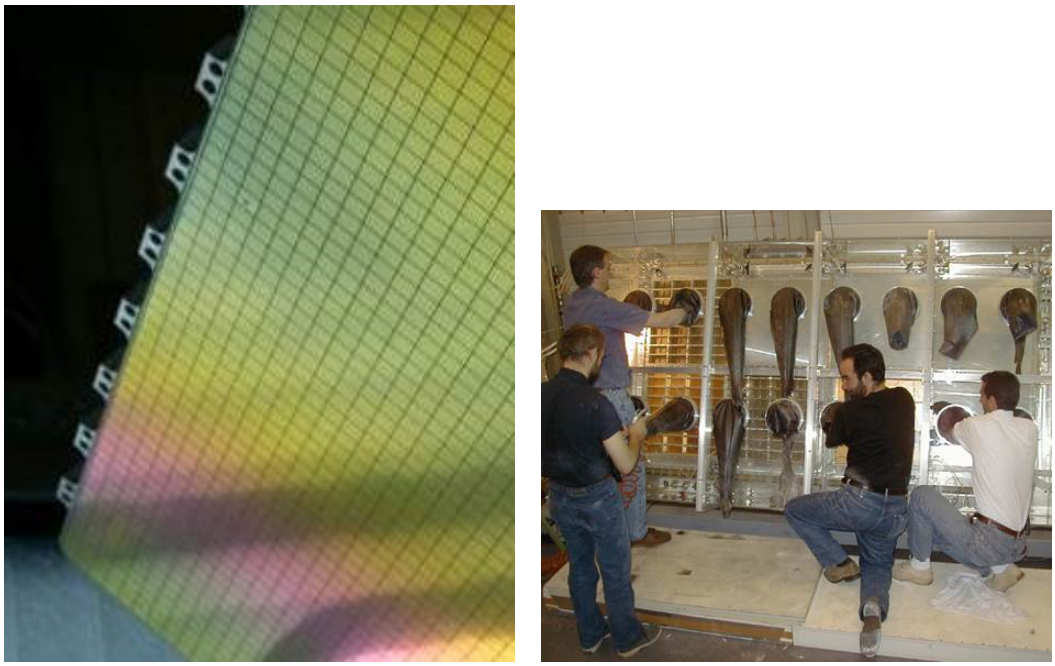

FIGURE 4.16: Left: CsI deposited MWPC readout pads. Right: Endeavors during the installation of the detectors using controlled glove box

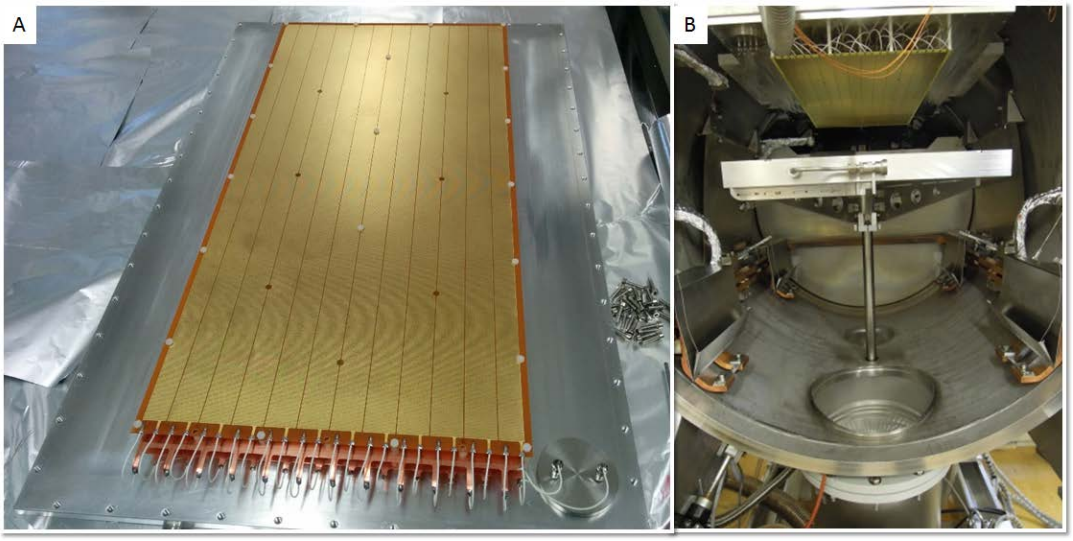

FIGURE 4.17: Left: THGEMS to be coated with CsI Right: CERN CsI deposition facility

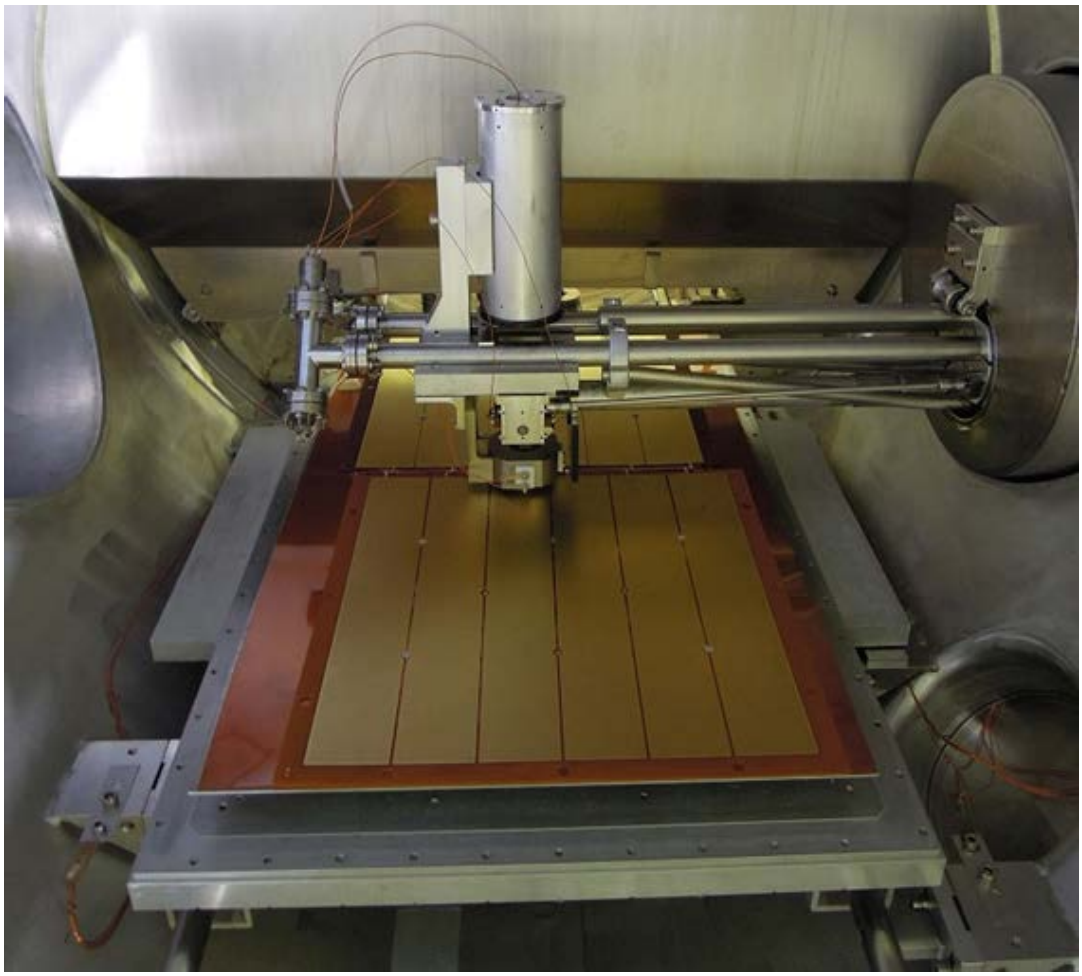

FIGURE 4.18: Measurements related to the related QE of the coated THGEMs

4.3.2 MPGD based single photon detection for RICH-1

PHENIX-HBD [35] has successfully used the Micro Pattern Gaseous Detectors based PDs, in the form of triple GEMs operating in windowless mode, in pure CF_4 gas. Over a wide wavelength range (108-200 nm) Cherenkov photons are converted by the CsI layer on the first GEM and large readout pads (6.2 mm^2) provide 5 to 10 photons per ring. The eight years old dedicated *R&D* programme to develop MPGD based single photon detectors at narrower wavelength range has been successfully completed and 4 MWPC detectors of the COMPASS RICH-1 have been replaced with MPGD based single photon detectors of hybrid structure, consisting of two layers of THGEMs and one MM [119, 120, 121, 122, 123].

THGEMs [124, 125, 126, 127] are derived from the GEM design, where the geometric parameters are scaled and standard printed circuit boards (PCB) are used instead of the GEM foils. The geometrical parameters have been thoroughly optimised and their performance have been studied in detail [100].

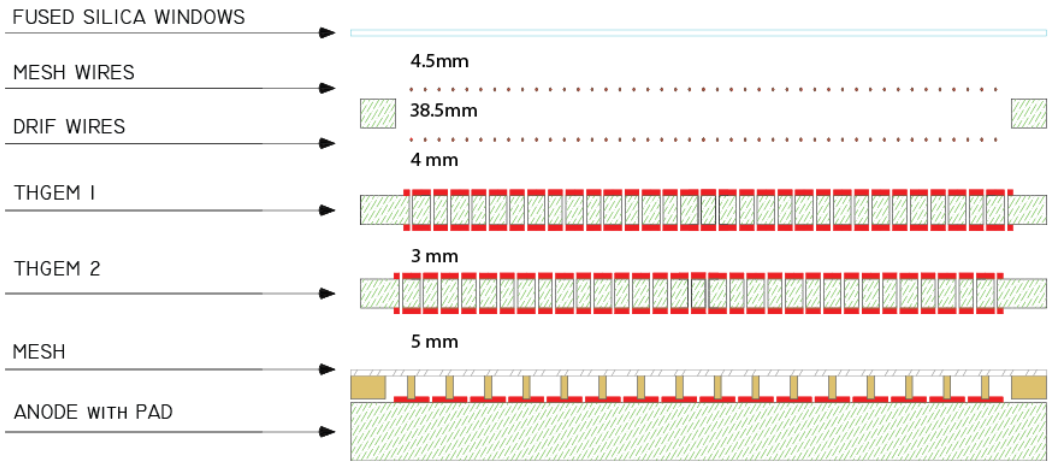

FIGURE 4.19: Schematic of the THGEM-MM based hybrids in COMPASS RICH-1

The hybrid detector architecture.

The schematic of the hybrid PDs is shown in figure 4.19. Each photon detector has an active area of $600 \times 600\ mm^2$ and is formed by two identical modules of $600 \times 300\ mm^2$, arranged side by side. They consist of two layers of THGEMs one bulk MM, and two planes of wires. A CsI layer of 300 nm thickness on the top of the first THGEM electrode acts as a reflective photocathode for VUV photons. All the THGEMs have identical geometrical parameters: thickness 470 μm, hole diameter 400 μm, pitch 800 μm. Holes are produced by mechanical drilling and have no rim, viz. there is no metallic clearance area around the hole. The diameter of holes at external borders is 500 μm in order to avoid an increased electric field in the peripheral THGEM holes. The top and bottom electrodes of each THGEM are segmented in 12 parallel sectors separated by 0.7 mm clearance area. 1 $G\Omega$ resistor electrically decouples one sector from the other. Six consecutive sectors are grouped together and fed by independent high voltage power supply channels [128, 129].
A wire plane made of 100 μm diameter wires with 4 mm pitch is located 4.5 mm away from the quartz window, which separates the radiator gas volume from the detector volume. It collects the ions generated above the THGEMs. A similar wire plane, installed 4 mm from the CsI coated THGEM, is biased to a suitable voltage to maximise the extraction and collection of the converted photo-electrons into the THGEM holes where they start the avalanche multiplication processes. The electron cloud generated in the first multiplication stage is driven by a 1.5 kV/cm electric field across the 3 mm transfer region to the second THGEM, where thanks to the complete misalignment between the two layers, it splits among two or three holes, where a second independent multiplication process takes place. Finally, the 0.8 kV/cm field across the 5 mm gap to the bulk MM guides the charge to the last multiplication step in the MM. Pillars with 300 μm diameter and 2 mm pitch keep

the micromesh (18 μm woven stainless steel wires, 63 μm pitch) at 128 μm distance from the anodic plane. The intrinsic ion blocking capabilities of the MM as well as the arrangements of the THGEM geometry and fields grant an IBF on the photocathode surface lower or equal to 3% [130, 131, 132, 133, 134].

Production of THGEMs and quality assessments of the hybrid photon detector components.

The THGEMS were produced from halogen-free raw PCB foils (EM 370-5 by Elite Material Co, Ltd.). A selection of the raw material based on homogeneous thickness, is needed in order to ensure homogeneous gain: a foil is accepted when $(th_{max} - th_{min}) \leq 15\ \mu m$, where th_{max}, th_{min} are the maximum and minimum of the measured thickness values. The selected foils are mechanically drilled by ELTOS S.p.A. using a multi-spindle machine.
A dedicated polishing method was applied to get rid of drilling residuals in the holes and to make the hole edges smooth, and to refine the surface polishing.
THGEMs were validated by measuring gain uniformity, breakdown voltage and discharge rates when illuminated by X-ray source.
The quantum efficiency of the CSI photocathodes was measured in the CsI evaporation plant and it is compatible with the maximum Q.E. values expected. The figures 4.17 and 4.18 show the THGEMs prior to the CsI coating, and the measurements performed at the CERN CsI deposition facility.

Performance

The new hybrid PDs have been installed on COMPASS RICH-1 and commissioned during 2015-16 Physics Run. They operate at a gain of 15-30K in $Ar : CH_4$ 50 : 50 gas mixture. The σ_{noise} is $\sim 1500\ e$ Electron Noise Equivalent, which ensures high efficiency in single photo-electron detection. A detailed characterization of the newly installed photon detectors has been done and is reported in the following chapter .

4.3.3 Readout pads for gaseous detectors

The virtual size of the pads for the MWPC and the Hybrids are the same. It is $8 \times 8\ mm^2$ which is 30 μm thick Cu pads. For the MWPC the Cu dimension $7.7 \times 7.7\ mm^2$. The separation between two Cu pads is 0.3 mm. The finite size of the pad leads to an uncertainty in the reconstructed Cherenkov angle. The pads are distributed in a uniform way. The uncertainty due to granularity is therefore

$$(\sigma_\theta)_{pad-size} = \frac{s}{f\sqrt{12}} \tag{4.2}$$

Where s is the pad size and f is the focal length of the mirror. In COMPASS, we have the mirrors with focal length 3300 mm, which makes the $(\sigma_\theta)_{pad-size}$

for the gaseous detectors to be $700\mu rad$. 72×72 readout pads are used for each MWPC. Four pads at the corners are not sharp edged like the others. Those four pads are rounded at the edge of radius $0.3mm$. In order to shape the field externally to the virtual pads a 1 mm Cu strip is present. The strip is at $0.15mm$ from the border of the virtual pad. The virtual pad area is therefore $72 \times 72 \times 8 \times 8 = 576 \times 576\ mm^2$. This is the dimension of the active area of the MWPCs. The effective area of the PCBs is $580 \times 580\ mm^2$.
If we assume a cathode coordinate system with origin at the centre of the PCB, and the Z direction is the normal to the pad plane, then the borders of the PCB are at $(\pm 290, \pm 290)\ mm$ from the centre. This centre of the cathode is an input for the reconstruction software. If the coordinates of this centre are know in the lab frame, the coordinates of the centre of any pad of the cathode can be estimated, by transforming the information into the detector frame of reference. If we have an iterator x_i and y_j, then the centre of the pad is at $[(8i-4), (8j-4)]\ mm$ from this hypothetical centre. Each of the indices runs from -35 to 36. The distance between the nearest Cu pad borders of the neighbouring cathodes is 26.3 mm.

The charge generated by the multiplication process of the hybrids is collected by $7.5 \times 7.5\ mm^2$ anode pads which are biased at positive voltage and facing the grounded micromesh. This segmentation results in 4760 readout channels for detector. Each anode pad is biased through an independent 470 $M\Omega$ resistor. The signal is capacitively induced on a parallel buried pad and read out by the front end electronics based on the APV25 chip.

A future electron ion collider (EIC), which is believed to answer precisely to many fundamental questions regarding the spin contributions of the partons to the total nuclear spin, emergence of hadrons from dense quark-gluon system etc will need to identify high momentum hadrons in the final state. The collider setup will impose the RICH to be compact. In the experiments where the high momentum hadron PID is essential and strict constraints on the available space are present and hence for the RICH a restriction in choosing a large radiator size and mirror with large focal length, the possibility is to go for smaller pad size. An intense $R\&D$ activity has been done at Trieste INFN laboratory in this direction to minimise the pad size. I have taken part in the lab activity and the beam test activity for this project [135].

4.3.4 APV based electronics

The APV25-S1 chip [136] is a 128-channel preamplifier/shaper ASIC with analog pipeline, originally built for the CMS silicon micro-strip tracker[137]. COMPASS has successfully implemented APV25 chips for the GEM, silicon and pixel MM, tracking detectors [138, 56]. Its peaking time is adjustable in a wide range from 50 to 300 ns, opening the possibility to use the APV25-S1 to read "slow" detectors such as MWPCs. The amplifier output amplitudes are sampled at a frequency of 20 or 40 MHz and stored in a 192 cells analog

pipeline. When an event is triggered, the signals from cells to be read are multiplexed into a single differential output. In order to obtain timing information, two additional samples on the rising edge of the signal are read. The time gap between these individual samples can be varied in steps of 25 *ns*, depending on the shape of the input signal. For the RICH MWPCs, the sampling step size is set to 150 *ns*. A 10-bit flash ADC digitises the multiplexed analog data stream from each APV25-S1 chip, and a FPGA performs on-line zero suppression. In order to match the form factor of the present RICH front-end cards, four APV25-S1 chips, each reading 108 RICH pads, are included in one front-end card. Three front-end cards are then connected into one ADC module.

4.4 The Cooling system

The readout cooling system is an essential part of the COMPASS RICH-1. It controls the temperature of the read-out systems of the MAPMT , the CsI MWPCs and the Hybrid PDs. It has been designed to avoid too high temperature of the electronics components.The cooling system is based on the under-pressure circulation of temperature controlled water.

Chapter 5

Characterization of the Hybrid Photon detectors

5.1 Introduction

For the first time in a running experiment THGEM-MM based hybrid PDs are implemented as single photon detectors in a RICH for hadron identification. The motivations of the upgrade include: better stability, reduced IBF, larger gain, comparable number of photons and single photon resolution. The analysis of the data taken for the characterisation of the hybrid PDs is unique and has never been done before. The newly installed hybrid PDs were in commissioning phase in 2016 [139]. Between the end of 2016 and mid 2017 I spent time for detail understanding of the reconstruction algorithm and looking into the online performance of the hybrid PDs. I developed an analysis framework with Yuxing Zhao during these period in order to achieve a systematic characterisation of newly installed detectors. The data analysis framework for the characterisation is written in C++. It is a lightweight software. Three important properties have been studied : The gain of the photon detectors extracted from real data and its stability in time, the photon angle resolution and number of photons in different Cherenkov angle bins. Furthermore, I modified the reconstruction software to extract the time information for the signal formation of the detector, to study its time resolution. Precise knowledge of the time information can be used in future for further reduction of the out of time photons.
In 2016-2017 the data taking was mostly focused on the DVCS program where the primary objective is to look at the final state photon and the recoil proton, therefore the trigger was designed such that the final state particles in the very forward region are selected. We organised and setup a dedicated pion run in order to illuminate the newly installed detector in the peripheral region. The COMPASS collaboration allowed us to be the main users of two days of negative pion beam run fully dedicated for calibrations and characterisations. We choose to use pion beam since the strong interaction between pion and the proton target generates more final state hadrons, mostly pion, and covers a wide phase space. I developed a specific but simple trigger system to ensure that the hybrid detectors were well illuminated.

5.2 Hybrid PD Characterisation Trigger

To set up the special RICH hybrid characterisation trigger, I have taken into account the constraints imposed by the the geometry and threshold of the triggering elements, the allowed beam intensity and energy and the limitation of the data acquisition system. The event rate (N_E) of particle production is given by:

$$\frac{N_E}{\Delta T} = \mathcal{L}.\sigma \tag{5.1}$$

where ΔT is the measure of convenient time unit, can be spills like our case. $\mathcal{L}$ and σ are respectively the luminosity and interaction cross-section. The luminosity for a fixed target experiment takes into account both target and beam information:

$$\frac{N_E}{\Delta T} = \Phi \rho l \sigma$$

In this equation Φ, ρ and l are the incoming particle flux, density of target particles and length of the target respectively.

For our run in 2016-2017 we had used an unpolarised proton target. We have a 2.5 m long cylindrical volume filled with liquid hydrogen described in the section 2.2.2 of chapter 2. The density of liquid hydrogen is 71 g/l [18]. We used a π^- beam with 160 GeV/c nominal momentum. The pion beam flux recorded in the ion chamber was $\sim 2.4 \times 10^6$ per spill. The COMPASS centre of mass energy ($\sqrt{s}$) is given by 17.88 GeV/c. At 17.88 GeV/c the total cross-section for $\pi^- p$ is 24 $mbarn = 2.4 \times 10^{-26}$ cm^{-2} [18].
$\mathcal{L} = 71 \times 250 \times 2.4 \times 10^6 \times 6.2 \times 10^{23}$ $cm^{-2} spill^{-1}$
$\mathcal{L} = 2.7 \times 10^{31}$ $cm^{-2} spill^{-1}$
Therefore the expected event rate is $2.4 \times 10^{-26} \times 2.7 \times 10^{31}$ $spill^{-1}$, which is 0.65 million events/spill.

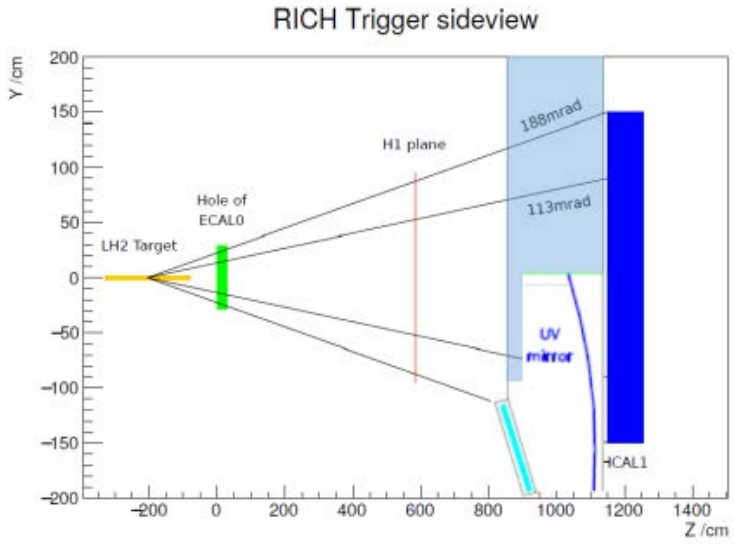

FIGURE 5.1: Schematic side view of the hybrid characterisation trigger set up

To illuminate the hybrids we need to illuminate the angular region $100 - 200\ mrad$ as shown in shown in figure 5.1.The trigger could select roughly 5% of the interactions on the bases of out coming hadron angle. We used the basic trigger logic scheme used for ECAL0 calibration for our characterization and set the thresholds of the HCAL1 modules according to our need as illustrated in figure 5.2. In the figure the green color corresponds to the HCAL1 modules which covers our expected illumination region for the hybrids and the blue one for the peripheral MWPCs.

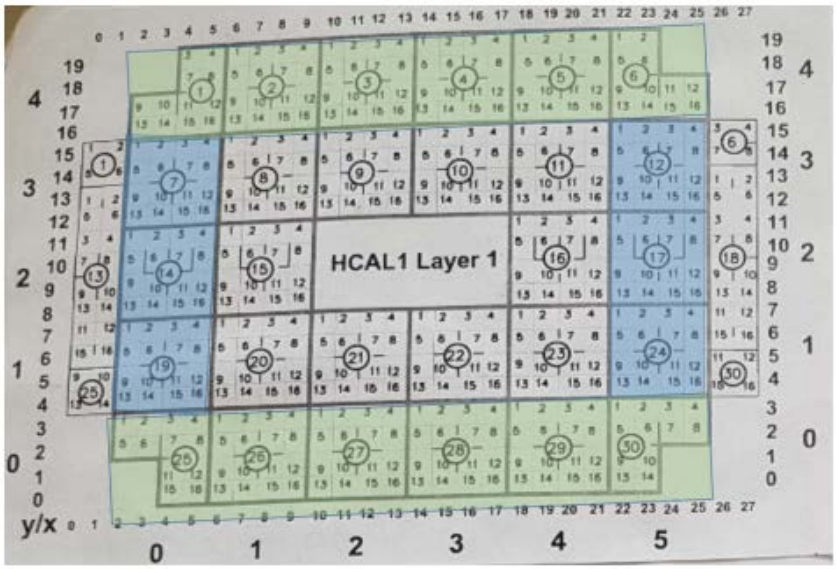

FIGURE 5.2: Front view of the HCAL1 cells used for hybrid characterisation trigger

The trigger condition ensured that there was an interacting beam: signal from beam trigger and no signal after beam stopper. This logic was in coincidence with the HCAL1. To maximise the data taking efficiency a threshold of $\sim 4\ GeV$ was applied in the HCAL1 for the trigger layer1 which is the white region of figure 5.2. With this condition the measured trigger rate was 20 K per spill, slightly lower than the expected trigger rate of 32 K computed beforehand. In total of 6408 spills were collected with pion beam, out of which 5429 spills were usable for Hybrid PD characterisation. We can follow table 5.1 and figure 5.3 for the number of spills used for different tasks performed during the pion data taking and the number of spills collected to perform the characterisation of the new detectors.

Task	Spills
Voltage Scan	240
Drift Scan	390
Others	51
Latency Scan	90
Test	70
pi Data for analysis	5429
Empty	138

TABLE 5.1: Table displaying the number of spills used for different purposes.

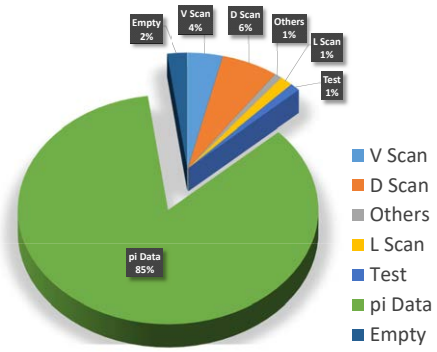

FIGURE 5.3: Comparison between collected and usable data.

5.3 Tuning and alignment

Prior to the analysis a very careful alignment and refractive index tuning has been performed. These studies have pointed to some required modifications of the geometrical description of the RICH-1, I have discussed the required modifications in the following chapter in details.

The knowledge of the refractive index of the radiator gas is an essential parameter for the particle identification; the estimation its value from the real data is an extremely powerful tool for monitoring the overall consistency of the detector description. From the real data the momentum (p) is measured by the spectrometer and for each photon the Cherenkov angle θ is measured by the RICH. These two independent measurements estimate the refractive index of the radiator gas with a hypothesis of the particle mass.

$$n = \frac{\sqrt{p^2 + m_\pi^2}}{p \cos\theta} \tag{5.2}$$

The sigma of the refractive index is related to the single photon resolution and the momentum resolution. During the analysis we found that the upper

and lower detectors do not provide consistent values of the refractive index. The problem was addressed by surveying the detector positions to obtain a modified geometry and later by a data driven estimation of the global positioning of the mirror. This major exercise was followed by a consistency check which allowed us to get back the refractive index according to expectation. The analysis presented in this chapter includes all the needed corrections.
In the gaseous detectors we have limited momentum coverage. Therefore, I estimated the shape of the background and then the signal has been estimated by subtracting the background bin by bin. In figure 5.4 we have plotted the histogram of refractive index extracted from each measured photon angle by the cathode 2 hybrid detector. An estimated background has been extracted bin bin bin and a Gaussian is fitted around the peak of the signal. They are consistent. During the pion run data taking the RICH was filled with N_2 gas. The fraction of C_4F_{10} present inside the radiator during the pion data taking is roughly $70 - 75\%$ of the total radiator volume. The plotted result is obtained after the RICH tuning which has been discussed in detail in chapter 6.

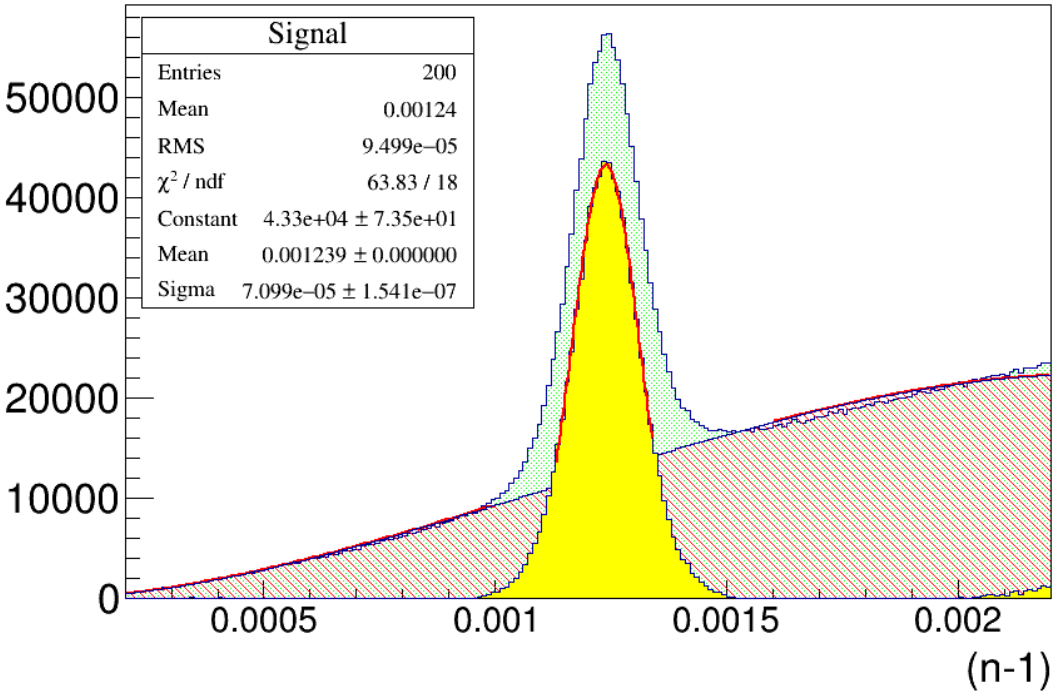

FIGURE 5.4: The (n-1) histogram for the refractive index of a hybrid detector, namely cathode 2

5.4 Effective gain of the hybrid PDs

Determination of the gain of the detector is very much related to the reconstruction of the shape of the signal generated by the detector. The gaseous

detectors are read out by APV25 chips, once a trigger is received after a latency time the APV25 chips provides three sample of the signal each at 150 ns interval along with the channel id of the APV25 chip to the daq, these are the relevant information for the detector signal. They are conventionally known as A_0, A_1 and A_2 where, ideally A_0 is the rising point of the signal, A_2 is the peak point and A_1 is exactly at the middle of A_2 and A_0. These three information are fed to the reconstruction software to determine the shape of the signal at a particular channel. At the reconstruction level if a channel passes the cut ($A_0 < A_1 < A_2$), it is considered as a hit, namely a pad with physical signal and not a noisy pad. After this selection a clustering method is applied which I have described in the description of the RICHONE software. In the clustering algorithm adjacent to the pad with the maximum signal 'connected' pads are searched. The A_2 of the pad with maximum signal is passed to the photon object as the signal information, which is according to our APV25 calibration in the unit of about 300 equivalent electrons per ADC channel. The distribution of the A_2 is expected to be an exponential distribution due to the fact that it comes from single Cherenkov photo-electron multiplication in Gaseous detector as can be seen in figure 5.5.

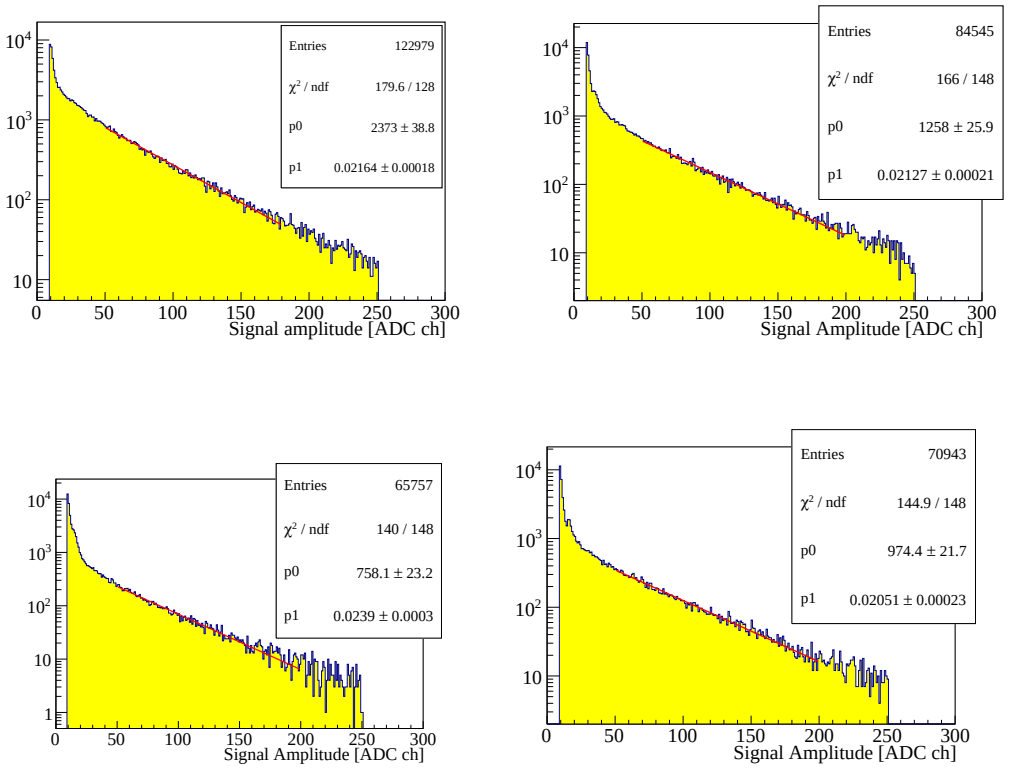

FIGURE 5.5: Histogram of signal amplitude in ADC units for one run are shown in four panels. Top left: Cathode 2 Jura Top Hybrid; Top right: Cathode 4 Saleve Top Hybrid; Bottom left: Cathode 11, Jura Bottom hybrid and Bottom right: Cathode 13, Saleve bottom hybrid.

The value of the gain and the associated error have been extracted from the fit parameters according to the following equations.

$$\begin{aligned} gain &= 300 * 1/p_0 \\ \delta gain &= 300 * 1/p_0^2 \delta p_0 \end{aligned} \tag{5.3}$$

The first part of the equation 5.3 describing the estimation of the gain and the following part is the error associated to it. The gain values extracted from the whole pion data taking are summarised in the following table:

Cathode	Average Effective Gain
2	$\sim 14000 \pm 200$
4	$\sim 14200 \pm 250$
11	$\sim 12500 \pm 300$
13	$\sim 14700 \pm 300$

The gas electron multiplication depends on the Townsend coefficient, which is the inverse of the mean ionisation length. The mean ionisation length depends on the thermodynamics conditions of the gas. The effective gain depends on the product $(E\frac{T}{P})$, so a 1% variation in the T/P can be compensated by a 1% variation in the field E. As for the THGEMs and MMs the field is proportional to the applied voltage difference with different proportionality constants, a correction in the applied voltage is made to compensate the change in the variation in the environmental temperature and pressure. The variation in the values of the pressure and temperature of the gas inside Jura Top hybrid during the two days of pion data taking can be seen in figure 5.6 and figure 5.7 respectively. These fluctuations in the absence of the high voltage correction would have induced a gain variation larger than 15%. Followed by a detail study [129, 128] an automatic voltage correction has been implemented into the high voltage software. With respect to a reference temperature and pressure a correction factor is computed and whenever the correction implies a one per mil change in the voltage value the voltage is adjusted accordingly. In the data structure of RICHONE tree the effective gain can be measured run by run. In figure 5.8 we have plotted the average effective gain of the Jura Top hybrid for each pion run versus the run number. The plot displays the time evolution of the average effective gain for Jura Top hybrid and shows that the gain is stable within 2% level. In figure 5.9 the same average effective gain values are plotted versus the average of the correction terms within the corresponding run. The associated error bar along X shows the spread of the temperature and pressure correction factor. The error associated to the determination of the average effective gain is computed by propagating the error on the statistical effects only. We can see that the gain remained stable with rms value of about 2% of the gain for the pion data taking, corresponding to a reduction of fluctuations by almost an order of magnitude with respect to the situation without correction. The same conclusion has been obtained for data taken over the whole year.

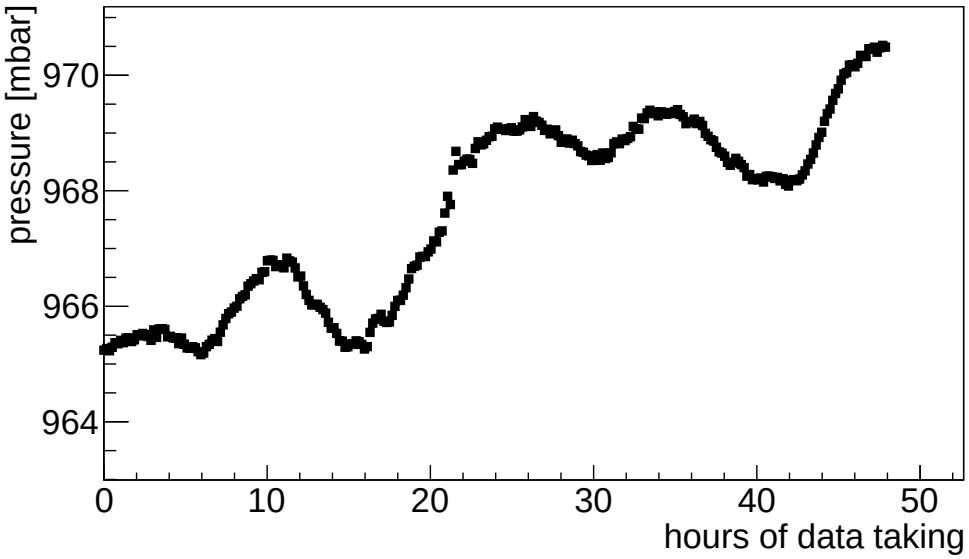

FIGURE 5.6: Variation of gas pressure recorded for Jura Top hybrid during the pion data taking

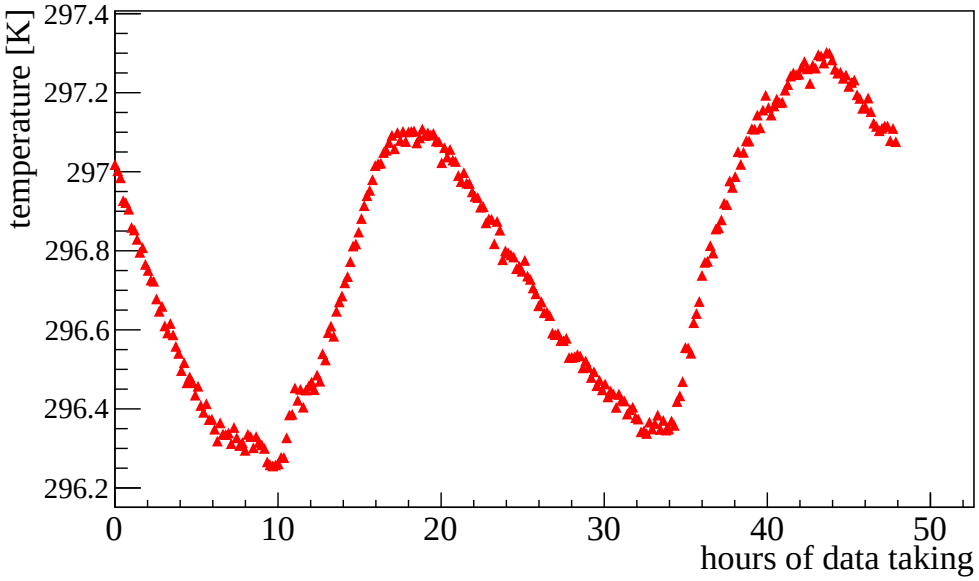

FIGURE 5.7: Variation of gas temperature recorded for Jura Top hybrid during the pion data taking

The gain showed stability within the error limit.

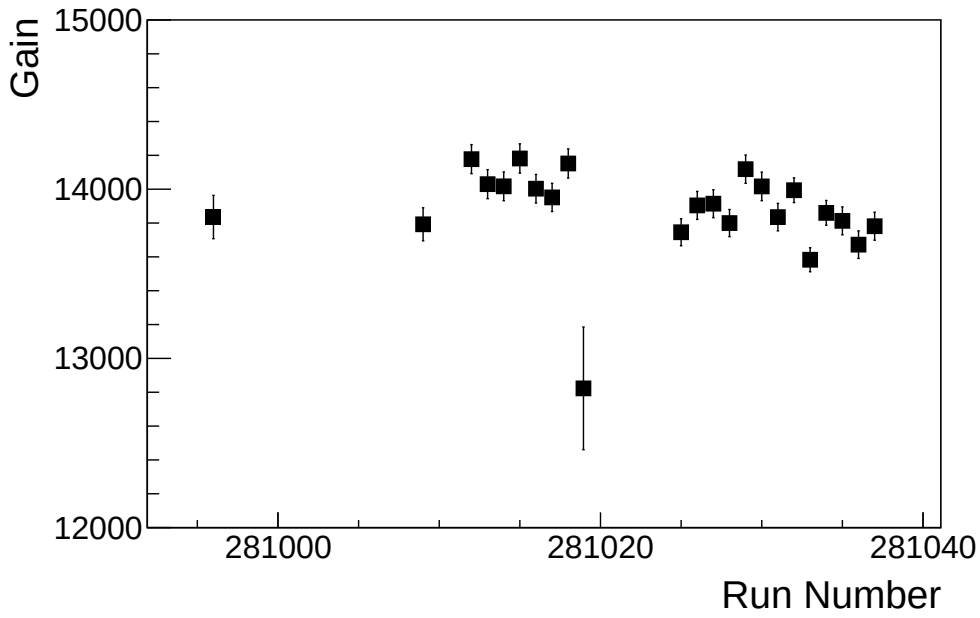

FIGURE 5.8: Average effective gain values of the Jura Top hybrid versus run number

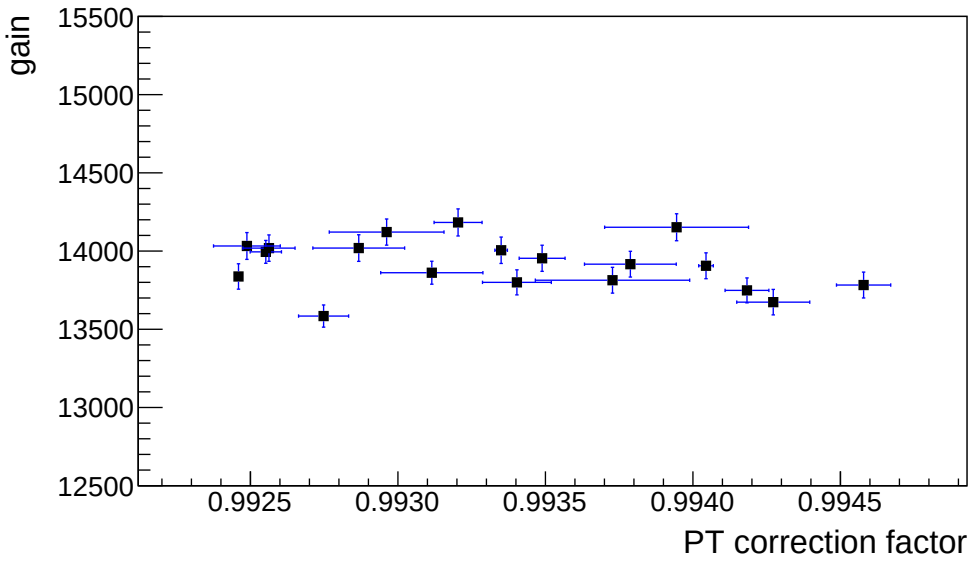

FIGURE 5.9: To stabilise the variation in the gain due to temperature and pressure fluctuation in the environment, the voltage is adjusted to compensate the change. Similar gain values at different correction factor suggests the gain remains stable for the pion data taking

5.5 Single Cherenkov Photon angle resolution

High single photon resolution is one of the decisive parameters for efficient particle identifications. Therefore estimation of the single photon resolution is a key exercise for the characterization of a single photon detector. In the reconstruction algorithm each cluster is associated to a Cherenkov and azimuthal angle. Selecting pion like tracks, we can calculate the resolution of single photon detection of the Hybrids. The residual of the constructed Cherenkov photon angle is given by:

$$\theta_\pi = arccos(\frac{\sqrt{p^2 + m_\pi^2}}{np}) \qquad (5.4)$$
$$\Delta_{theta} = \theta_{ph} - \theta_\pi$$

If the refractive index is correctly set the distribution of the residuals will be centered around zero and distributed like a Gaussian. The sigma of the fit gives an estimate of the resolution of detecting single photon in mrad unit. In order to estimate the single photon resolution, I used a selected set of tracks identified as pions by the RICHONE PID algorithm which will be explained in detail in Chapter 7. The pion samples were relatively pure. We assumed that the π-p interactions have pion enriched final states, and filtered out events with highest likelihood value less than 1.2 times the second highest hypothesis. In figure 5.10 we see the histograms of the single photon angle residual for individual hybrid PDs for a particular run. In figure 5.11 histogram for the photon angle residual of all hybrids combined together are plotted. The resolution is found to be $1.83 \pm 0.01 mrad$.

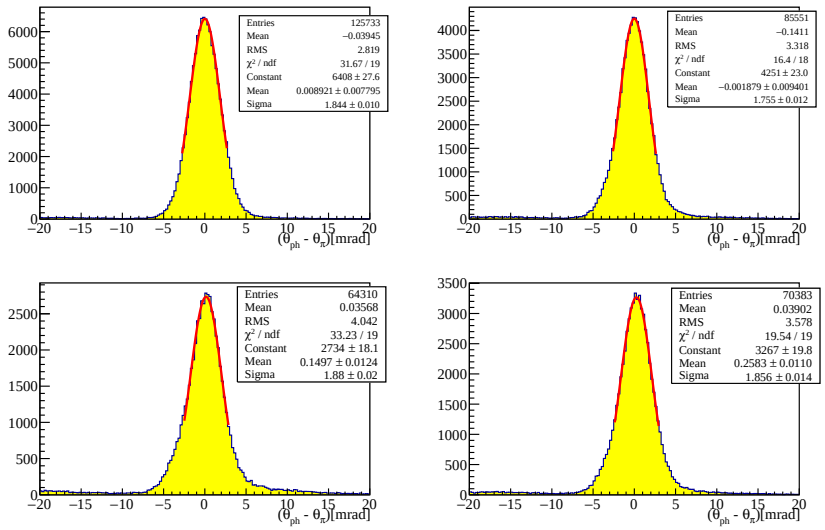

FIGURE 5.10: Histogram for the photon angle residual of hybrids. Top-left Jura Top (cathode 2), Top-right: Saléve Top (Cathode 4); Bottom-left Jura Bottom (cathode 11); Bottom-right Saléve bottom (Cathode 13).

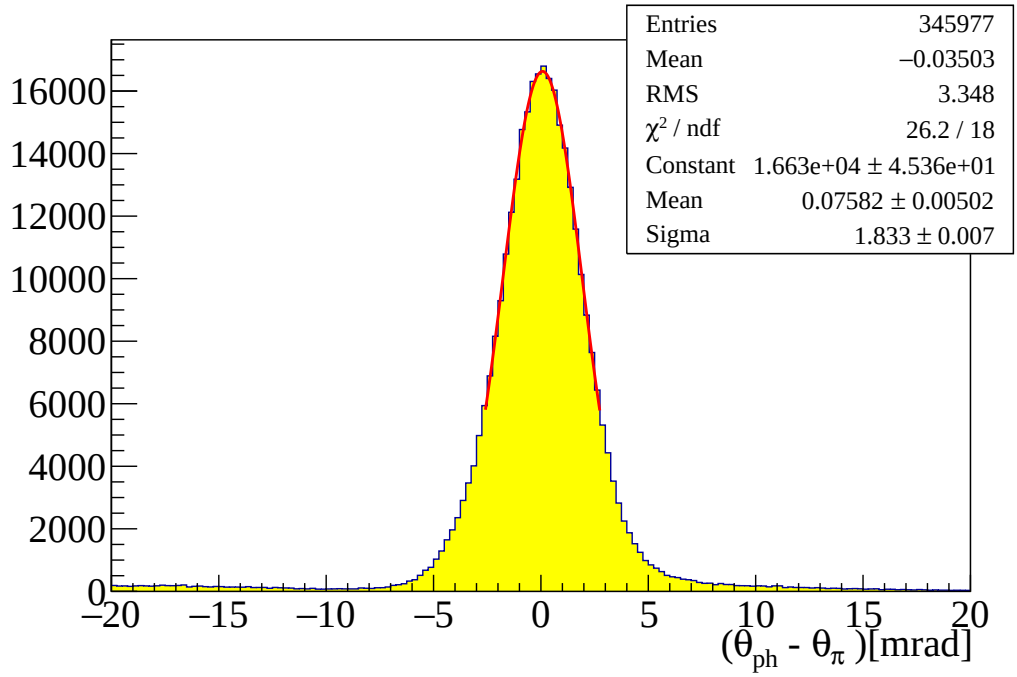

FIGURE 5.11: Histogram for the photon angle residual of all hybrids combined

The MWPCs have the similar pad size compared to the hybrids. A similar single photon resolution is expected. Nevertheless, the MWPCs beside the Hybrids are affected by larger spherical aberrations. The situation can be seen, when we analyse the individual cathodes. In the figure 5.12 it is seen that, cathode id 0 (top-left plot) and cathode id 9 (bottom right plot) have lower resolution compared to cathode id 1 and 8. These detectors are significantly affected the by the spherical aberration.

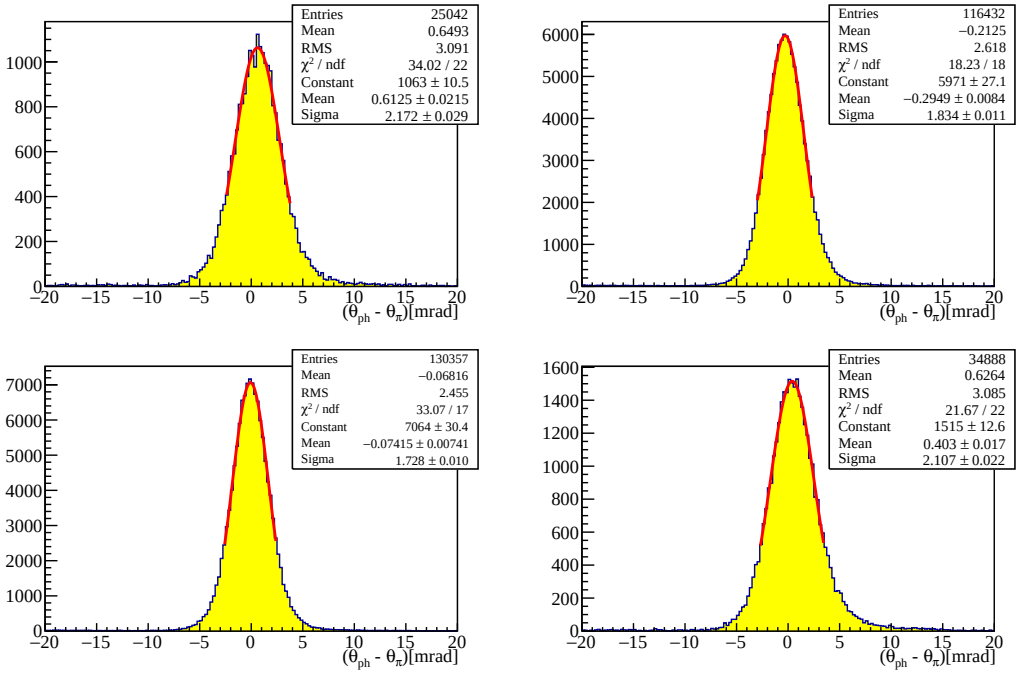

FIGURE 5.12: Histograms of the single photon residual for individual MWPC cathodes are shown. Top Left corner: MWPC cathode id 0, top-right: MWPC cathode id 1, bottom-left: MWPC cathode id 8; bottom-right: MWPC cathode id 9.

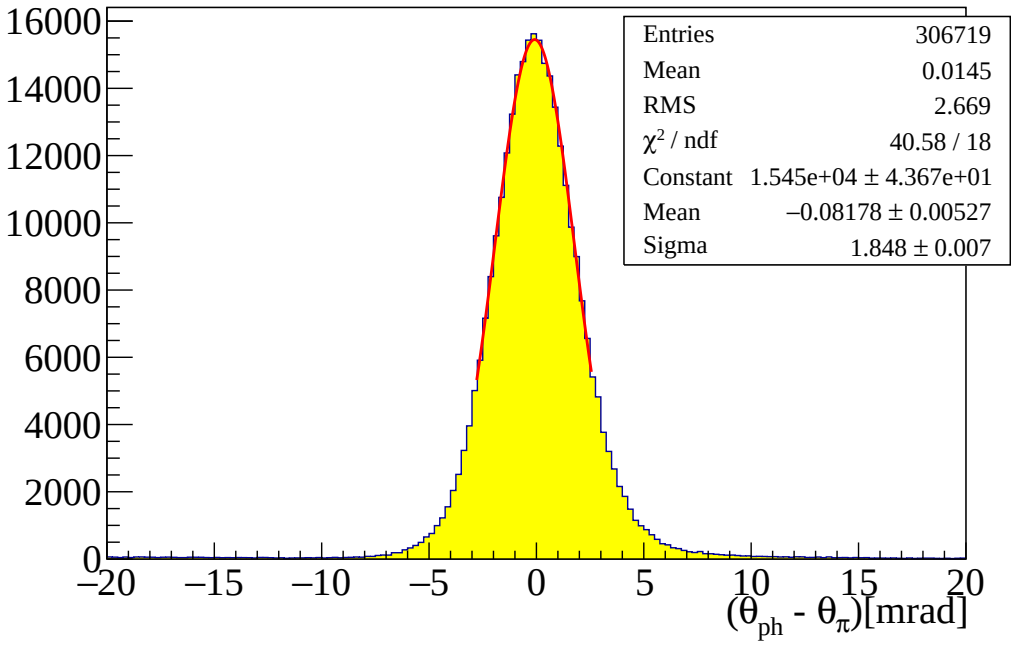

FIGURE 5.13: Histograms of the single photon residual for all MWPC cathodes combined are shown.

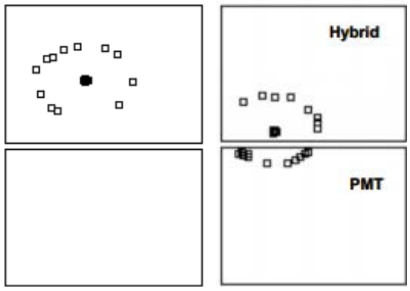

FIGURE 5.14: Event display showing rings in the Hybrid. Left: fully contained ring in the hybrid, right: ring shared between the MAPMTs and the hybrids.

The global resolution of the MWPCs is $1.85 \pm 0.01 mrad$, which is similar to the Hybrid ones, as can be seen in figure 5.13.

5.6 Study of the number of photons per ring

The average number of photons per ring is proportional to the square of the sine of the Cherenkov angle. The observed number of detected photons shows the behavior expected according to the Frank and Tamm law. The Frank and Tamm law has been described in chapter 3. This expected behavior can be seen in figure 5.15 where the points marked by crosses represent the measured numbers of photons, while the open circles represent the numbers corrected for the effect of the non negligible probability of a statistical outcome of zero photons when the average is very small. Although, the trigger was designed to optimise the illumination in the hybrid detector region the statistics of fully contained ring in the hybrid is insufficient for a detailed study.

Most of the photons in the hybrid detector belong to rings which are shared between the MAPMTs and the hybrid detectors. Figure 5.14 shows a typical fully contained ring in the hybrids and also a typical ring which is shared between hybrids and MAPMTs. The sample of shared ring is richer in statistics. To increase the statistical accuracy of the estimate, the shared rings are used too, provided at least half of the ring corona is contained in the active area of the novel hybrid PD. The RICHONE ring reconstruction combines the information from the gaseous detectors and the MAPMTS to provide the ring parameters. The details of the ring recognition are mentioned in appendix C. The horizontal axis of all the number of photon figures refers to the global reconstructed ring angle. The vertical axis instead refers to the number of photons found in the half corona inside the hybrid detector

multiplied by two. We expect the histogram to be a sum of background contribution proportional to the area of the corona and the quadratic Frank and Tamm signal.

$$f(\theta) = p_0 sin^2(\theta) + p_1\theta \tag{5.5}$$

For instance, in figure 5.15 the crosses represent the observed average number of photons multiplied by two. For each bin of the Cherenkov angle values the number of photons in the half corona is distributed according a Poisson distribution. The events with no hits in the hybrid half corona will not enter into the histogram, therefore, the crosses are the average of the nonzero part of the Poisson distribution. The circles represent the corrected average of the full Poisson distribution taking also into account that the probability of a photon being detected in the correct half of the ring has Binomial distribution. The circles therefore represent the best estimation of the number of photons for each theta bin. The fit described in equation 5.5 of the corrected distribution with a quadratic (Frank- Tamm) + linear (random background) function is then performed in the range of Cherenkov angles where high statistical accuracy and small correction effects are present. Parameter p_0 and p_1 are the coefficients of the signal and the background terms respectively. The Frank and Tamm plot for cathode 2 and cathode 4 are presented in figure 5.15 and figure 5.16. The full characterisation has been performed only for the top two hybrid detectors. The quality of the fit is good and the parameter values do not depend significantly on the fitting range for both detectors. For cathode 2 the curve shown in figure 5.15 provides a value of 13.6 hits at a Cherenkov angle value of 55.2 mrad, which is the traditional reference Cherenkov angle value at saturation for CsI photoconverter and a C_4F_{10} radiator at s.t.p.; the number of detected photons from the fit is $\sim 12.0 \pm 0.7$ and the background contribution is $\sim 1.6 \pm 0.6$.

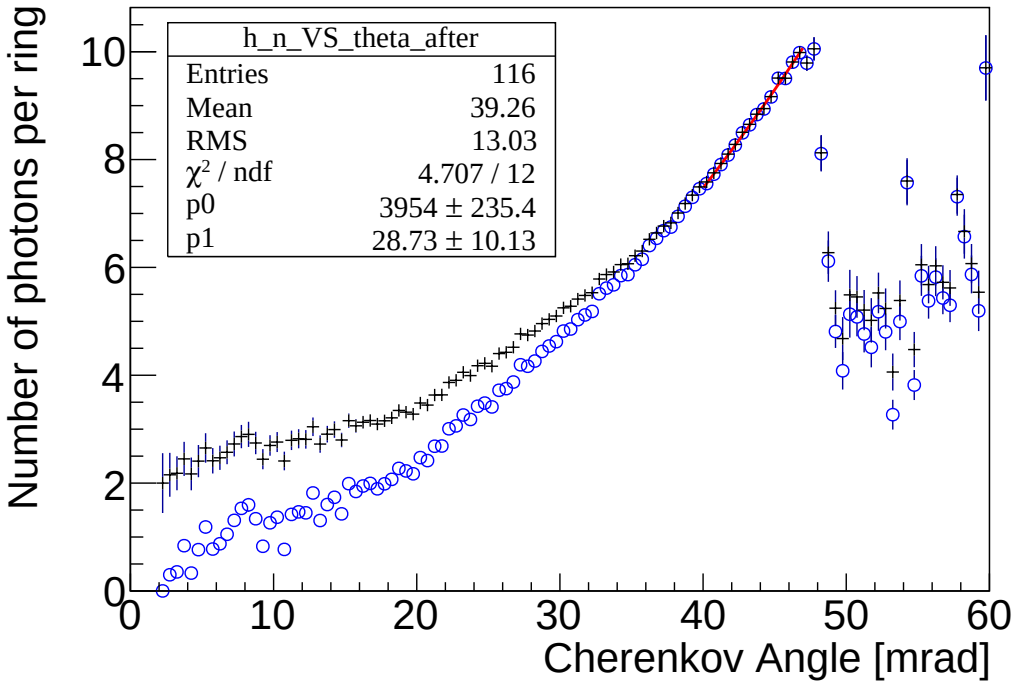

FIGURE 5.15: The number of photons per ring versus Cherenkov angle of the ring. The parameters have been extracted fitting the range 40-47 *mrad*, for cathode 2

The total number of photons per ring when extrapolated to 55.2 *mrad* is found to be 13.6, where the signal part of the function contains 12.0 +/- 0.7 number of photons and the background part of the function contains 1.6 +/- 0.6 number of photons.
In figure 5.15 we see that after the saturation angle we do not have the presence of signal term anymore. The background term is seen to be increasing with the ring θ linearly.

Similarly for cathode 4 we have obtained the numbers: The number of photons per ring when extrapolated to 55.2 *mrad* is 10.3, where the signal part of the function = 10.1 +/- 0.8 number of photons and the background part of the function= 0.2 +/- 0.60 number of photons.

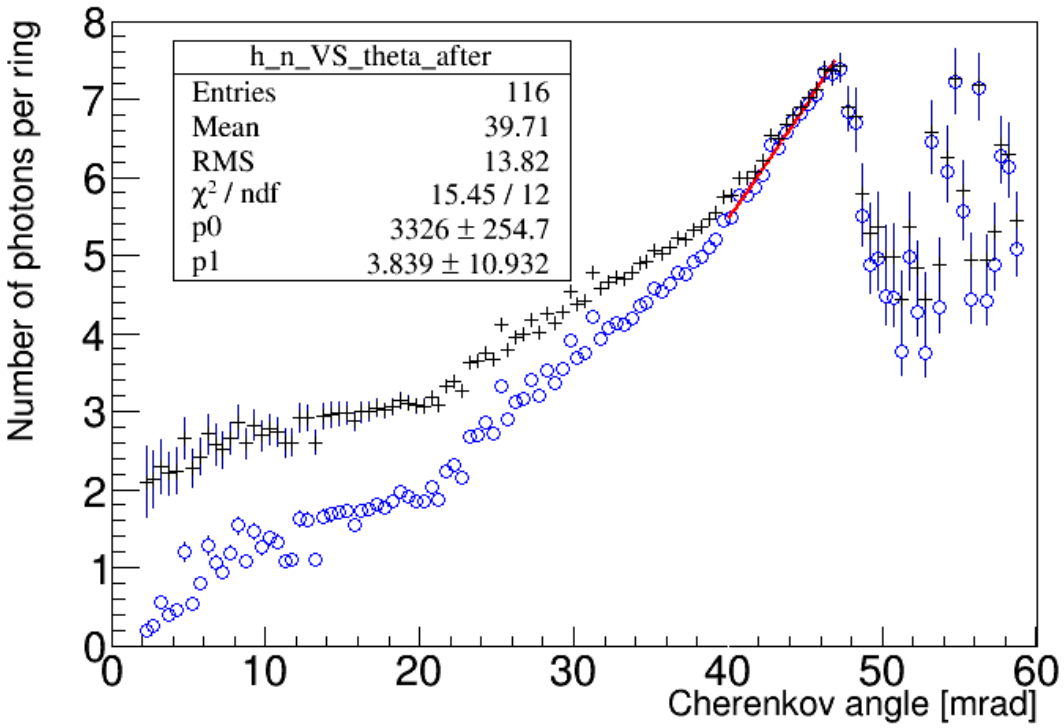

FIGURE 5.16: The number of photons per ring versus Cherenkov angle of the ring. The parameters have been extracted fitting from 40-47 mrad, for cathode 4

An independent estimate of the noise fraction can be obtained from the distributions of all the hit amplitudes for the photons within the theta ring range used for the fit (40-47 mrad). The amplitude distribution is fit in a stable range. The fitting curve is extrapolated down to the first bins. The bin contents of the first bins are added and the difference between this sum and the extrapolated integral is defined as the noise. The ratio of the noise over the total entries is computed as the noise fraction.
The fit also provides an estimate of the noise fraction in the fitting range (40,47 mrad). The integral of the fitted part of the background over the total integral in the fitting range gives an estimation of the noise fraction. They are compatible for both hybrids. Table 5.2 summarises the results.

Noise Fraction		
Top Cathode	Jura	Saleve
From Frank and Tamm fit	0.19	0.30
Amplitude Spectra	0.20	0.26

TABLE 5.2: Noise Fraction of the top two hybrids

We do not expect the number of photons to be exactly the same for the cathode 2 and 4, since we know that the relative quantum efficiency of the coated CsI is slightly different and also the single photoelectron detection efficiency, defined in equation 5.6, is different. The single photon detection

efficiency (ϵ) can be computed from the threshold channel by channel.

$$\begin{aligned}\epsilon &= \int_0^{\infty} \frac{1}{g} exp[-(x/g)]dx \\ \epsilon &= \int_0^{th} \frac{1}{g} exp[-(x/g)]dx + \int_{th}^{\infty} \frac{1}{g} exp[-(x/g)]dx \\ \epsilon &= exp[-th/g]\end{aligned} \tag{5.6}$$

where th is the applied threshold and g is the operating gain of the detector. The quantity ϵ can be computed from channel by channel threshold values. The average of the distribution is used for our used quantity. The histogram has been shown in figure 5.17

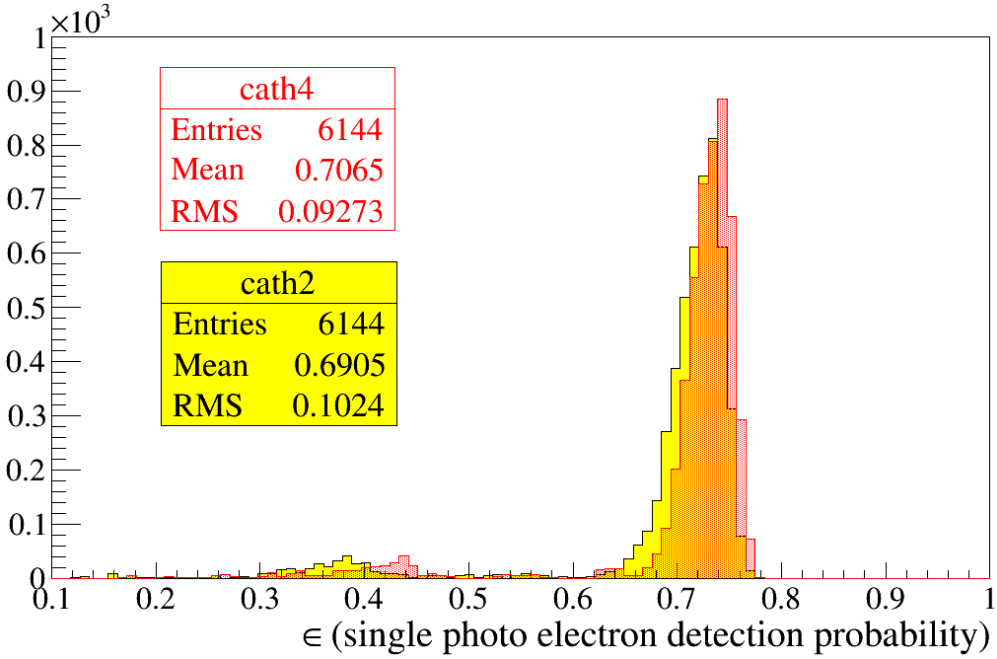

FIGURE 5.17: Histogram of the single photoelectron detection probability for cathode 2 and cathode 4.

In table 5.3 we see that the product of <QE> and ϵ has been normalised to cathode 2.

	J	S
QE	1.12	1.01
ϵ	0.690	0.706
QE.ϵ	0.773	0.713
norm	1	0.92
$N_{Ph}^{exp} = normX12$	12	11.1
N_{Ph}^{Obs}	12 ± 0.7	10.1 ± 0.6

TABLE 5.3: Consistency in extracted number of photons for top two hybrids

The observed numbers of photons for the hybrids are consistent.

5.6.1 A comparison with the MWPC

A similar exercise has been performed on the two MWPCs to have a comparison.

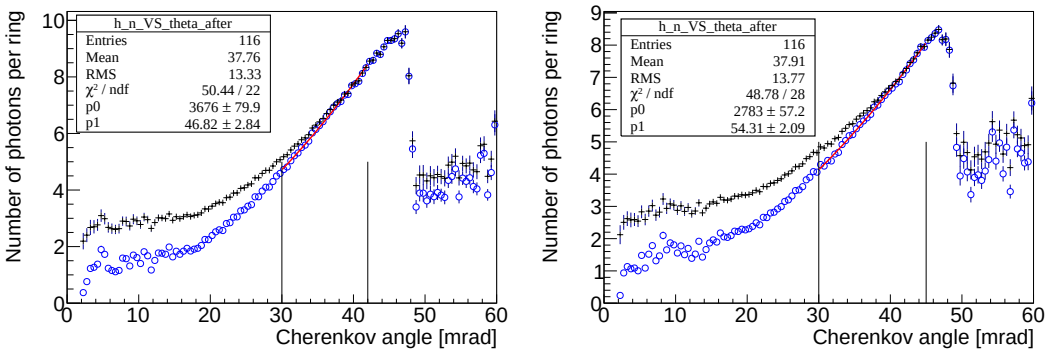

FIGURE 5.18: Cherenkov angle versus number of photon plots for MWPC detectors

For the MWPC cathode 1, the optimal fitting range is (30-42 *mrad*) the signal part of the function is 11 ± 0.2 and the background part of the function is 2.5 ± 0.1. For cathode 8 in the same fitting range 8.4 ± 0.2 photons have been detected as the signal and 3.0 ± 0.1 as background. The number of photon distributions for the MWPCs can be seen in figure 5.18. In the figure the left panel corresponds to cathode 1 and the right panel corresponds to cathode 8.

5.7 Time resolution

A test has been made to extract the time resolution of the hybrid detectors from the existing data. The difficulty is to define the time resolution itself. I adopted a method to roughly estimate the time resolution of the hybrid detectors. The algorithm to extract time information is based on 3 signal amplitudes of the APV readouts. The inclusion of the trigger time uncertainty in the RICHONE ROOT tree level is not straightforward, therefore this estimation of the time resolution is only approximate.

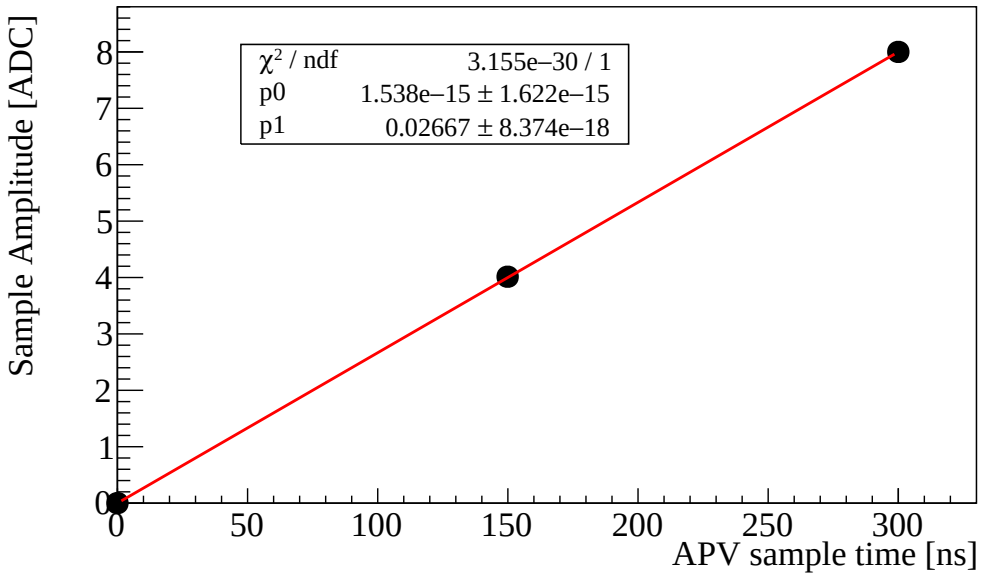

FIGURE 5.19: An example of three signal samples ($A_0, A_1 and A_2$) of APV-25 chip versus time

If A_0, A_1 &A_2 are assumed to have linear dependency and we extrapolate the fit at 10% of the A_2 amplitude, which is chosen empirically, then the time (t) for the signal formation can be written as:

$$t = \frac{(0.1 * a_2 - p0)}{p1} \tag{5.7}$$

The sigma of this extrapolated time distribution (σ_t) does not depend on the choice of the point at which the time is extrapolated. In figure 5.19 we see a typical linear fit using the three signal samples. For different values of A_2 the σ_ts can be extracted. In equation 5.7, a_2 is the amplitude of the A_2 sample and $p0, p1$ are the usual parameters of first order polynomial fit. In the current RICHONE software, the absolute time (t_0) based on the trigger, to which the APV25 signal time should be compared, is not stored. The phase of the trigger can be assumed to be randomly distributed and the corresponding uncertainty contribution can be subtracted by deconvoluting the quadrature sum. The sigma of the time distribution presented here contains the trigger phase uncertainty and an overestimation of the signal jitters due to the underestimation of the rising slope of the signal. Anyhow, the goal of the exercise was to check if an effort in future can be made to modify the RICHONE such that the time uncertainty in the signal formation can be extracted from the APV25 signal samples, so that when it is compared to the absolute time (t_0) we obtain the absolute time resolution of signal formation of the hybrid PDs.
Figure 5.20 shows the distribution of the time of signal formation at different A_2 binning.

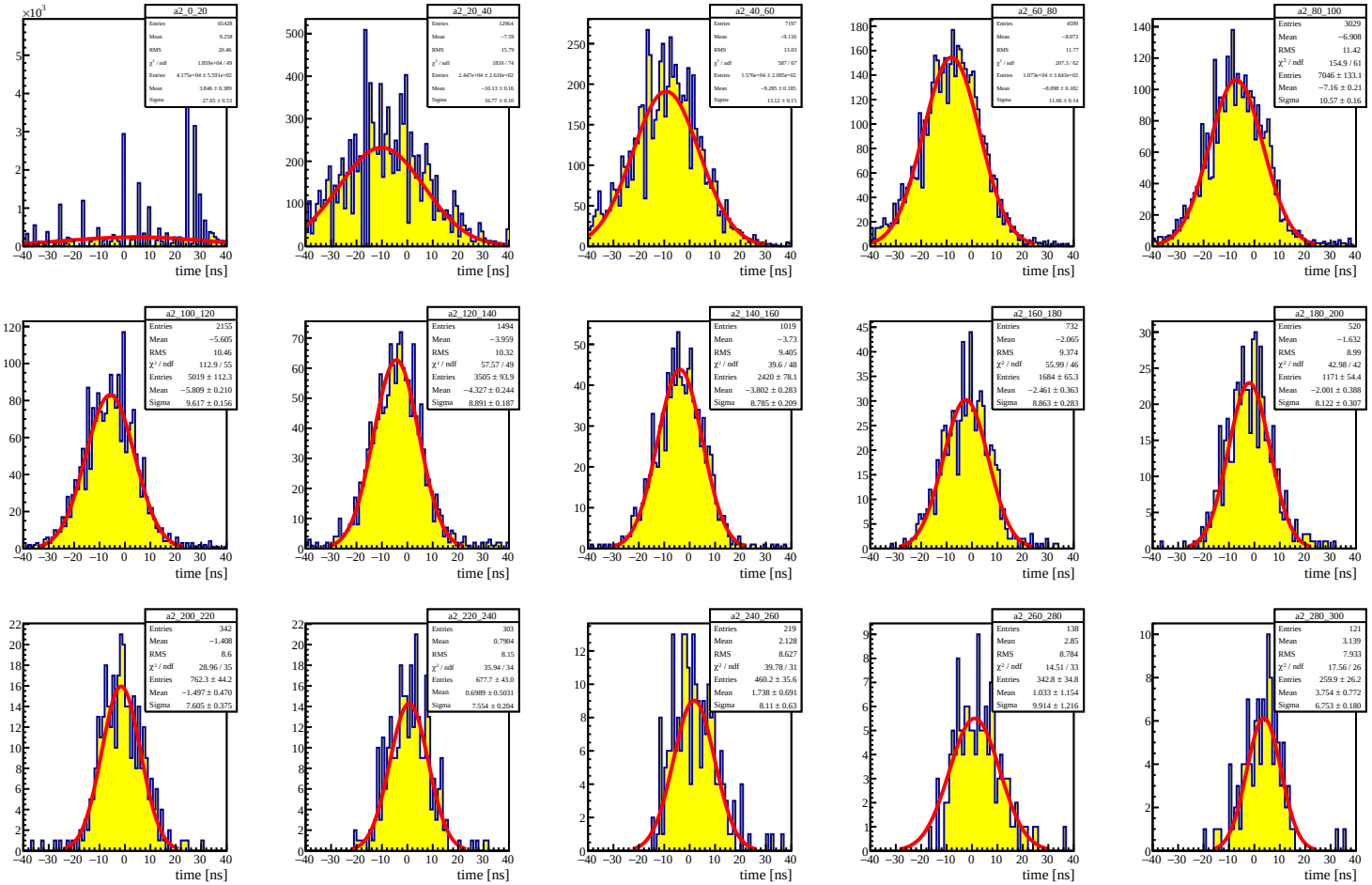

FIGURE 5.20: Histograms at different signal amplitude binning of time distributions. We have plotted the time information obtained from equation 5.7 along the X axis

The sigma of each distribution is plotted versus the corresponding A_2 signal amplitude; the error is associated to the error of the fit times the χ^2/NDF. The average time resolution is 8.8 ± 0.1 ns which is significantly lower than the corresponding MWPC one [136]. This will allow us to select a smaller time window where to search for ring photon signals, enhancing the background rejection. In figure 5.21, we see the dependence of the time resolution with the signal size. We can identify the hump around 250 ADC channel, which corresponds to the saturation of the ADC channels.

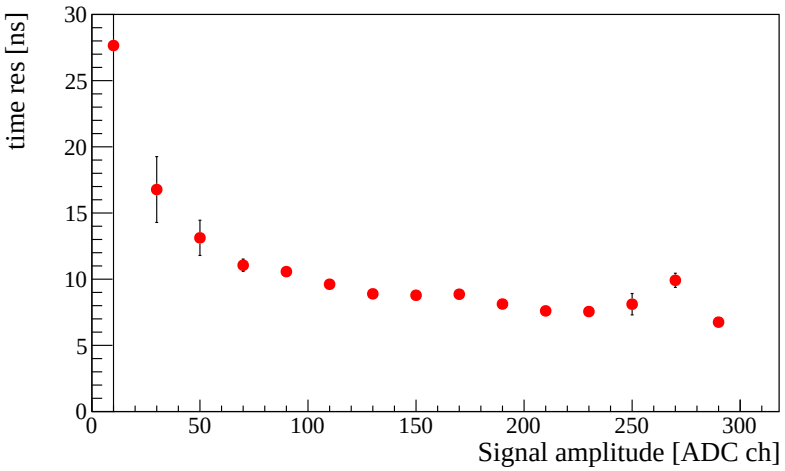

FIGURE 5.21: The ADC amplitude versus sigma fit of the time distribution.

In conclusion we can say that the upgrade of the RICH with hybrid PDs enabled to achieve several goals and overcome several limitations of the MWPCs previously installed. The new detectors have shown an improved stability in time since at variance with MWPCs where in case of discharges some sectors had to be turned off loosing completely the corresponding photon detection efficiency these kind of events never appeared with the hybrid PDs. This is due to the strong reduction of the IBF which has been restricted to be below 3% level. Furthermore this level of low IBF extends the lifetime of the CsI proportionally.
The detectors have also proven to be operated with a gain at least five times larger than the MWPCs, while keeping a very low electronic thresholds cut ($3\sigma = 1500$ ENC), with a gain stability in the order of 6% during the 8 months of data taking on a remarkable surface of 4 times ~ 0.4 m^2.
The detected number of photons per ring is similar or larger compared to the MWPCs one and the single Cherenkov photon resolution is similar. The analysis outcome presented in this chapter is unique in the world: for the first time it demonstrates that the THGEM-MM based hybrid PDs are successfully operated in a running experiment for single photon detection.

Chapter 6

Tuning status of COMPASS RICH-1 for 2016-2017 run

6.1 Introduction

The RICH measures the Cherenkov angle for each single photon for each track, as an example at the RICHONE level we have $\sim$ 10 million events and $\sim$ 20 million tracks for one run. The knowledge of the refractive index of the radiator and the measured momentum from the tracking are coupled to the measured Cherenkov angle to estimate of the mass of the particle for the PID using RICH method. If instead we assume the mass of the particle emitting the photon, we can estimate of the refractive index of the radiator from each single photon. The refractive index at a particular temperature and pressure for a photon of particular wavelength range on an average should not change event by event. Once a stable value of refractive index is retrieved from the RICH data, the RICH can be assumed to be tuned. The refractive index of the radiator depends on the temperature and pressure according to the Lorentz-Lorenz equation [65].

$$\frac{n^2-1}{n^2+2} \propto \frac{p(atm)}{T(K)} \tag{6.1}$$

A constant monitoring of the refractive index is an essential for the RICH performance. Assuming, that the effects of the pressure and of the temperature gradients inside the RICH-1 vessel are negligible, the refractive indexes are experimentally determined at fixed time intervals (namely every 24 h of data taking) [140] and then the evolution of the index value is calculated as a function of the pressure and of the temperature of the radiator, which are continuously monitored.
In COMPASS, the events are mostly π dominated, therefore the extraction of the refractive index is performed by using the π mass hypothesis. The standard approach is to select tracks with momentum up to 30 GeV/c, and for the monitoring purpose the estimate is technically expressed as (n$-$1) for MAPMTs and gaseous detectors in ppm units. Two global indices are passed, for the APV based gaseous detectors the refractive index values are in the UV range and for the MAPMTs the refractive index values are in the visible range. The technical estimation of the refractive index is done by estimating

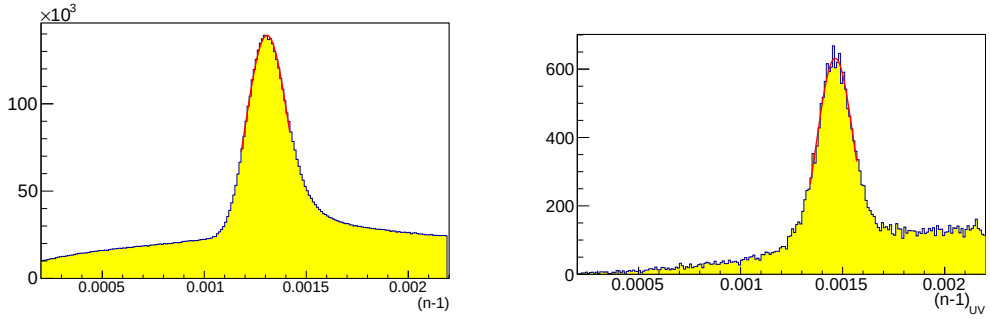

FIGURE 6.1: Example histogram of tuned (n−1) distribution of COMPASS RICH in visible and UV range for 2016 data for tracks up to 30 GeV/c

(n−1) from the measured photon Cherenkov angle [141]. The equation 3.5 can be re-expressed as:

$$(n-1) = \frac{\sqrt{p^2 + m_\pi^2}}{\cos\theta . p} - 1 \tag{6.2}$$

Figure 6.1 presents a typical histogram of the estimated (n−1) distributions in the visible and UV regions, with central values around 1300 ppm and 1500 ppm. Along the horizontal axis the (n−1) value is plotted. The sigma of the distribution is around 110 ppm for the MAPMTs. The sigma of the (n−1) distribution is larger in the MAPMTs compared to the gaseous detectors, because the MAPMTs have larger pad size, a detailed account on the pad size of the different detectors has been given in chapter 4. The RICH has been upgraded in 2016, as mentioned in chapter 5 using MPGD based hybrid single photon detectors. During the characterisation of the newly installed hybrids detector, it was seen that the refractive index histograms are not consistent with that of 2010 data. In figure 6.2, 6.3 we see although, the background level is significantly different with respect to 2010 data the peak distribution is severely distorted, in particular for the bottom MAPMT panels the deviation was more severe. In figure 6.2 we can see for 2010 data: the left panel the histogram of the (n−1) distribution for the MAPMTs and for the right panel the (n−1) distribution for the gaseous PDs. In figure 6.3 we can clearly see the global (n−1) distribution of the MAPMTs on the left panel and the (n−1) distributions for the bottom two MAPMT panels for 2016 data. For all these histograms the X axis plots the (n−1) values.

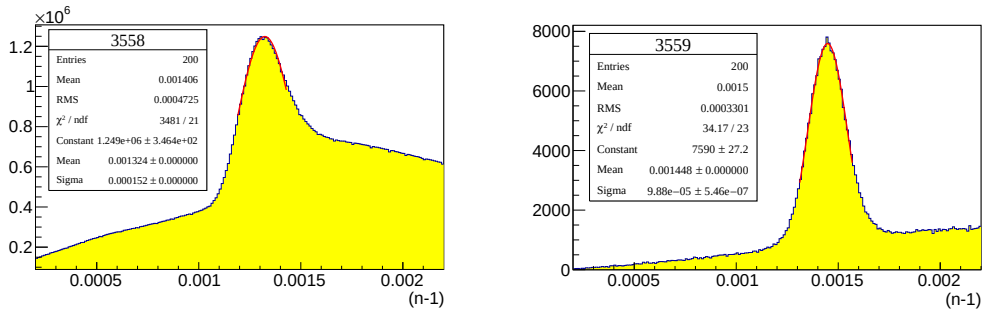

FIGURE 6.2: Histograms showing the (n−1) distribution obtained from 2010 data. Left: MAPMTs, Right: MWPCs in 2010 data taking

The 2016 trigger was set for DVCS physics program where the data is collected in the very forward region, as already mentioned in chapter 5. The RICH had most of the tracks in the MAPMT regions. The following figure shows the distorted distribution of the (n−1) histogram.

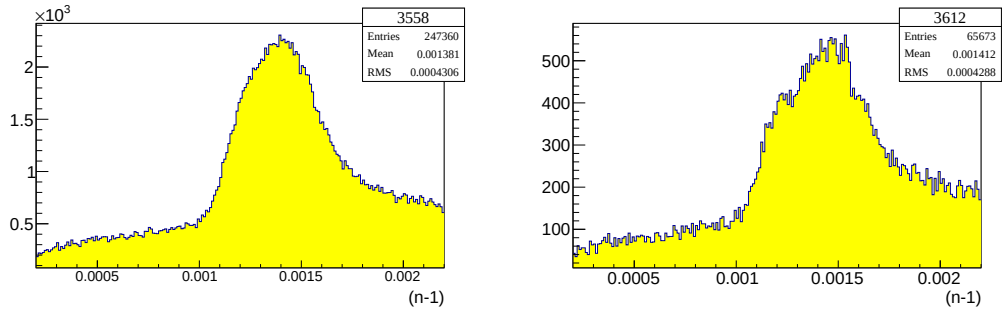

FIGURE 6.3: The histogram of the estimated (n−1) distribution from 2016 data. Left: All MAPMTs, Right: Specially the bottom MAPMTs

The search for the origin of the inconsistencies in the estimated refractive index of the RICH radiator was started by a performing campaign of surveys to determine the detector position in the experimental hall, after the upgrade of 2016. The RICH-1 was upgraded with novel MPGD based photon detectors in 2016 but the detector frames are hosted in the chamber frames of the MAPMTs. Therefore for the upgrade each of the four frames was unmounted, the old MWPCs were replaced with the new PDs and were reinstalled on the RICH.The CAD drawing presented in figure 6.7 shows the scheme of the two detectors hosted in the same frame.
Several data points on the RICH surface were measured setting the origin at the centre of the target. Figure 6.5 shows the region of the RICH where coordinates were measured with special sensors.
In the following sections I will describe in detail the study made with the survey data for the consistency checks and the final modifications made into the detector mapping suggested by the survey analysis. Nevertheless, the associated inconsistency has not been fully solved only by the survey. A data driven method has been developed to check the global mirror position in the

hall, and a different region of momentum to extract the refractive index had been also improvised to finally cure the observed discrepancy in the refractive index of the radiator gas. A further consistency check post modification RICH has been done in terms of PID. It will be mentioned in the following chapter. The MAPMTs are the central detectors and hence mostly populated. Therefore, we performed the analysis based on the MAPMT data.

6.2 Survey of the RICH

A survey campaign had been organised for the determination of the COMPASS RICH-1 detector positions in the spectrometer hall in collaboration with the CERN Engineering Department, the survey report can be found at CERN Engineering Data Management Service (EDMS). The survey was performed during January, February and April 2018. Special adaptors were used for the sensors used in the surveys. In figure 6.5, the left panel describes the points where the survey data were taken to determine the detector position; on the right panel, the upper section shows the dimensions and type of the survey sensors used with the respective adaptors and the bottom section is an example of real data taking situation. The survey used the following coordinate system:

- Origin: centre of the nominal COMPASS target
- X axis: horizontal, along the beam line, positive in the beam direction
- Y axis: horizontal, perpendicular to the beam line, positive toward the Jura
- Z axis: vertical, positive to the top

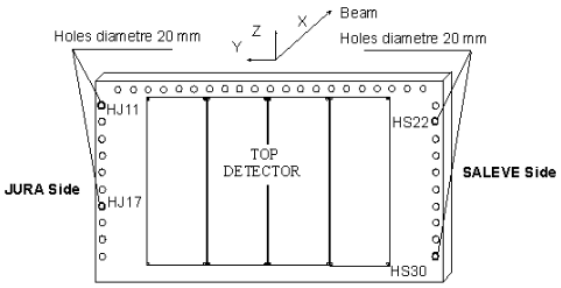

FIGURE 6.4: The reference system of the survey: The beam is entering into the plane of the screen. The right hand side is the Saléve mountain side, and the left hand side is the Jura mountain side.

The adaptors were prepared at the workshop of the University of Trieste. The survey was done on the screw-holes of the frame of the PDs, electronic cards and in the places with specific geometrical significance to measure the coordinates and to extract back the position of the photon detectors. The coordinates were measured with a precision of ± 0.3 mm the centre of the target with one sigma level. A total of 174 data points had been measured all over the RICH on the font and rear sides. An extensive analysis was done of the data points afterwards to check the consistency with previous surveys and to estimate the position of the detectors. In the figure 6.4 we see an example of the the measured points and their nomenclature and the working reference system. In the analysis of the survey data we have taken into account the fact that the detector frames are not perpendicular to the beam direction. It has an inclination of 150 *mrad* with respect to the Z axis, defined in the survey.

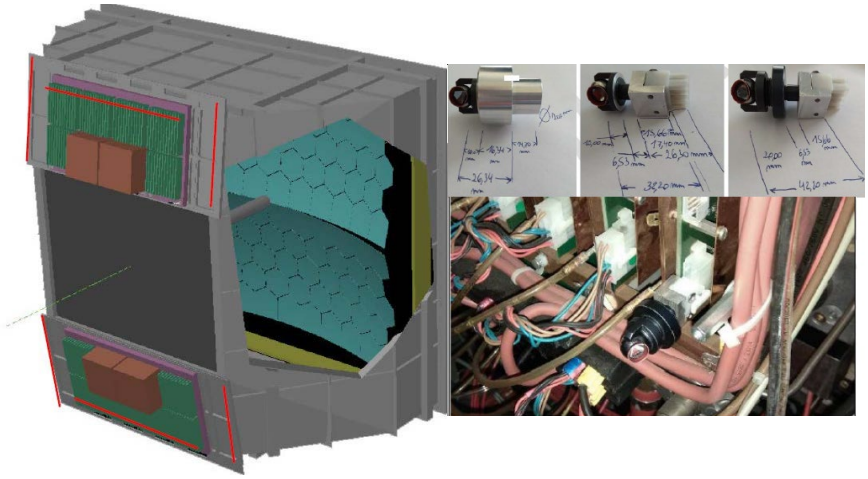

FIGURE 6.5: Left: Schematic of COMPASS RICH, the red lines indicate the surveyed regions which give estimation to global detector position, Right-Top: Survey sensors, Right-Bottom: One example of real measurement set-up

The detector positions are fed into the reconstruction software CORAL by means of a settings file called the detector.dat (detail description has been given in describing the CORAL software package in chapter 3). For the RICH, the centre of the detector frame and the relative positions of the cathode with respect to the frame center are the inputs. The extraction of these numbers was the goal of the survey. The MWPCs which were not touched during the upgrade and the nominal RICH vessel position were used for the consistency checks.

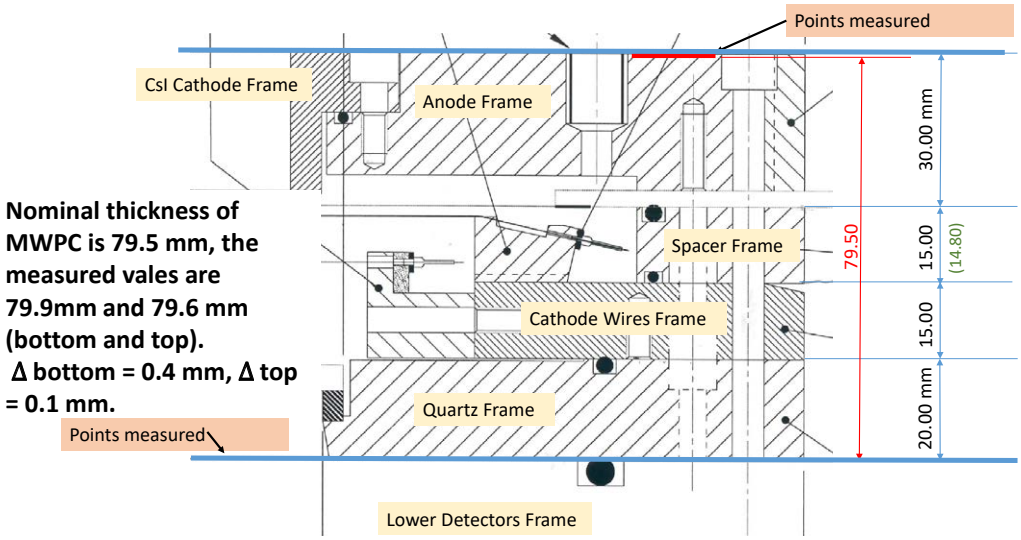

FIGURE 6.6: fig: mechanical drawing of the relative distances of different parts of the MWPC detectors and the location of the surveyed points

6.2.1 Consistency Checks of Survey Data

In order to modify the detector.dat with the new values coming from the analysis suggested by the survey exercise, I checked the quality of the data obtained from the survey and its consistency with the nominal drawings. In order to check the relative position of the MAPMTs and the newly installed hybrids, it is important to retrieve back the nominal positions and dimensions of some physical quantities which had remained intact before and after the upgrade.

- The quartz window, which is common to all of the photon detectors, is a reliable source of reference. The distance between the quartz window and the outer edge of the electronics of the MWPC detectors is 79.5 mm according to the CAD drawings. The details for this distance is shown in the mechanical drawing of figure 6.6. The analysis of the survey data provided us this value to be 79.9 mm and 79.6 mm for the bottom and top MWPCs, respectively. Note that our survey precision was ± 0.3 mm.

- The nominal CAD drawing suggests that the distance between the outer most part of electronics card of the MWPC and the Hybrid has a well defined distance along the Z direction. If we assume the CsI plane of the MWPCs as our reference, then detector plus front-end electronics thickness, the numbers for the MWPCs, hybrids and the relative differences are well-defined numbers with respect to the reference. For the MWPCs the values are 219.3 mm, according the survey the values are 219.6 mm and 218.9 mm respectively for the bottom and top MWPCs in the Saléve sides. This exercise shows that the nominal values are within 0.4 mm considering the precision of the survey, which is ± 0.3 mm, we

can infer that these numbers are consistent. For the Hybrid PDs a similar exercise had been performed. The nominal value of the detector and the front-end electronics thickness for the Hybrid PDs has been constrained by the CAD drawings to be 245.9 *mm*, the survey driven analysis gave us this value to be 246.1 *mm* and 245.7 *mm* for the bottom and top hybrid PDs. Again, within the survey precision we found a good consistency. Finally, the nominal distance between the hybrids and the MWPCs is 27 *mm* according to the CAD drawings. The survey analysis gave us a result of 26.6 *mm*, considering the survey precision associated to both the MWPCs and Hybrids, this is also in good agreement with expectations.

- The nominal distance between the CsI plane of the hybrid to the frame is 67.5 *mm*, the same for the MWPC is 52 *mm*, the delta distance between them is a well known quantity, which is 15.5 *mm*. The survey data suggested this distance to be 15.1 *mm*.

Figure 6.8 and 6.9 are the examples of the CAD drawings. All the nominal distances are very well known from the electronics and from the screw-holes, where the survey targets were placed. Following all these checks, we can infer that the survey has shown a full consistency with the nominal values of the geometry obtained from CAD drawings and mechanical designs. Therefore, its suggested modifications can be implemented in the detector.dat file with reasonable precision.

6.2.2 Modifications suggested by the survey analysis

The centre of the two unique detector frames in the top and bottom of the RICH and the relative position of the individual cathode centres hosted there from the center of that frame are the input of the detector.dat file. The coordinates of the screws which hold the big frame hoisting the detectors to the RICH-1, the screws holding the individual detector panels on the big frames and the external most part of the electronic boards had been measured in the survey. The survey data coupled with information of CAD diagram and the mechanical drawings allow us to know relevant information of RICH for the detector.dat. All of these coordinates are very well known in the CAD diagram and mechanical drawings. Each survey measurement is an independent estimate of these relevant numbers. This information to be accompanied by the knowledge of the physical size of the detector, relative distances between the edge of the cathode frames to that measured point, the pitch of the detectors etc to make the input of the detector.dat free from ambiguities. From figure 6.4 we can have a simplistic view.

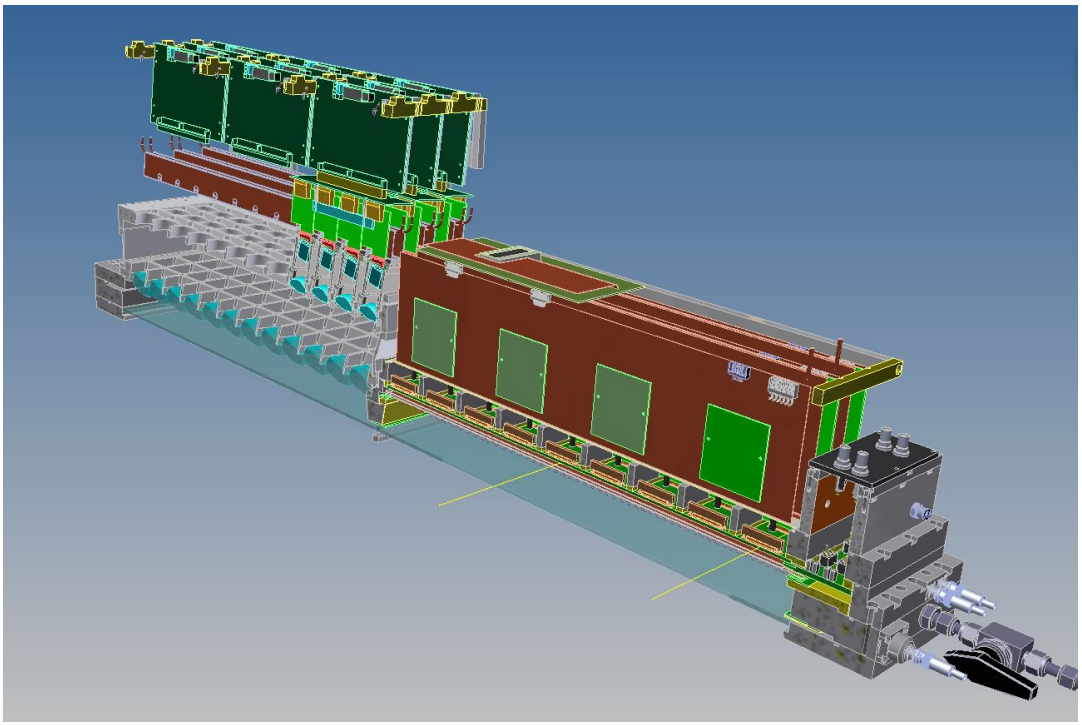

FIGURE 6.7: Sliced view of the MAPMTs and the Hybrids. The unique quartz window, the lens system and the MAPMTs with the electronics and the Hybrids with its APV based electronics are displayed

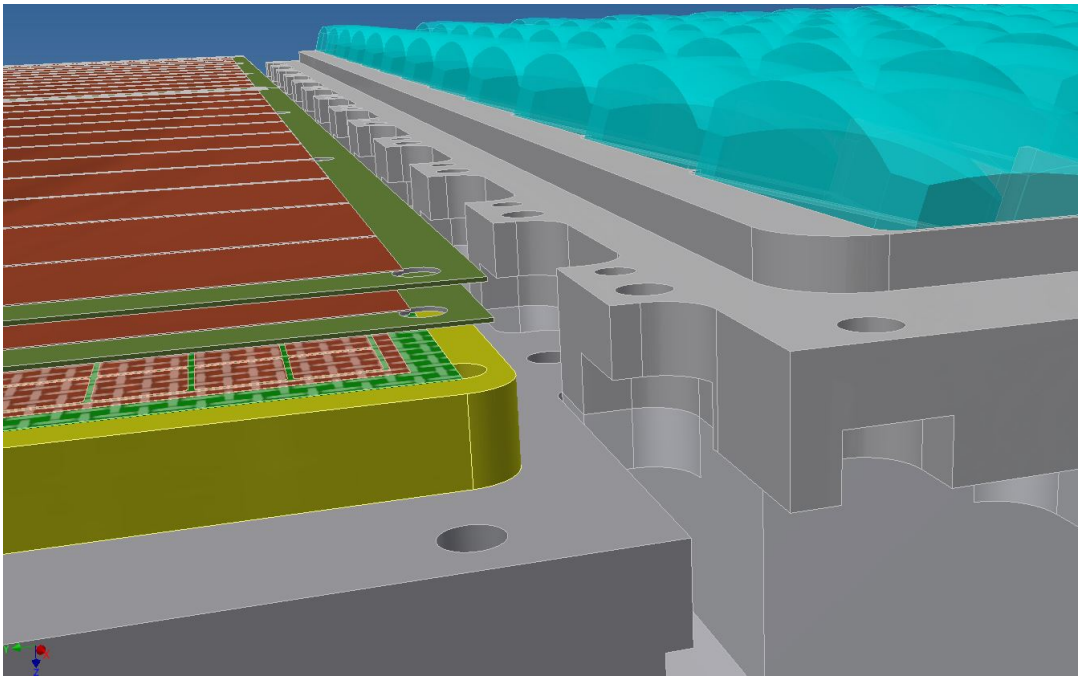

FIGURE 6.8: Exploded view of Hybrid detector and the section of MAPMT in CAD

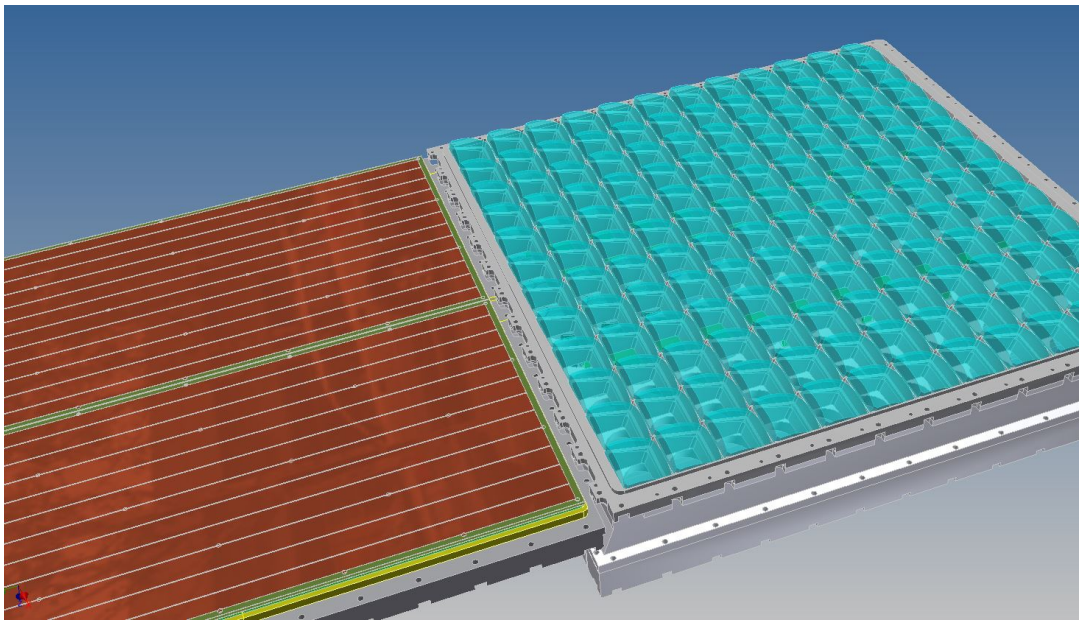

FIGURE 6.9: TOP view of the MAPMTs and the Hybrid, hosted in the same frame

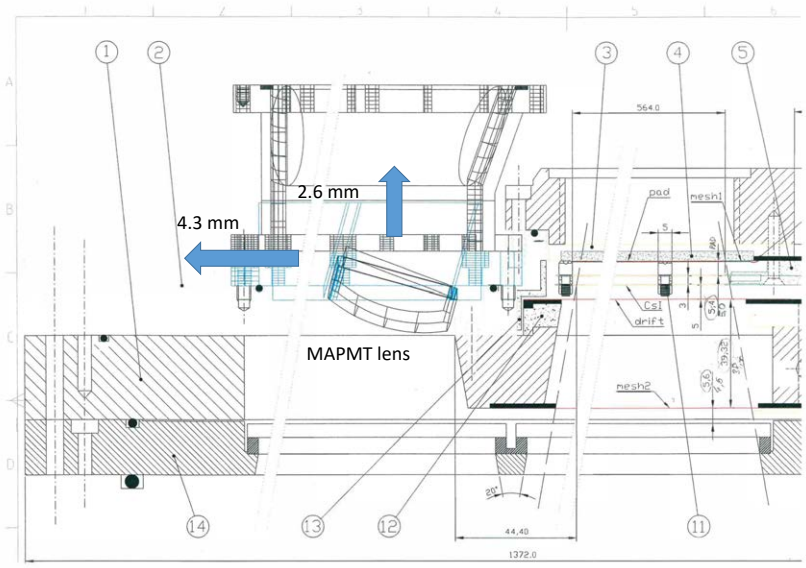

FIGURE 6.10: The mechanical drawing shows the CsI plane and the MAPMT lens system.The survey suggested that the frames are to be moved 4.3 *mm* is toward beam axis, 2.6 *mm* is upstream outside vessel compared to the position of 2015.

As an example of the mechanical drawing of the upper half of the RICH has been shown in figures 6.10 and 6.11. The displacements of the MAPMTs centre position suggested by the survey analysis are shown with arrows.

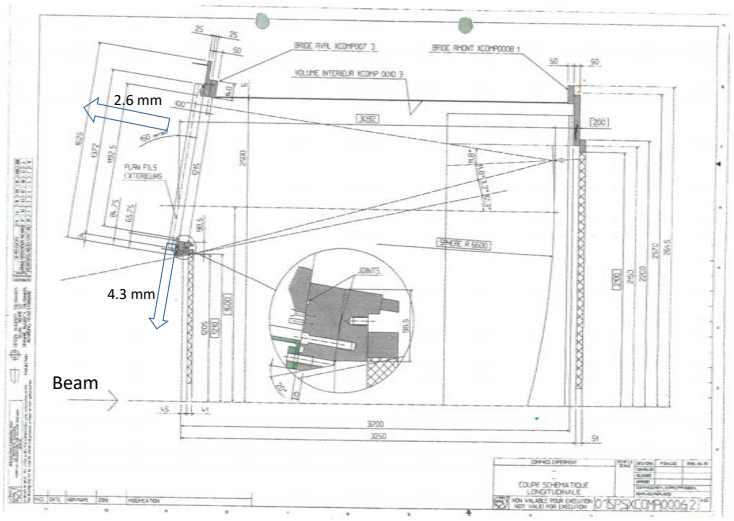

FIGURE 6.11: The mechanical drawing shows the CsI plane and the MAPMT lens system.The survey suggested that the frames are to be moved 4.3 *mm* is toward beam axis, 2.6 *mm* is upstream outside vessel compared to the position of 2015.

The centre of the big frame and the individual cathodes were modified according to the results of the survey. The survey analysis suggested that the centre of the top and bottom big frames are to be re-positioned. Along the beam both top and bottom frames are 5 mm downstream. The bottom is 3.6 mm toward Jura and the top is 5 mm toward Jura. The bottom frame is 4 mm lower and top frame is 1 mm lower. These information were coupled with the MAPMT-Hybrid centre positions are a new table has been generated and communicated with the COMPASS software and reconstruction group. The changes in the detector.dat are shown in the changes can be seen in the appendix D.

For the movement in the global detector frame centre position the mirror centre coordinate was accordingly adjusted, assuming that the physical distance between the detectors and the mirrors of the RICH has not changed.

6.2.3 Residual inconsistencies

The survey of the detector position has suggested important modifications in the detector positions. After applying the required modifications we saw the improvements in the status of the refractive index. The situation after this correction became similar to the n-1 distribution obtained from 2010 data with lower level of background, mainly due to the different physics cases. However, two puzzling features were still present in the distribution. Firstly, there are still miss-match in the refractive index values obtained from different MAPMT cathodes. Namely, $\sim 50ppm$ discrepancy in the top and bottom MAPMTs and also a residual discrepancy $\sim 20ppm$ in the Saléve-Jura MAPMTs. Secondly, the globally averaged refractive index for the visible

region is providing a value which is around 2% higher from the theoretical value. A coarse method had been adopted to check if some further corrections were needed to the detector positions, which may have not been estimated by the analysis of the survey data. The goal of this exercise was to estimate the optimal position, where the detector position is changed toward and away from the nominal beam position and to obtain the Full Width Half Maxima (FWHM) of the refractive index distribution for different MAPMT cathodes. The minimal FWHM gives an estimate of the data driven optimal position. However, it is not a best estimation. The nonlinear nature of the background will not allow us to obtain the right value of FWHM as seen in figure 6.12. Nevertheless, this analysis shows that the optimal position of the top two MAPMTs are 5 *mm* toward the beam axis and the bottom MAPMTs are 10 *mm* toward the beam axis w.r.t the surveyed position, figure 6.13 shows the outcome of the exercise. In figure 6.12 the (n−1) distributions of all MAPMT cathodes are obtained by moving the detector frame centres away or toward the beam pipe. The negative sign corresponds to the movement towards the beam direction. Each curve refers to each movement.
In figure 6.13 the FWHM has been obtained from each curve, namely the different (n−1) distribution and is plotted versus relative movement of the detector frame centres. Despite the accuracy of the estimation, this optimal position obtained by changing the centre of the detector frame position in the geometry file is incompatible with the survey, which has been made with a $\sim$ 0.3 *mm* resolution. Such a large deviation both for the top and bottom MAPMTs from the survey position is likely to be impossible.

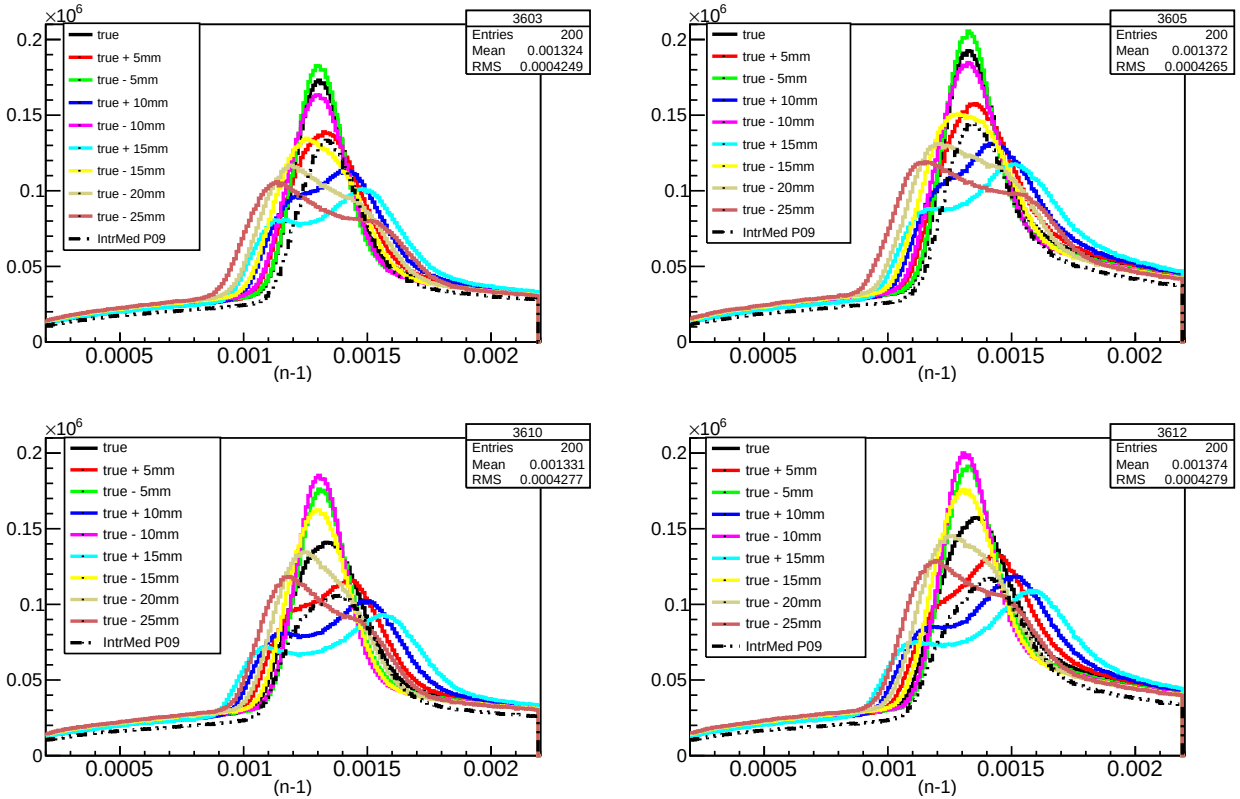

FIGURE 6.12: The effect in the (n−1) distribution when the survey constrained positions (true position) is shifted by different amount toward and away from the beam pipe (Z direction movement) Left panels: Jura and Right Panels: Saléve

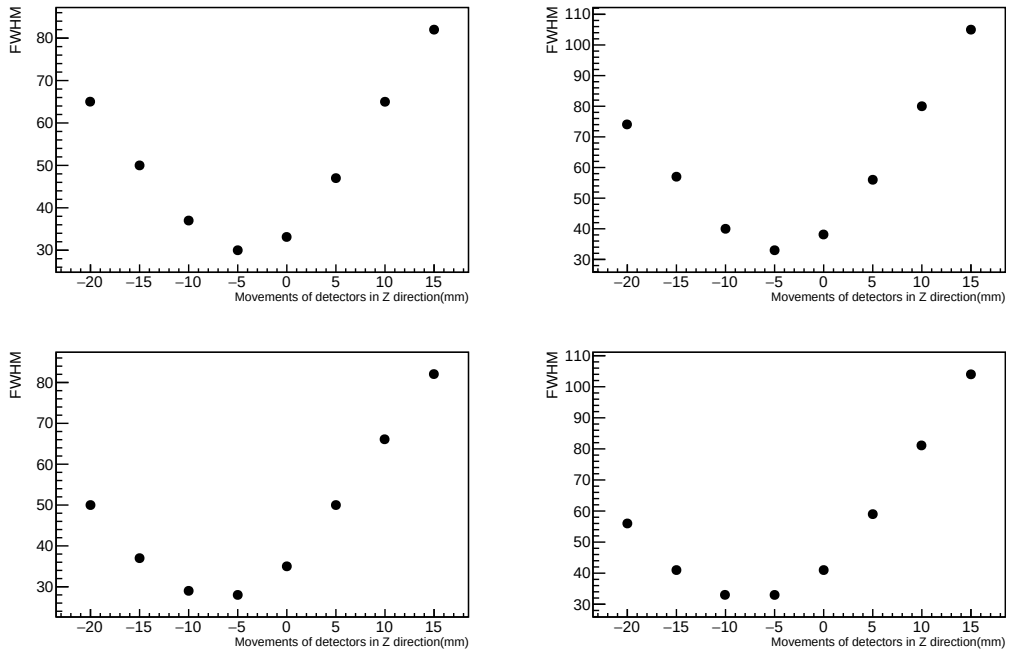

FIGURE 6.13: FWHM (in ppm units) of the (n−1) distribution at different Z position of the cathode centers. Left panels: Jura and Right Panels: Saléve

At this point we assumed that the alignment of the spectrometer plays a role in this puzzle. Therefore I tried to see the effect of the (n−1) histograms at different alignment and detector position conditions. I used two different detector position files and two different alignment files available during the analysis. In my analysis jargon I called those set of files bad and good files, to be specific they are actually untuned and the best available configuration files possible during the analysis. I reprocessed the same data to have these four combinations.The table 6.1 and figure 6.14 summarise the effect of different files:

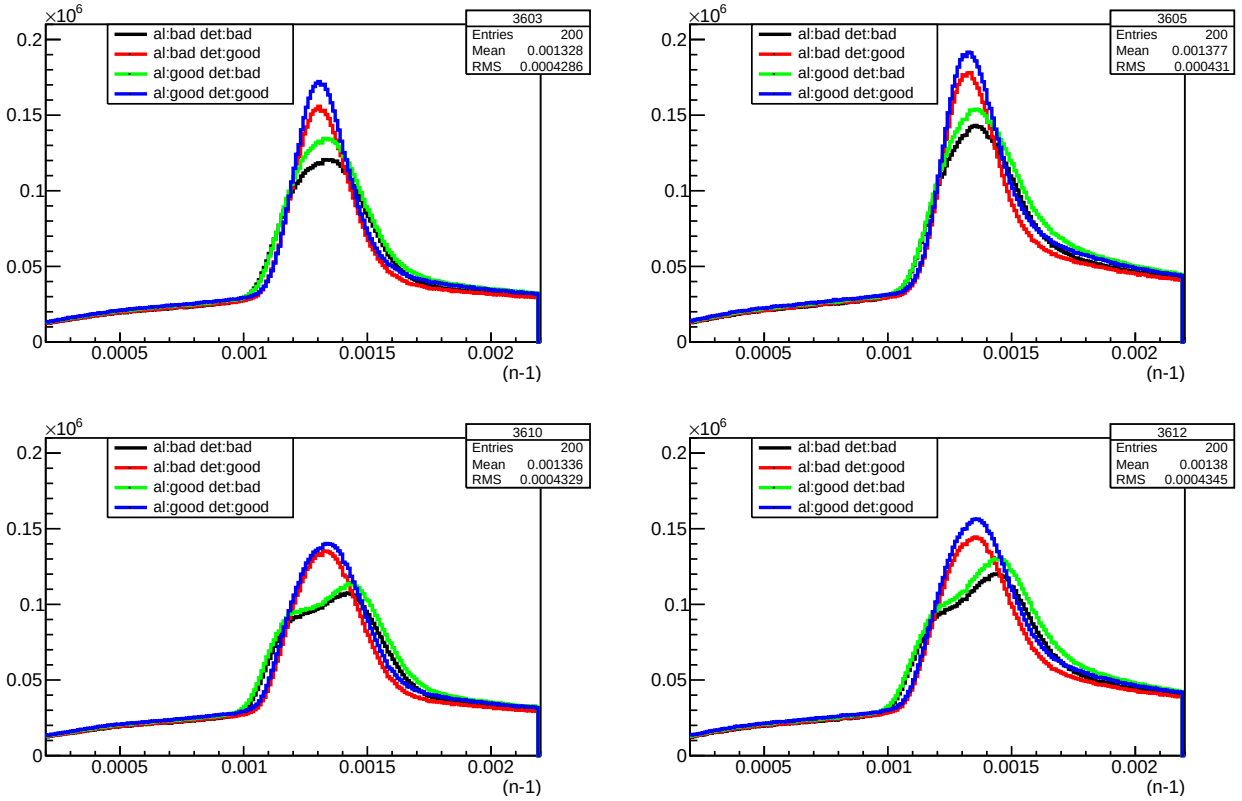

FIGURE 6.14: Effect of different alignment and detector position on the top and bottom detectors

Here, similar to 6.12, we have plotted the (n−1) histograms processing same set of data with tuned and untuned detector and alignment files. Of course by tuned detector position we mean the detector position before and after the survey.

Case	Detector File	Alignment File	(n−1) distribution
1	untuned	untuned	Distorted distribution
2	untuned	Tuned	Distorted distribution
3	Tuned	untuned	Distribution improved
4	Tuned	Tuned	Distribution improved

TABLE 6.1: Situations with different alignment and detector position files

From figure 6.14 it is evident that the alignment had played minimal or even negligible role in our current problem. I have cross-checked with another alignment file used for the data of a different period the data of that period and the outcome was similar. In conclusion, the discrepancy had origin somewhere else. This discrepancy led me to look into the internal RICH geometry.

6.3 Geometric Reconstruction of the single photon Cherenkov angle

Each emitted photon impinges on the mirror and then is reflected to the detector surface by the mirror; the normal to the mirror at the photon impact position points to the reference system origin (it coincides with the mirror centre). Thanks to the Snell's law: incident ray, normal to the reflecting surface and reflected ray are co-planar. It follows that the photon emission point, the reflection point on the mirror, the detection point on the detector and the mirror centre lie on the same plane (photon plane).

The RICHONE software computes the Cherenkov angle of the detected photon cluster in an iterative way. Thanks to the focusing technique of our RICH, we can assume to the first order that the photon was emitted at the middle point of the track. Therefore, if the track position and the direction at the entrance and the exit of the RICH is known, the track can be extrapolated inside the RICH. The midpoint of the track is fixed as the photon emission point. The goal of the algorithm is to compute the direction of the photon emission unit vector. The projection of the unit vector along the particle direction gives the estimated Cherenkov angle of the cluster.

$$\cos\theta^{photon} = \hat{v} \times \hat{P} \tag{6.3}$$

In this expression the $\hat{v}$ is the direction of propagation of the emitted photon, $\hat{P}$ is the direction of the Particle in the RICH. Once roughly we have estimated

Cherenkov angle, then it is corrected to the presence of the quartz window. For the MAPMTs additional corrections are made. After these corrections again the Cherenkov angle is computed and stored for each single photon. In the figure 6.15 I tried to describe the reconstruction mechanism for a single photon.

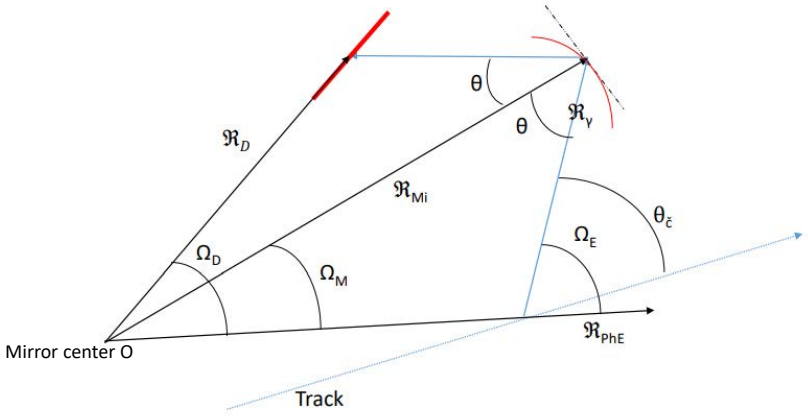

FIGURE 6.15: Reconstruction geometry of Cherenkov angle for single Photon

We can also visualise the same effect from the first principle of RICH. In the simplest case, namely, the particles with zero impact parameter, and the photon detectors are placed in the focal plane, the Cherenkov theta can be written is the following way:

$$\tan\theta \simeq \theta = r/f \tag{6.4}$$

r is the ring radius and f is the focal length of the mirror. In real case we have a non zero impact parameter, although pretty small, but in the first order approximation we can assume that this linear relationship holds. This argument allows us to assume that in the first order approximation for $\beta \to 1$ particles, the refractive index is also related to the ring radius by the following equation 6.4.

$$\begin{aligned} \cos\theta &\simeq \frac{1}{((n-1)+1)} \\ 1-\frac{\theta^2}{2} &\simeq 1-(n-1) \\ \theta &\sim \sqrt{2(n-1)} \\ r/f &\sim \sqrt{2(n-1)} \end{aligned} \tag{6.5}$$

If we propagate the error in equation 6.5, we have

$$\frac{\delta(r)}{r} = \frac{\delta(n-1)}{2(n-1)} \tag{6.6}$$

Therefore from equation 6.6 1% error in the determination of ring radius will lead to 26 ppm error in the estimation of the (n−1), if we assume 1300 ppm to be nominal value of (n−1). Hence, an over estimation of a ring radius would therefore lead to an over estimation of the refractive index and vice versa.

From figure 6.15 is evident that if the 'true' detector position is closer toward the beam-pipe; this means that if the particle emits the photon at the same Cherenkov angle θ from the same point and it hits the same mirror element; then the angle between the reflected photon vector and the radius of curvature drawn at the photon impinging point on the mirror will be smaller compared to the 'current' detector position, and hence the Cherenkov angle will be smaller. This same effect can be realised without moving the detector position downwards, but moving the mirror center of curvature upwards.

6.4 Cherenkov theta and phi dependency on alignment

In the first approximation the Cherenkov photon emission is uniformly distributed within the radiator length (l) and the azimuthal angle (ϕ). The particle trajectory normal to the mirror surface, the photons fill a circular area on the mirror. This density of photons is inversely proportional to the distance of the particle impact point, in the first approximation. The reflection focalises the photon around a closed line, the ring. On the detector surface, which is in general rotated with respect to the orthogonal plane, for all l, the ring has then an approximate elliptical shape. The dependence of the residual, $\delta_\theta = (\theta_{photon} - \theta_{ring})$, with ϕ will not be uniform. However, it is already discussed that the particle position in the detector surface is not directly measured. The trajectory is reflected from the knowledge of tracking and mirror position.

Therefore, any change in the detector or mirror position will dislocate the ring centre. The ring theta is the based on a peak search mode. In this method Cherenkov θ of the photons are distributed $0 - 60$ $mrad$. The ring is defined by the window with more counts. The residual should follow a Gaussian distribution around zero over a background which depends on the cathode type. In the case of MAPMTs, it can be well approximated as a flat background. This distribution is in ideal case uniformly distributed over the azimuthal angle(ϕ).

In case the ring centre is not rightly set. A movement along Z direction of the detectors will lead to a sinusoidal modulation of the residual with the ϕ

angle. The phi angle is described as the following:

$$\cos\phi^{photon} = \frac{(\hat{v} \times \hat{P}).(\hat{P} \times \hat{R})}{\sin\theta^{photon} \sin\alpha} \tag{6.7}$$

Where $\hat{v}$ is the direction of the photon, $\hat{P}$ is the direction of the particle, θ^{photon} is the angle between them. $\hat{R}$ is the unit vector from the centre of the mirror to the particle impact position on the mirror. This is defined in a frame of reference (MWR) where the centre of the mirror is the origin and its z-axis is normal to the detector surface. α is the angle between $\hat{P}$ and $\hat{R}$.

The movement of the detector along the Z direction will make the residual maximum around 0^o and minimum around 180^o.

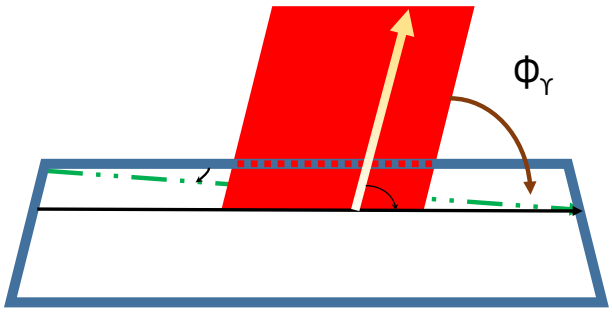

FIGURE 6.16: Azimuth angle (ϕ) of the Cherenkov with respect to the track.

In figure 6.16 we have shown two planes, one is containing the photon (the red plane) and the other plane is containing the particle plane. The green dashed line which is the vector from the centre of the mirror to the particle impact position on the mirror defines the particle plane. The projection of the unit vectors of these two planes are described in equation 6.7

6.5 Half Ring analysis: Accurate estimation of Ring center alignment

The reconstructed ring centre is the particle track reflected back to the detector. From the reconstruction we have the coordinate of the ring center in the detector frame of reference. The exact amount of required movement of either the detector or the mirror can be estimated very precisely by minimizing the difference of the average radii of two halves of the ring. This exercise

is known as the half ring analysis. Let us assume, a ring fully contained in a cathode, with N number of photons. Each photon is an independent estimation of the (n−1), as each photon has been assigned a Cherenkov angle during reconstruction. Following equation 6.4, it is clear if the track center is optimally placed, then the estimated refractive index of the photons above the center of the ring and the refractive index estimated by the photons below the center of the ring will be the same. The virtue of this analysis method is that the method is not dependent on the absolute value of the refractive index. Consequently, it provides the optimal alignment.

Algorithm:

- Select tracks in which all the Cherenkov photon clusters are contained in that particular cathode.
- Get the center position
- Compute the refractive index of the radiator, from the photons above the ring center and below the ring center.

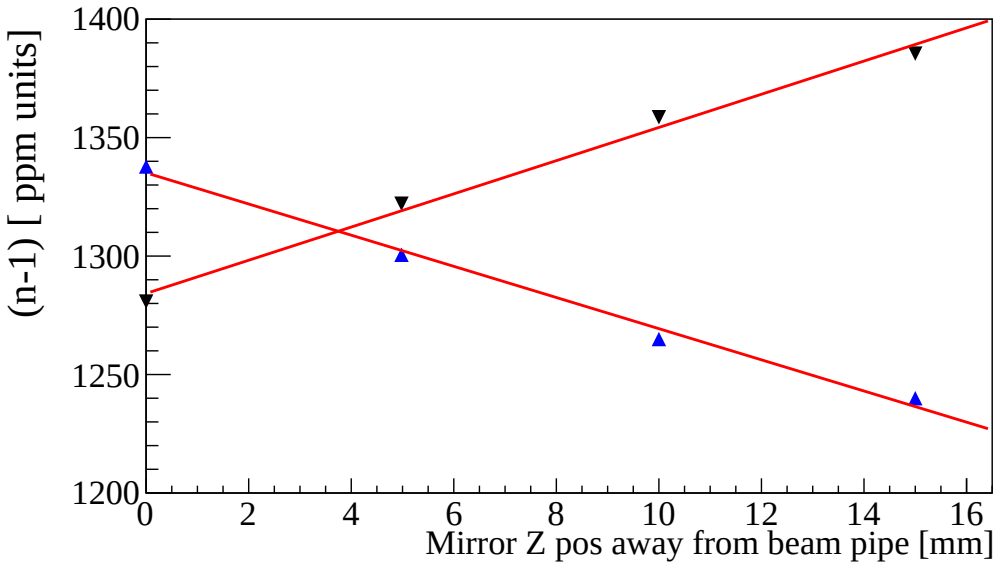

FIGURE 6.17: For the top two detectors mean (n−1) of the photons of the half part of the ring at different mirror orientation along Z axis

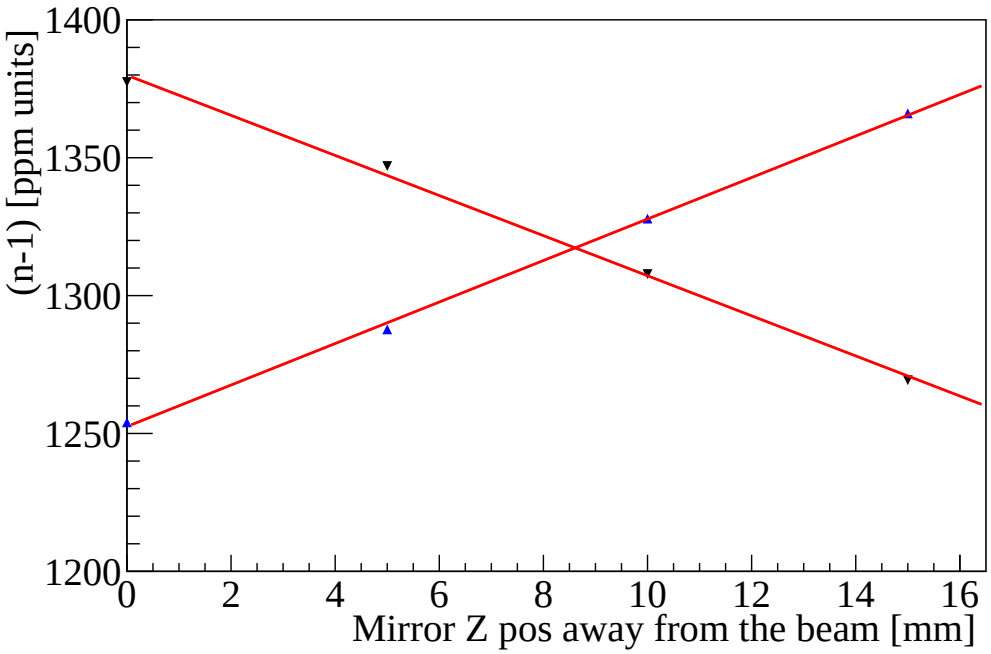

FIGURE 6.18: For the bottom two detectors mean (n−1) of the photons of the half part of the ring at different mirror orientation along Z axis

In figure 6.17 and figure 6.18 along the X axis we have plotted the movement of the mirror centre position away from the beam pipe. along the Y axis we see the mean (n−1) contributed by the photons belonging to the upper half and lower half of the ring. The point of intersection of the two lines are the optimal mirror position which has been used to modify the mirror position in the detector.dat file.
In our case the global upper mirror centre Z coordinate has been moved 3.6 mm away from the beam pipe and the global lower mirror centre Z coordinate has been moved 8.9 mm away from the beam pipe.

In figure 6.19 the dependence of the photon angle residual with the azimuthal angle ϕ is shown: the photon angle residual is defined as the difference of the single Cherenkov angle and the ring angle. The ring angle are scaled to the UV range, therefore for our studies we see that central band has an offset of about 2 *mrad* from zero. But, along the Y axis, we see a cosine modulation, which is caused by the misaligned mirror position.
After the tuning of the mirror position, we see in figure 6.20 the absence of the cosine modulation thanks to the mirror alignment. This alignment and the tuning correspond to a satisfactory and consistent RICH geometry which has been updated to the official COMPASS geometry database.

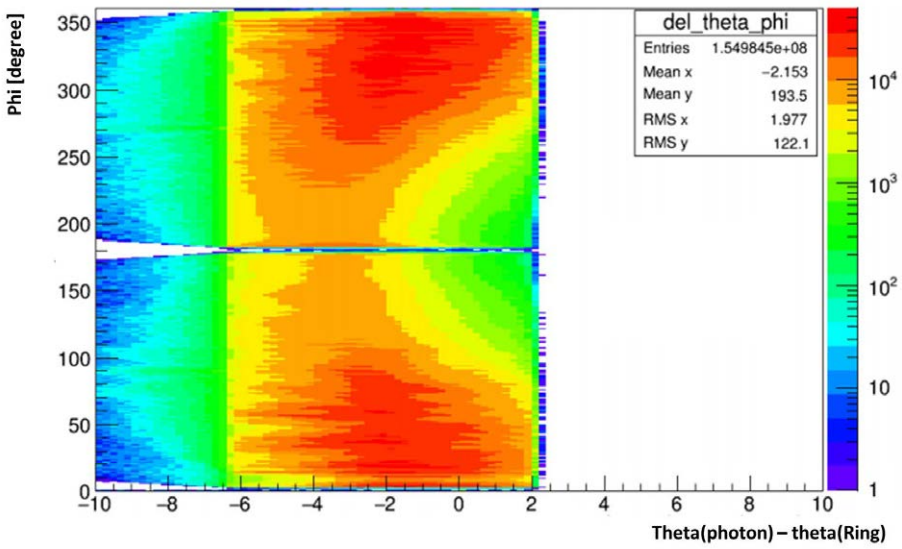

FIGURE 6.19: Dependence of $\theta_{photon} - \theta_{ring}$ at different ϕ_{photon} angle, without the aligned mirror

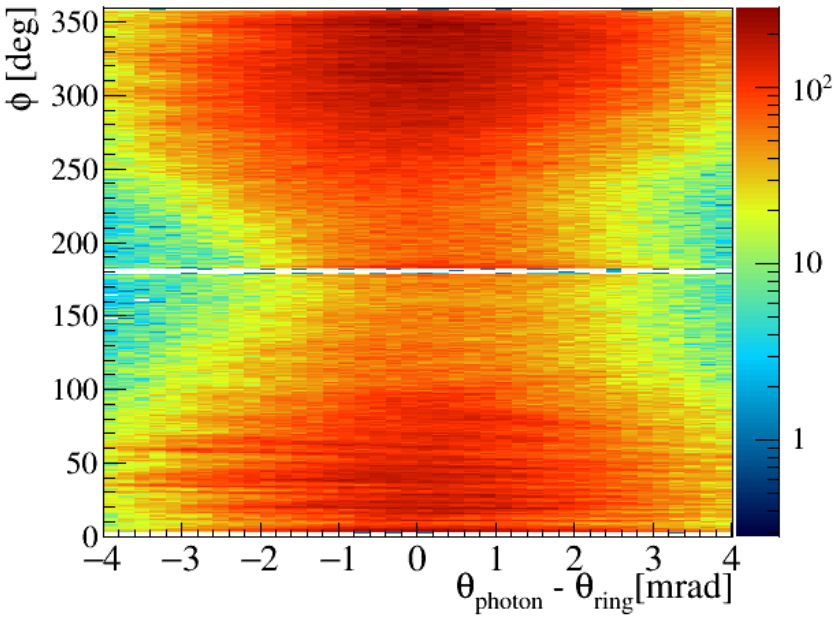

FIGURE 6.20: Dependence of $\theta_{photon} - \theta_{ring}$ at different ϕ_{photon} angle

6.6 Background of n-1 distribution

To estimate the (n−1) value precisely the understanding of the background under the physical (n−1) peak is essential. Traditionally the (n−1) distribution is obtained from the tracks up to 30 GeV/c assuming the π hypothesis. The distributions of (n−1) for the MAPMTs and the gaseous detectors are not

free from background. Depending on the acceptance of the these detectors the shape of the background changes. Before estimating the contributions of different particles in the background a subtraction the background from the distribution was made aiming to obtain an improved estimation of the mean (n−1) value and an improved sigma. Similar to figure 5.4 for the hybrid PD case mentioned in chapter 5. For the tuning and checking the performance of the RICH a ROOT Ntuple format called 'RICH' is saved along with other histograms, this is described in chapter 3. In this data set, information related to the single photons associated to a ring are saved. Events which have more than 300 hits are skipped however.
Knowing the track momentum, the Cherenkov angle of each photon and with the assumption of the π mass hypothesis; we can use each Cherenkov photon of the Ntuple data structure as an independent estimator of the(n−1). This estimation will of course have less background. These extracted (n−1) values from each photon can also be redistributed with a different mass hypothesis followed by the equation 6.2. The (n−1) values obtained from the Ntuple were distributed with a same binning and range of the standard (n−1) histograms of RICHONE software. A bin by bin subtraction of the filtered n-1 histogram obtained by using the 'RICH' Ntuple information, from the standard (n−1) histograms of RICHONE will allow us to roughly estimate the shape of the background. Unfortunately, this procedure does not help to achieve a more accurate estimate of the real central value of the (n−1) distribution.

6.7 Systematic studies to cure the residual inconsistencies

For a correct mass hypothesis the estimated value of the (n−1) will be centered around the true value, while bands at smaller and larger values of the physical refractive index will be observed, corresponding to the signal generated by the particles of different mass. For example, the extracted refractive index can be transformed into refractive index of other mass hypothesis by the following relation.

$$n_e = n_\pi \sqrt{\frac{p^2 + m_{el}^2}{p^2 + m_\pi^2}} \tag{6.8}$$

where n_{el} and n_π are the refractive indices with electron mass (m_{el}) and π mass(m_π) hypothesis at the same angle and same momentum. The left-right asymmetry and the larger background at an (n−1) value greater than the main peak suggest that this contribution is mostly coming from electrons, which are copiously produced at lower momentum. An example can be $\pi^0 \rightarrow \gamma\gamma \rightarrow e^+e^-$. In the Spectrometer the RICH is located after the first magnet SM1. The magnetic field is oriented such that the beam particles are always deflected to the Jura side. A charge separated analysis has been performed to see the effect in extracted refractive index with momentum and different charge of the particles.

6.7.1 Analysis with μ^- beam

The contribution of different charged particles in the (n−1) histogram at different momentum ranges, has been studied for individual cathodes based on the available data structure. In figure 6.21 we plot the 2D (n−1) map of cathode 3, where along the X axis we have plotted the (n−1) and charge multiplied momentum along the Y axis for different negatively charged particles with negative muon beam. Due to the spectrometer magnet SM1, most of the forward tracks will be bent to Jura side.
In the figure identify the negative kaons, anti-protons and the electrons contributing to the refractive index. The particles with mass higher compared to the πs will appear in the left half (lower values of the indices) of the "central" value, and the particles with lower mass will be appearing at the right half (higher values of the indices) compared to the physical value. At higher momentum tracks approach to the saturation hence the bands are merged. The color axis of the histogram in figure 6.21 represents the number of entries in each bin. The maximum colour scale is to 3×10^3.
In the low momentum region, upto 15 GeV/c the electron arm is seen, the contamination is large enough that it restricts to statistically recuperate the physical value of the refractive index within 30 GeV/c. The rest masses of muon and π are very similar,$\sim$ 106 MeV/c^2 and $\sim$ 139 MeV/c^2, without information from other sub-detectors of the spectrometer the RICH is not able to separate the πs and muons event by event above 15 GeV/c. In the high momentum region, above 100 GeV/c, we have the effect of the beam halo as out of time tracks. With similar beam condition the Saléve top MAPMTs have shown less electron contamination in the estimation of the refractive index. In figure 6.22 we can see the dependence of the refractive index with momentum and the colour scale is similar to 6.21.

6.7.2 Analysis with μ^+ beam

The contamination of the electrons in the sample will distort the refractive index distribution leading to an overestimated (n−1). The overestimation will depend on the amount of the electron contamination. The electrons appeared in the sample is independent of the charge of the beam. Using the μ^+ beam, the (n−1) distribution in the momentum space has been studied for the cathodes of the Saléve side. The negatively charged tracks will be bent towards the Saléve side by SM1, as the field lines of the SM1 is adjusted such that the beam is always bent towards the Jura side. Analysing the Saléve side (n−1) we see the contribution of the contaminated portion in the n-1 distribution is around 1900 ppm within 3-5 GeV/c. The π peak is centered at around 1310 ppm. This peak starts merging with the physical peak and redistributes around a mean value of 1400 ppm in the 5-10 GeV/c momentum bin. The distribution can be seen in figure 6.23

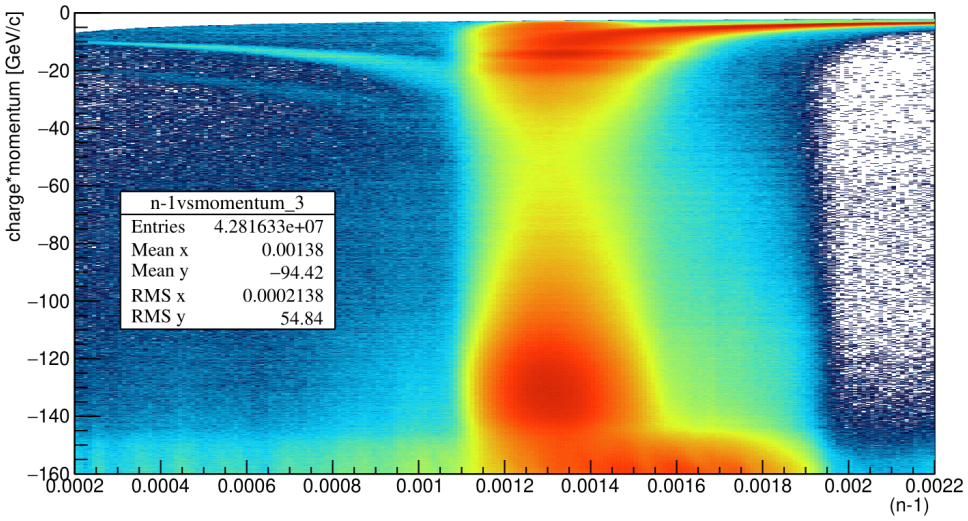

FIGURE 6.21: (n−1) distribution in the visible range for negative charged tracks at different momentum for Jura Top cathode. Negative muon beam.

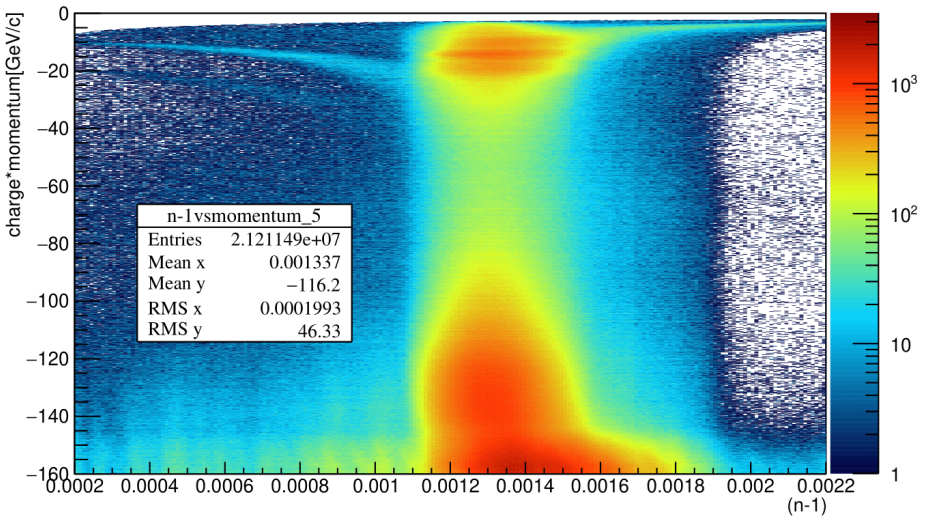

FIGURE 6.22: (n−1) distribution estimated in the visible range for the Saléve top MAPMTs. Negative muon beam. The colour scale is the similar for figure 6.21

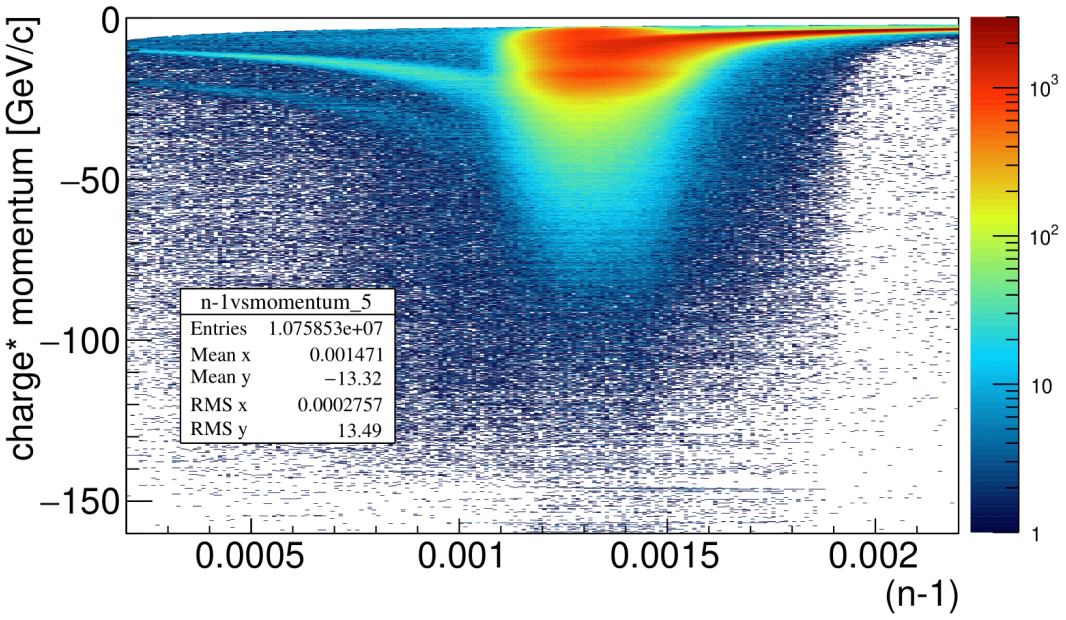

FIGURE 6.23: 2D histogram showing the dependence of (n−1) on momentum. Along the X axis we have plotted the (n−1) and along Y axis we have plotted the charge times momentum of the particles.The displayed figure is of cathode 5, namely the MAPMT in the top panel in Saléve side. Positive muon beam.

6.8 Scenario with electron mass

The assumption of electron contamination in (n−1) estimation has been cross-checked by asserting the electron mass in the algorithm of (n−1) extraction. The electron mass hypothesis will bring the contaminated portion of the (n−1) distribution at the physical region. Also the π band will shift towards a lower value and will merge with the physical band at around 10 GeV/c. The analysis of both μ^+ and μ^- beam data are consistent. Figure 6.24 shows the 2D map of the (n−1) with momentum, where (n−1) is along the X axis and the charge multiplied momentum is along the Y axis. We identify the π band after its threshold ($\sim$ 2.7 GeV/c), and it is contributing to a lower (n−1) value, the band overlaps with the physical (n−1) contributed by the electrons around 10 GeV/c. Similar analysis has been done with the muon, kaon and the proton mass hypotheses.

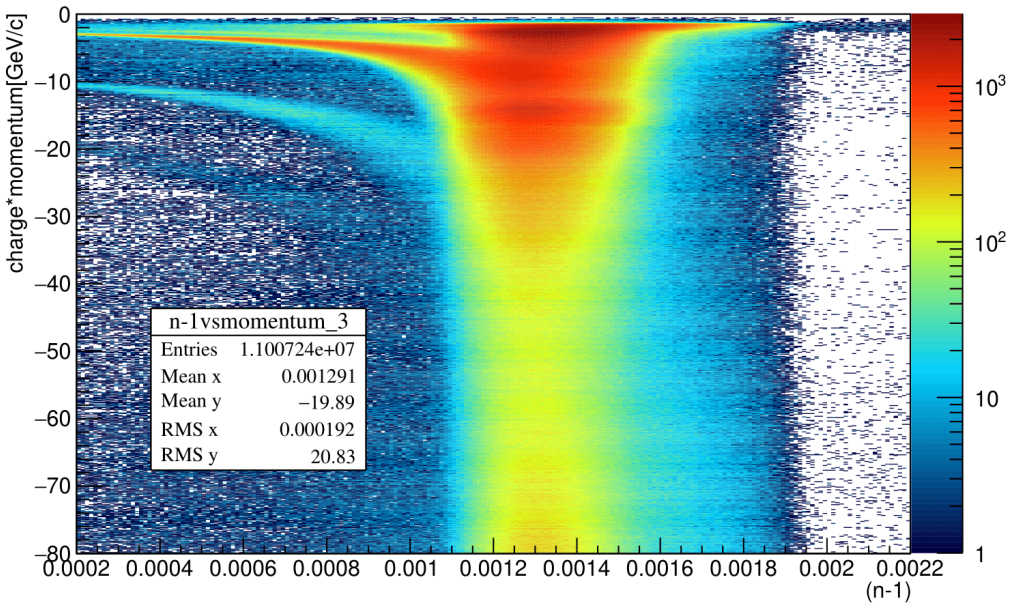

FIGURE 6.24: Refractive index computed with electron mass hypothesis and its dependence on momentum.

The distribution of figure 6.24 is from a μ^- run and therefore all the negative particles will be bent toward the Jura side of our RICH. In the plot π^-, K^- and $\bar{p}$ are clearly visible. The slices of the (n−1) distribution at different momentum bin is also shown in figure 6.25. The first two momentum bins provide a physical refractive index value with electron mass hypothesis. After the pion threshold, the pions start contributing contributing at lower refractive index values, dictated by their higher mass. Above 15 GeV/c two bands merge, however, in the previous range of refractive index extraction, viz. tracks with momentum up to < 30 GeV/c, overestimates the refractive index by 15-20 ppm on an average of all 4 cathodes.

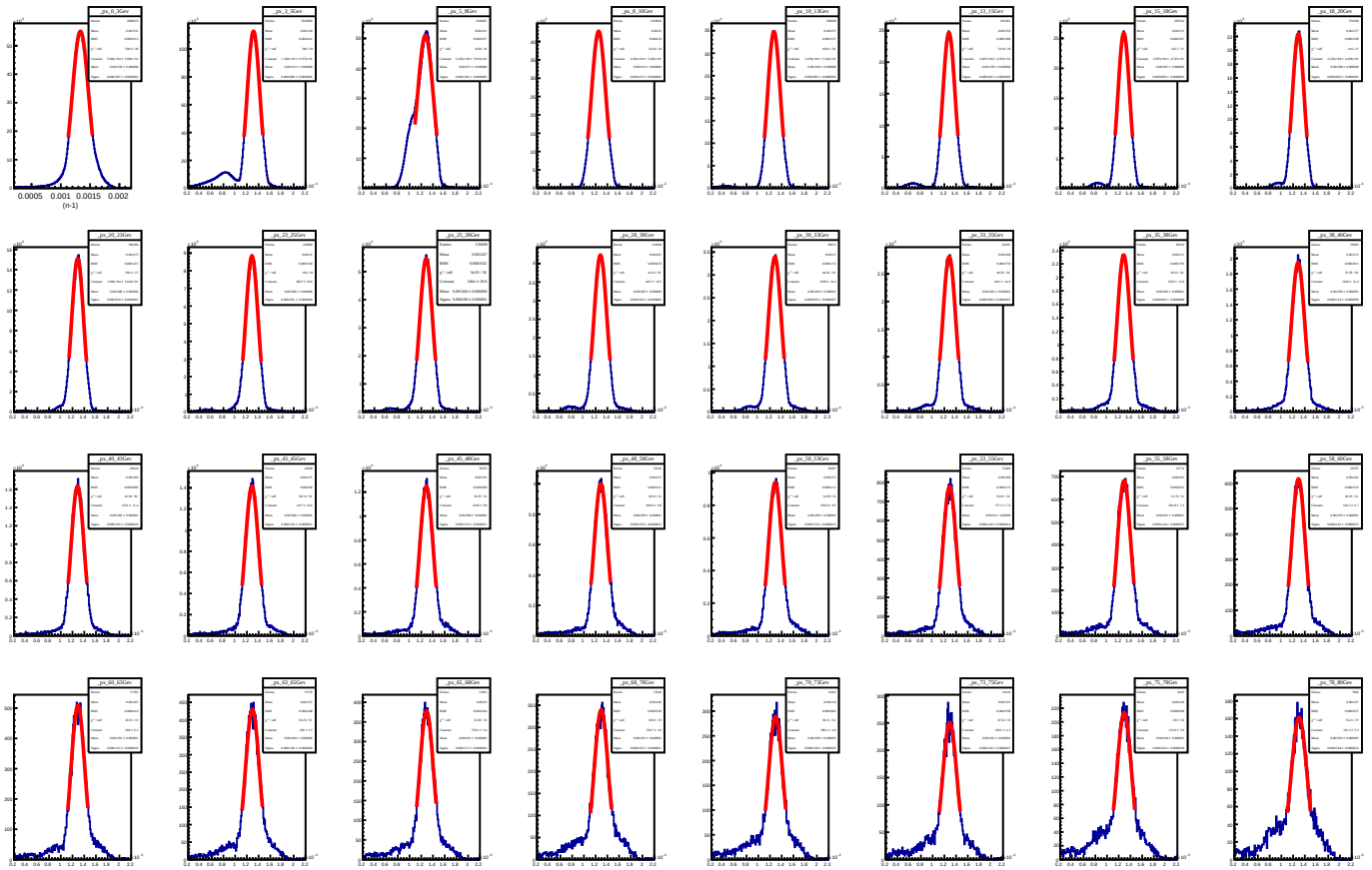

FIGURE 6.25: An example set of histograms of the (n−1) distribution obtained with electron mass hypothesis at different momentum values, ranging from 0-160 GeV/c with bin size of 5 GeV/c. The X axis corresponds to the (n−1) of the radiator, ranging from $0.0002 to 0.0022$ in 200 bins. The example cathode is Jura Top.

6.9 Stability of the refractive index with the momentum

It is clear from the 2D maps presented for both μ^+ and μ^- runs that the refractive index is unstable at the low-momenta region due to the facts described in section 6.7 in detail and also at the very high-momentum region. At the very high momenta region the beam halo comes as out of time particle and produces uncorrelated photons. In this case the Cherenkov photon impinges on the optical system of the MAPMTs at large angle, which is outside the optimal operation range of the optics associated to the MAPMTs. This essentially distorts the reconstruction of the angle. All these effects restrict to select the momentum range, where the refractive index remains stable and shows internal consistencies within different cathodes.

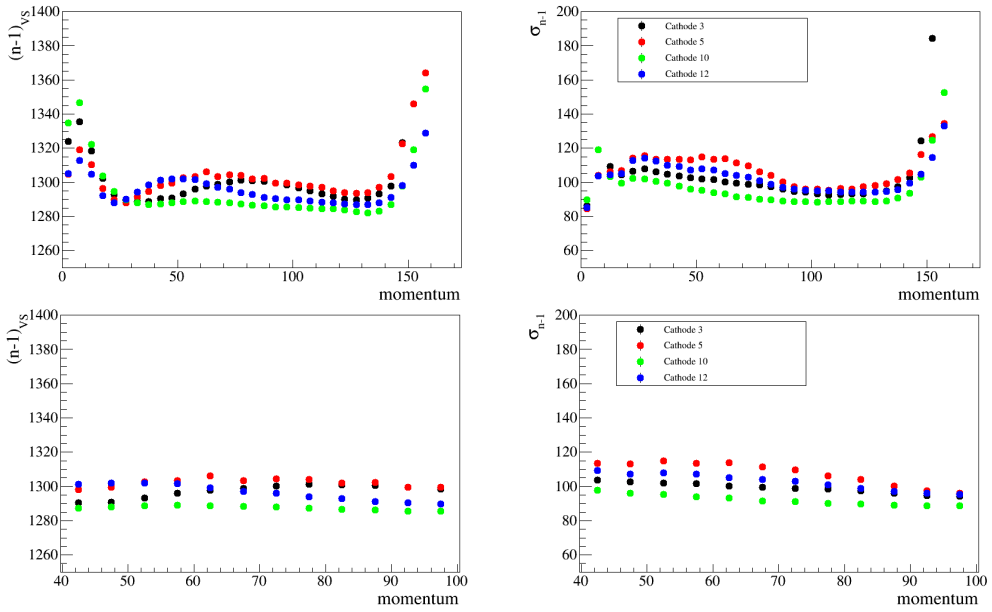

FIGURE 6.26: Top-Left: mean value of (n−1) distribution versus momentum, Top-Right: sigma of (n−1) distribution vs momentum; Bottom Left:mean value of (n−1) distribution versus momentum at track momentum $40-100\ GeV/c$, Bottom-Right: sigma of (n−1) distribution vs momentum at $40-100\ GeV/c$

From figure 6.26 it is clear that the stability conditions are satisfied within $40-100\ GeV/c$, in this region the refractive index shows reasonable stability with momentum and figure 6.27 shows the stability within different cathodes. In this momentum range we have observed a fluctuation of $< 1\%$in the central value of the (n−1) within the cathodes. Not only this, but also the $\sigma_{(n-1)}$ has been reduced to $\sim 100\ ppm$. This was not achieved before.

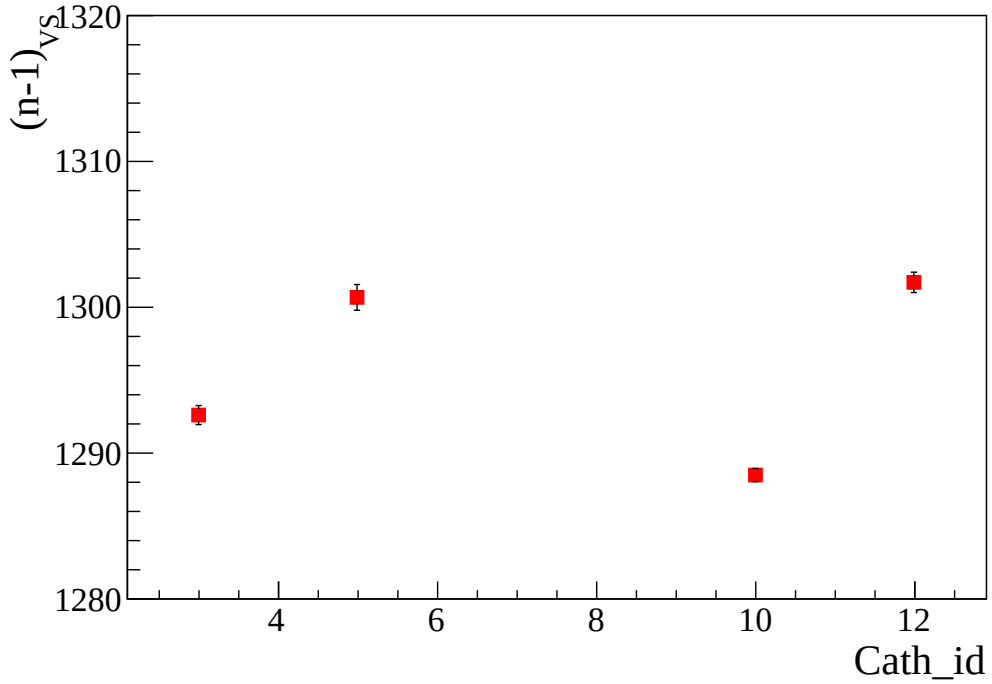

FIGURE 6.27: Fluctuation of (n−1) at different MAPMT Cathodes

Final Extraction: For the extraction of the refractive index run by run, for the COMPASS analysis, I have therefore modified the part of the RICHONE code to include the new range of momentum and to save additional histograms namely the global.The estimation from the individual cathode has been obtained and the sigma weighted mean is computed to to give least bias to any central (n−1) value. This value has remained compatible with the global mean (n−1) within 1-2 ppm. The stability of the refractive index at different momentum bins is described in table 6.2 and the evolution of the refractive index distributions after different applied corrections can be seen in 6.28.

Momentum (GeV/c)	Cathode 3		Cathode 5		Cathode 10		Cathode 12	
	mean(n−1)	sigma(n−1)	mean(n−1)	sigma(n−1)	mean(n−1)	sigma(n−1)	mean(n−1)	sigma(n−1)
40-45	1290.38	103.624	1298.03	113.356	1287.32	97.6638	1301.27	109.169
45-50	1290.82	102.548	1299.36	113.028	1288.08	96.0715	1301.99	107.24
50-55	1293.11	101.912	1302.72	114.956	1288.6	95.1653	1301.93	107.728
60-65	1297.83	100.313	1306.29	113.964	1288.55	93.1236	1299.15	105.096
65-70	1298.65	99.6256	1303.35	111.197	1288.42	91.5624	1297.18	103.885
70-75	1300.37	98.7949	1304.29	109.743	1287.92	91.0188	1295.85	103.077
75-80	1301.29	98.3257	1304.07	106.223	1287.13	90.1995	1293.9	100.74
80-85	1300.81	97.283	1302.01	104.062	1286.48	89.7463	1292.93	98.9373
85-90	1300.66	96.1645	1302.25	100.232	1286.26	89.0361	1291.19	97.135
90-95	1299.66	94.6221	1299.63	97.3175	1285.56	88.504	1290.31	95.8397
95-100	1298.52	94.1863	1299.47	96.0516	1285.48	88.7479	1289.79	95.3436

TABLE 6.2: The estimated refractive index for different cathodes showed stability, if estimated at a higher momentum range. The cathode wise dependencies of central value of the (n−1) and the sigma in ppm units with momentum, ranging from 40-100GeV/c in 5GeV/c bins, is displayed in this table.

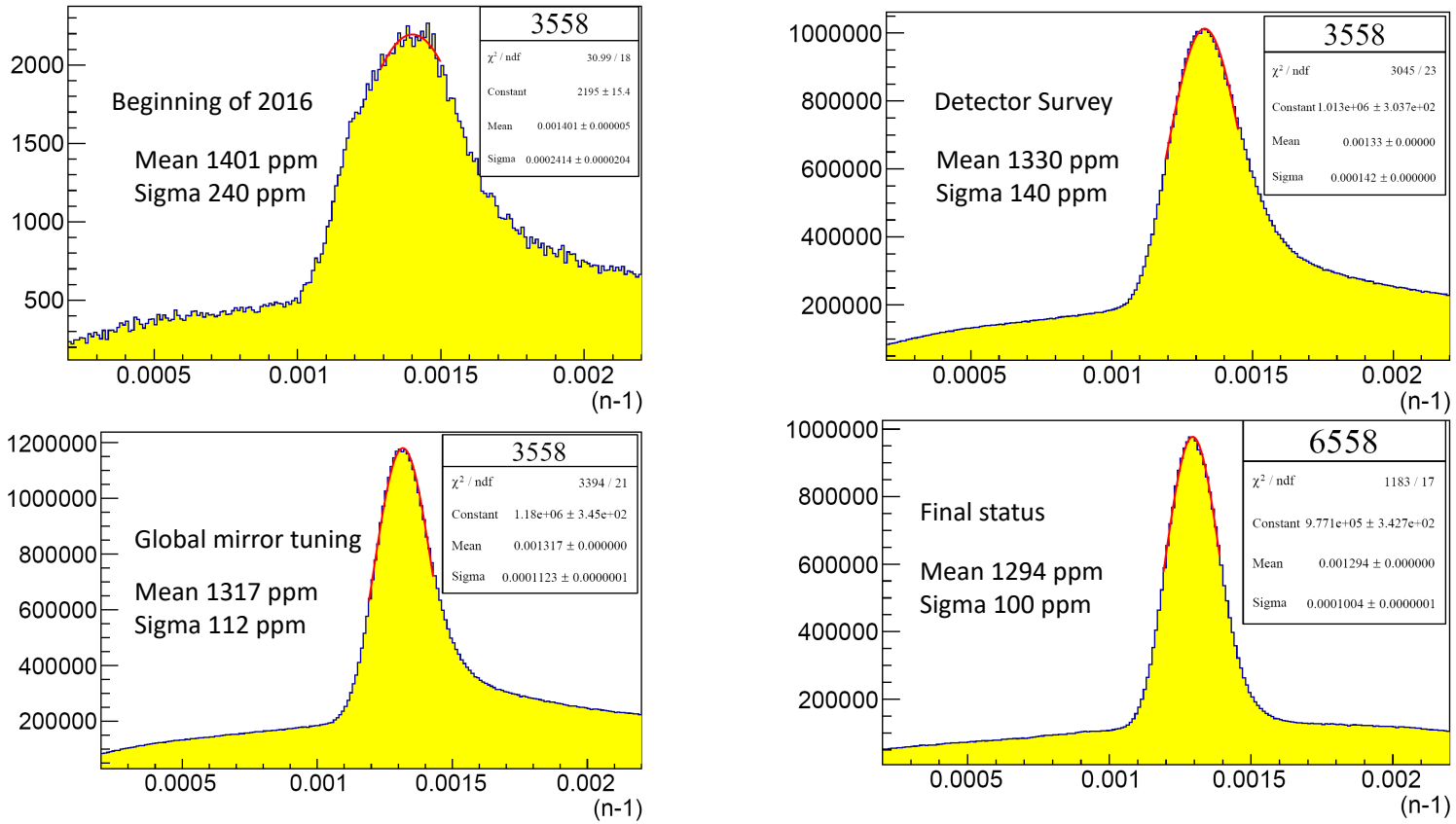

FIGURE 6.28: The evolution of refractive index for all MAPMTs combined all together shows a significant improvement after the whole exercise.The top left corner is the situation at the beginning. The reconstruction with untuned detector and mirror position with contamination from electrons are all convoluted together to provide a distorted shape. Improvements achieved at every stage of exercise is shown.

6.10 Improvements after the RICH tuning

I have observed several improvements after these three modifications, which I will list in this section. Firstly, we have seen reasonable improvements in the status of the extracted (n−1).

TABLE 6.3: Changes obtained in the estimated (n−1) of COMPASS RICH-1.

Situation	n-1 [units of 10^{-6}]	
	mean	sigma
1	1398	228
2	1329	142
3	1317	112
4	1295	99.6

TABLE 6.4: Status of (n−1) with in different situations: 1. beginning of 2016-17 data analysis; 2. detector positions upgraded from Survey analysis; 3. updated detector position and real data driven global mirror center positioning; 4. Updated detector and mirror position and (n−1) extracted in the new momentum region

In the RICH technique, the mass is estimated by measuring the Cherenkov angle, provided momentum and refractive index is known precisely. A proper alignment of the RICH by tuning its geometric parameters and estimation of precise refractive index will improve the measured Cherenkov angle. In COMPASS our final states are π dominated.
Therefore, we can take the residual of the individual photon angle from the Cherenkov angle at that momentum using the π mass hypothesis. The same can be done for the ring angle. The alignment will refine the resolution and the tuning in refractive index will bring the central value close to zero. The RICHONE scales the ring angle to UV reference value. The transformation has the following equation

$$\theta_{UV} = \arccos\left(cos\theta_{VS}\frac{n_{VS}}{n_{UV}}\right) \tag{6.9}$$

where, the absolute refractive index has been used in this transformation. For the ring level analysis I have transformed back the rings in the MAPMTs to its original angle. Moreover, The region near the beam pipe has been also excluded for both of the the resolution studies. The beam pipe essentially shadows the large number of photons generated by the beam particles. Near the beam region the beam halo will also be present. In order to remove the beam region first I have plotted the track position at the RICH entrance. The coordinate is such: the centre is at the nominal target centre, the X axis is from Saléve to Jura and the Y axis is from bottom to top, and Z is the beam

direction. The effect of the magnet does not allow the particle to have the X centre exactly at 0, rather a bit shifted towards the Jura side, due to the magnetic field. The beam positions and direction of the tracks at the entrance of the RICH are shown in figure 6.29 and 6.31 respectively.

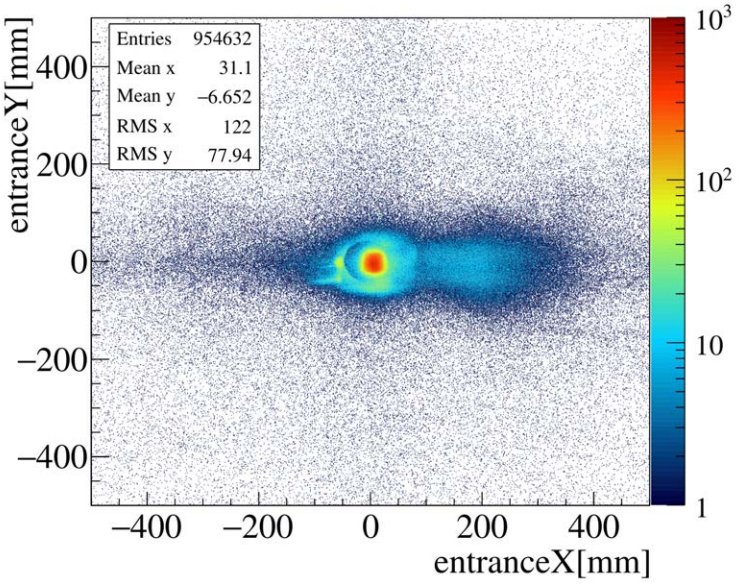

FIGURE 6.29: 2D histogram displaying position of the track at the RICH entrance. X axis runs from Saléve to Jura

The tangent of charged particles in a magnetic field is given by the equation

$$\tan\alpha = 0.3\frac{\int \vec{B}.\vec{dl}}{p} \tag{6.10}$$

For charged particles of momentum 160 GeV/c, the expected bending is $\sim$ 0.2 $mrad$ due to a magnet of bending power of $1Tm$. The distance between the Centre of the SM1 magnet and the entrance of the RICH is $\sim$ 3 m, which implies the beam spot will bent toward Jura by 5-6 mm. Which is clearly seen in the figure 6.30. The survey suggested that the RICH is not exactly centred at the nominal beam-line rather it is 2.5 mm downwards. This can be seen in the profile of the tracks at the entrance.

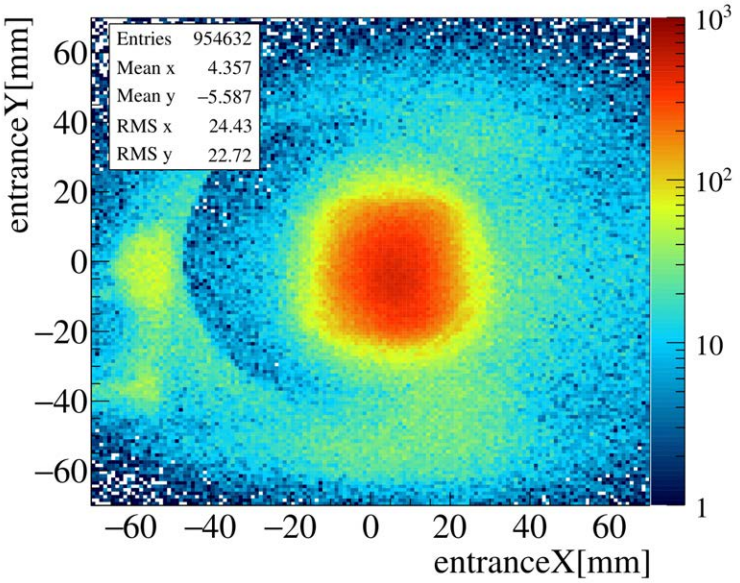

FIGURE 6.30: A zoom of figure 6.29

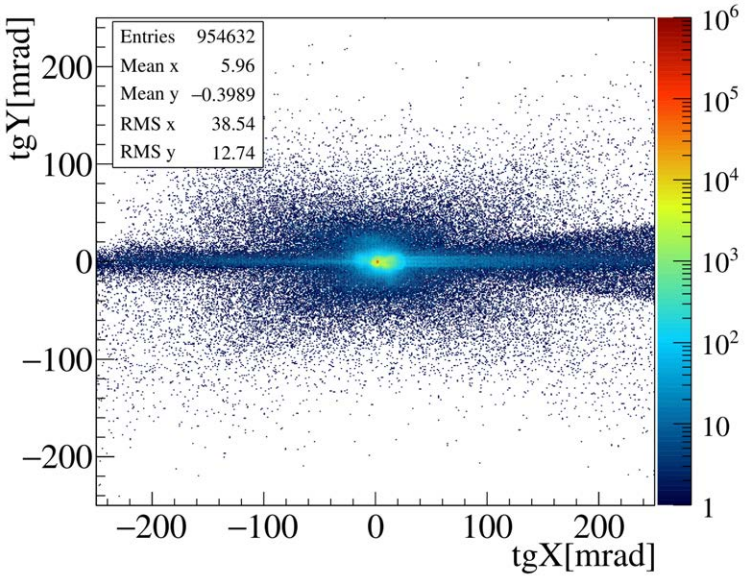

FIGURE 6.31: A 2D histogram of the direction of the tracks at the RICH entrance. The X axis is from Saléve to Jura

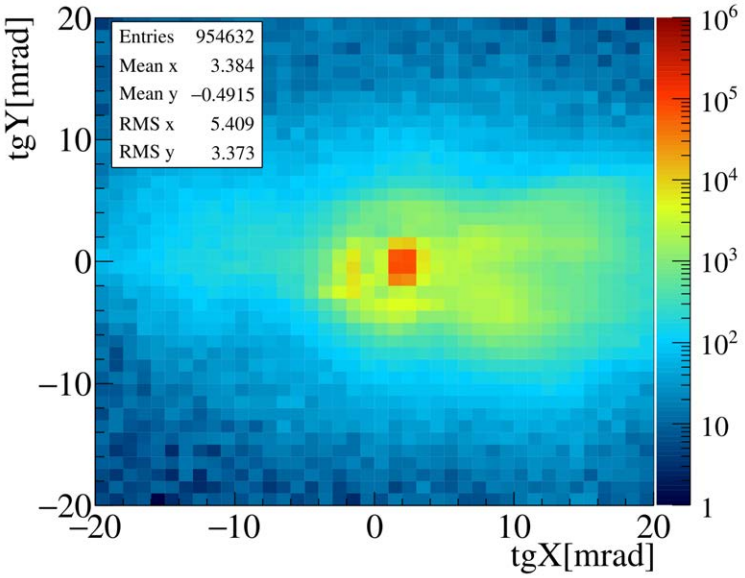

FIGURE 6.32: A zoom of figure 6.31

Secondly, we can study the photon angle residual, which is the direct indication of the improved RICH tuning. The residual can be defined as the difference between the single photon Cherenkov angle and the π angle computed using the momentum of the track and the tuned refractive index. We assume that the tracks entering RICH are mostly dominated by pion like tracks at the higher momentum, as we do not separate track by track pions, electrons and muons above 10 GeV/c. Therefore the physics distribution will be Gaussian around zero. If we do not select tracks with a strong cut on the likelihood then at a very first order approximation a linear background will reside under the main peak. The reason is the following, at a particular momentum p, the kaons and protons will have smaller Cherenkov angle due to low β, the electrons will have a larger Cherenkov angles. Therefore the residual will be positive for electrons and negative for kaons and protons. Now from statistics we can at the very first order approximate that the background is linear.

Figure 6.33 shows the distribution of the single photon Cherenkov angle residual for the untuned situation, which is definitely far from a Gaussian. The central value is also not around zero. This observation demonstrates that the refractive index is also not properly tuned. After the tuning, the distribution improved significantly. Figure 6.34 shows that the sigma, which is the single photon resolution, has improved from 2.96 ± 0.01 $mrad$ to 1.91 ± 0.00 $mrad$. The central value is more centered closer to zero, this is evident of a better estimation of the refractive index.

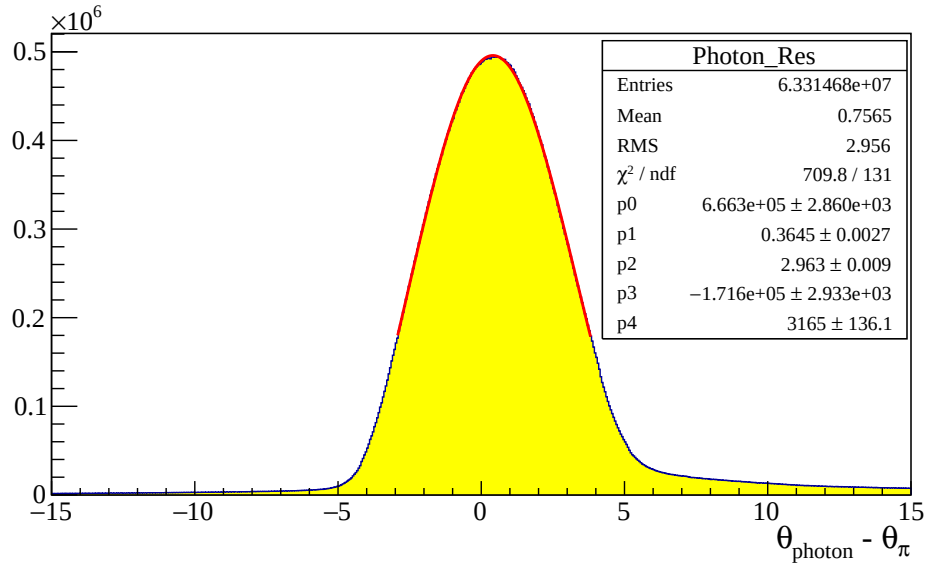

FIGURE 6.33: Distribution of the photon theta residual with respect to computed π theta. The mirror position and the refractive index were not tuned

Situation of the global photon angle residual after the tuning in RICH geometry:

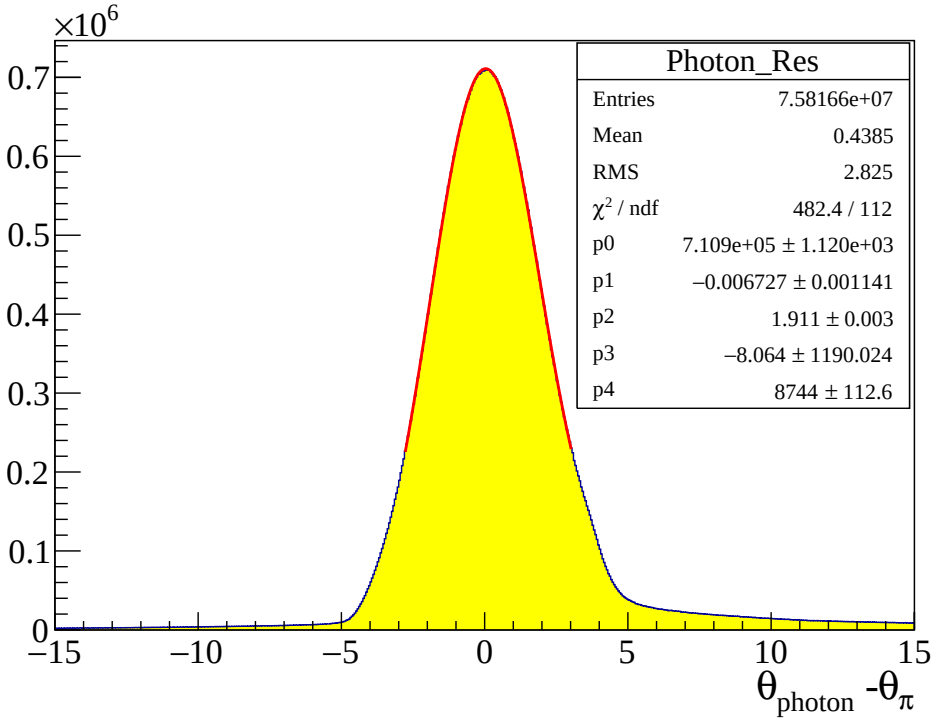

FIGURE 6.34: Histogram of the photon theta residual after the alignment of RICH and extraction of new refractive index at different momentum region

The dependence of the residual with the momentum of the particle has been shown in figure 6.35. Along the X axis the momentum is plotted and along Y axis the single photon resolution has been plotted after the tuning.

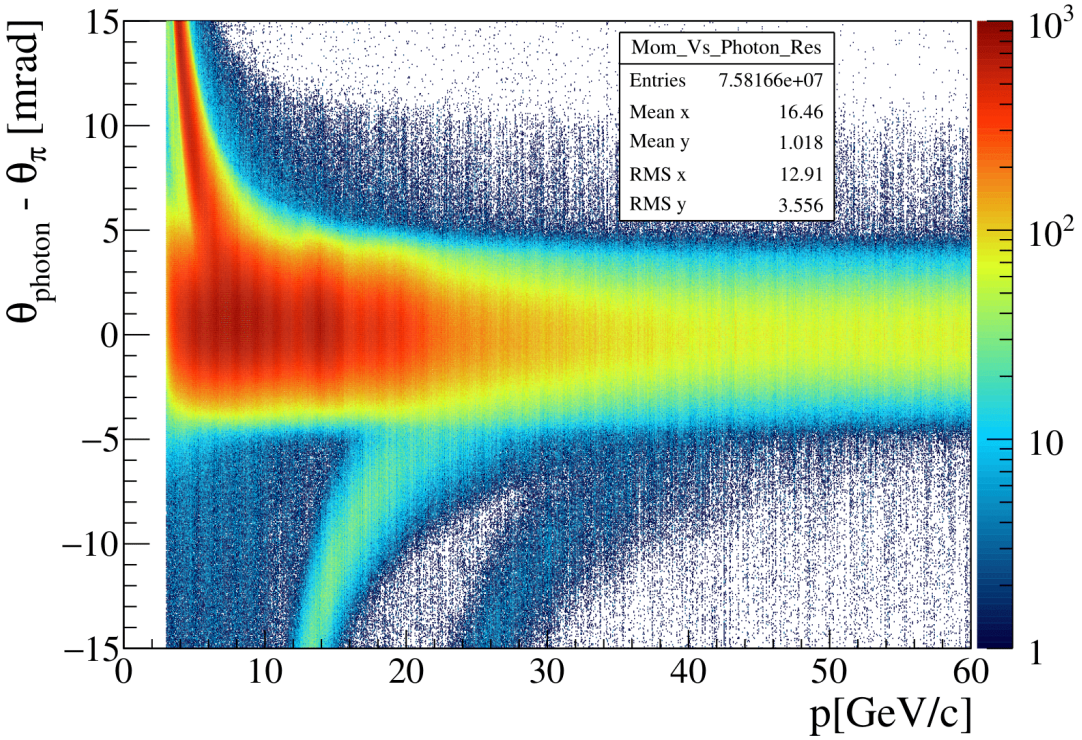

FIGURE 6.35: The 2D histogram displays the momentum dependence of the photon angle residual. The colour scale represent the entries, which is in log scale.

Finally, the residual of the ring can be also computed. Instead of single photon Cherenkov angle, the reconstructed ring angle is used. Each photon cluster is an independent estimate of the Cherenkov angle, in the absence of the background, the number of single photon (N_{ph}) and inaccuracy in the single photon angle measurement (σ_{photon}) can be related to reconstructed ring resolution σ_{ring} by the following relationship:

$$\sigma_{ring} = \frac{\sigma_{photon}}{\sqrt{N_{Ph}}} \tag{6.11}$$

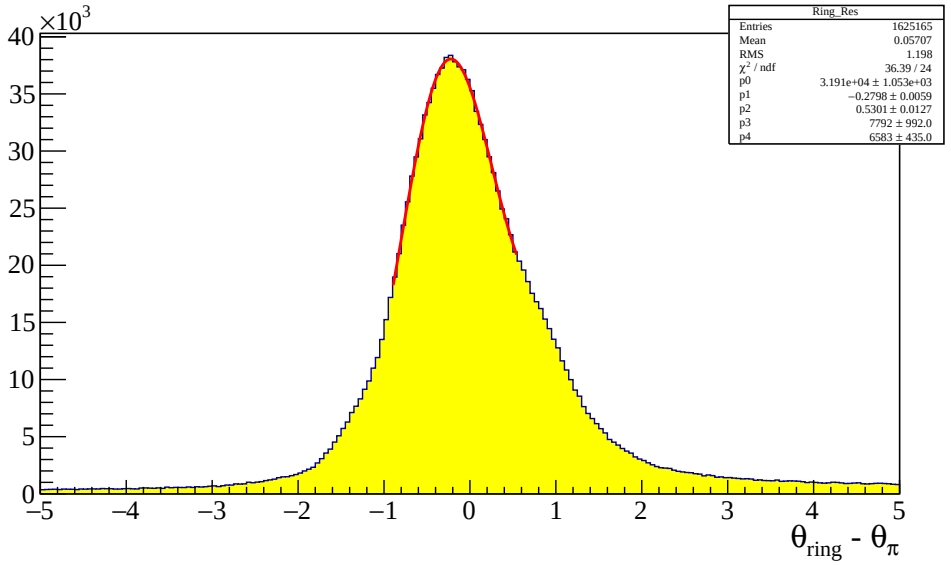

FIGURE 6.36: Distribution of the ring theta residual with respect to computed π theta, where the mirror position and the refractive index was not rightly tuned.

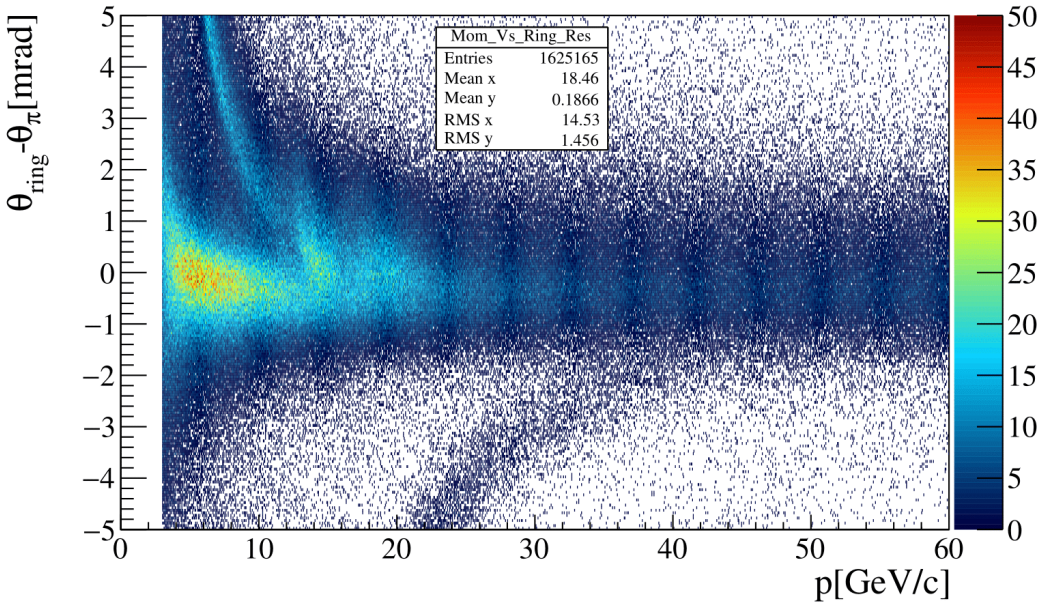

FIGURE 6.37: Momentum dependence of the ring theta residual with respect to computed π theta, when the mirror has not been tuned

In figure 6.36 we see that the main peak is severely distorted without the mirror position tuning. The standard deviation of the Gaussian signal is around 0.5 *mrad* which is in disagreement with our expectation. After the mirror tuning and correctly estimating the refractive index, the central value has become more centred toward zero, -0.069 ± 0.003 *mrad*. The sigma is improved to 0.319 ± 0.005 *mrad* as shown in figure 6.38. The dependence of the

residual of the ring angle has been shown in figure 6.37 and 6.39. Before and after the corrections respectively. Few striking improvements are noticed.

- The central value is clearly visible at different momentum regions after correcting the mirror position. The consistent residual over a wide momentum range indicates a good stability.
- The population of events up to 20 GeV/c has significantly increased, roughly speaking within 20 GeV/c in between -1 $mrad$ to 2 $mrad$ a factor of three times more population is observed. A nice and clear band for the muons can be seen. It is important here to mention that at around 5 GeV/c the π-μ β resolution is of the order of 10^{-5}. This associates as $\Delta\theta \sim 4$ $mrad$. A faint line of the muon is now visible. A very untuned filtering has been made to remove the majority of the muon by means of charge separation, taking the magnetic bending into account. But, it is not absolutely free from muon contamination.
- After the tuning of the RICH geometry the we observe that the Kaon band has got enhanced. This has definite positive effect in PID of RICH.

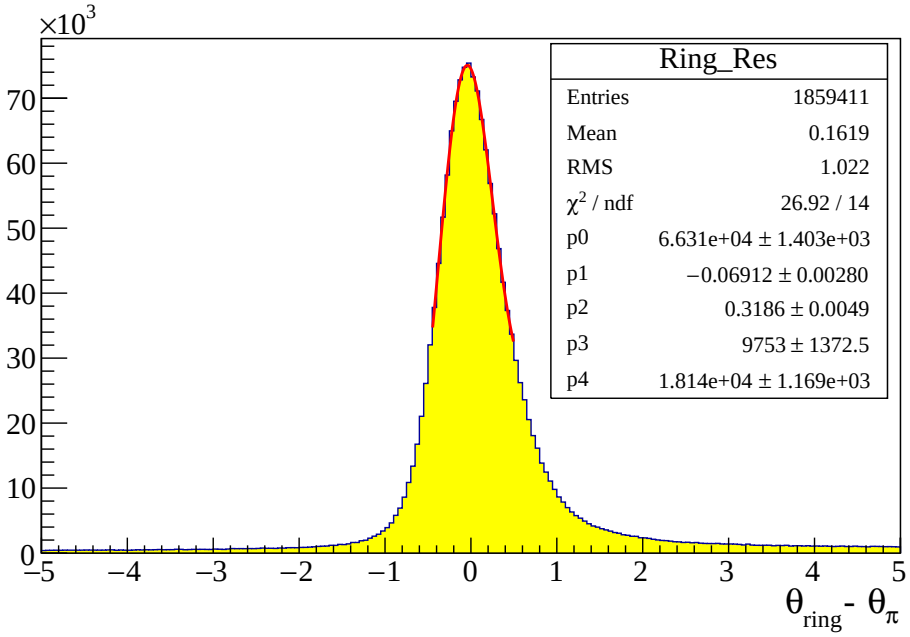

FIGURE 6.38: Distribution of the ring theta residual with respect to computed π theta

The electron band is prominent, muon band is faintly visible above the central band. The population along the central region has increased.

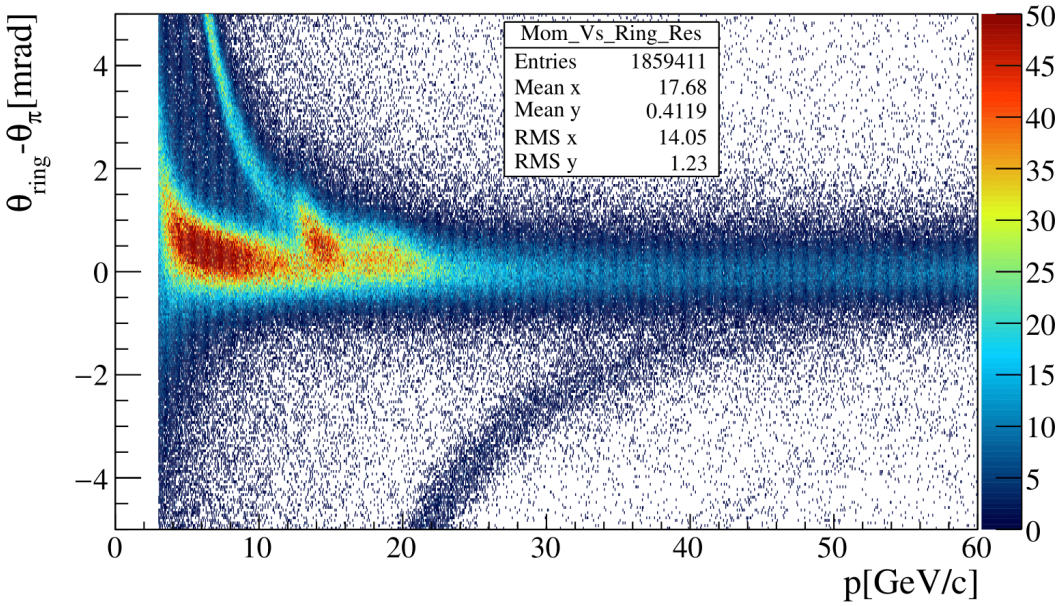

FIGURE 6.39: Momentum dependence of the ring theta residual with respect to computed π theta. The color scale is the same as the 6.37

At the lower momentum, tracks are affected by multiple scattering which smears the ring, and hence the emitted Cherenkov angle will increase. The expression for multiple scattering is given by

$$\theta_0 = \frac{13.6}{cp\beta} q \sqrt{x/X_0} \tag{6.12}$$

We have used symbols with their usual meanings. The x/X_0 of 3.3 m C_4F_{10} radiator is 1/10. Therefore for πs with momentum 5 GeV/c will have a multiple scattering angle of 0.8 $mrad$.

The dependence of the Cherenkov ring angle, which has been scaled to the VS refractive index, with momentum has been shown in figures 6.40 and 6.41.

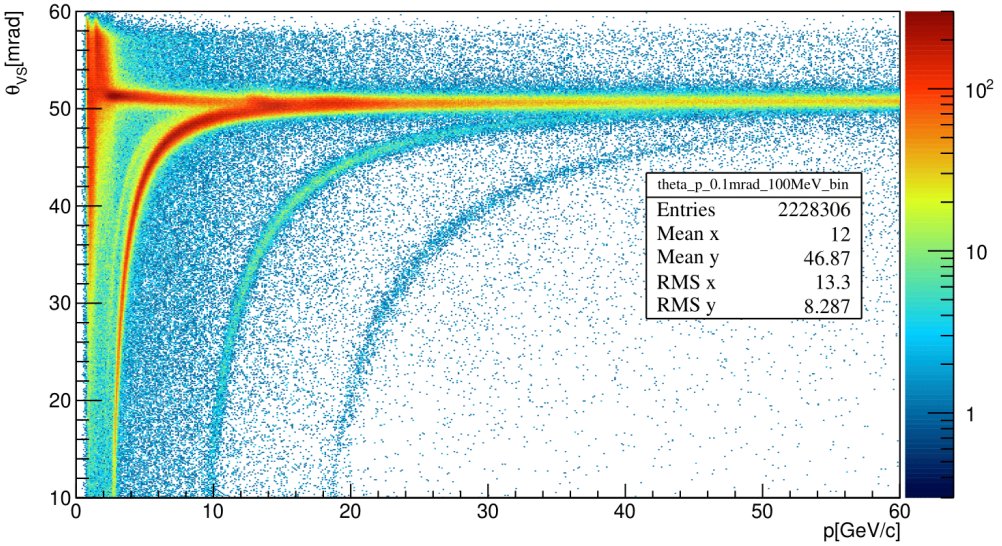

FIGURE 6.40: 2D histogram of ring theta versus momentum for particles with positive charge

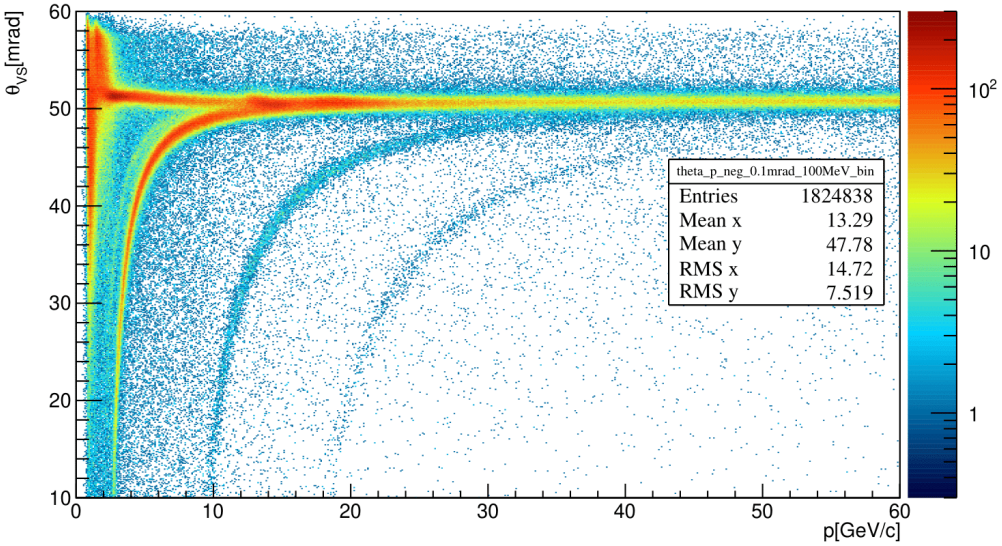

FIGURE 6.41: 2D histogram of ring theta versus momentum for particles with negative charge

The ring resolution improves if we determine the resolution of pion like rings fully contained within a cathode. The expected ring radius is computed from the pion hypothesis. The knowledge of the detector geometry is crucial in this analysis. The distance between the detector centre and the cathode edge has to be larger than the distance between the reflected particle position on the detector surface and the calculated radius. The detector will have four quadrants and this condition has to be satisfied in all quadrants, to accept

a ring as a full ring. The residual is computed using pion hypothesis. The sigma is the resolution of the ring. The sigma of the histograms shown in figure 6.43,6.44 and 6.45, are the estimation of the ring resolution for fully contained ring with pion assumption in the MAPMTs.

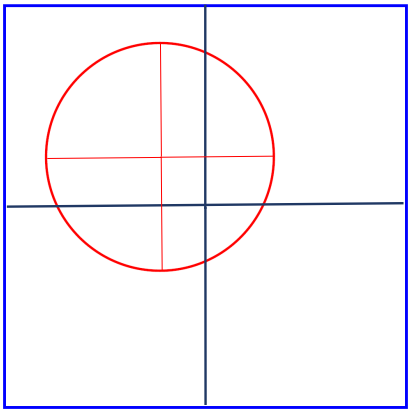

FIGURE 6.42: An geometric example of full ring. The blue rectangle can be assumed as a cathode and the red circle as the ring. The distance between the ring centre position and the radius of the ring should be smaller than the half cathode distance along horizontal and vertical direction of the cathode, simultaneously.

Estimated ring resolution is obtained by the sigma weighted average of the individual resolution is 0.24 ± 0.0030 *mrad* and is reasonably distributed as a Gaussian. The picture is consistent at different momentum bins. The estimate has been obtained as the mean weighted by the corresponding sigma.

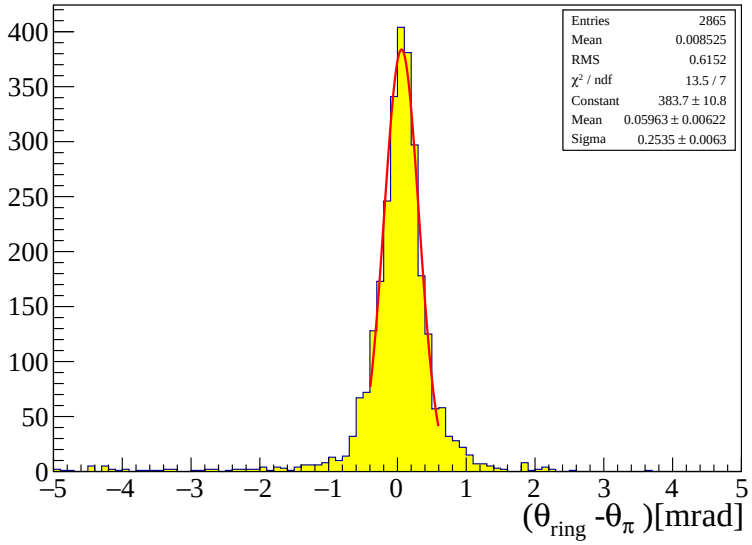

FIGURE 6.43: Histogram of the ring residual for tracks with fully contained ring in the MAPMTs with π mass assumption within momentum range 15 to 17 GeV/c

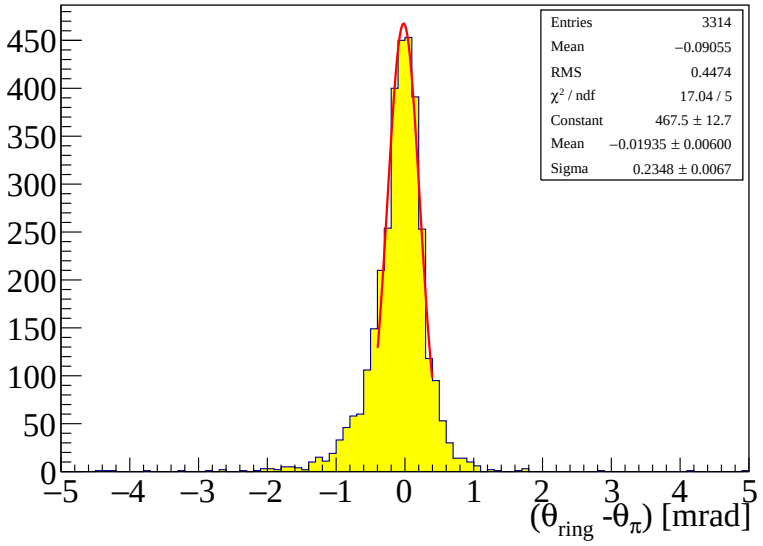

FIGURE 6.44: Histogram of the ring residual for tracks with fully contained ring in the MAPMTs with π mass assumption within momentum range 24 to 28 GeV/c

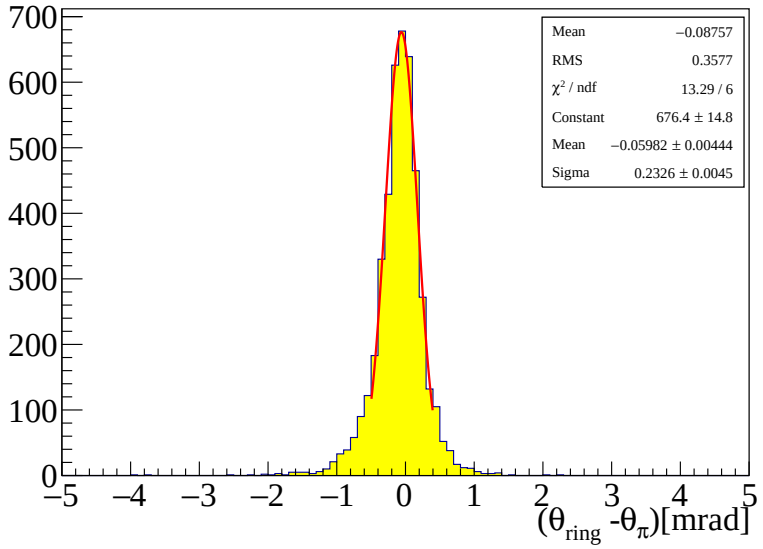

FIGURE 6.45: Histogram of the ring residual for tracks with fully contained ring in the MAPMTs with π mass assumption within momentum range 34 to 42 GeV/c

The Cherenkov theta versus the momentum plot can be visualised in the linear form. After the algebric transformation of the plotting variables we

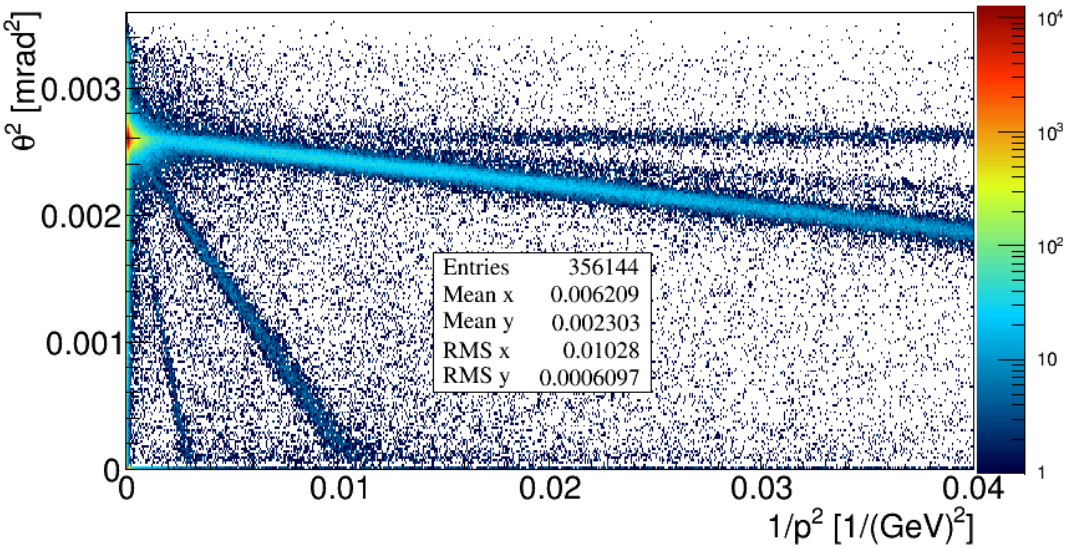

FIGURE 6.46: The 2D histogram of square of the Cherenkov angle versus the inverse square of the momentum.

estimate the 2(n-1) .

$$
\begin{aligned}
cos\theta &= \frac{1}{n\beta} \\
(1-\frac{\theta^2}{2}) &= (1-(n-1))(1+1/2\frac{m^2}{p^2}) \\
(1-\frac{\theta^2}{2}) &= 1-(n-1)-(n-1)/2\frac{m^2}{p^2}+1/2\frac{m^2}{p^2} \\
\theta^2 &= 2(n-1)-\frac{m^2}{p^2}(2-n)
\end{aligned}
\tag{6.13}
$$

From equation 6.13 we see that, in the plane θ^2 vs $1/p^2$ the particles will generate straight lines and the slope will be governed by the mass of the particle. The negative slope implies the θ^2 goes lower in value with $1/p^2$, which can be related from the Cherenkov equation, also the higher the mass of the particle the steeper the line. The intercept carries a physical meaning. At saturation which is very low $1/p^2$ all the hypotheses merge together. Thus the intercept define the θ^2_{sat}, which is approximately 2(n−1). In the first two X bins I have projected the Y axis and have taken the mean of the Gaussian as the estimation of 2(n−1). Figure 6.47 shows the mean is around 0.002596, The error due to statistical estimation can be neglected. The figure 6.47 is the projection of the θ^2 value for the first two X bins of 6.46. In figure 6.46 we observe an excellent agreement with the value of the refractive index extracted from the single photons.

In conclusion, at the beginning of the study, the reconstruction of the RICH with untuned detector and mirror position and severe contamination from electrons were all convoluted together to provide a distorted shape of

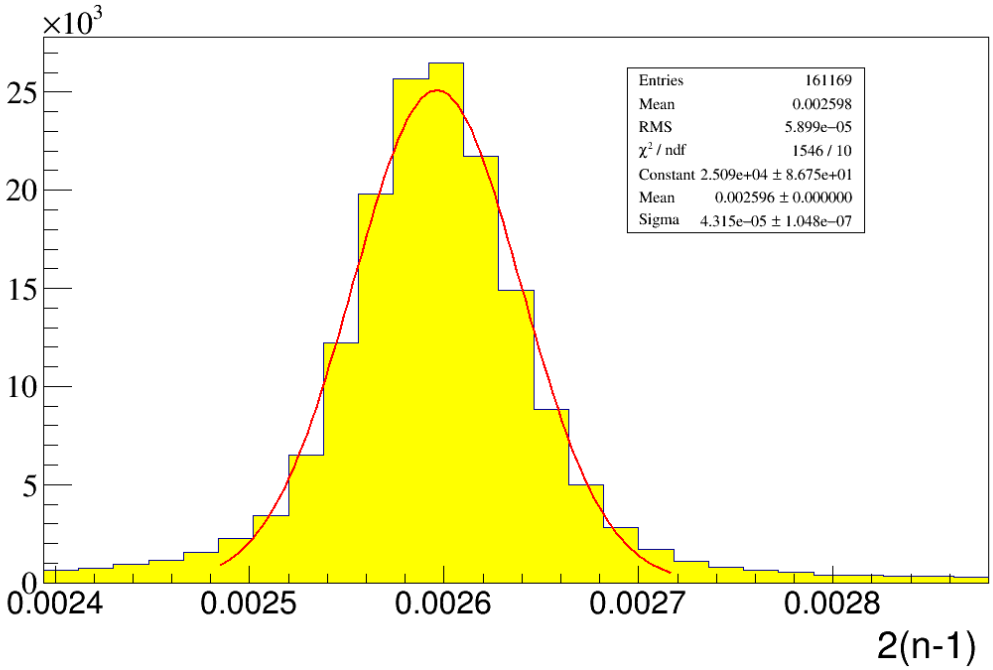

FIGURE 6.47: Estimation of the intercept of equation 6.13 from figure 6.46

the extracted refractive index. These errors have different causes and origins but essentially their combined effect will penalise the PID performance. The RICH has shown improved performances at every stage of tuning and alignment exercises performed.

Chapter 7

PID performance of COMPASS RICH

7.1 Introduction

RICH is a device to estimate the mass of the charged particle passing through the radiator, by measuring the Cherenkov angle of the photons emitted by the charged particle. This estimated mass value can be assigned to a particle either from the Cherenkov ring information where the individual photon level information is lost, or using the single photon information in a likelihood algorithm. RICHONE reconstruction software contains two independent PID algorithms as mentioned in chapter 3, the current PID is performed using the extended maximum likelihood (EML) algorithm only.

The brief summary of the likelihood estimation is the following: the single photons detected by the photon detectors can be ascribed as signal or as background. In a likelihood estimation, the description of signal and background is crucial. In COMPASS, the theoretical description of signal and background is not easy, the description is extracted from the data. The Cherenkov photon angle (θ^{photon}) around the reconstructed ring theta (θ^{ring}) is approximately distributed as a Gaussian with a standard deviation σ_{θ}^{photon} for each ϕ^{photon} value. Currently, we use the background information from the cluster distribution in the PD surface contributed by the electronic noise of the chambers and the physical background (mainly the beam halo). This 'map' of the noise is read by the software at its initialisation stage to compute the fractional contribution as background of the cluster position on the PD surface which enters as a 'single photon' into the likelihood algorithm.

7.2 The mass-spectrum from the RICH-1

The RICH detector provides an estimate of the mass square using the equation 3.11. The associated error can be propagated on the m^2 term according to equation 3.14 where the approximation made is that the $\cos\theta$ has been expanded up to θ^2 term. The resolution of the momenta can be assumed to be 0.5%. The error in the estimation of the refractive index is taken as 0.4% and the ring angle resolution is 0.35 *mrad* as suggested by the data. We can simulate the mass distribution with one sigma error. The outcome of this

simple simulation can be seen in figure 7.1. In the figure we have plotted the momentum (p) of the tracks in the Lab frame along the X axis and the $mass^2$ along the Y axis where we see the dependence of the $mass^2$ with the quadratic nature of the momentum. We have extracted the estimated $mass^2$ of the tracks entering the RICH with respect to its momentum from both the positive and negative μ runs of 2016 data taking at different momentum bins.

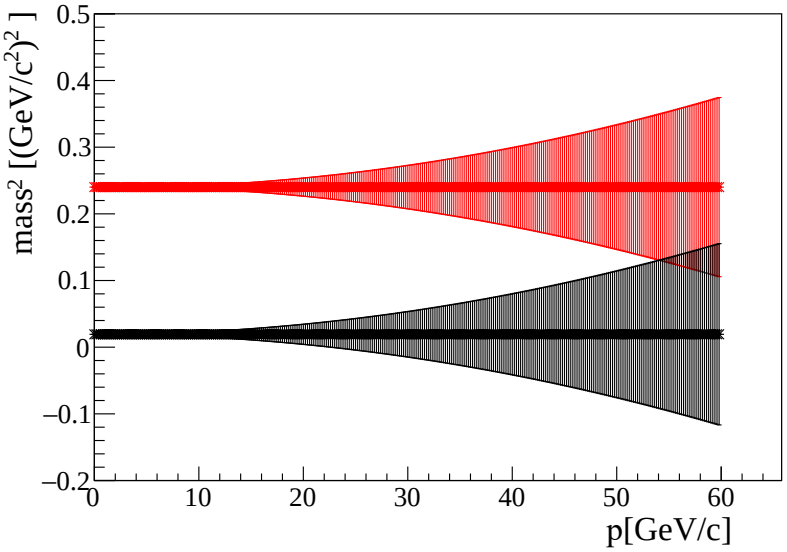

FIGURE 7.1: A toy simulation to understand the expected dependence of the $mass^2$ with momentum. The one sigma error-bar added is computed by propagating the error on the $mass^2$ term.

This nature is expected, provided the refractive index is rightly set. If the refractive index is not correctly set the central value of the $mass^2$ will no more lay on a straight line. It will tend to move with the increment of the momentum upwards or downwards according to the overestimation or underestimation of the refractive index respectively. The figure 7.2 shows the 2D histogram of events where along the X axis the lab momentum of the tracks is plotted, the Y axis corresponds to the $mass^2$ of the track, estimated from the track angle for negative tracks. Prior to the final tuning a large dependence of the $mass^2$ can be seen at large momentum. In terms of π-K separation by likelihood algorithm, this overestimation of the $mass^2$ will definitely favor the kaon hypothesis, compared to the pion one. To clean the sample from the beam particles and the halo I have adopted a coarse solution. The premise for such approach is to minimise the use of information coming from other detectors to identify any particle and hence to restrict the entire exercise with RICHONE tree. I have selected tracks with opposite charge that of the beam particles. In order to study the effect of the RICH alignment on both charges I have taken runs of differently charged beam particles. The results have shown full consistency.

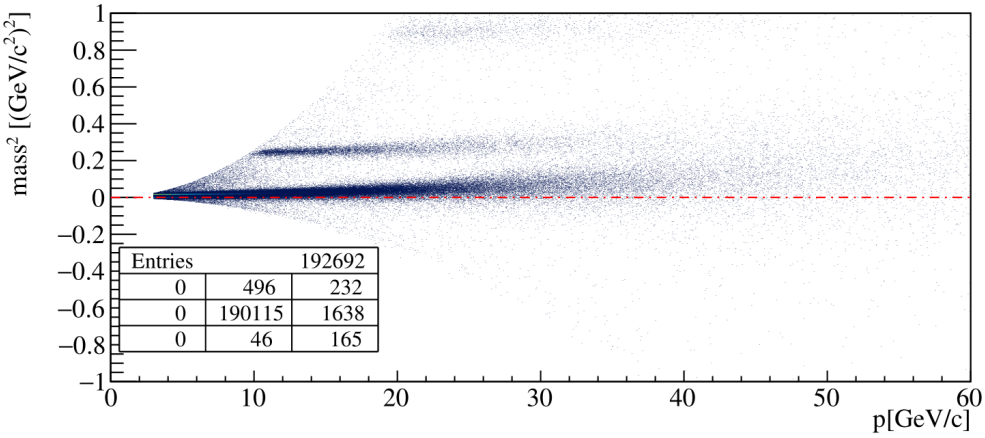

FIGURE 7.2: A 2D histogram showing the dependence of the $mass^2$ with momentum. The color scale is irrelevant. The data has been processed with correct geometry but wrong refractive index extracted from previous method. The wrongly estimated (n-1) is larger by $\sim 30\ ppm$. An over estimation of mass is seen at larger momentum. In the likelihood approach this will definitely favor the kaons over pions

.

After the final tuning we achieved a situation as presented in figure 7.3. Similarly, to reject the beam μ and its halo I have selected the particles with opposite charge of the beam particle. This will clearly skim the pions out of muons in the beam and halo of the beam.

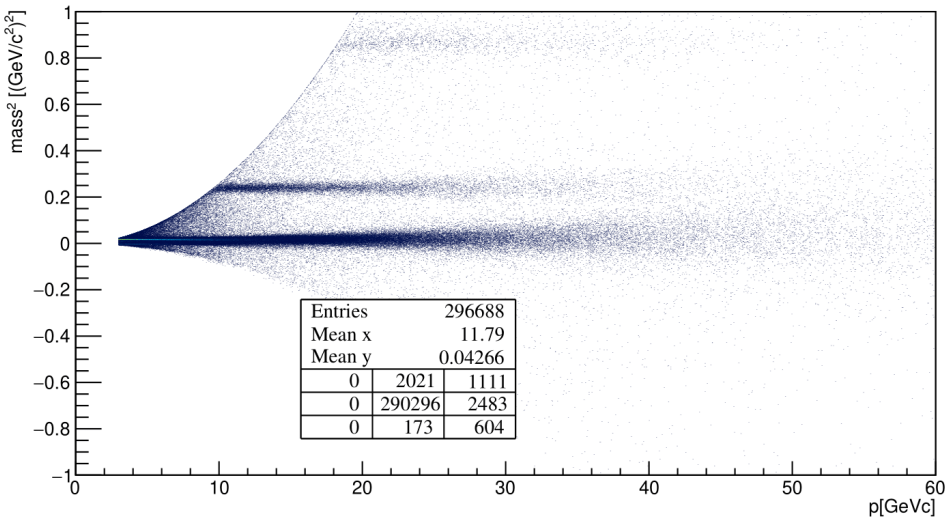

FIGURE 7.3: RICH estimated squared mass of positively charged particles and its dependence on momenta after tuning

Near saturation $2(n-1) \sim \theta^2$. The Gaussian nature of the measured theta distribution suggests squared theta can be greater than $2(n-1)$. Returning

a negative mass squared. Plotting mass versus θ will loose part of the information. Similar to 7.3 we have obtained $mass^2$ dependence on momentum for the negative charged tracks which can be seen in 7.4.

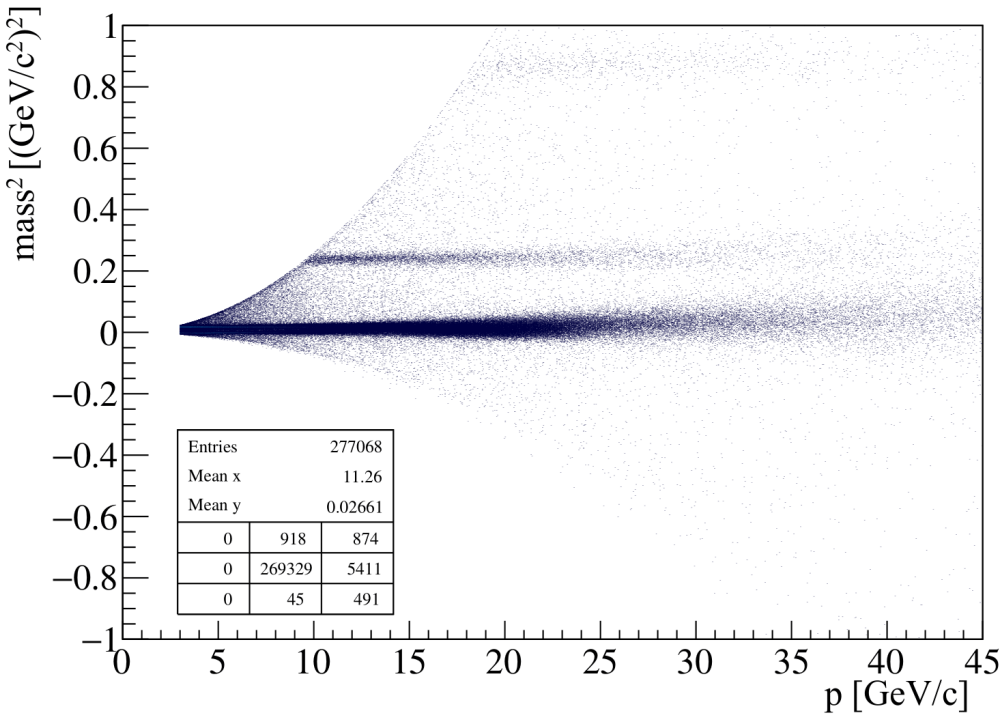

FIGURE 7.4: RICH estimated squared mass of negatively charged particles as function of particle momentum after tuning.

Figure 7.5 shows the $mass^2$ histograms of the positive charged particles, taken from a negative muon run. We can clearly identify the pions, kaons and proton peaks. I have chosen the Y scale which is the number of entries such that we have a visualization of the reduction in statistics with the increasing momentum. For each momentum bin I have fitted the histogram with a function added by three Gaussian distributions, in the fitting method first I have fitted individually the peaks, more or less defining the pion, kaon and proton peaks, providing a range of fit. In this range I have searched for the highest peak,and then fit a Gaussian with 2σ around the peak, I have taken the mean values of the fit and then I have set parameters defining the three means of the fitting function with the 3 Gaussian, which are $p1$, $p4$ & $p8$, to the values of the mean obtained by the individual fittings. These three parameters define the estimated $mass^2$ of pions, kaons and protons. If the χ^2/NDF remains larger than 5 after three consecutive fits, I reject that momentum bin. After passing this I take the final values as the mass. If I propagate the error on the estimation of the *mass* from the error of the fit associated to these three parameters $p1$, $p4$&$p8$, I find the error in estimation of mass of the order of 10^{-3} in the first momentum bin and at few $\sim 1-2\%$ level in the last two bins.

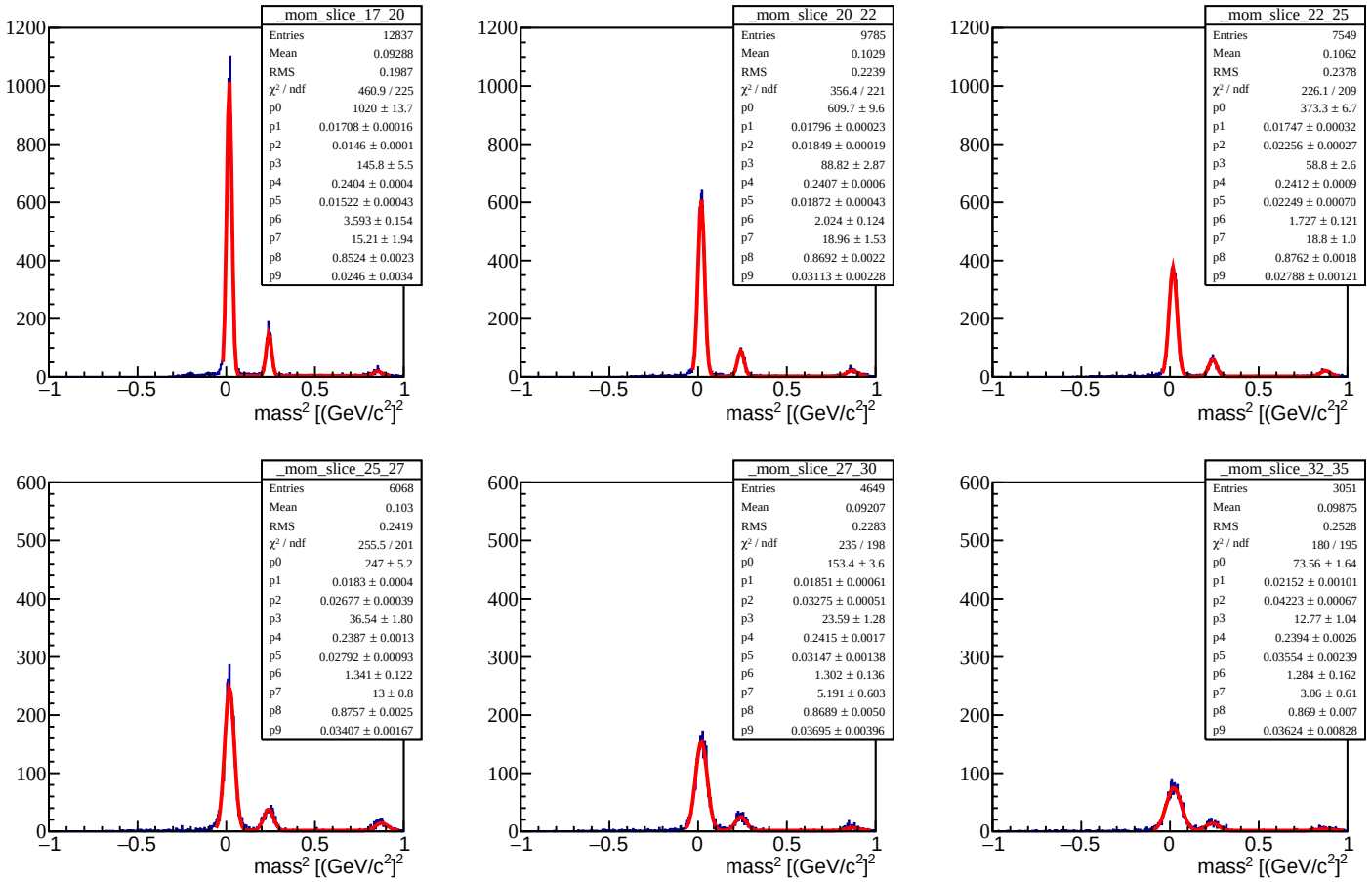

FIGURE 7.5: The distribution of the $mass^2$ estimated by COMPASS RICH-1 is shown at different momentum bin. In the top three panels the vertical scale has been normalised to 1200 and for the bottom three panels the vertical scale has been normalised to 600. The vertical scale corresponds to the number of entries

The mass spectrum brings us the information about the systematic and the dependence of the estimation with squared momentum. Recall that the error associated to the $mass^2$ determination is a product of the p^2 and σ_θ. Assuming that σ_θ remains the same for two momenta not very far apart then the ratio of sigma of the mass distributions of these two momentum will be the similar to the ratios of the square of the momentum. In figure 7.5 if we take two momentum bins as example $20-22$ GeV/c and $27-30$ GeV/c. The sigma of the Gaussian fitted around the kaon peak is 0.01872 and 0.03147 respective. The ratio of the first to the second is $(0.01872/0.03147) = 0.594$, and if we assume for simplicity that the average corresponding to the first range is 21 GeV/c and for the second 28.5 GeV/c, then the ratio of their squares is $(21^2/(28.5)^2) = 0.542$. The numbers are verified for other mass hypotheses and over different momentum ranges.
I have also estimated the $mass^2$ for the negative charged tracks. The negative charge tracks are highly contaminated with the electrons, and therefore even after merging with the pions at higher momentum the mass of the pions will be slightly underestimated. When the effect started to become less trivial, we run out of statistics. Therefore, to check the estimated mass of the negative pions I have selected the low momentum regions where the pions and electrons are clearly separated and there I have estimated the mass of the pions. The kaons and anti-protons are free from this effect. The $mass^2$ of the kaons over a wide momentum range remains reasonable with respect to the PDG values. In figure 7.6, 7.7, 7.8 and 7.9 we have plotted the histogram of the $mass^2$ of negatively charged particles, namely negative pions, negative kaons and antiprotons.

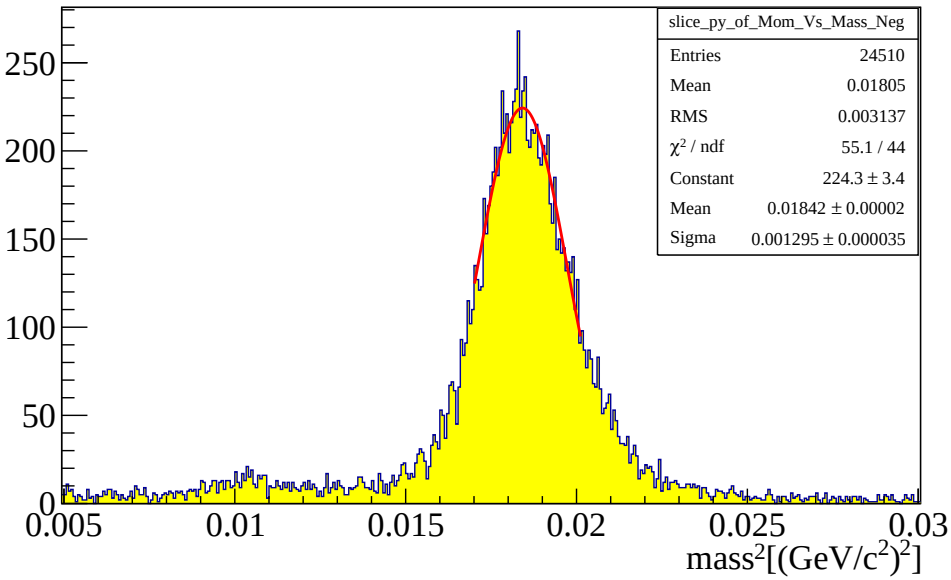

FIGURE 7.6: Histogram showing the RICH extracted $mass^2$ for the negative pions in the momentum range of 3-5 GeV/c. A reasonable Gaussian distribution is describing the data

The kaon $mass^2$ has shown reasonable consistencies with expectations. For the negative kaons the example of extracted $mass^2$ at different momentum bins are shown in the figures 7.7 and 7.8.

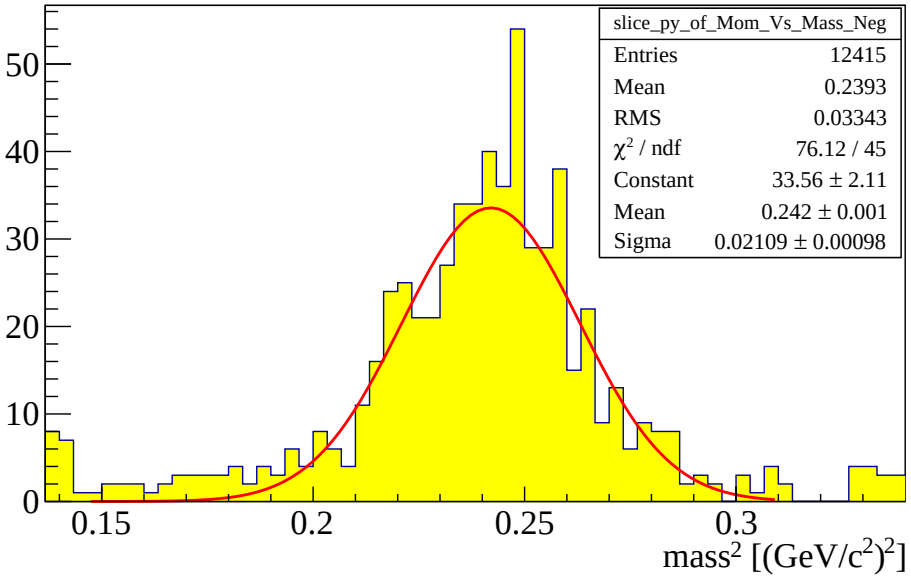

FIGURE 7.7: Histogram shows the RICH extracted $mass^2$ negative kaons in the momentum range of 20-25 GeV/c. The histogram is described reasonably by a Gaussian distribution.

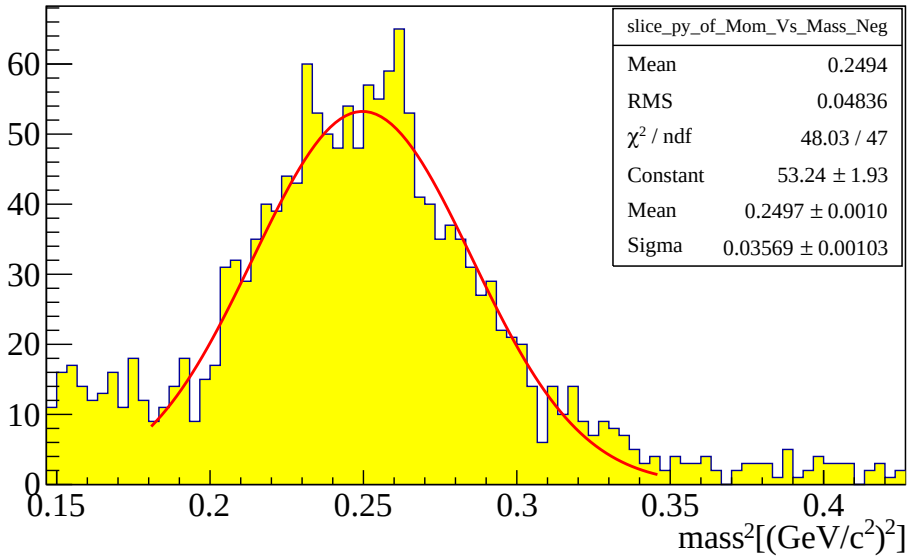

FIGURE 7.8: RICH extracted $mass^2$ negative kaons in the momentum range of 27-32 GeV/c

For the determination of the antiproton mass, I have taken a large sample of the momentum region (20-40 GeV/c)where I have adequate sample size

to fit the Gaussian to estimate the $mass^2$. The example distribution is shown in figure 7.9.

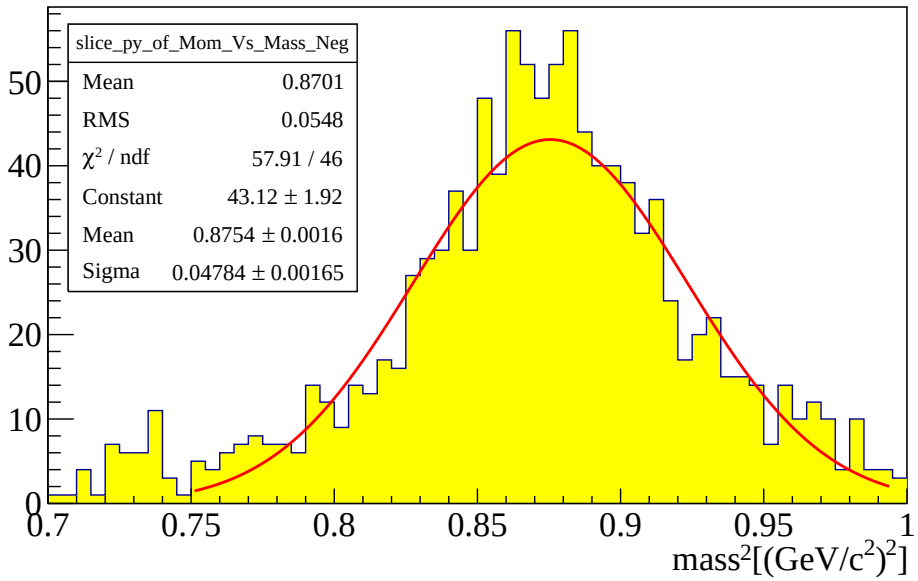

FIGURE 7.9: RICH extracted $mass^2$ anti-protons in the momentum range of 20-42 GeV/c

7.3 Separation Power

Particle identification is based on the fact that, at any situation the detector responds differently to different particle species. For the RICH detector, the measured Cherenkov angle is the only sensitive quantity to different particles at the same momentum. Therefore, we can define a method of separation power, as suggested in [65] based on the measured Cherenkov angle and the accuracy of the measurement. The improved resolution is therefore mandatory for efficient particle identification. The θ_{ring} for the pions and kaons are assumed to be distributed as a Gaussian around the mean value, θ_π and θ_K, and $\sigma_{\pi K}$the average value of the standard deviation of the measured distribution, then the separation power N_σ is the following:

$$N_\sigma = \frac{\theta_\pi - \theta_K}{\sigma_{\pi K}} \tag{7.1}$$

For computing the separation power of $\pi - K$ and comparing with our expectation, I have adopted these two following techniques:

- The first method is a simplistic data driven calculation, with mass assumption. The values of N_σ obtained by this method allows us to estimate our expectation. We assume that our momentum is known with adequate precision. The knowledge of the refractive index allows us to compute the Cherenkov theta for pion and Kaon hypothesis for that

momentum. The theta difference divided by the ring resolution obtained for the MAPMTs without selecting special tracks provides n_σ separation from the first method.

- The second method is more directed to the measurements. In each momentum bin, I extracted the mean of the theta distribution by a Gaussian approximation fitting pion and Kaon region separately. The difference in the two mean values divided by the average of the two sigma distributions estimates the n_σ separation at that momentum bin. This method is however affected by the selection of the fitting region. As the population is very limited at the higher momentum and hence the associated error in determining the peak is larger.

In figure 7.10 we see the $\pi - K$ N_σ separation as a function of momentum.

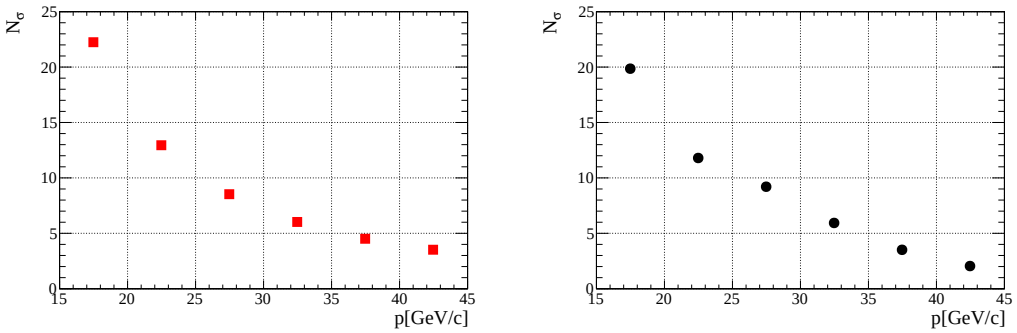

FIGURE 7.10: Momentum dependence of the $\pi - K$ separation power N_σ of COMPASS RICH-1. Left Panel: Cherenkov angle computed by using the average mass estimated by COMPASS RICH-1 of a particular run and the refractive index of that particular run. Average ring resolution of 0.35 *mrad* is used for computing N_σ. Right panel: by fitting the the two peaks of pion and kaon separately with Gaussian functions. The separation power is defined as the difference in the mean of the two peaks divided by the average of the sigmas.

7.4 Likelihood values for RICHONE PID

Consistency between the likelihood (in short form LH) values of different mass hypothesis and the constructed ring angle points to the optimal functionality of the RICH detector. I have studied the consistency between the reconstructed ring and the likelihood of a track for different mass hypothesis. Before describing the studies, I will describe the extended likelihood algorithm adopted by the software.

7.4.1 Principal of likelihood algorithm

Equation 7.2 describes a situation where a set of unknown parameters l_k is estimated by maximizing the standard likelihood L, by means of a set of

measured quantities (θ_i).

$$L = \prod_{i=1}^{N} p(\theta_i; l_k) \tag{7.2}$$

The probability density function which defines the sampling variable θ_i is given by p(θ_i;l_k). The likelihood values or similarly the log of the likelihood values are to be maximised for obtaining the solution of the equations.
Experiments where data taking is restricted to predetermined number of samples, and no fluctuation in the number of events is expected, are fundamentally different than our case. For the estimation of the likelihood for each track for each mass hypothesis, the single photons in the ring are our events. For each track the number of photons is randomly varying following a Poisson distribution. The number of events (N) is relevant to the quantities being estimated, and the incorporation of the fact that the number of photons observed has the actual value N improves the estimates of our parameter. Under this circumstance it is not surprising that we have to take into account the number of photons track by track and hence, we have to relax the absolute normalisation. Although for a particular track, the likelihood value for different mass hypothesis will have same number of photons, but the size of our distribution (number of photons) will change at the next track, and this fluctuation is governed by a Poisson statistics [142]. The extension of the maximization of the likelihood allows us to relax the constraint
$\int p(\theta_i; l_k) = 1$
and to have an estimation of the total number of events expected over the whole range of observation. So the probability density is extended to:

$$\int P(\theta; l_k) = \mathcal{N}(l_k) \tag{7.3}$$

The $\mathcal{N}(l_k)$ is our size of our distribution. The value of (N) is obtained from the fit and can be a better estimation of the "true" total number of events than physically observed value N.

We have adopted the extended maximum likelihood (EML) method for the PID done by the COMPASS RICH. Therefore, it is the heart of our PID algorithm is to know the number of photons from the fit. It is understandable that just replacing the normalised $p(\theta)$ by the unnormalised $P(\theta)$ is not possible, as the maximisation process will tend to make the normalisation large. To remedy this, we not only corroborate the photons were observed events at (θ_1,θ_2,...,θ_m) but also ensure that events were not observed anywhere else. This is why, we integrate our signal and background over a large fiducial region of 70 *mrad*. If we can divide our bins small enough where more than one event is negligible in each bin($\Delta\theta$). Then we can write the probabilities for 0 and 1 event for a bin are given by Poisson statistics:

$$\begin{aligned} P_0 &= e^{-\Delta\theta P(\theta)} \\ P_1 &= \Delta\theta P(\theta) e^{-\Delta\theta P(\theta)} \end{aligned} \tag{7.4}$$

For the MAPMTs this assumption is realised as that one physical pixel is detecting one single photon, and for the gaseous detectors one cluster is a detected single photon. Using equation 7.4 we can write down the extended likelihood by equation 7.5. In this equation the first product term corresponds the product over all bins with one event and the second product term is over all bins. Physically, the extended likelihood describes the combined probability for a complete data sample.

$$\mathcal{L} = \prod_i \Delta\theta P(\theta_i) \prod_j e^{\Delta\theta P(\theta_j)} \tag{7.5}$$

In the limit $\Delta\theta \to d\theta$ the first term of equation 7.5 can be written as $\prod_i P(\theta_i) d^N\theta$, where terms like $d^N\theta$ incorporates the fact that $P(\theta)$ is a probability density not real probability, analogous to equation 7.2. With aid of equation 7.3, second product term of equation 7.5 in the limiting case becomes: $e^{-\sum_j \Delta\theta P(\theta_j)} \to e^{-\int P(\theta) d\theta} = e^{-\mathcal{N}}$. Therefore, in the limiting case we can write extended likelihood or alternatively its logarithmic form as:

$$\begin{aligned} \mathcal{L} &= \left[\prod_i P(\theta_i)\right] e^{-\mathcal{N}} \\ ln(\mathcal{L}) &= \sum_i P(\theta_i) - \mathcal{N} \end{aligned} \tag{7.6}$$

The maximisation of this extended likelihood will give us the solution to the EML; the solutions are estimated by finding a balance of the two terms in the logarithmic expression. The first term increases with increasing normalization and the second term decreases. A legitimate solution of this equation can be:

$$\mathcal{L} = \prod_{i=1}^{N} P(\theta_i) e^{-\mathcal{N}} \frac{\mathcal{N}^N}{N!} \tag{7.7}$$

Whence written in unnormalised form the equation 7.7 turns out to be

$$\mathcal{L} = \prod_{i=1}^{N} P(\theta_i) \frac{e^{-\mathcal{N}}}{N!} \tag{7.8}$$

To get a nonzero value of the computed likelihood value the assumption is that there is at least one photon associated to a track for the extended likelihood calculation, otherwise the value passed is 0.

7.4.2 Extended maximum likelihood methods for COMPASS PID

For the cases where each event can be a contribution of the signal or the background term, then the power of likelihood resides in the correct definition of the signal and the background. Maximisation of the extended likelihood is

a powerful tool for the determination of the unknown parameters of events where the event size is fluctuating. The theoretical description of signal and background terms of the extended likelihood is not easy in our case. The distributions are therefore needed to be taken from the data. The signal can be reasonably described by a Gaussian distribution in the $\theta - \phi$ plane, with a standard deviation σ_{theta}. A detailed Monte-Carlo study had been done in 2000 by Paolo Schiavon, during the construction of the code. The detailed study was done with MWPC detectors. An example is shown in figure 7.11 taken from his notes.

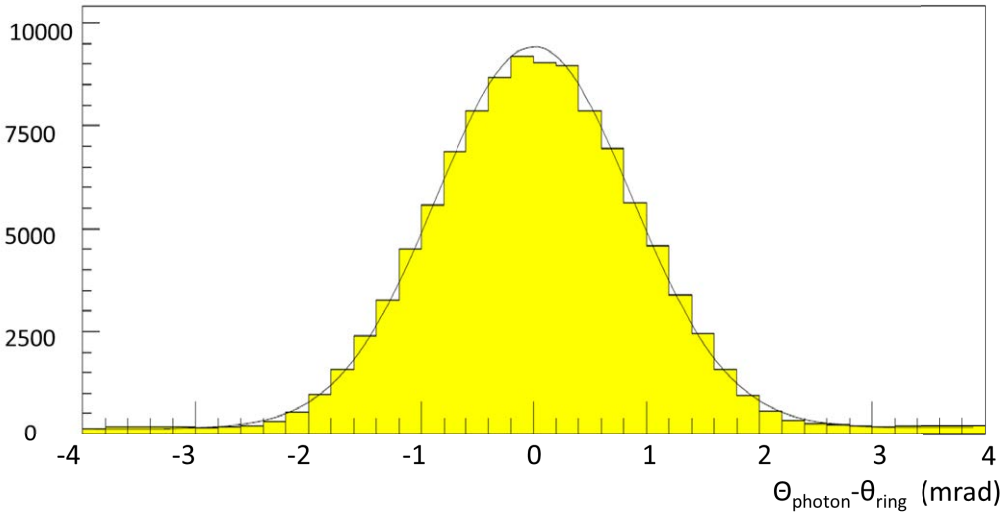

FIGURE 7.11: An example distribution of $\theta_{photon} - \theta_{ring}$ for fixed ϕ_{photon} ($112.5 \pm 7.5\ deg$); it has been obtained from the simulated data of the MWPC detectors; the distribution is reasonably described by a Gaussian plus a linear background. The definition of ϕ angle is defined already in equation 6.7

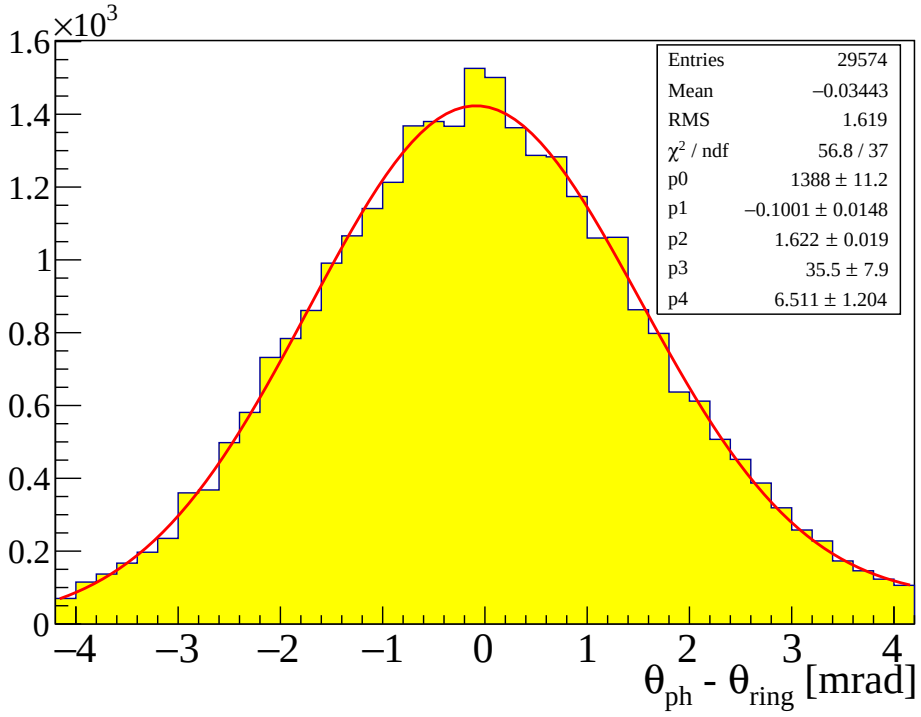

FIGURE 7.12: An example histogram of the $\theta_{photon} - \theta_{ring}$ at a particular $\phi = 220 \pm 10$ *deg*; it has been obtained from the simulated data of the MWPC detectors; the distribution is reasonably described by a Gaussian plus a linear background. The definition of ϕ angle is defined already in equation 6.7

From figure 7.12, we see that the distribution of the observed parameter θ is reasonably distributed according to a Gaussian, over a linear background. The shape of the background will depend on the type of the detector. Therefore, the the background is parameterised from a 2D distribution of the hit maps on the detector surface.

The first operation in this algorithm to compute the likelihood is to evaluate the normalisation: integrated signal and background. For our case, the integration is made over a fiducial region of 70 *mrad*. This wide range of fiducial region is such that it is larger than the maximum Cherenkov angle of the two types of detectors, namely MAPMTs and gaseous detectors working in the visible (VS) and ultra violet (UV) ranges respectively. This wide range is chosen essentially to ensure that the signal photons are not detected elsewhere in the detector. The normalization is necessary every time the likelihood is computed. For each track, for each mass hypothesis the likelihood is computed, however the background does not depend on the mass hypothesis hence the background normalization can be computed only once. Our

expected signal and expected background terms can be defined in the following way:

$$S_M = \int_C s_M \, d\theta \, d\phi$$
$$B = \int_C b \, d\theta \, d\phi \tag{7.9}$$

After completing the normalisation of the likelihood extraction algorithm we need to compute the LH values taking into account all the photons associated to a particle. All these photons are chosen within the fiducial region. They are used for the evaluation of the signal and background part. This approach essentially makes the PID based on likelihood independent of the PID based on the ring χ^2 and hence independent of pattern recognition. From equation 7.9 the total normalization is $\mathcal{N} = (S_M + B)$. The unnormalised probability density function is $P(\theta) = s_M(\theta_j, \phi_j) + b(\theta_j, \phi_j)$ for the j^{th} photon. Following equation 7.3 we can write the equation of the extended likelihood as

$$\mathcal{L}_{\mathcal{M}} = \left(\prod_{j=1}^{N} \frac{(s_M + b)}{S_M + B} \right) exp(-(S_M + B)) \frac{(S_M + B)^N}{N!}$$
$$\mathcal{L}_{\mathcal{M}} = \left(\prod_{j=1}^{N} (s_M + b) \right) exp(-(S_M + B)) \frac{(S_M + B)^N}{N!} \frac{1}{(S_M + B)^N} \tag{7.10}$$
$$\mathcal{L}_{\mathcal{M}} = \left(\prod_{j=1}^{N} (s_M + b) \right) \frac{exp(-(S_M + B))}{N!}$$

For the PID we compare LH values of individual mass hypothesis (e,μ,π,K and P and *background*) for each track, therefore $N!$ is irrelevant as this just scales the LH value. Whatever it is, it is same for all the mass hypotheses. So we don't compute this term. This relaxation makes equation 7.10 to

$$\mathcal{L}_{\mathcal{M}} = exp(-(S_M + B)) \prod_{j=1}^{N} a_M \tag{7.11}$$

Where, a_M is unnormalised probability density, taking into account that each photon can belong to signal or background. The signal is reasonably described by a Gaussian distribution, shown in figure 7.12, the functional description is:

$$s_M = \frac{S_0}{\sigma_{\theta j}\sqrt{2\pi}} exp(-\frac{1}{2} \frac{(\theta_j - \Theta_M)^2}{\sigma_{\theta j}^2}) \epsilon(\theta j, \phi j) \tag{7.12}$$

Where Θ_M is the expected Cherenkov angle of the photons emitted by a particle of mass M.

$$\cos \Theta_M = \frac{\sqrt{p^2 + M^2}}{np} \tag{7.13}$$

The term $S_0 = N_0 L \sin^2 \Theta_M$ is the expected number of photons from the Frank-Tamm law. N_0 is the expected number of photons tuned on data for each photon detector. $\sigma_{\theta j}$ is the single photon resolution obtained from data. The Θ_M is computed using refractive index of the cathode, which is $(n-1)_{VS}$ for the MAPMTs and $(n-1)_{UV}$ for the gaseous detectors. The importance of correct knowledge of the refractive index is one of the key ingredients of likelihood algorithm.

For each particle a probability ($\epsilon(\theta j, \phi j)$) of the photon survival from the beam pipe and mirror dead-zones is computed. Where for each photon it is checked that the probability of being absorbed by the beam pipe or the dead-zones of the mirror along the particle path length(L_p) with a step size of $L_P/10$. The fraction is multiplied to the unormalised signal.

The background $b(\theta j \phi j)$ is obtained from a map of the cluster distribution over the detector surface, called background map. In this approach the background parametarisation is more detailed and derived from the detector surface. This term is multiplied with the computed cluster theta and a factor which is the square of the focal length described in meters. This is the Jacobian transformation for the Cartesian to the spherical system. In equation 7.11 the term $exp(-B)$ is common for each mass hypothesis and the background hypothesis. Where the LH value background hypothesis is computed where $s_M = 0$

The LH values are saved in a buffer if the number of photons is greater than 1, likelihood values of particles below threshold is stored as 0. As an example, if we do not have any background photon cluster associated a track and the track is originally a proton below the threshold momentum, it will not emit any physics photon in the RICH, and hence it will be assigned a likelihood value 0 to it. This information can be carefully treated to identify particles below threshold. In our case the likelihood is Poissonian. The background is obtained from the background map and it is also integrated like the signal as described in equation 7.9. Therefore, the LH is a product over the $(S_M + B)$ term of all the individual photons. As we are comparing the LH for different hypotheses and using the background map we are relaxed not to compute the term $e^{-B/N}/N!$ in the LH formula.

7.4.3 Improvements

Maximisation of the extended likelihood is extremely powerful to separate pions and kaons, if the parameters of the RICH are correctly set. During the tuning of the RICH, we tuned the geometry and the refractive index. Each of the modification has showed an improvement in the estimation of the LH values. Before any tuning we saw an effect, which was unexpected. The ratio of LH values of pion and kaons ($\frac{LH(\pi)}{LH(K)}$) remain less than 1 after $20 GeV/c$ even if the muons were not filtered out from the sample. The muons are not separable from pions at this momentum based only on the LH values. Three figures have shown the direction of improvements. We can plot along the X axis the momentum of the tracks and along Y axis $\frac{LH(\pi)}{LH(K)}$ and we see the

following situations: for figure 7.13 only the survey suggested RICH photon detector position have been implemented, which did not provide us an optimally tuned RICH. Whereas, for figure 7.14 I have plotted the same quantities but updated the RICH geometry with the survey suggested detector position and the data driven mirror alignment, but refractive index used for LH value computation was from the old data base, where contamination due to the proliferated electron arm was present, which has been shown in several figures of Chapter 6, the visibility of the electron arms in the 2D maps of (n-1) distribution with momentum. Finally, figure 7.15 represents the situation when detector and mirror positions are tuned with an estimation of $(n-1)$ obtained from the new momentum range.

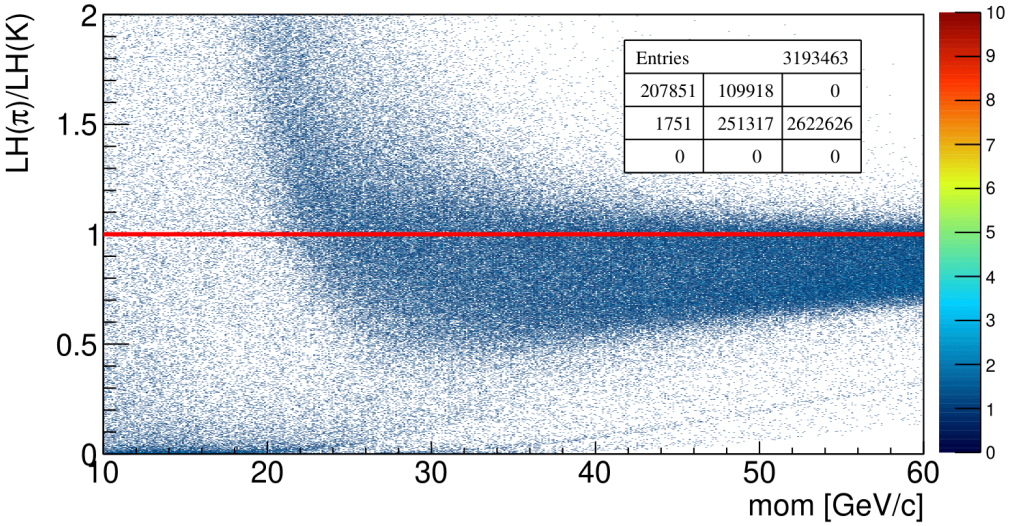

FIGURE 7.13: 2D histogram to show dependency of LH ratio of pion and kaon with momentum. Where the colour scale, representing the number of entries, has been normalised to 10. The distribution has rightly tuned detector position obtained from the survey

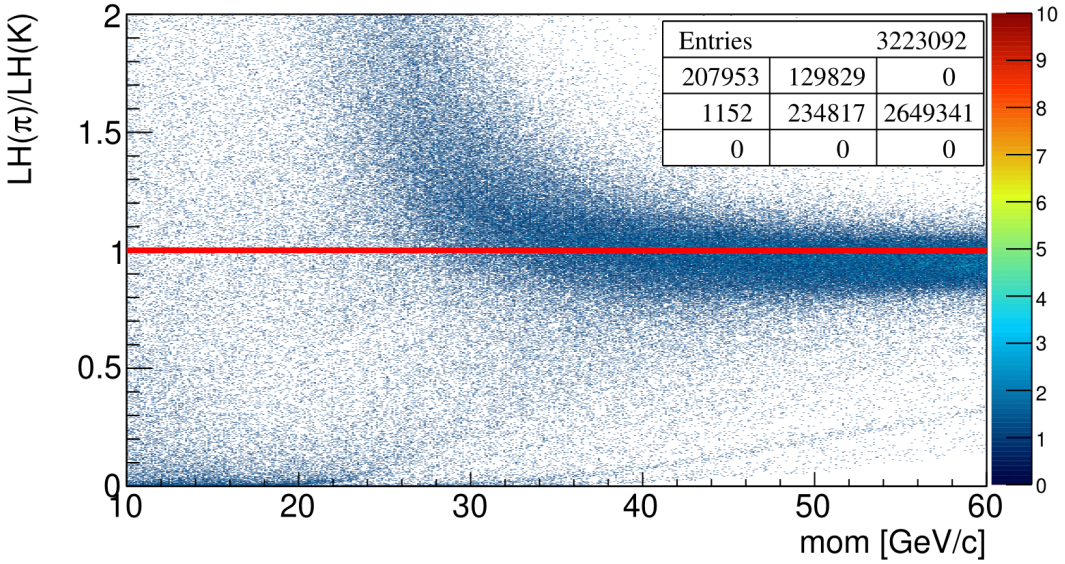

FIGURE 7.14: 2D histogram to show dependency of LH ratio of pion and kaon with momentum. Where the colour scale, representing the number of entries, has been normalised to 10. The distribution has rightly tuned detector and mirror position but untuned refractive index.

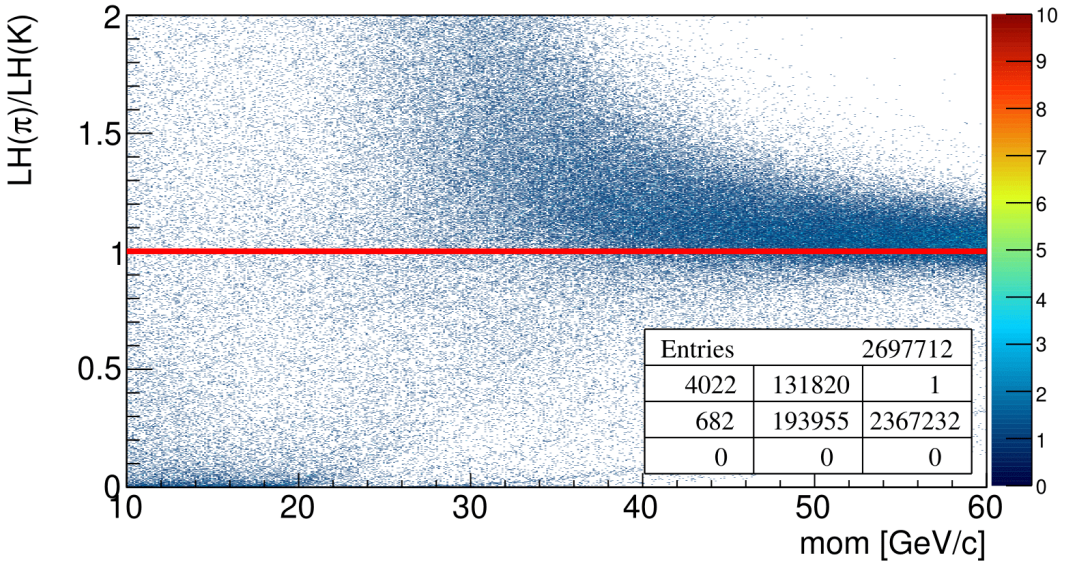

FIGURE 7.15: 2D histogram to show dependency of LH ratio of pion and kaon with momentum. Where the colour scale, representing the number of entries, has been normalised to 10. The distribution has rightly tuned detector and mirror position and tuned refractive index.

We see, that the current situation has improved significantly. The LH ratio of pion like and kaon like tracks are according to the expectation. The large

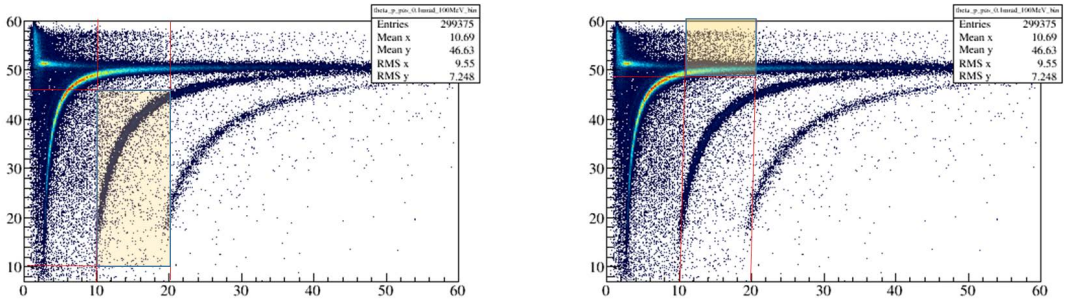

FIGURE 7.16: Example of selection of tracks based on theta and momentum.

pion contamination in the kaon sample, which was our initial problem seems to be understood and addressed.

7.4.4 Consistencies with RING angle

The ring information can be used to tune and characterise the RICH. For a well tuned RICH, the particle identification which is based on the LH algorithm should have consistencies with the reconstructed ring. The ring recognition has been done with a pattern recognition algorithm. The algorithm takes all the photon θ distribution relative to a particle up to θ_F, using a window width $\Delta\theta$. It then counts the number of photons in each window, the maximum number is then taken as the ring angle θ_{ring}. The window $\Delta\theta$ is typically $\pm\sigma_\theta$. If regions are selected where based on ring theta and momentum for a tuned RICH this will indicate estimated values for the ratios of the LH values of two mass hypothesis.

For example, the kaons in the momentum range between 10-20 GeV/c, will emit Cherenkov photons at an angle which is far from the pions. Therefore, if we select samples in this momentum range and put a limit on the Cherenkov angle which reasonably defines the kaon band, we expect the ratio of the LH value of the kaons over the LH value of the pion will be larger than one. Moving on toward the higher values of momentum range and selecting the kaons with constrained ring angle will bring the LH ratio closer to unity, as in the higher momentum range the PID power reduces. Figure 7.16 shows an example of the selected track. The approach brings uncertainty, when we go higher in momentum. The pions are already at saturation. Therefore within two sigma ring of the pion saturation,I consider tracks are most likely to be pions. For the kaons in the 20-30 GeV/c no ambiguity is

seen, but in the 30-40 GeV/c bin, I have tried to compute the angle expected for kaon like tracks, from momentum and refractive index. Then within 1.5 sigma of the ring resolution, I have assumed a track to be kaon likely.

Followed by the selection, an exercise has been done to check consistency of the ring recognition and the likelihood estimations. At a moderate momentum range, namely, from 20-30 GeV/c. Tracks are selected based on the theta and momentum cuts. Therefore in this region the RICH should be able to identify pion like tracks as pion like tracks. And we see that figure 7.17 shows the histogram of the LH ratio of pion and Kaon hypothesis, for the selected tracks. The value is largely above 1, which ensures efficient PID. Figure 7.18 is another representation of this observation. The 2D histogram displays the natural log of the LH values, where along the X axis the pion hypothesis and along the Y axis the kaon hypothesis. The red line corresponds to the inability to isolate pions and kaons.

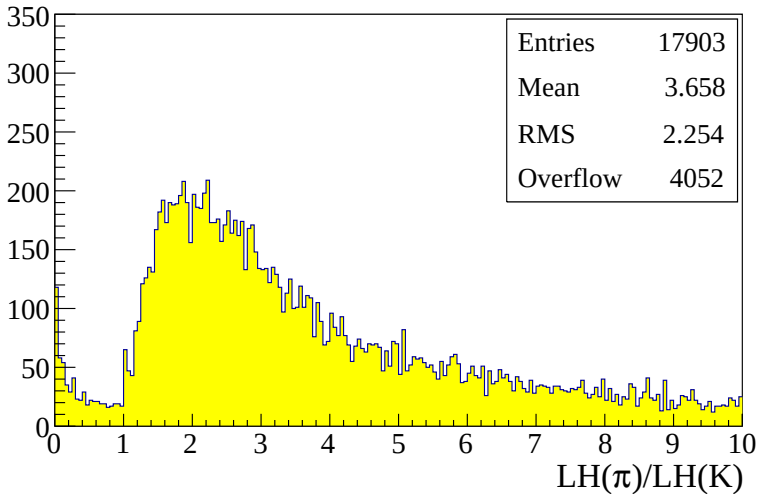

FIGURE 7.17: Histogram of the LH ratio of pion to kaon for the selected pion tracks based on Cherenkov angle in the momentum range of 20-30 GeV/c

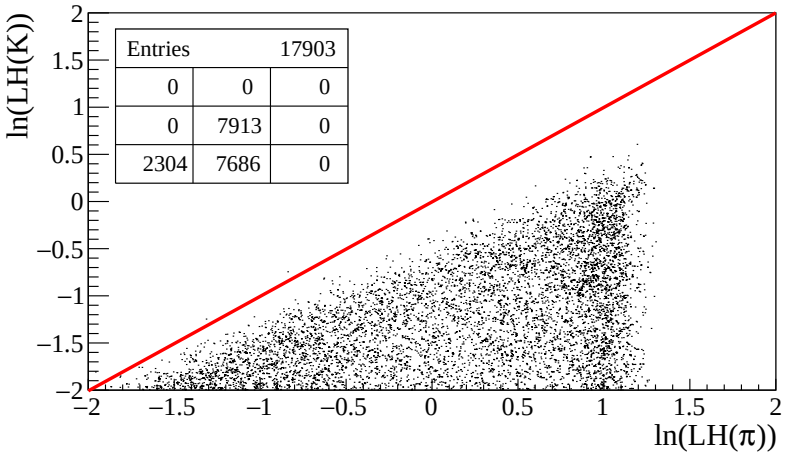

FIGURE 7.18: For the selected tracks of momentum range 20-30 GeV/c 2D histogram showing the log likelihood values of pion (along X axis)and kaon hypothesis (along Y axis). In this histogram each track is an entry. The color scale is not important as we are only interested in the separation of the pion and kaons. The pions and kaons are not separable at the red line.

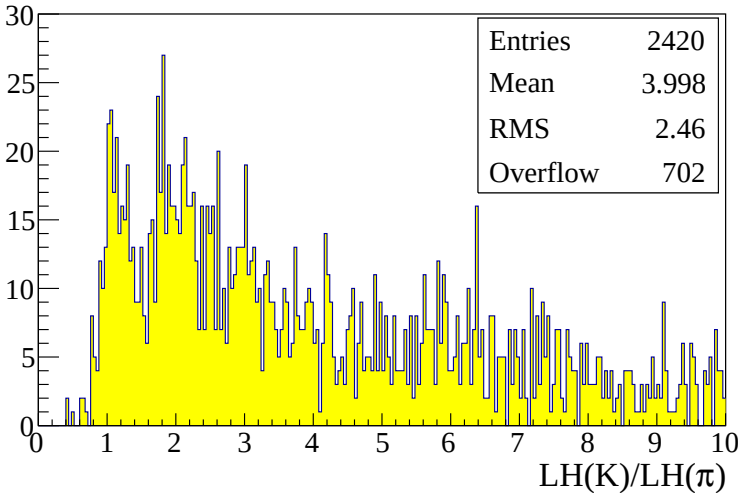

FIGURE 7.19: For the selected kaon tracks of Cherenkov angle and momentum range 20-30 GeV/c 1D distribution of the LH ratio of kaon over pion

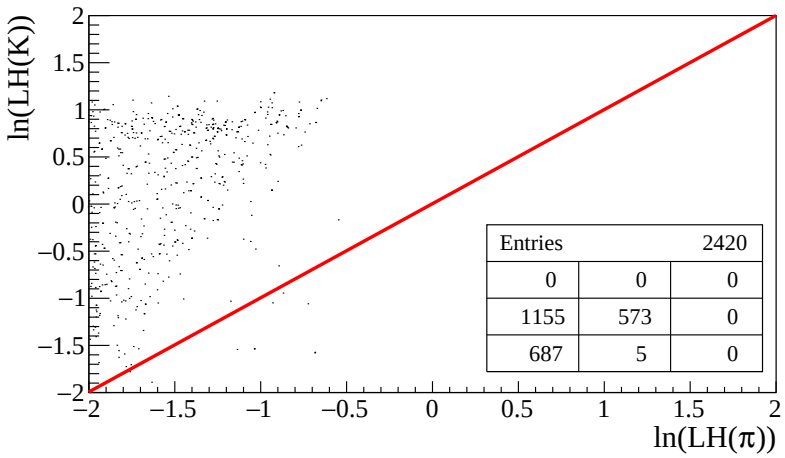

FIGURE 7.20: For the selected tracks of momentum range 20-30 *GeV/c* 2D histogram showing the log likelihood values of pion (along X axis)and kaon hypothesis (along Y axis). In this histogram each track is an entry. The color scale is not important as we are only interested in the separation of the pion and kaons. The pions and kaons are not separable at the red line.

The same exercise has been repeated at a higher momentum range. Namely, from 30-40 GeV/c. The tracks are again selected based on their ring and momentum values. And we have seen in figure 7.21 shows the histogram of the LH ratio of pion and Kaon hypothesis, for the selected tracks. The value is fairly above 1, which ensures efficient PID. Similarly, figure 7.22 is another representation of this observation. The 2D histogram displays the natural log of the LH values along X axis the pion hypotheis and along Y axis the kaon hypothesis. The red line corresponds to the inability to isolate pions and kaons.

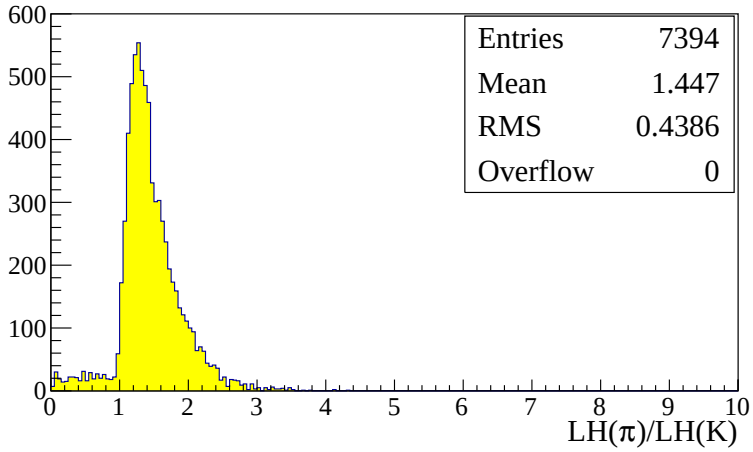

FIGURE 7.21: The LH ratio of pion and kaon at 30-40 *GeV/c* of the selected tracks. The selection is based on theta and momentum cuts. The RICH is still capable of doing PID

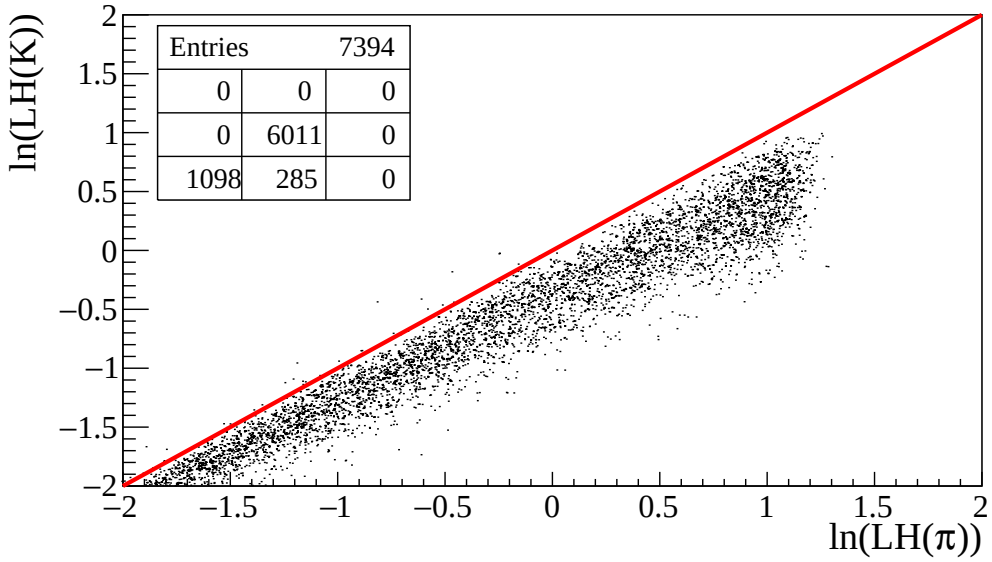

FIGURE 7.22: For the selected tracks of momentum range 30-40 GeV/c 2D histogram showing the log likelihood values of pion (along X axis)and kaon hypothesis (along Y axis). In this histogram each track is an entry. The color scale is not important as we are only interested in the separation of the pion and kaons. The pions and kaons are not separable at the red line.

The similar effect has been observed for the kaons. Figure 7.23 displays the 1D histogram and 7.24 shows the 2D histograms of the RICH separation of kaon like tracks.

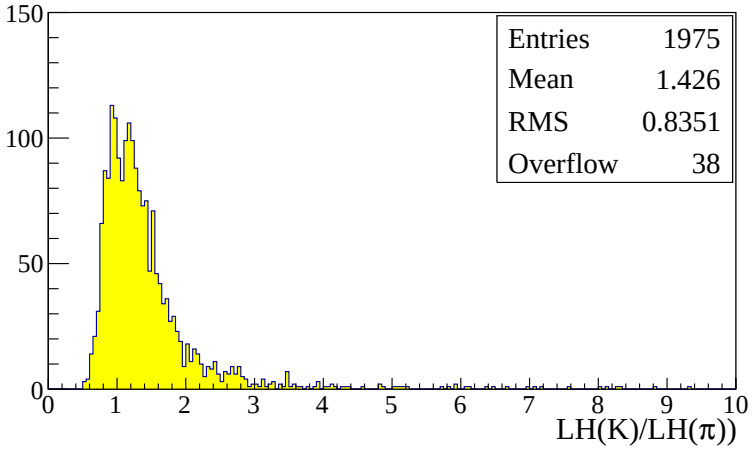

FIGURE 7.23: For the selected tracks of momentum range 30-40 GeV/c histogram showing the LH ratio of kaon over pion

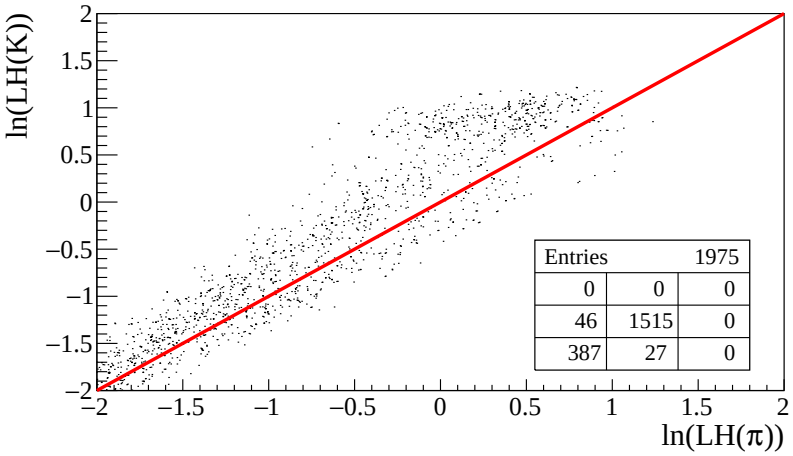

FIGURE 7.24: For the selected tracks of momentum range 30-40 GeV/c 2D histogram showing the log likelihood values of pion (along X axis)and kaon hypothesis (along Y axis). In this histogram each track is an entry. The color scale is not important as we are only interested in the separation of the pion and kaons. The pions and kaons are not separable at the red line.

The consistencies has also been checked in the opposite direction. We have to check if the likelihoods of the pions are larger compared to the kaons, then the χ^2 of the ring with pion hypotheses should be smaller compared to the χ^2 of the ring with kaon hypothesis. The χ^2 of the ring is dependent on the pattern recognition. The same algorithm of pattern recognition is applied to compute the ring angle and the χ^2. The χ^2 is computed for the photons which have been recognised for the ring. The refractive index have been scaled globally to UV for all the ring related computations. The definition of the reduced χ^2 is the following:

$$\frac{\chi^2_M}{\nu} = 1/\nu \sum_{j=1}^{N_{rPh}} \frac{(\theta_j - \Theta_M^{UV})^2}{\sigma_{\theta j}} \tag{7.14}$$

Where ν is the normalisation parameter and N_{rPh} is the number of photons in the ring, θ_j is the Cherenkov angle of the ring photons and single photon resolution is $\sigma_{\theta j}$. The knowledge of the momentum and the UV refractive index coupled to a particular mass hypothesis allows to compute the Θ_M^{UV}. To check the likelihood values, a cut was applied on the ring angle depending on momenta, the two defining parameters of the estimated mass, if the refractive index is known precisely. In the next method a cut in the likelihood is applied to check the ratio of pion and kaon χ^2 values. This redundancy test allows to confirm the stability of the PID algorithm. Figures 7.25 and 7.26 shows the ratio of the reduced χ^2 kaon hypothesis over pion hypothesis with momentum 20-30 GeV/c, in terms of likelihood two cuts are applied for each plot.

1. The LH value of the pion hypothesis is larger compared to the LH value of the kaon hypothesis. For figure 7.25 $\frac{LH(\pi)}{LH(K)} > 1.2$ and $\frac{LH(\pi)}{LH(K)} > 2$ in figure

7.26.
2. The LH of the background is smaller than the pion hypothesis is the same for both plots.

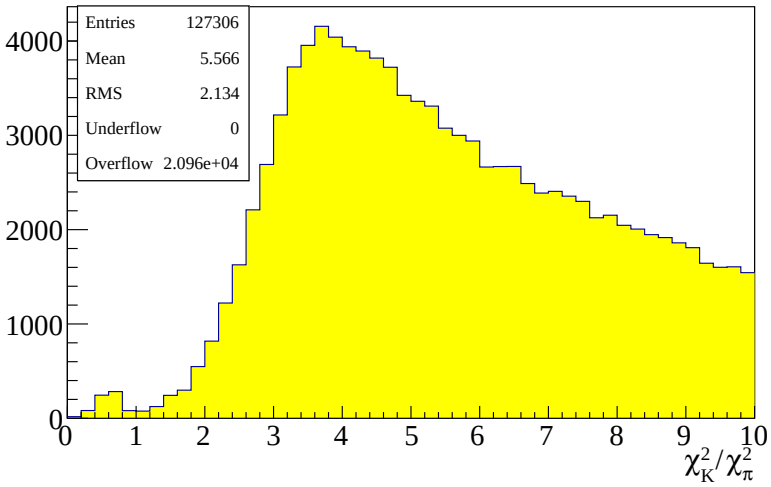

FIGURE 7.25: The histogram shows the ratio of $\chi^2(K)$ and $\chi^2(\pi)$ for tracks where $LH(\pi)$ is greater than $LH(K)$ by 1.2 times, the selected tracks are in the momentum range of 20-30 GeV/c

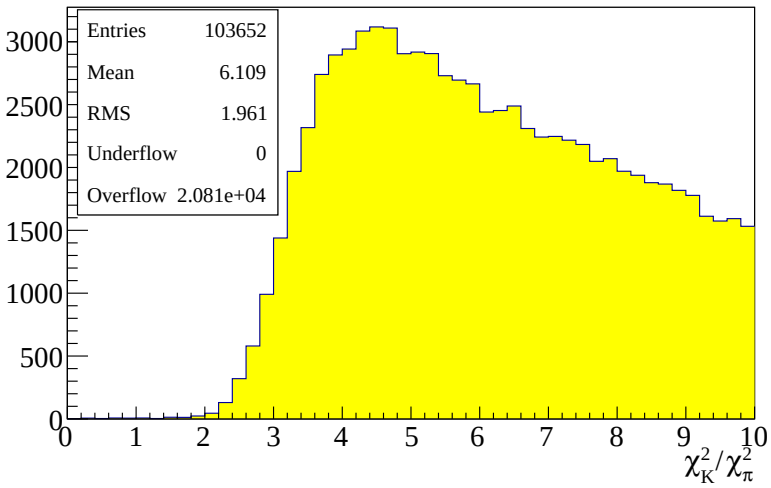

FIGURE 7.26: The histogram shows the ratio of $\chi^2(K)$ and $\chi^2(\pi)$ for tracks where $LH(\pi)$ is greater than $LH(K)$ by 2 times, the selected tracks are in the momentum range of 20-30 GeV/c

The observations are consistent. For pion like tracks the χ^2 with kaon hypothesis will be larger. Around 0.7% of the events where $LH(\pi)$ is larger than $1.2 \times LH(K)$, have lower χ^2 for kaon hypothesis. Which decreases to almost zero when the LH cut is 2. This is also consistent.
In the higher momentum, the Cherenkov angle of the pions and kaons comes closer, hence the PID is reduced.

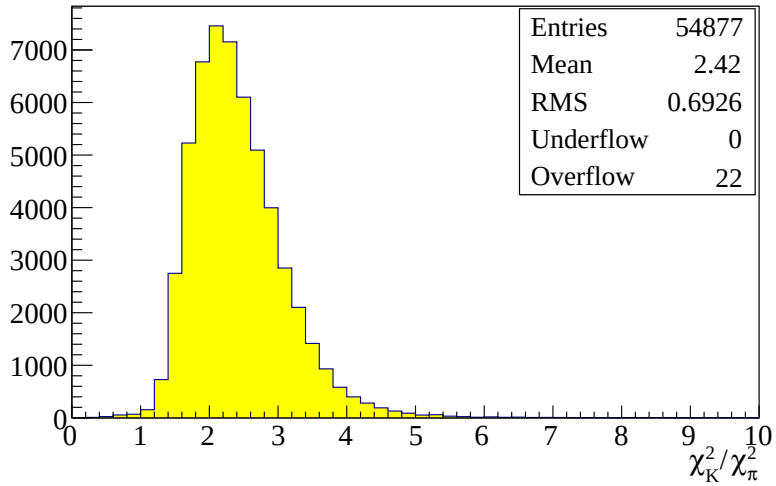

FIGURE 7.27: The histogram shows the ratio of $\chi^2(K)$ and $\chi^2(\pi)$ for tracks where $LH(\pi)$ is greater than $LH(K)$ by 1.2 times, the selected tracks are in the momentum range of 30-40 GeV/c

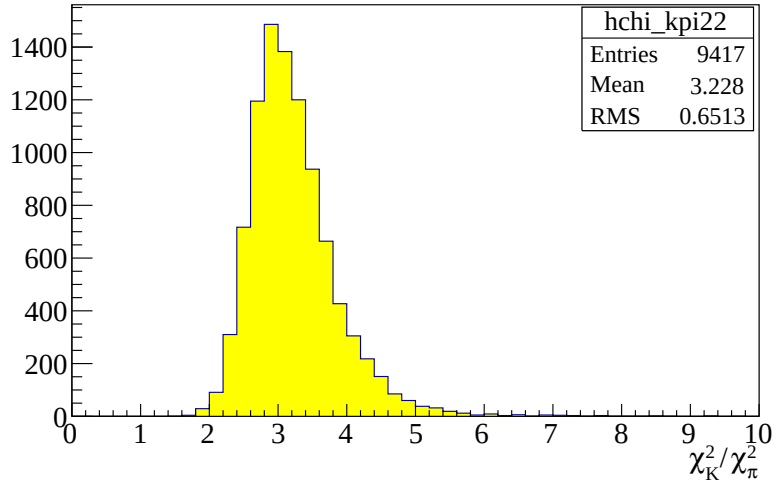

FIGURE 7.28: The histogram shows the ratio of $\chi^2(K)$ and $\chi^2(\pi)$ for tracks where $LH(\pi)$ is greater than $LH(K)$ by 2 times, the selected tracks are in the momentum range of 30-40 GeV/c

Similar exercise has been done for the kaons. In this case we have plotted, the ratio of the $\chi^2_\pi/\chi^2 + K$ in the histograms for the tracks which have been selected based on likelihood ratios. In the momentum ranges $20 - 30$ GeV/c and 30-40 GeV/c.

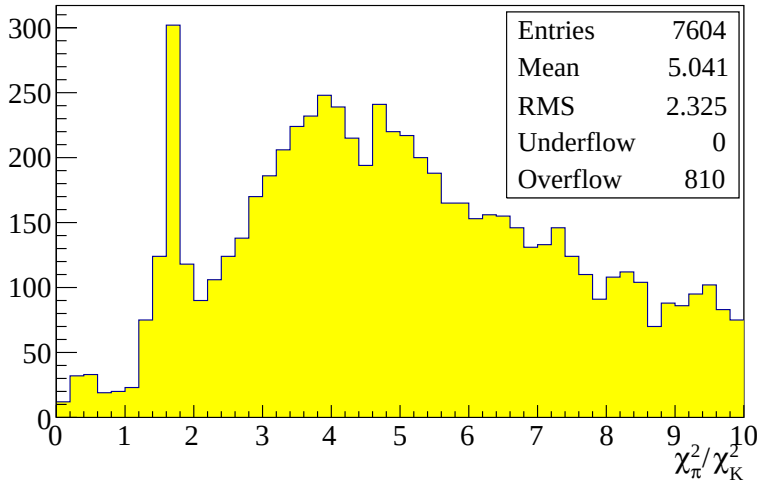

FIGURE 7.29: Histogram displaying the χ^2_π/χ^2_K for tracks where $LH(K)$ is greater than 1.2 times the $LH(\pi)$, the selected tracks are in the momentum range of 20-30 GeV/c

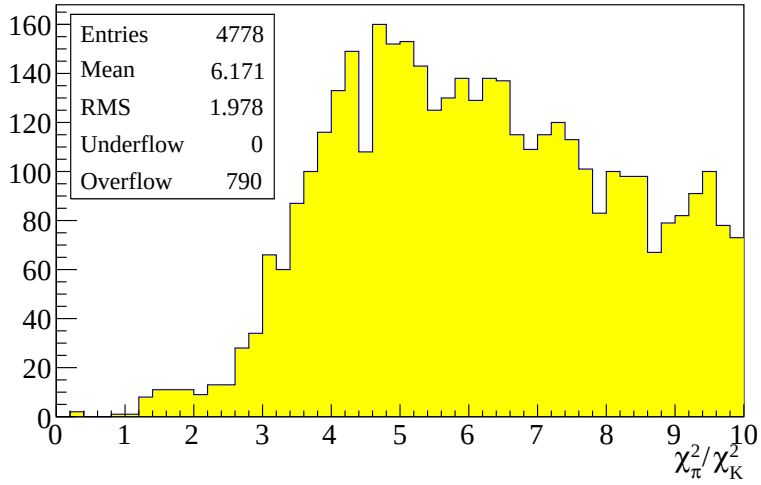

FIGURE 7.30: Histogram displaying the χ^2_π/χ^2_K for tracks where $LH(K)$ is greater than 2 times the $LH(\pi)$, the selected tracks are in the momentum range of 20-30 GeV/c

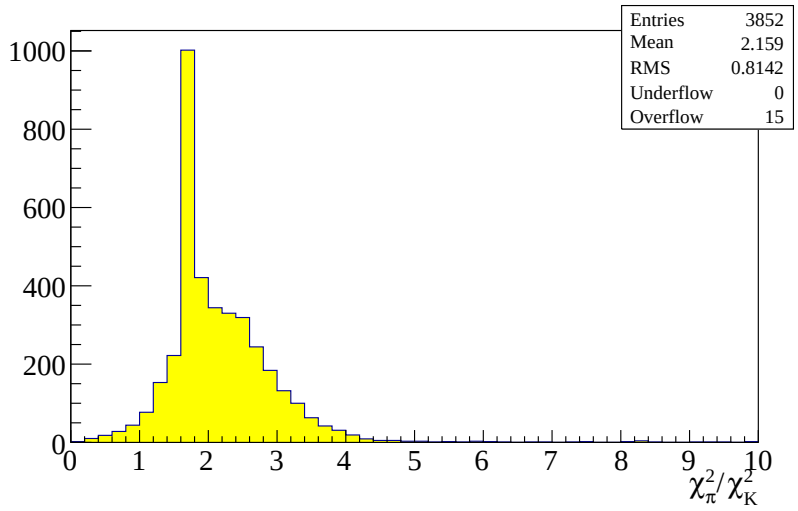

FIGURE 7.31: Histogram displaying the χ^2_π/χ^2_K for tracks where $LH(K)$ is greater than 1.2 times the $LH(\pi)$, the selected tracks are in the momentum range of 30-40 GeV/c

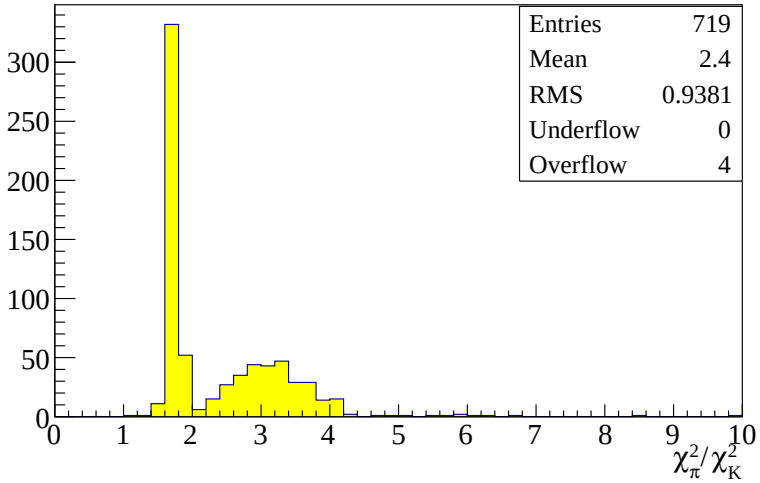

FIGURE 7.32: Histogram displaying the χ^2_π/χ^2_K for tracks where $LH(K)$ is greater than 2 times the $LH(\pi)$, the selected tracks are in the momentum range of 30-40 GeV/c

For tracks which are kaon like, a structure can be observed in the histograms displaying the χ^2 ratio. This feature is mainly related to the LH values of the proton. The structure appears only if the track momentum is larger than the proton threshold. Near the proton threshold if the kaon LH value is sufficiently large the peak is not visible. If a cut is applied that the LH value of the proton to be smaller than that of the pion, this peak disappears from all the plots.
The two methods (χ^2 and the likelihood) for particle identification implemented in the RICHONE code are computed independently. However, their

performance should not be independent. In terms of the particle identification the outcome of these two methods must show correlation and consistency. Before the alignment and tuning exercise it was assumed that the likelihood method is preferring the kaon hypothesis systematically which turn out not to be the case. These exercises show the expected consistencies.

7.5 Characterisation of the COMPASS RICH

The efficiency and the contamination are the intrinsic figure of merit of any PID detector. Therefore, to obtain a complete figure of performance of the RICH, we need to identify tracks which are known. The performance of the RICH in terms of PID is hence tested by checking the capability of the RICH to identify these well-known particles correctly. In our case, we have only one particle identification detector for identification of the charged hadrons, therefore we rely on the track reconstructed vector mesons, scalar mesons, strange baryons etc and their very well known decay channels. Pure kinematic calculations allow us to select within our tracking precision the desired tracks. The idea of computing the rich efficiency and purity of the sample is apparently straightforward. Efficiency can be defined as the number of particles correctly identified. As an example: the ratio of number pions identified as pions from a well-defined sample of pions over the total number of sample, is the pion identification efficiency of the RICH. A false identification will incorporate either the misidentification probability, which is how many times the a particle has been wrongly identified, or a contamination which is the probability to identify a different type of particle as the one of our interest. For the COMPASS RICH, the selection of pure tracks and the extraction of the efficiency is done by using the already existing software framework of COMPASS for extracting the RICH efficiencies. At the beginning of 2016 it was reported that the pion efficiency is substantially lower and the pion to kaon contamination is higher at higher momentum.

$$\epsilon(j \to i) = \frac{N(j \to i)}{N(j)} \tag{7.15}$$

Where $N(j)$ is the of total number of particles of type j is taken as the sample. $N(j \to i)$ is the number where particle j has been identified as i. The RICH characterisation is the determination of the identification (ϵ ($j \to j$)) and the misidentification probabilities of the RICH. This probabilities are written in a matrix form. The matrix is called the 'RICH matrix'.

$$M_{RICH} = \begin{pmatrix} \epsilon(\pi \to \pi) & \epsilon(\pi \to K) & \epsilon(\pi \to p) & \epsilon(\pi \to X) \\ \epsilon(K \to \pi) & \epsilon(K \to K) & \epsilon(K \to p) & \epsilon(K \to X) \\ \epsilon(p \to \pi) & \epsilon(p \to K) & \epsilon(p \to p) & \epsilon(p \to X) \end{pmatrix} \tag{7.16}$$

Where X is the denoted to describe the particles where the RICH has not identified the particle either as a pion or a kaon or a proton).

The inverse of the matrix will allow us to estimate the true number of hadrons from the identified hadrons.

$$\vec{T_h} = M^{-1}_{RICH}.\vec{I_h} \tag{7.17}$$

The RICH matrix is determined by selecting particles of well-know decay channels, purely based on kinematics. In the next section the selection of the particles is described.

7.5.1 Track Selections

The selection of the tracks is done based on the COMPASS software package PHAST. K^0, ϕ mesons and Λ baryons have very specific decay channels. In the following table I summarise the branching ratios of the decay channels of the hadrons reconstructed by kinematics. The tracks have been selected

TABLE 7.1: Decay Channels and Branching ratios of selected tracks

Hadrons	Decays	
	Channel	BR
K_S	$\pi^+\pi^-$	$(69.20 \pm 0.05)\%$
ϕ	K^+K^-	$(48.9 \pm 0.5)\%$
	K_SK_L	$(34.2 \pm 0.5)\%$
	$\varrho\pi + \pi^+\pi^-\pi^0$	$(15.32 \pm 0.32)\%$
$\Lambda(\bar{\Lambda})$	$p\pi^-(\bar{p}\pi^+)$	(63.9 ± 0.5) %

TABLE 7.2: Decay channels and branching ratios of the tracks reconstructed from kinematics

using the PHAST software. It needs user's input to select particular tracks. The following cuts are applied to all the samples:

- Bad Spills are excluded
- Best primary vertex is selected with incoming and scattered muon.
- Primary vertex is inside the target.
- Extrapolated track of the incoming muon should cross the target.
- $0.1 \leq y \leq 0.9$.

The K^0, Λ and ϕ particles have been selected by applying different cuts. The weak force governs the decay of the K^0, Λ particles. This gives a sufficiently long lifetime and hence the decay length is long enough. This allows us to search for secondary vertices. The ϕ meson decays via strong force. Which is why the decay length is extremely short and we can not separate the secondary vertex from the primary one.

Selection of K^0 and Λ particles

The cuts applied for selection of these two particles can be grouped into three parts.

1. Selection of good secondary vertex
2. Selection of good hadron tracks
3. Additional kinematic cuts.

The selection of good secondary vertex is assured by the following steps.

- Loop over all events
- There exists a primary vertex, which contains the beam μ particle and scattered μ' particle.
- Exactly two oppositely charged tracks are coming out of a vertex, which is not a primary vertex.
- These two tracks are not connected to any other primary vertex.
- The primary and the secondary vertex is separated by more than 2σ.

The following cuts assure that the two oppositely charged tracks are good hadrons.

- Both particles have not crossed more than 10 radiation length. The muon will travel much longer path and hence can be filtered out from the pions.
- Last measured position of the tracks (Z_{last}) is behind the first stage spectrometer magnet SM1.
- Transverse momentum of the daughter particles are larger than 23 MeV/c with respect to the mother particle. This cut filters the electrons.
- The decaying particles are connected to the primary vertex ($\theta \leq 0.01$), where θ is the angle between the resultant vector of the decaying momentum vectors and the distance vector of the primary vertex to decay vertex.

Additional kinematic cuts are applied, which cuts out

- Hadrons with momentum $p_h < 1\ GeV/c$.
- mass difference between K^0 and Λ the invariant mass of the two decay hadrons assuming the correct masses smaller than 150 MeV/c^2

In the figure 7.33 the Armenteros plot shows the arc of the K^0 and Λ particles. The asymmetry in the longitudinal momentum of the two daughter particles in the Lab frame are plotted against the transverse momentum of a particle. The red dashed line indicates the cut applied on the transverse momentum to filter out the low p_T electrons. The asymmetry α is defined as :

$$\alpha = \frac{p_{L1} - p_{L2}}{p_{L1} + p_{L2}} \tag{7.18}$$

For the particles which decay into particles of same masses will be symmetric around zero (a detailed derivation is described in appendix B). The decaying particles will acquire the maximum p_T, if they are decayed perpendicular to the boost direction of the parent particle in the centre of mass frame. Therefore, in the lab frame the longitudinal momentum of these two particles will be the same, and hence $\alpha = 0$. For K^0s decaying into π^+–π^- pairs will result in the symmetric arc. For the Λ particles, they will result in smaller arcs, left and right half of the centre.

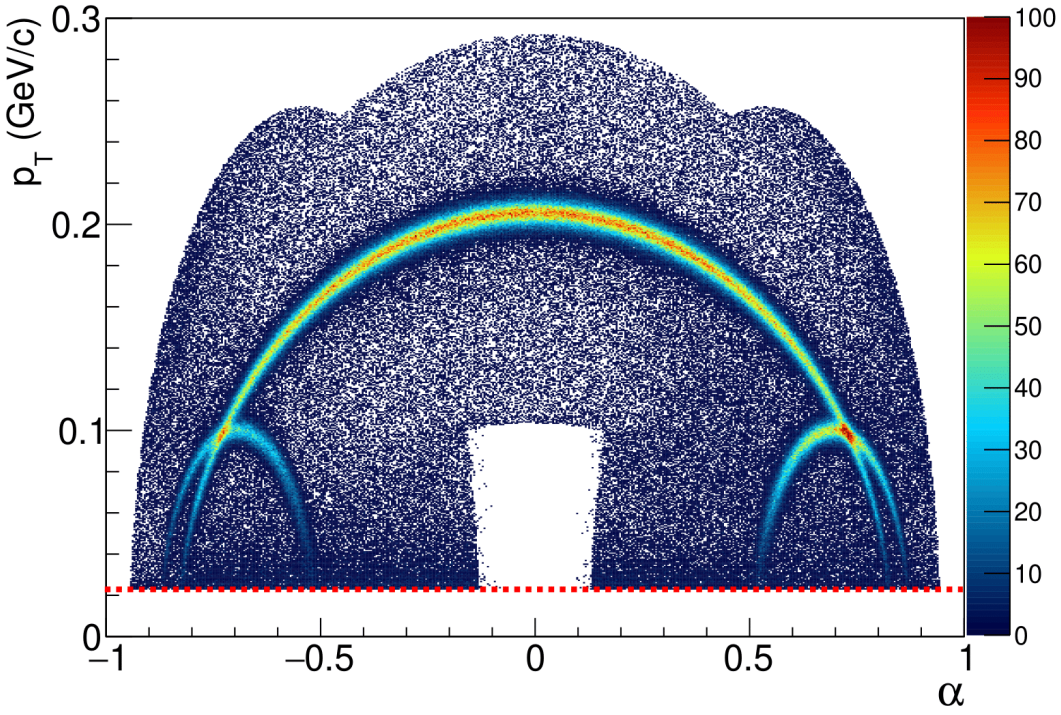

FIGURE 7.33: The Armenteros plot for K^0 and Λ; the red dashed line shows the applied cut to filter the low p_T electrons

Selection of ϕ mesons

The selection of the phi mesons is different than the K^0 and Λ particles. The ϕ particles decay via strong interaction, and hence their decay length is so small that the secondary vertex can not be resolved from the primary vertex. Therefore to search for ϕ meson decay product we look for three charged

tracks outgoing from the primary vertex. The sets of cuts can be grouped into three groups.

1. Selection of possible events with ϕ candidates
   - At least three outgoing particles including the scattered muon are associated to the primary vertices.
   - Looped over all outgoing particles
   - Other than the scattered muon, the tracks are oppositely charged and not a muon.
2. Selection of good hadron tracks as ϕ decay products
   - Last measured position behind SM1
   - Transverse momentum with respect to the mother particle larger than 23 MeV to suppress electrons
3. Additional kinematic cuts
   - Hadron momentum is between $9 - 55$ GeV/c
   - Mass difference between mass of the ϕ particles and the invariant mass of the two hadrons with an assumption that they have the kaon mass should be smaller than 120 GeV/c^2

For the selected samples, the RICH likelihoods of the two decay particles are stored for further analysis. For each track an array of likelihood values are stored for six hypotheses $[e, \mu, \pi, K, P, Bkg]$.

7.5.2 PID performance based on likelihood

To check the PID performance of the RICH set of selected tracks are used. The identification of these tracks are done based on RICH likelihood cuts. The exercise has been performed selecting good runs from 4 COMPASS data taking periods. The idea behind in selecting kinematically reconstructed tracks is to have pion, kaon and proton samples as clean as possible. The selection of the ϕ meson candidate however brings large combinatorial background. As mentioned already, the likelihoods values are used to check among the finite numbers of mass hypotheses. Using the likelihood values, the particle identification is done by comparing these values with one another. In the simplest case, the highest one determines the particle type. For proton identification between kaon threshold and proton threshold different approach is adopted. The RICH performance has been studied in term of identification and miss-identification probability.The probabilities have been computed at different momentum and angular bins. In this analysis I have not shown the proton identification or misidentification. For each momentum bin, the elements of the efficiency matrix M_{RICH} are determined separately for positive and negative particles. The elements of this matrix contain the probability for a particle i to be identified as a particle of type j, for example a pion that

is correctly identified as pion or wrongly as a kaon. The different elements of the matrix are determined by $\epsilon\ (i \rightarrow j) = N(i \rightarrow j)/N(i)$ where $N(i)$ is the total number of particles i and$N(i \rightarrow j)$ is the number of particles i, which are identified as particle j. These numbers are evaluated using samples of the selected decays. We take an example of extracting the elements for the π^+. For the other particles the basic methods are the same. In the case of positive pions, the events from the K^0 sample are used where the negative hadron, or the spectator, is identified as a pion using the likelihood cuts in table 7.3. Therefore if the decaying particle was a K^0, the second particle has to be a pion too. Using the RICH, the particle type is determined for the second particle, which results in the number $N(\pi^+ \rightarrow j)$. An equivalent procedure is used for positive kaons and protons using the ϕ and Λ samples. In order to obtain these numbers for the negative particles, the same samples are used but this time performing the identification of the positive particle in the first place. The numbers $N(i \rightarrow j)$ are extracted using a fit, which is described here for the K^0 sample, where the negative pion is already identified. The events are put into five different groups, depending on the particle type determined by the RICH:
1. All events (RICH not used for second particle)
2. Events where π^+ is identified as π^+
3. Events where π^+ is identified as K^+
4. Events where π^+ is identified as p
5. Events where π^+ is not identified

for each of these groups and the number of events in the peak and the background are determined by a simultaneous fit of all five spectra. For K^0 spectrum the signal of these spectra is described using two Gaussian distributions with the same mean for the signal, where the idea behind the two Gaussian is to account different resolution at two stages. The signal is termed as f_{Sig} in equation 7.19, and a polynomial to describe the background, f_{Back}. This polynomial depends on the type of the decays. Their expressions are given in table 7.4. The fitted function for each of the groups is given by:

$$f(x) = N_{Sig} f_{Sig} + N_{Back} f_{Back} \tag{7.19}$$

where N_{Sig} is the amount of K^0 and N_{BG} the amount of background events. Here, the same width, σ_1 and σ_2, of the two Gaussian distributions was used for all five spectra.

	π	K
mom	$p > p_{\pi,thr}$	$p > p_{K,thr}$
LH(i)/LH(π)	-	1.08
LH(i)/LH(K)	1.0	-
LH(i)/LH(P)	1.0	1.0
LH(i)/LH(Bkg)	1.0	1.24

TABLE 7.3: Likelihood ratios applied to select the spectator hadron, table used in [143]

The terms $p_{\pi,thr}$ and $p_{K,thr}$ correspond to pion threshold momentum and kaon threshold momentum respectively. The ratio δ of the amount of events in both Gaussian distribution is the same. The background is same for all the other spectra except where a pion has been identified as a proton, it is slightly different.
An additional constraint has been added to the fit, by imposing that the total number of K^0 should be the sum events of the individual spectrum.

Sample	Signal	Background
K^0	δ G(μ,σ_1) + (1 -δ) G(μ,σ_2)	$a + bx + cx^2 + dx^3$
ϕ	BW(μ,σ_2)$\otimes$G(μ,σ_2)	$(x-t)^m exp(-a(x-t))$ where $t = 2.m_K$

TABLE 7.4: Description of signal and background term for K^0 and ϕ meson fitting

Therefore, the additional constraint is:

$$N(K^0) = N(\pi \to \pi) + N(\pi \to K) + N(\pi \to P) + N(\pi \to NoID) \quad (7.20)$$

This results in 16 free parameters of the fit.

In figure 7.34 we have shown the invariant mass histogram of the selected Λ and $\bar{\Lambda}$ baryons with and without the RICH information. The Λ particles dominantly decay into $P\pi^-$ pairs and $\bar{\Lambda}$ particles decay into $\bar{P}\pi^+$ pairs. Based on the Armenteros plot the kinematic selection is made such that for Λ like candidates the positive track has a momentum greater than the proton threshold and the negative track follows the same criteria for the $\bar{\Lambda}$. The invariant mass of such candidates are shown in the histogram filled in yellow of figure 7.34, where we identify the signal over a significant background. If in addition we select candidates where the track of our interest has been identified as a proton like track by the RICH we plot the invariant mass of the candidates; this can be seen in the red histogram of the same figure. We see that the background has been significantly suppressed by the RICH PID.

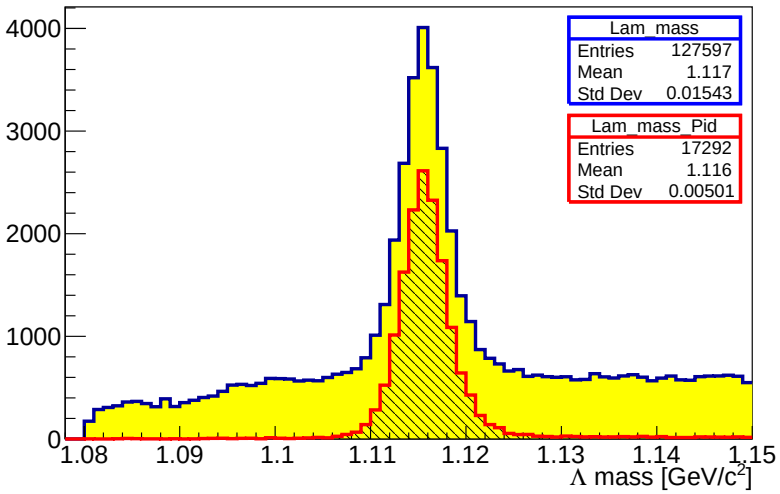

FIGURE 7.34: Mass spectrum of the Λ particles without and with RICH information. The Histogram area filled in yellow is the invariant mass distribution of Λ like particles without RICH information, the histogram with RICH identified proton has lower level of background.

Similar exercise has be done for the invariant mass spectrum of the K^0 mesons where the RICH likelihood information has been used to reject the kaon contamination. Figure 7.35 shows the rejection of kaon like tracks reduces the background of the K^0 invariant mass distribution.

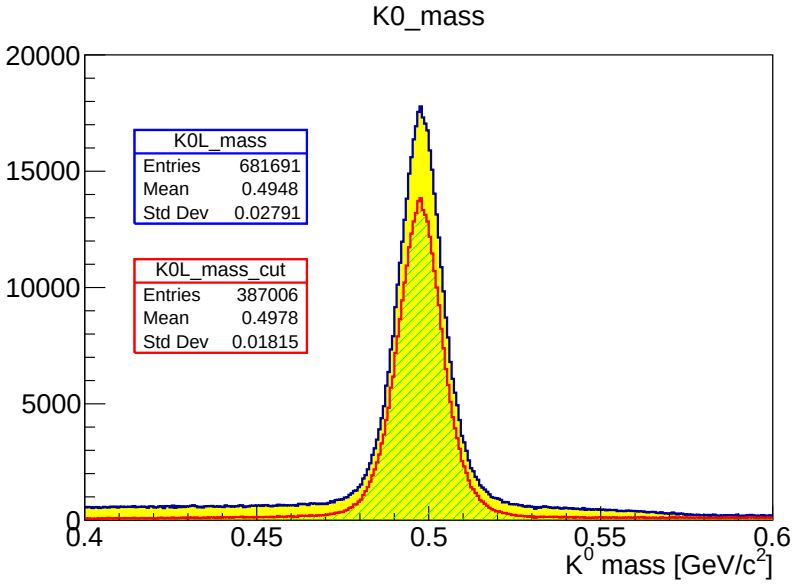

FIGURE 7.35: Mass spectrum of the K^0 mesons with and without RICH information

The ϕ mesons have large combinatorial background. For example, during the kinematic selection of the decaying mesons, pion tracks can be wrongly assigned a kaon mass and decay products of the ϱ mesons may come in a

combination of with the kaons. Figure 7.36 shows the ϕ meson peak over a large combinatorial background.

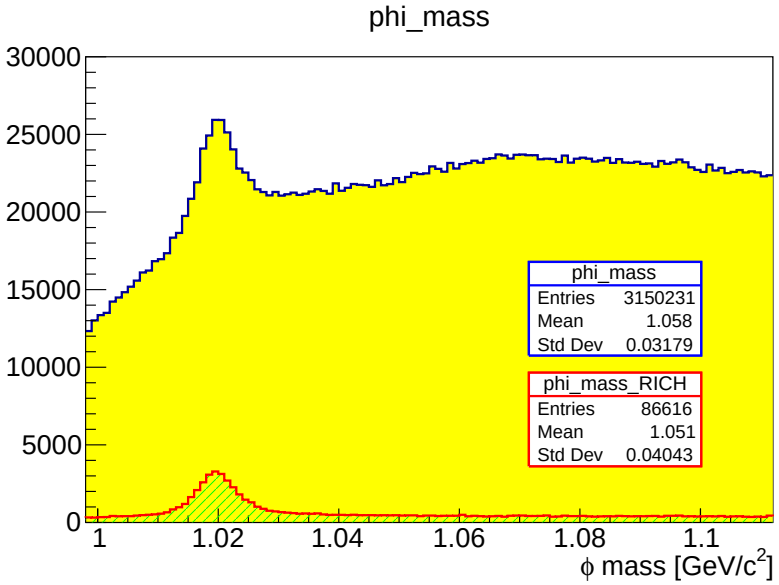

FIGURE 7.36: Mass spectrum of the ϕ mesons with and without RICH information. One of the arm identified as a kaon by the RICH suppresses the large combinatorial background

Using tracks with ratio of the kaon likelihood over the pion likelihood larger than 1.2, we have obtained a clean Armenteros plot for the phi mesons, which can be seen in figure 7.37. Their physical parameters are in good consistency with the kinematics. This observation enhances the fact that the pion rejection appears to be very effective and the kaon efficiency is good.
A detailed derivation of Armenteros plot is performed in appendix B.

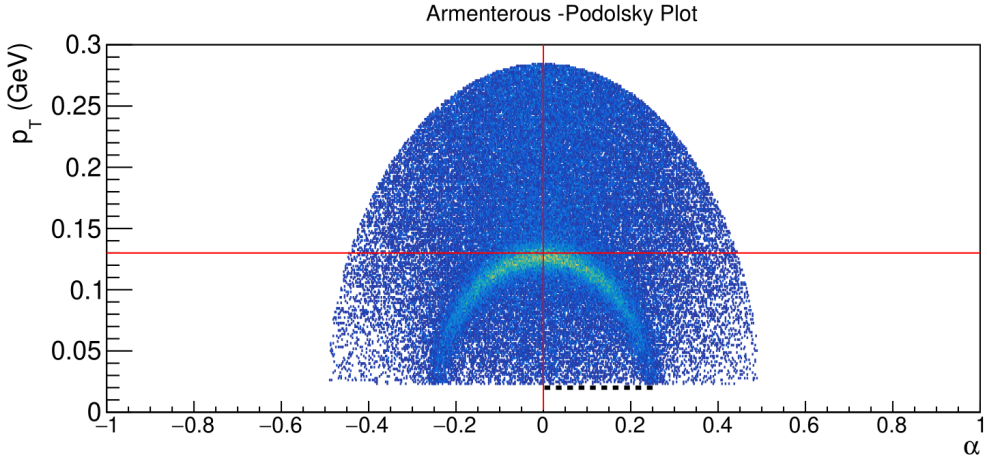

FIGURE 7.37: Armenteros plot obtained from COMPASS data, applying RICH identification

7.5.3 Efficiency and purity

The kaons produced in the muon proton reaction have much lower statistics compared to the pions. Therefore, reduction of the contamination of the pions in the kaon samples is critical to study the physics channels where kaon like particles are to be detected in the final state. At the beginning of 2016, a lowering in the pion efficiency and increment of the pion to kaon contamination at higher momentum was reported in section 5.7 of [144].
We have computed probabilities to identify a species i as i and also the probability to misidentify i as j and their dependence as a function of the particle momentum. We have used the samples from the decay product of the K^0 and ϕ mesons. For this computation we have taken hadrons entering the RICH with an angle larger than 10 $mrad$, to avoid the beam pipe effect, and smaller than 40 $mrad$, to stay within the forward region, which has large statistics. The pion efficiency, namely the probability to identify a pion as a pion and the pion to kaon misidentification probability are shown in the top two panels from the left of figure 7.38 for positive pions and in figure 7.39 for negative pions. The third column corresponds to cases where no identification was possible because either electron or background hypotheses provided larger LH values. The bottom panels of the two figures present the corresponding probabilities for the kaons. The left most plot is for a kaon identified as a pion; the middle plot is for the cases where a kaon is correctly identified as a kaon; and the third plot corresponds to cases where no identification was possible. The probability values are determined from the simultaneous fit of the mass distribution of the decaying hadrons using the fitting functions described in equation 7.19.The error bars represent the statistical uncertainty only and have been obtained by propagating the errors on the fitted parameters. As the nominator and the denominator of the efficiency formula are correlated, the full covariance matrix of the fit has been used. In the figures 7.38, 7.39 we see that the pion identification efficiency is larger than 95% over a wide momentum range and above 98% up to 30 GeV/c. The pion misidentification as kaon has a probability below the 1% level. This will allow selecting highly pure kaon samples. The kaon identification near the kaon threshold momentum is critical, it can be identified as a pion for 10% of the cases, nevertheless near its threshold a kaon is also likely to be wrongly identified as a proton. Using the RICH information for the identification of protons below threshold needs further studies and hence it is not discussed in this thesis. The kaon identification efficiency is also very high up to 35 GeV/c and around 95% up to 30 GeV/c. An independent analysis done by using the ring level information shown in figure 7.10 tells us that the RICH is capable of 5σ separation of the pion and kaon hypothesis up to 35 GeV/c.
Regarding the extraction of the kaon efficiency, the ϕ samples are not as clean as the K^0 since they include a large combinatorial background mostly coming from pion tracks. The pion contribution can be suppressed by selecting one arm to be a RICH selected kaon. This analysis has adopted the standard approach of COMPASS to select the ϕ sample. The purity of the ϕ sample

can be determined from the invariant mass spectrum of the ϕ mesons, computing the ratio between signal and signal plus background.
Furthermore, for the pion samples the study has been extended to different polar angles as presented in figure 7.40. The pion detection efficiency and pion misidentification as a kaon are consistent and show the expected angular dependence. Globally the pion identification efficiency is above 95% and the misidentification as a kaon is below the 2% level, which guarantees an efficient suppression of pions in the kaon samples.
In conclusion, the tuning and alignment of the RICH allowed to obtain a significant improvement in the RICH performance in terms of LH values.
An alternative PID method, namely the ring χ^2 analysis has been used for cross-checking the RICH LH method and it has demonstrated to be fully consistent with it.
The improvement in the pion identification efficiency and the significant reduction in pion to kaon misidentification probability are not coupled to a change in the overall kaon to pion misidentification probability.
The matrices for efficiencies and misidentification probabilities, which are an essential element for the COMPASS physics analysis, have been computed using the LH values provided by the RICHONE software.
COMPASS RICH-1 provides 5σ π-K separation and 98% pion identification efficiency up to 35 GeV/c.
The overall hadron PID performance of COMPASS RICH-1 is outstanding.

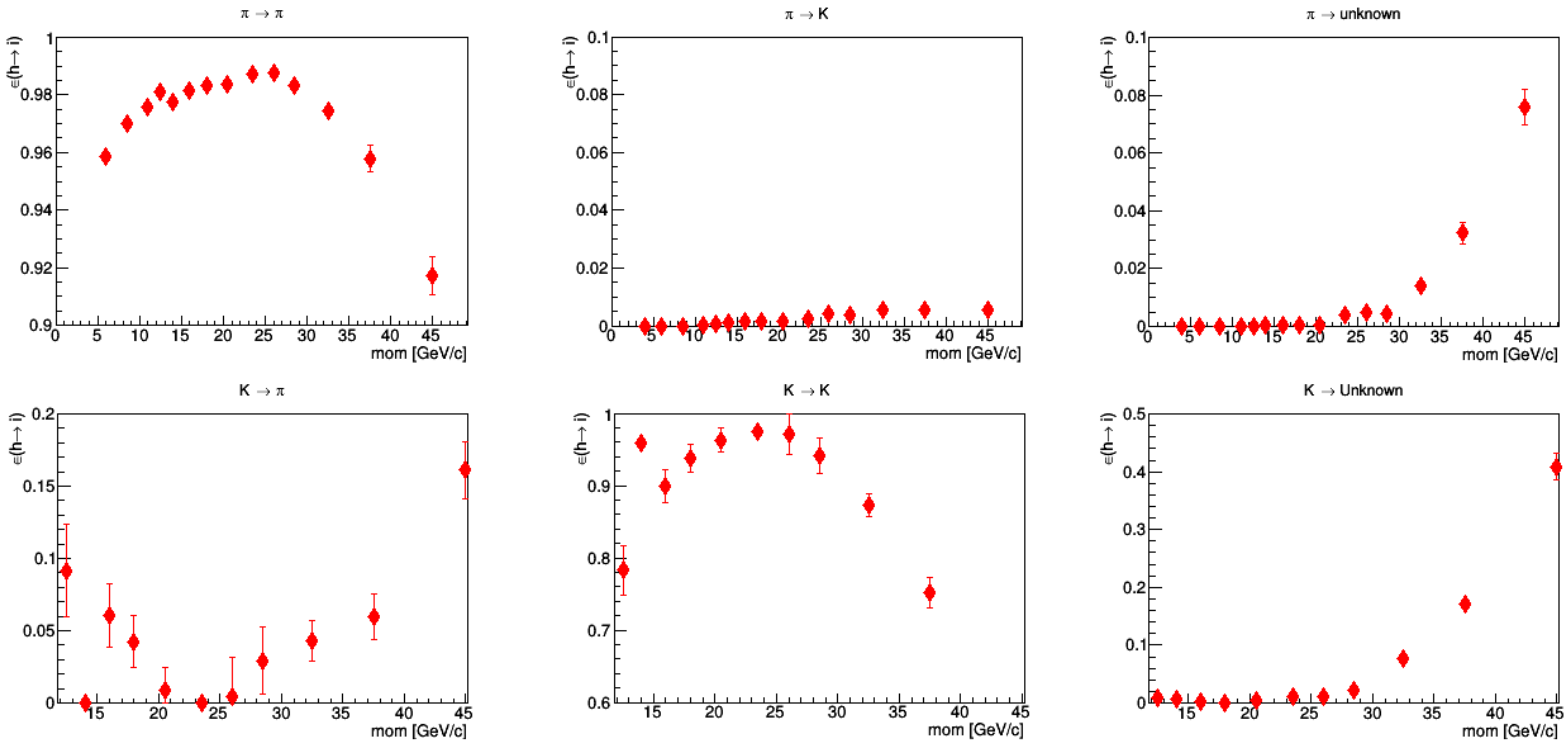

FIGURE 7.38: Efficiency of π^+ and K^+ as a function of hadron momentum, where the spectator negative hadron detected by the RICH LH cut set in table 7.3. The top panels correspond to identification and misidentification of pions and the bottom panels correspond to the identification and misidentification of kaons.

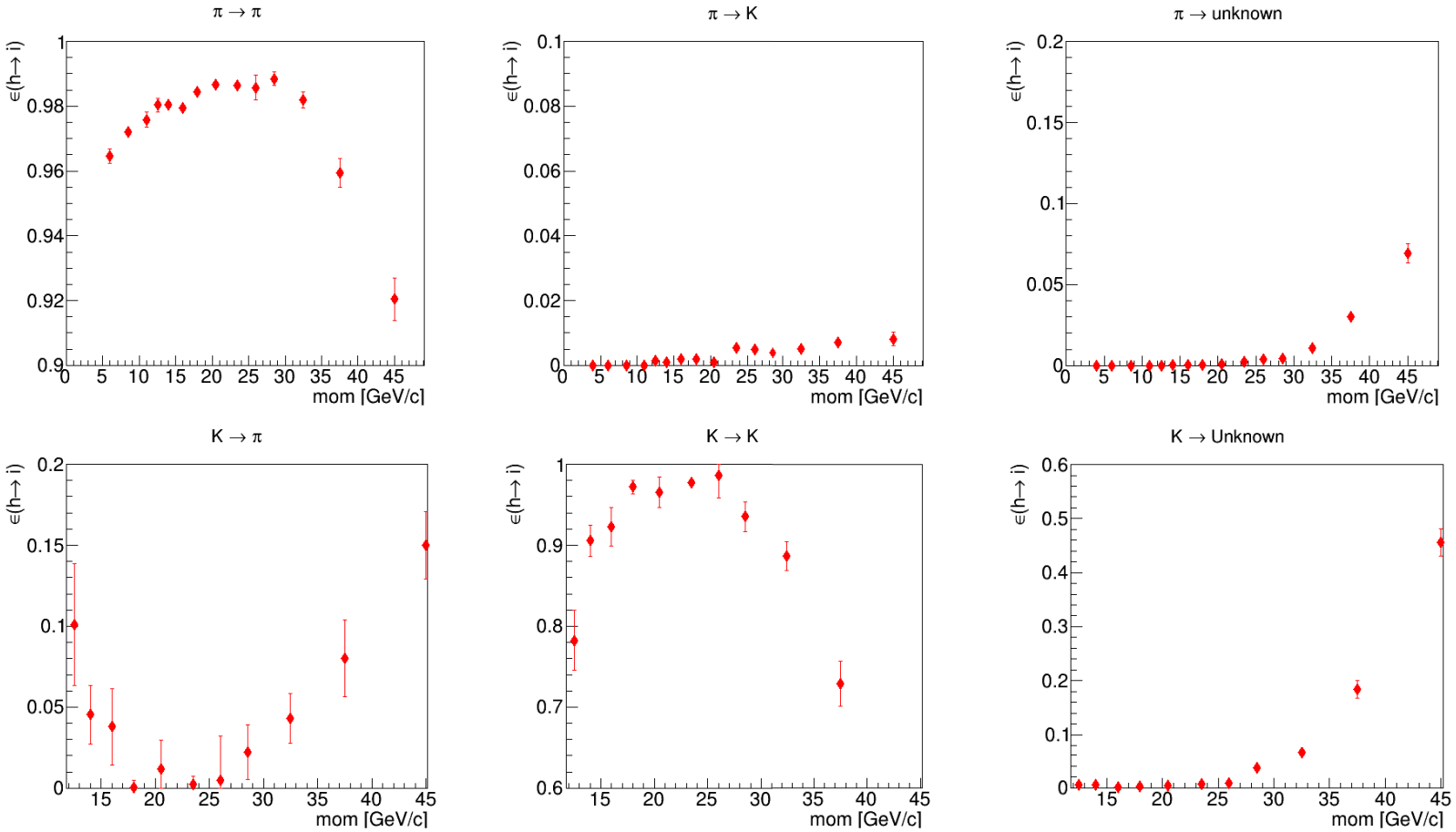

FIGURE 7.39: Efficiency of π^- and K^- as a function of hadron momentum, where the spectator positive hadron detected by the RICH LH cut set in table 7.3. The top panels correspond to identification and misidentification of pions and the bottom panels correspond to the identification and misidentification of kaons.

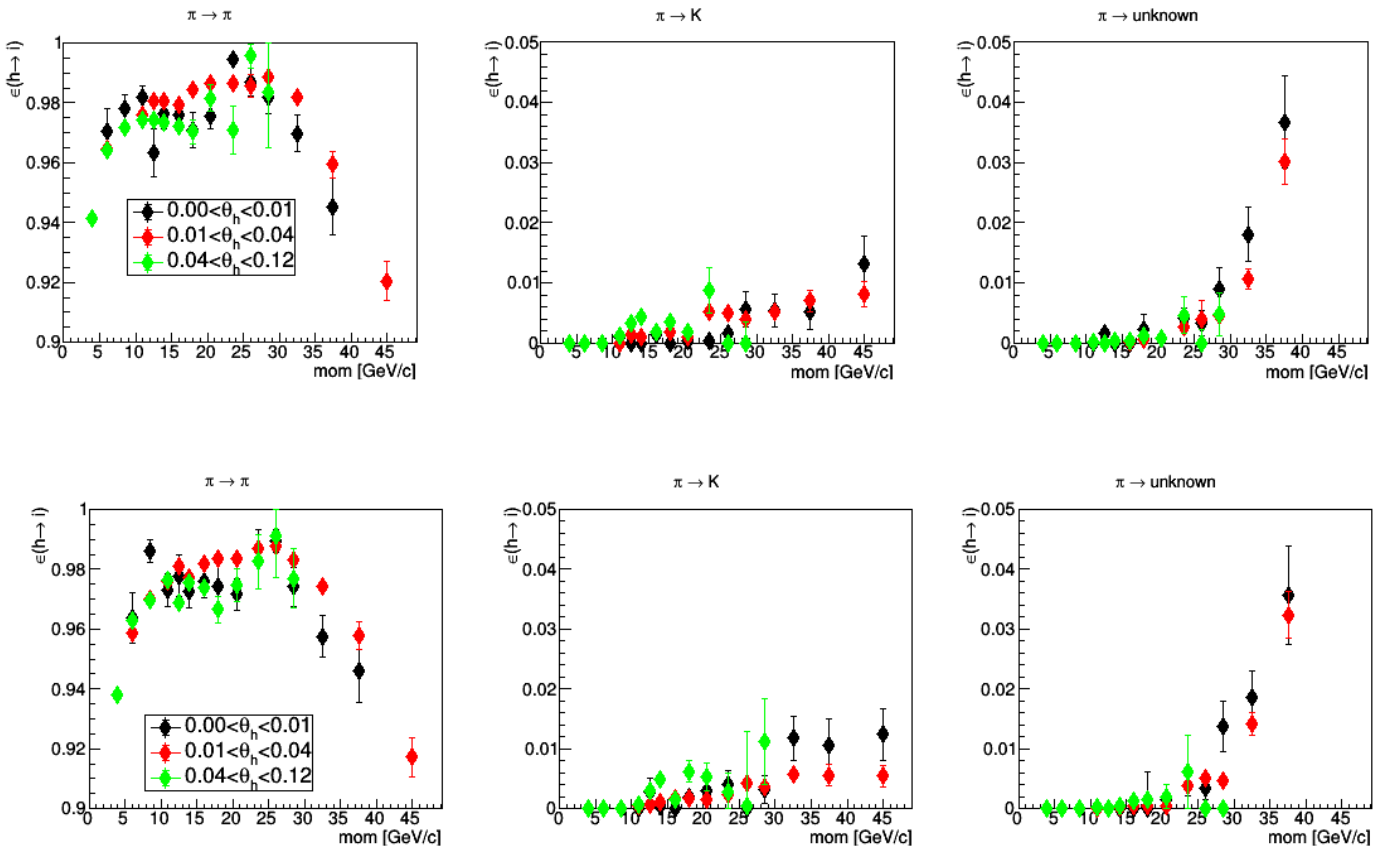

FIGURE 7.40: Efficiency of π^+ (top panel) and π^- (bottom panel) as a function of hadron momentum and at different entrance angle in the RICH, where the spectator hadron detected by the RICH LH cut set in table 7.3

Chapter 8

Conclusion

8.1 Hybrid detectors characterisation

A complete characterisation of the THGEMs has been done. To collect the data for this characterisation, I have set up a trigger, checked the data quality and have analysed the data. The THGEM-MM based hybrids have been characterised for the first time. Three of the four hybrids are working at an effective gain $\sim 14000 \pm 250$. One of them is working at an effective gain $\sim 12500 \pm 250$. The effective gain is stabilised at a 2% level, thanks to the automatic voltage correction, without which the fluctuation could have been order of magnitude more.
The photon angle resolution is according to expectations. The global resolution is 1.83 ± 0.007 *mrad*. A nice consistency is observed within individual cathodes.
In terms of the number of photons. The top two cathodes have shown full consistency among themselves. For cathode 2:
Signal part of the function = 12.0 +/- 0.7
Background part of the function= 1.6 +/- 0.6
For cathode 4:
Signal part of the function = 10.1 +/- 0.8
Background part of the function= 0.2 +/- 0.6
We do not expect the number of photons to be exactly the same for the cathode 2 and 4, since we know that the relative quantum efficiency of the coated CsI is slightly different and also the single photo-electron detection efficiency.
An approximate time resolution of the hybrids have been extracted by largely modifying the reconstruction code. It does not take into account the uncertainty in the trigger timing. However, the time resolution 8.8 ± 0.1 *ns* is promising.

8.2 RICH tuning and particle identification

A large discrepancy in the estimated (n-1) histogram has been observed during 2016 data taking. The global refractive index in the forward region appeared with double peak. Also cathode wise inconsistencies were observed. To address the problem, a large campaign of survey was done. The analysis of survey data coupled with revisiting the mechanical drawing leads us

to modification in the RICH geometry. Further residual inconsistencies had been addressed by aligning the global mirror position based on real data. A movement of the mirror centre largely resolved the top bottom asymmetry in the refractive index.
Further tuning was done and contamination of the electron from the pion sample to extract the refractive index has been achieved by selecting an optimal momentum region. Cathode wise fluctuation of the (n-1) has been constrained within 1% level. The current tuning has achieved $\sigma_{(n-1)} \sim 100 ppm$. After the mirror tuning and correctly estimating the refractive index, the central value of the ring residual distribution has improved. The distribution has become more centred toward zero, -0.070 ± 0.003 *mrad*. The sigma is improved to 0.32 ± 0.005 *mrad*.
The effect of the alignment and refractive index on the dependence of estimated $mass^2$ of the particle versus the momentum has been studied. At large momentum a clear improvement has been observed.
A consistency check has been done within different PID methods, namely likelihood and the χ^2 fitting. A total consistency is seen. In terms of particle identification the performance is enhanced. The misidentification of a pion to a kaon has largely decreased. There is no sign of favoring the pion hypothesis due to a bias, solving the reported problem at the beginning of 2016. After the RICH tuning independent work by different groups has shown an agreement with the claim of the thesis in terms of PID.

The novel MPGD bases hybrid detectors of single photons introduced by COMPASS RICH group have shown efficient performance and good stability. This technology is validated and has good perspective of future applications. The overall COMPASS RICH-1 PID performance is excellent and has improved over years, this state of the art detector provides unique and outstanding tools for physics investigation related to hadron structure and spectroscopy.

8.3 Papers signed by the author during the PhD period

The publication list here presented is signed by the author, it also includes publications which are not listed in ArTs.
J. Agarwala et al: *The high voltage system with pressure and temperature corrections for the novel MPGD-based photon detectors of COMPASS RICH-1*. NUCL. INSTR. METH **A 942** (2019) 162378
2. R. Akhunzyanov et al: *Transverse extension of partons in the proton probed in the sea-quark range by measuring the DVCS cross section*. Phys. Lett. **B 793** (2019) 188.
3. M. Baruzzo et al: *Direct measurements of the properties of Thick-GEM reflective photocathodes*.Submitted to Nucl. Instr. Meth A https://arxiv.org/abs/1910.05257
4. J. Agarwala et al: *Study of MicroPattern Gaseous detectors with novel nanodiamond based photocathodes for single photon detection in EIC RICH*. Submitted

to Nucl. Instr. Meth. A DOI:10.1016/j.nima.2019.03.022 **as the corresponding author**

5. M.G. Alexeev et al: *Measurement of PT-weighted Sivers asymmetries in leptoproduction of hadrons*. Nucl. Phys. **B 940** (2019) 34.

6. J. Agarwala et al: *The MPGD-based photon detectors for the upgrade of COMPASS RICH-1 and beyond*. NUCL. INSTR. METH **A 936** (2019) 416

7. J. Agarwala et al: *Optimized MPGD-based Photon Detectors for high momentum particle identification at the Electron-Ion Collider*. NUCL. INSTR. METH **A 936** (2019) 565

8. C. Adolph et al: *Azimuthal asymmetries of charged hadrons produced in high-energy muon scattering off longitudinally polarised deuterons*. Eur. Phys. J. **C 78** (2018) 952.

9. M. Aghasyan et al: *Light isovector resonances in* $\pi^- p \to \pi^- \pi^- \pi^+ p$ *at 190 GeV / c*. Phys. Rev. **D 98** (2018) 092003

10. J. Agarwala et al: *Novel MPGD-based photon detectors of COMPASS RICH-1*. NUCL. INSTR. METH **A 912** (2018) 158

11. R. Akhunzyanov et al: K^- *over* K^+ *multiplicity ratio for kaons produced in DIS with a large fraction of the virtual-photon energy*. Phys. Lett. **B 786** (2018) 390.

12. M. Aghasyan et al: *Search for muoproduction of X (3872) at COMPASS and indication of a new state X ~ (3872)*. Phys. Lett. **B 783** (2018) 334.

13. COMPASS Collaboration, C.Chatterjee : *The novel photon detectors based on MPGD technologies for the upgrade of COMPASS RICH-1*. IL NUOVO CIMENTO **41 C** (2018) 74 **as the corresponding author**

14. A. Jackura et al: *New analysis of* $\eta\pi$ *tensor resonances measured at the COMPASS experiment*. Phys. Lett. **B 779** (2018) 464

15. M. Aghasyan et al: *Longitudinal double-spin asymmetry A 1 p and spin-dependent structure function g 1 p of the proton at small values of x and Q 2*. Phys. Lett. **B 781** (2018) 464.

16. M. Aghasyan et al: *Transverse-momentum-dependent multiplicities of charged hadrons in muon-deuteron deep inelastic scattering*. Phys. Rev. **D 97** (2018) 032006.

17. R. Akhunzyanov et al: K^- *over* K^+ *multiplicity ratio for kaons produced in DIS with a large fraction of the virtual-photon energy*. Phys. Lett. **B 786** (2018) 390

18. J. Agarwala et al: *The Hybrid MPGD based detectors of single photons in COMPASS RICH-1*.
Submitted to: Nucl. Instr. Meth. A DOI:10.1016/j.nima.2017.11.011

19. M. Aghasyan et al: *First Measurement of Transverse-Spin-Dependent Azimuthal Asymmetries in the Drell-Yan Process*. Phys. Rev Lett. **119** (2017) 112002

20. C. Adolph et al: *First measurement of the Sivers asymmetry for gluons using SIDIS data*. Phys. Lett. **B 772** (2017) 854.

21. C. Adolph et al: *Sivers asymmetry extracted in SIDIS at the hard scales of the Drell-Yan process at COMPASS*. Phys. Lett. **B 770** (2017) 138.

22. C. Adolph et al: *Final COMPASS results on the deuteron spin-dependent structure function g 1 d and the Bjorken sum rule*.Phys. Lett. **B 769** (2017) 034

23. C. Adolph et al: *First measurement of the Sivers asymmetry for gluons from SIDIS data*. Phys. Lett. **B 772** (2017) 854
24. C. Adolph et al: *Multiplicities of charged kaons from deep-inelastic muon scattering off an isoscalar target*. Phys. Lett. **B 767** (2017) 133
25. C. Adolph et al: *Multiplicities of charged pions and unidentified charged hadrons from deep-inelastic scattering of muons off an isoscalar target*. Phys. Lett. **B 764** (2017) 001

Appendix A

Theoretical Interpretation of Cherenkov relation: Frank and Tamm relation

A.1 Classical Electromagnetic Description

In section 3.2 I have given a qualitative description of the Cherenkov equation and Frank and Tamm Relationship.In this appended part I will describe a bit more theoretical detail. This part is mostly based on Classical Electromagnetism by J.D. Jackson and Cherenkov Radiation and its applications by J.V. Jelley. I will simplify the derivation with the following assumptions:

1. The medium is continuum, which means the microscopic structures are not considered and dielectric constant or in other words refractive index is the only parameter of the radiating media.
2. In the first approximation, we have no dispersion in our medium.
3. No radiation reaction is changing the state of the medium.
4. The magnetic permeability of this medium is unity, and the conductivity is zero. Simply, our medium is isotropic dielectric.
5. The charged particle is of unit charge and moving with a constant speed and moving length within the medium which is infinitely large compared to the atomic scale.

The relationship between the electric field and the Polarisation can be as followed:

$$\vec{P_\omega} = \epsilon_0 \chi_e \vec{E_\omega} = (n^2 - 1)\vec{E_\omega} \tag{A.1}$$

where sub-scripted omega denotes the molecular level oscillation. χ_e, ϵ_0 are electric susceptibility and dielectric constant at vacuum respectively. Therefore the dynamics of the Polarisation can be written:

$$\frac{\partial^2 \vec{P}}{\partial t^2} + \sum_s \omega_s^2 . \vec{P_s} = \alpha \vec{E} \tag{A.2}$$

where the sum is over all atomic frequency level and alpha represents the atomic polarisibility per unit volume. The problem to find the electric field and the Polarisation field created by the passage of the charged particle can be done, by expanding all the field variables in Fourier series:

$$\vec{E} = \int_{-\infty}^{+\infty} \vec{E_\omega} e^{i\omega t} d\omega, \qquad \vec{P} = \int_{-\infty}^{+\infty} \vec{P_\omega} e^{i\omega t} d\omega \tag{A.3}$$

Similar to the relationship A.1 we can write $D_\omega = n^2 E_\omega$, where D is the dielectric field. From the knowledge of Maxwell's equation we can write for the medium equation in terms of scalar and vector potentials.

$$\vec{H_\omega} = curl \vec{A_\omega} \tag{A.4a}$$

$$\nabla^2 \vec{A_\omega} + \frac{\omega^2 n^2}{c^2} \vec{A_\omega} = -\frac{4\pi}{c} \vec{j_\omega} \tag{A.4b}$$

$$\nabla^2 \phi_\omega + \frac{\omega^2 n^2}{c^2} \phi_\omega = -\frac{4\pi}{n^2} \varrho \tag{A.4c}$$

$$\vec{E_\omega} = -\frac{1}{c} \frac{\partial \vec{A_\omega}}{\partial t} - grad \phi_\omega \tag{A.4d}$$

where we assume that the two potentials are interrelated by Lorenz gauge

$$div.\vec{A} + (\frac{n}{c})^2 \frac{\partial V}{\partial t} = 0$$

If the charged particle is moving in +z axis with a speed v, then corresponding current density can be written as:

$$j_z = ev\delta(x)\delta(y)\delta(z - vt),$$

the other two components are zero. Expanding j_z, we can write:

$$j_z(\omega) = e/(2\pi) e^{-i\omega z/v} . \delta(x)\delta(y)$$

The cylindrical form is:

$$j_z(\omega) = e/(4\pi^2 \rho) e^{-i\omega z/v} . \delta(\rho)$$

Putting the expression of current in equation A.4a, and assuming the z component of the vector potential is only nonzero. If we assume the expression of $A_z(\omega) = u(\rho) e^{-i\omega z/v}$, we can insert this expression of vector potential and

current in equation A.4b we get:

$$\begin{aligned}
&\frac{1}{\rho}\frac{\partial}{\partial\rho}\left(\rho\frac{\partial u(\rho)e^{-i\omega z/v}}{\partial\rho}\right)+\frac{1}{\rho^2}\frac{\partial^2 u(\rho)e^{-i\omega z/v}}{\partial\phi^2}+\frac{\partial^2 u(\rho)e^{-i\omega z/v}}{\partial z^2}\\
&+\frac{\omega^2 n^2}{c^2}u(\rho)e^{-i\omega z/v}=-\frac{4\pi}{c}\frac{e}{4\pi^2 c}\delta(\rho)e^{-i\omega z/v}=-\frac{e}{c\rho\pi}\delta(\rho)e^{-i\omega z/v};\\
&\Rightarrow\left[\frac{\partial^2 u(\rho)}{\partial\rho^2}+\frac{1}{\rho}\frac{\partial u(\rho)}{\partial\rho}-\frac{\omega^2 n^2}{v^2}+\frac{\omega^2 n^2}{c^2}\right]e^{-i\omega z/v}=-e^{-i\omega z/v}\frac{e}{c\rho\pi}\delta(\rho);\\
&\Rightarrow\left[\frac{\partial^2 u(\rho)}{\partial\rho^2}+\frac{1}{\rho}\frac{\partial u(\rho)}{\partial\rho}+s^2\right]=-\frac{e}{c\rho\pi}\delta(\rho).
\end{aligned}\tag{A.5}$$

where $s^2=\frac{\omega^2 n^2}{c^2}-\frac{\omega^2 n^2}{v^2}=\frac{\omega^2}{v2}\left(\beta^2 n^2-1\right)=-\lambda_p^2$. Now, the final expression of equation A.5 is a cylindrical Bessel function satisfied by $u(\rho)$ is the right-hand side is equal to zero, everywhere except $\rho=0$. This Pole can be tackled by assuming that the right hand side, let's say,

$$f=-\frac{e}{\pi c\rho_0}\qquad\forall\qquad\rho<\rho_0;\tag{A.6}$$

and

$$f=0\qquad\forall\qquad\rho>\rho_0$$

Therefore, we can construct a Bessel equation which is satisfied by the cylindrical function u, with the aforesaid boundary condition.

$$\left[\frac{\partial^2 u(\rho)}{\partial\rho^2}+\frac{1}{\rho}\frac{\partial u(\rho)}{\partial\rho}+s^2\right]=0\tag{A.7}$$

Thus, we can integrate the final expression of equation A.5 of a disc of radius ρ', and finally to go over limit $\rho\to 0$. Nevertheless, we can assume that our function is well behaved and for $\rho=0$. That means, if the function is not finite we allow $\rho=0$ to be a pole of order 1, i.e., we assume:

$$\lim_{\rho\to 0}\int_0^{2\pi}d\phi\int_0^{\rho}d\rho'\rho' u(\rho',\omega)=0\tag{A.8}$$

We can integrate the final expression of A.5. The second term will turn zero after the integration. The first term of the left hand side and the right hand side can finally be expressed as:

$$\lim_{\rho\to 0}\rho\frac{\partial u}{\partial\rho}=-\frac{e}{\pi c}\tag{A.9}$$

A Bessel type differential equation has two linearly independent solutions

which may be expressed in different forms. The Henkel functions are the linear combination of the linearly independent two solutions, describing the travelling wave. Then the solutions can be written finally as;

$$u^{(1)(2)}(\chi) = \zeta^{(1)(2)} H_0^{(1)(2)}(\chi)$$

Where $\chi = s\rho$. For very small argument approximation the asymptotic form for the solutions of Bessel functions can be written as:

$$\begin{aligned} \lim_{\chi\to 0} \chi \frac{\partial u^{(1)(2)}}{\partial \chi} &= \lim_{\chi\to 0} \chi \frac{\partial \zeta^{(1)(2)} H_0^{(1)(2)}(\chi)}{\partial \chi} \\ \lim_{\chi\to 0} \chi \zeta^{(1)(2)} \frac{\partial}{\partial \chi} \Big(1 \pm (\ln(\chi/2) + \gamma)\Big) &= \pm \frac{2}{\pi} \zeta^{(1)(2)}. \end{aligned} \tag{A.10}$$

Therefore, requiring the fact that the right hand side of equation A.10 has to be the same with the right hand side of equation A.9 the individual solutions can be written as:

$$\begin{aligned} u^1(\chi) &= i\frac{e}{2c} H_0^1(\chi) \\ u^2(\chi) &= -i\frac{e}{2c} H_0^2(\chi) \end{aligned} \tag{A.11}$$

Now, in order to have a physical radiation at large distance (compared to the atomic scale) large value of the argument is needed. The Henkel asymptotic for large arguments are described as:

$$\begin{aligned} H_0^1(i\lambda_P \rho) &= \sqrt{\frac{2}{\pi i \lambda_P \rho}} exp[i.(i\lambda_P \rho - \frac{\pi}{4})] \\ H_0^2(s\rho) &= \sqrt{\frac{2}{\pi s \rho}} exp[-i(s\rho - \frac{\pi}{4})] \end{aligned} \tag{A.12}$$

With the aid of equation A.12, A.11 and the functional form of $A_\omega$assumed to derive equation A.5, we get and expression of the vector potential for slow particles and relativistic particles respectively. For the slow particles the $s^2 < 0; \lambda_P > 0$, and hence for the condition $\lambda_P.\rho \gg 1$, we can express the vector potential as;

$$A_Z = \frac{e}{c} \int_0^{+\infty} \frac{exp[-\lambda_P.\rho + \omega(t - z/v)]}{\sqrt{(2\pi\lambda_P.\rho)}} \tag{A.13}$$

We can see, that for large values of ρ the exponential term rapidly falls and hence there is no observable radiation in remote parts from the trajectory. On the contrary, for the condition $\beta.n(\omega) > 1$, we can write the vector potential where $s^2 > 0$, and hence A.5 represents a cylindrical wave equation, at infinity. Specifying u as the outgoing wave, we can have

$$\vec{A_Z} = -\frac{e}{c}\hat{z} \int_0^{+\infty} \frac{exp[i\omega(t - z/v) - i(s\rho - \frac{\pi}{4})]}{\sqrt{(2\pi.s.\rho)}} \tag{A.14}$$

Now, we can calculate the physical field. It is clear that the electric field vector of the wave lies in meridian plane(z,ρ). We can compute the field intensities from Maxwell's equations and we get three non zero surviving field intensity vectors. If we use our intuitive defintion of Cherenkov angle $\cos\theta = \frac{1}{n\beta}$, we get the expressions of the non-zero field intensities as:

$$\begin{aligned} H_\phi &= -\frac{a}{\sqrt{\rho}} \int \sqrt{s} \cos\chi d\omega \\ E_\rho &= -\frac{a}{c\sqrt{\rho}} \int \frac{\sqrt{(\beta^2 n^2 - 1)}}{\beta^2 n^2 \sqrt{s}} \cos\chi \omega d\omega \\ E_\rho &= +\frac{a}{c\sqrt{\rho}} \int (1 - 1/\beta^2 n^2) \cos\chi \omega d\omega \end{aligned} \tag{A.15}$$

where H is not to be confused with Henkel function. It is the physical magnetic field in the matter. $a = e/c\sqrt{2/\pi}$ is a constant and $\chi = \omega\left[t - \frac{z cos\theta + \rho sin\theta}{c/n}\right] + \frac{\pi}{4}$. The Poyenting vector accounts the directional energy flux. It can be used for the total outward radiation. Classically Poyenting vector is defined as $\vec{S} = \vec{E} \times \vec{H}$. Hence, the total energy (W) radiated by the particle through the surface of a cylinder of length l whose axis is coincidental to the track of its motion, is equal to:

$$\begin{aligned} W &= 2\pi\rho l \int_{-\infty}^{+\infty} \frac{c}{4\pi} \vec{S} dt \\ W &= \frac{e^2 2}{c^3 \rho \pi} 2\pi\rho l \frac{c}{4\pi} 2\pi 2\pi \int \left(1 - \frac{1}{\beta^2 n^2}\right) \omega d\omega \end{aligned} \tag{A.16}$$

We have use the identity; $\int_{-\infty}^{+\infty} cos(\omega t + \alpha) cos(\omega' t + \alpha') dt = \pi\delta(\omega - \omega')$. The important equation that is the energy radiated by the track per uni length is therefore:

$$\frac{dW}{dl} = \frac{e^2}{c^2} \int \left(1 - \frac{1}{\beta^2 n^2}\right) \omega d\omega \tag{A.17}$$

There has been no frequency cut-off has been in the derivation of the relation.The two factors are setting an upper limit to the frequency spectrum. From equation A.17 we can obtain the number of photons emitted by the charged particle (N):

$$N = 2\pi . L\alpha \int_{\beta.n>1} \left(1 - \left(\frac{\beta_{th}(\lambda)}{\beta}\right)^2\right) \frac{d\lambda}{\lambda^2} \tag{A.18}$$

where α is the fine structure constant and the particle traverses a distance L in the dielectric medium and the photon wavelength is λ. The total number of photons depends upon the wavelength integration, but the number of photons emitted per unit length and per unit energy can be taken as a constant, whenever there are no absorption bands in the interested frequency region. The conclusions are the following:

- the energy loss for Cherenkov radiation is of the order of keV/cm.
- the amount of Cherenkov radiation is proportional to the square of the particles charge, where in equation A.17 the particle charge can be generalised to Ze for particles with more than one electronic charge. However, the amount of Cherenkov radiation does not depend on the mass of the particle.
- the photon yield per unit wavelength interval $d\lambda$ is proportional to $\frac{d\lambda}{\lambda^2}$, hence most photons are emitted in the UV region.
- the number of photons emitted per unit length and per unit frequency is constant.

Appendix B

Armenteros plot

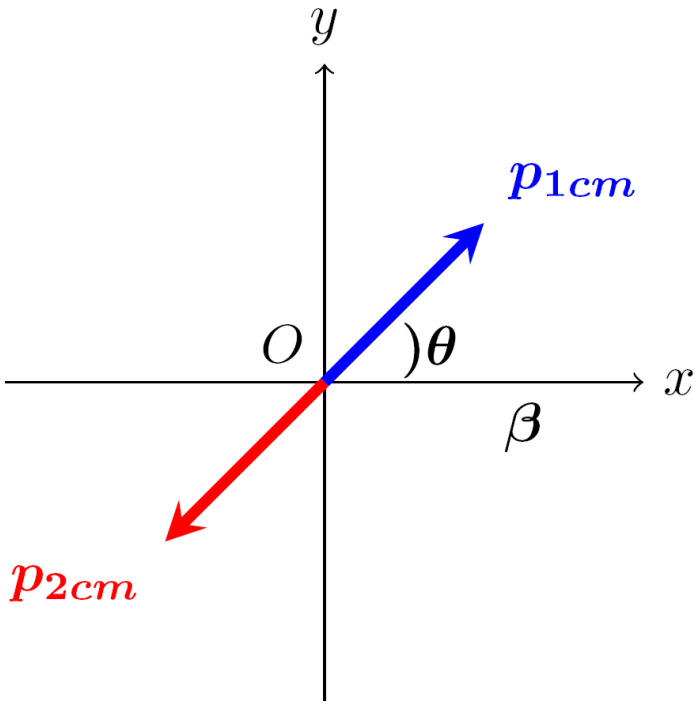

FIGURE B.1: 2 body decay in centre of mass frame

Let us assume a particle of mass M decays into two daughter particles of rest mass m_1 and m_2 respectively. At the centre of mass frame of the decaying particle the its momentum four vector can be written as $(M, 0, 0, 0)$. The decaying particles will be emitted back to back due to conservation of linear momentum. Therefore we can write, $p_{1cm} = -p_{2cm} = p_{cm}$ and their momentum four vectors are written as: (E_{1cm}, p_{cm}) and $(E_{2cm}, -p_{cm})$.

The conservation of energy makes: $M = E_{1cm} + E_{2cm}$. Using Einstein's energy equation we can write:

$$\begin{aligned} M &= \sqrt{m_1^2 + p_{cm}^2} + \sqrt{m_1^2 + p_{cm}^2} \\ (M - \sqrt{m_1^2 + p_{cm}^2})^2 &= (\sqrt{m_2^2 + p_{cm}^2})^2 \\ p_{cm}^2 &= \\ \frac{1}{4M^2}&(M^4 + m_1^4 + m_2^4 - 2M^2m_1^2 - 2M^2m_2^2 - 2m_1^2m_2^2) \end{aligned} \tag{B.1}$$

Based on the equation B.1 we can also estimate the energy of the daughter particles in the center of mass frame. The center of mass energy (E_{1cm}) of particle 1 is given by:

$$\begin{aligned} E_{1cm}^2 &= p_{cm}^2 + m_1^2 \\ E_{1cm}^2 &= \\ &\frac{(M^4 + m_1^4 + m_2^4 - 2M^2m_1^2 - 2M^2m_2^2 - 2m_1^2m_2^2 + 4M^2m_1^2)}{4M^2} \\ E_{1cm}^2 &= \frac{(M^2 + m_1^2)^2 - 2m_2^2(M^2 + m_1^2) + m_2^4}{4M^2} \\ E_{1cm}^2 &= \frac{(M^2 + m_1^2 - m_2^2)^2}{4M^2} \end{aligned} \tag{B.2}$$

Similarly we can compute the center of mass energy (E_{2cm}) of particle 2.

$$E_{2cm}^2 = \frac{(M^2 + m_2^2 - m_1^2)^2}{4M^2} \tag{B.3}$$

In figure B.1 we assumed that one of the particles made and angle θ along the direction of the boost of the parent particle. The daughter particles will have a component p_{Lcm} along the boost direction and component p_{Tcm} transverse to p_{Lcm}. The component p_{Tcm} will not have an effect of the boost. The particles emitted at perpendicular to the boost direction will have no longitudinal component and therefore the transverse component in such case will be maximum. The Lorentz transformation of the longitudinal component of the two particles in the Lab system is:

$$\begin{aligned} p_{1L} &= \gamma(p_{Lcm} + \beta E_{1cm}) = (p_{cm}\cos\theta\beta E_{1cm}) \\ p_{2L} &= \gamma(-p_{cm}\cos\theta + \beta E_{2cm}) \end{aligned} \tag{B.4}$$

Equation B.4 suggests that the momenta in the lab frame of the two decaying particles coming from the same decayed particle, is dependent on the angle at which they were emitted in the centre of mass frame of the parent particle.

The asymmetry α of the two daughter particles are given by:

$$\begin{aligned}
\alpha &= \frac{p_{1L} - p2L}{p_{1L} + p2L} \\
&= \frac{(p_{cm}\cos\theta + \beta E_{1cm}) - (-p_{cm}\cos\theta + \beta E_{2cm})}{(p_{cm}\cos\theta + \beta E_{1cm}) + (-p_{cm}\cos\theta + \beta E_{2cm})} \\
&= \frac{2p_{cm}\cos\theta + \beta(E_{1cm} - E_{2cm})}{\beta(E_{1cm} + E_{2cm})} \\
&= \frac{2p_{cm}}{\beta M}\cos\theta + \frac{E_{1cm} - E_{2cm}}{E_{1cm} + E_{2cm}} \\
&= \frac{2p_{cm}}{\beta M}\cos\theta + \frac{(E_{1cm} - E_{2cm})(E_{1cm} + E_{2cm})}{(E_{1cm} + E_{2cm})^2} \\
&= \frac{2p_{cm}}{\beta M}\cos\theta + \frac{(m_1^2 + p_{cm}^2) - (m_2^2 - p_{cm}^2)}{M^2} \\
&= \frac{2p_{cm}}{\beta M}\cos\theta + \frac{m_1^2 - m_2^2}{M^2}
\end{aligned} \tag{B.5}$$

For particles with $\beta \longrightarrow 1$ equation B.5 limits the upper and lower values of α. If we write $\alpha_0 = \frac{m_1^2 - m_2^2}{M^2}$ and $\delta = 2p_{cm}/M$.
Then the asymmetry is constrained $\alpha_0 - \delta \leq \alpha \leq \alpha_0 - \delta$. The $\cos\theta = \frac{\alpha - \alpha_0}{\delta}$ and $\sin\theta = \frac{p_T}{p_{cm}}$. In the plane ($\alpha$,$p_T$) a elliptical shape will define the decay of the particles from a two body decay.

$$(\frac{\alpha - \alpha_0}{\delta})^2 + (\frac{p_T}{p_{cm}})^2 = 1 \tag{B.6}$$

From equation B.6 the centre of the ellipse is at $(\alpha_0, 0) = (\frac{m_1^2 - m_2^2}{M^2}, 0)$ and the radii of the ellipse are $(r_\alpha, r_{p_T}) = (2p_{cm}/M, p_{cm})$.

Decay	$Mass(GeV)$	Products	$m_1(GeV)$	$m_2(GeV)$	$p_{cm}(GeV)$	r_α	α
K_0	0.498	$\pi^+\ \pi^-$	0.139	0.139	0.206	0.826	0
Λ	1.116	$P\ \pi^-$	0.938	0.139	0.101	0.18	$\pm$0.69
ϕ	1.02	$K^+\ K^-$	0.493	0.493	0.130	0.254	0

TABLE B.1: The table showing variables with physical values obtained from kinematics

In the figure 7.37 we see the Armenteros plot for the ϕ decays from COMPASS spectrometer, with identified Kaons from the RICH. We see the values of r_α and p_{cm} are reasonably consistent.

Appendix C

Essential Classes for RICHONE

The code has some conventions, some of which I will mention as example:

- Each member of the class is extracted by a method, this ensures no overlapping of variables.
- Some methods start with an unique identity "Check", these classes books the relevant histograms.
- Individual 116 mirror elements are listed as "MirrorElem". The two mirrors, namely Up and Down are listed as "MirrorNorm".
- Some variables have the suffix “W”, which signifies the working reference system. For instance, the two references of the 2 photon detectors. The origin is the mirror center, the z axis is perpendicular to the detector surface and the y is >0 (< 0) for the up (down) detector. This system is used for the Rugh transformation. It is not the Lab coordinate system. Variables in the lab coordinate system has a suffix “0”.

C.1 Description of associate Classes of RICHONE

C.1.1 CsRCEventParticles.cc

The class CsRCEventParticle reads as input by looping over all the tracks from the CORAL by looping over all the items stored by CORAL tracking classes listed as CsTrack, and stores a list of objects is created in CsRCParticle as output. Inside the loop :
– unusable events are skipped.
– each reconstructed track is checked and in case their momentum is not zero, the first helix(position, direction and momentum) is after the target and the last helix is after the first magnet SM1, they are selected for the RICH analysis. There are four methods for the different types of data:

- raw data : setDataParticle: put the track information relevant for RICH reconstruction in CsRCParticles.
- gFiles data : setMyParticle: In this case information from CsTracks is not available, so CsRCEventParticle puts the object found in the gFiles in CsRCParticles; gFiles are binary files, so with this method the information are translated in CsRCParticles.

- 2 options for Monte Carlo data: setMCParticle and setMCRecParticle; store the info from the simulation after the digitization.

In the real data analysis of 2016, we only investigate the RICH algorithm of the first kind to study the RICH performance. Nevertheless, after the task of the class is finished, RICHONE interacts only with CsRCParticles, not with CORAL tracks.

C.1.2 CsRCEventPads.cc

The class CsRCEventPads reads the digits which are listed as CsDigits as the input and a list of objects is created in CsRCPad as output object. The "pads" are the digits of CORAL, it is taken from DDD via another class CsGeom, where the geometry of all the objects of the spectrometer is defined. For the RICH the pads are mainly:

- CsI: based on the fired pads several information are stored. Identity of the cathode/s where the pads belong, number of pad has been fired, the coordinates of the pad in the cathode, the 3 amplitudes of the APV signal, namely $A_0, A_1 and A_2$.

- MAPMT: the information stored are similar to the CsI based cathodes, but only difference is that the time information is stored instead of pulse heights;

We had a readout system based on Gesiplex, which is an obsolete electronics and I will not discuss it here. The subroutines associated to this particluar type of electronics are not called.

Also in this case there are 4 options as already mentioned and methods dealing with the different type of data. But for our analysis only the method associated to the raw data has been used.

The class has many methods, but the main functionality is contained in the following ones:
– checkPMTPad, checkAPVPad (set with an option "APVamplCuts") : these two methods are used to cut the events respectively w.r.t to the time information "T_O" and to the 3 APV amplitudes
–setDataPads(): it is a pointer to RichDetector , in which there is the method getMyDigits, giving the list of RICH digits. Each digit contains an address, used to have the cathode number,cordinate of the pad etc., based on the detector types. Currently, there are 2 types of digits for the RICH:

- APV : get the 3 amplitudes (in gFiles they are combined in one variable only)

- PMT : if the T_0s are stored in the conditionDB, the info is available in the digit;

–acceptPads: to process APV or PMT only (option in the option file). If the pad is accepted after passing the conditions, than the object pad is built.

C.1.3 CsRCEventCluster.cc

The photon hits detected by the photon detectors of COMPASS RICH are classified differently for the MAPMTs and the gaseous detectors. The hits of the MPMTs are ascribed by their time information and the gaseous detectors are by their three signal amplitude. The hit time information is used to reject out-of-time photons. Whereas the hit amplitudes are used to reduce the background both from out-of-time photons and from electronic noise.

A converted photon does not only induce the signal in one pad of the gaseous detectors, but also adjacent pads share the signal amplitude. A clustering algorithm is used for this purpose. The impact position or the centre of charge position is then taken as the cluster position, it is then stored in a list. The class CsRCEventCluster transform digits into clusters. It has been studied that the cluster size of the (ON for CsI, OFF for MAPMT; can be changed via options) and performs coordinate transformation. If clustering is OFF, CsRCPads info is directly transferred to CsRCCluster. If it is ON, every CsRCCluster object contain also a list of pointers to the corresponding CsRCPad

The class has two main methods, one for effective clustering (doClustering()) and the other to transform a pad in a cluster object (getClusFromPads()) Both methods have 2 overloading, one without arguments, the other with the cathode number as argument.

Inside the methods, we have the distinction between APV based photon detectors and the MAPMTs.

The transformation from pad to cluster (done with doClustering or getClusFromPads) implies the change of coordinate system: the Cluster has x and y coordinates in the detector system (not the lab frame of refernce).

C.1.4 CsRCEventPartPhotons

In this class the association of the clusters to the particles is done. The main method of the class is "getEventPartPhot". In a loop on the particles of the event, all the clusters (in a fiducial range of 70mrad around the track, both in the upper and in the lower detector) are associated to each particle (NB also a "global" approach could have been tried = one global, iterative reconstruction for one event). The particles are considered only if the method "doSelMirror" return a true value; the method checks if the track has an impact point on the mirrors; since the mirrors is considered larger than in reality, this control is only rejecting very rare case of wrong reconstructions.

Two angles θ and ϕ are reconstructed making the Rough transformation (the middle point of the track is defined for this purpose). Note that each particle has its own reference system. A list of "photons objects" is created and then corrections (lenses and quartz window) are applied. The definition of ϕ is arbitrary, and taken as the intersection with the yz plane in lab.

Methods "PartPhoSelection" checks if the PartPhoton are in the "range" asked for the processing: useful for example if one wants to process only annular regions, or in general make some geometrical request.

Method "partAllIdent()" : likelihood computation via "getLikelihood"; Loop on PartPhotons, in which the PID is called. The likelihoods are put in PartProbs, member of CsRCPartPhoton.

At the end, an object CsRCPartPhoton is created for each CsRCParticle. It is equivalent, but contains more information: it contains a list of objects CsRCPhotons, that are the clusters transformed in the θ and ϕ information.

C.1.5 CsRCEventRings

Note that in principle this class could be switched off. The CPU time decreases a lot, but half of the information of the buffer is lost.

The main method is getEventRings. The input are the "photons" objects, containing the Cherenkov angle. The angles in the PMT part are normalized for the refractive indexes, to have homogeneous values for the PMT and CsI part. The normalization is done like $\frac{cos(\theta_{PM})}{cos(\theta_{UV})} = \frac{n_{PM}}{n_{UV}}$ The angle variables are "the0_" (theta in PMT or UV part), "the_" (the current), "theNorm_" (normalized).

The ring is reconstructed, and its χ^2 and its likelihood are evaluated. This likelihood could be an alternative to the standard likelihood computed without ring reconstruction. The type of likelihoods can be selected using the options "ALL" and "RING". The ring reconstruction is via the method getRingPk, that counts entries inside windows in the θ distribution. The ring is defined by the window with more counts (Search for a peak: "peakSearchMode" COUNT in the option files).

At the end the class CsRCRing is created, containing a sub-list lPhotons of CsRCPhotons belonging to the ring.

C.1.6 CsRCEventAnalysis

The analysis class is used for internal analysis (e.g. fit rings methods), tuning, histos. The analysis part could be skipped in production, since it produces histograms.

C.1.7 CsRichOneDisplay

The event online display in ROOT by A.Bressan.

C.1.8 CsRCEventDisplay

The event display in PAW by P.Schiavon. it is not online, it is made by histograms and need a PAW macro in order to be interpreted.

C.1.9 CsRCntup

Filling and saving of ntuple, paw or root. If in the option file this section is switched on, then this section saves in the output histograms a root NTuple.

The root NTuple is called "RICH" and it can be categorized into four blocks depending on the stored information. The blocks are given below:

- Tracks
- Rings
- Photons
- PID

Tracks For the tracks the product of the charge and momentum is stored. Information related to the tracks at the RICH entrance is also stored in the tree. The x,y and z position at the RICH entrance is stored in units of mm. Where, z coordinate is along the nominal beam direction, x coordinate is along Saleve to Jura side of the spectrometer hall, and y is from bottom to top. Also the direction of the tracks are given by two tangents of the tracks at the RICH entrance is stored. Tangents are defined $tgx = x/z$ and $tgy = y/z$. This information is directly derived from the tracking classes of CORAL. The information related to the ring, single photons and likelihood values for the PID are derived from the RICHONE reconstruction source.
The Ring level information contain the reflected track onto the detector plane. Which is the ring centre along with the ring theta. The assumption is that each track has one ring at the RCHONE level. Therefore, for each track likelihood of six hypotheses is computed and stored. The rings do have information related to the χ^2 of the ring theta.
For each photon in the ring, its cathode id, coordinates, signal amplitudes are recorded at the RICHONE tree level information.

C.1.10 CsRCPartPhotons

Two ϕ are evaluated:

- ϕ_A: angle between particle-photon plane and particle-lab z axis plane: used for the corrections, for the error evaluation of ϕ in the LH.
- ϕ_{pp}: angle between particle-photon plane and particle-reflected particle plane (this corresponds to the principal axis of the ellipse in the detector plane)

C.1.11 CsRCLikeAll.cc

This class contains only virtual members; the true members are in the classes CsRCLikeAll*.c, that inherits from it. The Class in use is the '05'. The correct class is called from the functions CsRCPartPhotons::getLikelihood(), CsRCPartPhotons::GetLikeAll(), reading the background name in the options files.The LH value is computed for each track for different mass hypothesis [140]. Likelihood computation: the first operation is the evaluation of the

normalization: signal (integral of the signal in the 70 mrad regions) + background. This normalization is called every time the likelihood is called (for each mass hypothesis: note that the background normalization could be also computed only once, since it does not depend on the mass hypothesis). this part can use a large amount of CPU if the "DoCheckLikelihood" option is ON, and when the maximum angle of the LH is computed (in this case the LH is called 25 times).

After the normalization, there is a loop on the photons, in which the evaluation of the signal and background part are evaluated. At the end of the loop, the output is the total LH and the LH of the background. The LH is stored in the buffer if the number of photons is greater that 1, otherwise the default values are stored. If the normalization option of the LH is ON (no "poissonian" LH), the square root of the LH is done, and the LH is divided for the integral (S+B). In the '05' LH case ("poissonian" LH), the LH is multiplied for (S+B) and multiplied for $e^{-S/N}$ ($e^{-B/N}/N!$ is not needed since I compare the LH from the different hypotheses).

Details on normalization terms:

–signal: For each called for each track, each hypothesis. the signal is evaluated from the Frank and Tamm relationship: $N = L * N0 * sin^2(\theta)$. θ is theta hypothesis, L from the track, N0 is from the option file: 12 for UV and 64 for PMT. The fraction of photons in one region and another is evaluated for the evaluation of the total number of photons (nPhoExp = nPhoPM + nPhoAPV). The number in the options are fixed.0

For each particle there is a part of toy MC, to evaluate losses due to the pipe or the dead zone as the lunettes. 50 photons are generated along the trajectory, and it is checked how many survive despite the dead zones. This probability is taken into account in the signal part.

– The normalization of the background is evaluated but not used. It is the integral of the map in the 70mrad region.

Signal part: evaluated for each photon, for each hypothesis. It the gaussian term, then muliplied for the normalization factor already evaluated for the normalization . Background: is the term read from the background map file (number of photons for pixel for event), multiplied for 2 terms coming from the Jacobian of the transformation between cartesian coordinates and spheric coordinate *theta * factor , coming from focal length).

C.1.12 CsGeom.cc

CORAL class containing all the geometry of the detectors. For the RICH calls the classes CsRCMirror, CsRCCathode, CsRCDetectors, that read the options from the RICH options file.

CsRCCathode: define the type of cathode reading the DBname from the detector.dat: (RI, RA (apv), RM o RP (pmt))

C.1.13 CsRCRecConst.cc

Contains some constant values (not options)

C.1.14 CsRCExeKeys.cc

Read the RICH options and makes them available from all parts of the program. For each key, a default value is defined (so in principle one could reduce the file of the richone options to few lines).

C.1.15 CsRCHistos.cc

Class to book the histograms. Note that there is an offset of 2000 between the number of the histogram in the code and in the output. Some histograms that can be useful:
– 1524 (saved as 3524) : A2 distribution in the 16 cathodes, for PADS. It is TH2D, in order to have the distribution for one cathode one has to make the projection.
– 1527 as previous one, for clusters.

Appendix D

Modifications in the detector table

The tables D.1 and D.2 are presented to show the modifications made in the detector table driven by the survey analysis. The first two rows in the tables under section 'RICH pd' correspond to the centre position of the big frame hosting the individual cathodes. The indices Up and Down correspond to the upper big frame and lower big frame of the detector. The data suggested a modification of these numbers.
In the following rows under section 'cath', we have the centre positions of the individual cathodes with respect to the big frame centre position hosting that cathode. The name of the cathodes are represented as 'UXX' or 'DXX', namely cathodes corresponding to upper or lower big frames. There are total of 16 cathodes, in each frame hosted 8. There indexing start from the Jura. For example in the top frame: Jura MWPC id 0 in figure 4.1 is 'U01', id 1 is 'U02', id 3 (Top Jura Hybrid PD) is 'U03', id 4 (Top Jura MAPMT) is 'U04' etc. The similar approach has been taken for the detectors in the bottom. The relative offset has been modified following survey data.

Rich pd												
	name	centre-x	centre-y	centre-z								
phot0	Up	609.1	0	193.1								
phot0	Down	609.1	0	-193.1								
cath												
	ID	TBname	name	offset-x	offset-y	offset-z	npadx	npady	padx	pady	qz-wind	gap
cath	901	RA01P0_u	U01	4.5	95.25	29.76	72	72	0.8	0.8	0.5	3.4
cath	902	RA01P0_d	U02	-4.5	95.25	-29.76	72	72	0.8	0.8	0.5	3.4
cath	903	RA01P1_u	U03	3.15	31.75	30.28	72	72	0.8	0.8	0.5	4.7
cath	904	RM01P1_d	U04	-4.5	31.75	-29.76	48	48	1.2	1.2	0.5	3.4
cath	905	RA01P2_u	U05	3.15	-31.75	30.28	72	72	0.8	0.8	0.5	4.7
cath	906	RM01P2_d	U06	-4.5	-31.75	-29.76	48	48	1.2	1.2	0.5	3.4
cath	907	RA01P3_u	U07	4.5	-95.25	29.76	72	72	0.8	0.8	0.5	3.4
cath	908	RA01P3_d	U08	-4.5	-95.25	-29.76	72	72	0.8	0.8	0.5	3.4
cath	909	RA01P4_u	D01	-4.5	95.25	29.76	72	72	0.8	0.8	0.5	3.4
cath	910	RA01P4_d	D02	4.5	95.25	-29.76	72	72	0.8	0.8	0.5	3.4
cath	911	RM01P5_u	D03	-4.5	31.75	29.76	48	48	1.2	1.2	0.5	3.4
cath	912	RA01P5_d	D04	3.15	31.75	-30.28	72	72	0.8	0.8	0.5	4.7
cath	913	RM01P6_u	D05	-4.5	-31.75	29.76	48	48	1.2	1.2	0.5	3.4
cath	914	RA01P6_d	D06	3.15	-31.75	-30.28	72	72	0.8	0.8	0.5	4.7
cath	915	RA01P7_u	D07	-4.5	-95.25	29.76	72	72	0.8	0.8	0.5	3.4
cath	916	RA01P7_d	D08	4.5	-95.25	-29.76	72	72	0.8	0.8	0.5	3.4

TABLE D.1: The detector.dat table prior to the survey where the Up down refers to the centre of the frame hosting the detectors. And each detector has its own centre w.r.t the big frame centre. The units are in cm.

Rich pd												
	name	centre-x	centre-y	centre-z								
phot0	Up	609.6	0.44	192.87								
phot0	Down	609.6	0.44	-193.36								
cath												
Det	ID	TBname	name	offset-x	offset-y	offset-z	npadx	npady	padx	pady	qz-wind	gap
cath	901	RA01P0_u	U01	4.5	95.25	29.76	72	72	0.8	0.8	0.5	3.4
cath	902	RA01P0_d	U02	-4.5	95.25	-29.76	72	72	0.8	0.8	0.5	3.4
cath	903	RA01P1_u	U03	2.952	31.75	29.620	72	72	0.8	0.8	0.5	4.7
cath	904	RM01P1_d	U04	-4.821	31.75	-30.146	48	48	1.2	1.2	0.5	3.4
cath	905	RA01P2_u	U05	2.952	-31.75	29.620	72	72	0.8	0.8	0.5	4.7
cath	906	RM01P2_d	U06	-4.821	-31.75	-30.146	48	48	1.2	1.2	0.5	3.4
cath	907	RA01P3_u	U07	4.5	-95.25	29.76	72	72	0.8	0.8	0.5	3.4
cath	908	RA01P3_d	U08	-4.5	-95.25	-29.76	72	72	0.8	0.8	0.5	3.4
cath	909	RA01P4_u	D01	-4.5	95.25	29.76	72	72	0.8	0.8	0.5	3.4
cath	910	RA01P4_d	D02	4.5	95.25	-29.76	72	72	0.8	0.8	0.5	3.4
cath	911	RM01P5_u	D03	-4.821	31.75	30.146	48	48	1.2	1.2	0.5	3.4
cath	912	RA01P5_d	D04	2.952	31.75	-29.620	72	72	0.8	0.8	0.5	4.7
cath	913	RM01P6_u	D05	-4.821	-31.75	30.146	48	48	1.2	1.2	0.5	3.4
cath	914	RA01P6_d	D06	2.952	-31.75	-29.620	72	72	0.8	0.8	0.5	4.7
cath	915	RA01P7_u	D07	-4.5	-95.25	29.76	72	72	0.8	0.8	0.5	3.4
cath	916	RA01P7_d	D08	4.5	-95.25	-29.76	72	72	0.8	0.8	0.5	3.4

TABLE D.2: The detector.dat table prior to the survey where the Up down refers to the centre of the frame hosting the detectors. And each detector has its own centre w.r.t the big frame centre. The units are in cm.

Bibliography

[1] I Estermann, R Frisch, and O Stern. "Magnetic moment of the proton". In: *Nature* 132.3326 (1933), p. 169.

[2] Ernest Rutherford. "Collision of α particles with light atoms; 4, an anomalous effect in nitrogen". In: *Philos. Mag.* 37 (1919), p. 581.

[3] Robert Hofstadter and Robert W McAllister. "Electron scattering from the proton". In: *Physical Review* 98.1 (1955), p. 217.

[4] Martin Breidenbach et al. "Observed behavior of highly inelastic electron-proton scattering". In: *Physical Review Letters* 23.16 (1969), p. 935.

[5] Elliott D Bloom et al. "High-Energy Inelastic e- p Scattering at 6^o and 10^o". In: *Physical Review Letters* 23.16 (1969), p. 930.

[6] MN Rosenbluth. "High energy elastic scattering of electrons on protons". In: *Physical Review* 79.4 (1950), p. 615.

[7] James D Bjorken and Emmanuel A Paschos. "Inelastic electron-proton and γ-proton scattering and the structure of the nucleon". In: *Physical Review* 185.5 (1969), p. 1975.

[8] Curtis G Callan Jr, Roger F Dashen, and David J Gross. "A theory of hadronic structure". In: *Physical Review D* 19.6 (1979), p. 1826.

[9] Richard P Feynman. *Photon-hadron interactions*. CRC Press, 1972.

[10] Murray Gell-Mann. "A schematic model of baryons and mesons". In: *Murray Gell-Mann: Selected Papers*. World Scientific, 2010, pp. 151–152.

[11] Stephan Narison. *QCD as a theory of hadrons: from partons to confinement*. Vol. 17. Cambridge University Press, 2004.

[12] Francis Halzen and Alan D Martin. *Quark & Leptons: An Introductory Course In Modern Particle Physics*. John Wiley & Sons, 2008.

[13] Antonio Pich. "Quantum chromodynamics". In: *arXiv preprint hep-ph/9505231* (1995).

[14] Richard P Feynman. "Very high-energy collisions of hadrons". In: *Physical Review Letters* 23.24 (1969), p. 1415.

[15] A D Martin. "Proton structure, Partons, QCD, DGLAP and beyond". In: *Acta Physica Polonica.B* 39.9 (2008), pp. 2025–2062.

[16] Robert L Jaffe and Xiangdong Ji. "Studies of the transverse spin-dependent structure function g 2 (x, Q 2)". In: *Physical Review D* 43.3 (1991), p. 724.

[17] S Wandzura and Frank Wilczek. "Sum rules for spin-dependent electro production-test of relativistic constituent quarks". In: *Physics Letters B* 72.2 (1977), pp. 195–198.

[18] Kaoru Hagiwara et al. “Review of Particle Physics: Particle data group”. In: *Physical Review D-Particles, Fields, Gravitation and Cosmology* 66.1 I (2002), pp. 100011–10001958.

[19] Mark Thomson. “Particle Physics”. In: *Lecture notes from the University of Cambridge, Michaelmas Term* (2011).

[20] Guido Altarelli and Giorgio Parisi. “Asymptotic freedom in parton language”. In: *Nuclear Physics B* 126.2 (1977), pp. 298–318.

[21] J_ Ashman et al. “A measurement of the spin asymmetry and determination of the structure function g1 in deep inelastic muon-proton scattering”. In: *Physics Letters B* 206.2 (1988), pp. 364–370.

[22] J Levelt and PJ Mulders. “Quark correlation functions in deep-inelastic semi-inclusive processes”. In: *Physical Review D* 49.1 (1994), p. 96.

[23] Bernd A Kniehl, Gustav Kramer, and Björn Pötter. “Testing the universality of fragmentation functions”. In: *Nuclear Physics B* 597.1-3 (2001), pp. 337–369.

[24] Vladimir Naumovich Gribov and Lev N Lipatov. *DEEP INELASTIC ep-SCATTERING IN A PERTURBATION THEORY.* Tech. rep. Inst. of Nuclear Physics, Leningrad, 1972.

[25] Yuri L Dokshitzer. “Calculation of the structure functions for deep inelastic scattering and e+ e- annihilation by perturbation theory in quantum chromodynamics”. In: *Zh. Eksp. Teor. Fiz* 73 (1977), p. 1216.

[26] Nour Makke. “Fragmentation Functions measurement at COMPASS”. In: *arXiv preprint arXiv:1307.3407* (2013).

[27] M Stolarski. “COMPASS hadron multiplicity measurements and fragmentation functions”. In: *EPJ Web of Conferences*. Vol. 112. EDP Sciences. 2016, p. 03008.

[28] Marcin Stolarski. “Final COMPASS results on hadrons, pions and kaons multiplicities in SIDIS”. In: *PoS* (2018), p. 235.

[29] M Alekseev et al. “Flavour separation of helicity distributions from deep inelastic muon–deuteron scattering”. In: *Physics Letters B* 680.3 (2009), pp. 217–224.

[30] M Alekseev et al. “Gluon polarisation in the nucleon and longitudinal double spin asymmetries from open charm muoproduction”. In: *Physics Letters B* 676.1-3 (2009), pp. 31–38.

[31] C Adolph et al. “Collins and Sivers asymmetries in muonproduction of pions and kaons off transversely polarised protons”. In: *Physics Letters B* 744 (2015), pp. 250–259.

[32] M Alekseev et al. “Collins and Sivers asymmetries for pions and kaons in muon–deuteron DIS”. In: *Physics Letters B* 673.2 (2009), pp. 127–135.

[33] John Collins. "Fragmentation of transversely polarized quarks probed in transverse momentum distributions". In: *Nuclear Physics B* 396.1 (1993), pp. 161–182. ISSN: 0550-3213. DOI: https://doi.org/10.1016/0550-3213(93)90262-N. URL: http://www.sciencedirect.com/science/article/pii/055032139390262N.

[34] Dennis Sivers. "Single-spin production asymmetries from the hard scattering of pointlike constituents". In: *Phys. Rev. D* 41 (1 Jan. 1990), pp. 83–90.

[35] C Aidala et al. "A hadron blind detector for PHENIX". In: *Nuclear Instruments and Methods in Physics Research Section A: Accelerators, Spectrometers, Detectors and Associated Equipment* 502.1 (2003), pp. 200–204.

[36] C Adolph et al. "Measurement of the charged-pion polarizability". In: *Physical review letters* 114.6 (2015), p. 062002.

[37] Andrea Ferrero, COMPASS collaboration, et al. "Study of DVCS and DVMP processes at COMPASS". In: *Journal of Physics: Conference Series*. Vol. 295. 1. IOP Publishing. 2011, p. 012039.

[38] Norihiro Doshita. "COMPASS polarized Drell-Yan experiment". In: *PoS* (2016), p. 040.

[39] C Adolph et al. "Multiplicities of charged pions and charged hadrons from deep-inelastic scattering of muons off an isoscalar target". In: *Physics Letters B* 764 (2017), pp. 1–10.

[40] R Akhunzyanov et al. "K- over K+ multiplicity ratio for kaons produced in DIS with a large fraction of the virtual-photon energy". In: *Physics Letters B* 786 (2018), pp. 390–398.

[41] Sebastian Uhl. "Future Measurement of the Proton Radius at COMPASS". In: *Verhandlungen der Deutschen Physikalischen Gesellschaft* (2018).

[42] P. Abbon et al. "The COMPASS experiment at CERN". In: *Nuclear Instruments and Methods in Physics Research Section A: Accelerators, Spectrometers, Detectors and Associated Equipment* 577.3 (2007), pp. 455–518.

[43] P. Abbon et al. "The COMPASS setup for physics with hadron beams". In: *Nuclear Instruments and Methods in Physics Research Section A: Accelerators, Spectrometers, Detectors and Associated Equipment* 779 (2015), pp. 69–115.

[44] *https://sba.web.cern.ch/sba/BeamsAndAreas/M2/M2-OperatorCourse.pdf*.

[45] N Doble et al. "The upgraded muon beam at the SPS". In: *Nuclear Instruments and Methods in Physics Research Section A: Accelerators, Spectrometers, Detectors and Associated Equipment* 343.2-3 (1994), pp. 351–362.

[46] Kaori Kondo et al. "Polarization measurement in the COMPASS polarized target". In: *Nuclear Instruments and Methods in Physics Research Section A: Accelerators, Spectrometers, Detectors and Associated Equipment* 526.1-2 (2004), pp. 70–75.

[47] N Doshita et al. "Performance of the COMPASS polarized target dilution refrigerator". In: *Nuclear Instruments and Methods in Physics Research Section A: Accelerators, Spectrometers, Detectors and Associated Equipment* 526.1-2 (2004), pp. 138–143.

[48] Andrzej Sandacz, COMPASS Collaboration, et al. "COMPASS results on DVCS and exclusive π 0 production". In: *Journal of Physics: Conference Series*. Vol. 938. 1. IOP Publishing. 2017, p. 012015.

[49] Gerhard K Mallot, Compass Collaboration, et al. "The COMPASS spectrometer at CERN". In: *Nuclear Instruments and Methods in Physics Research Section A: Accelerators, Spectrometers, Detectors and Associated Equipment* 518.1-2 (2004), pp. 121–124.

[50] Roger Bouclier et al. "The gas electron multiplier (GEM)". In: *IEEE Transactions on Nuclear Science* 44.3 (1997), pp. 646–650.

[51] Fabio Sauli. "GEM: A new concept for electron amplification in gas detectors". In: *Nuclear Instruments and Methods in Physics Research Section A: Accelerators, Spectrometers, Detectors and Associated Equipment* 386.2-3 (1997), pp. 531–534.

[52] Georges Charpak et al. "Micromegas, a multipurpose gaseous detector". In: *Nuclear Instruments and Methods in Physics Research Section A: Accelerators, Spectrometers, Detectors and Associated Equipment* 478.1-2 (2002), pp. 26–36.

[53] Y Giomataris. "Development and prospects of the new gaseous detector "Micromegas"". In: *Nuclear Instruments and Methods in Physics Research Section A: Accelerators, Spectrometers, Detectors and Associated Equipment* 419.2-3 (1998), pp. 239–250.

[54] B Ketzer et al. "Performance of triple GEM tracking detectors in the COMPASS experiment". In: *Nuclear Instruments and Methods in Physics Research Section A: Accelerators, Spectrometers, Detectors and Associated Equipment* 535.1-2 (2004), pp. 314–318.

[55] B Ketzer et al. "GEM detectors for COMPASS". In: *2000 IEEE Nuclear Science Symposium. Conference Record (Cat. No. 00CH37149)*. Vol. 1. IEEE. 2000, pp. 5–25.

[56] Damien Neyret et al. "New pixelized Micromegas detector for the COMPASS experiment". In: *Journal of Instrumentation* 4.12 (2009), P12004.

[57] D Thers et al. "Micromegas as a large microstrip detector for the COMPASS experiment". In: *Nuclear Instruments and Methods in Physics Research Section A: Accelerators, Spectrometers, Detectors and Associated Equipment* 469.2 (2001), pp. 133–146.

[58] E Albrecht et al. "COMPASS RICH-1". In: *Nuclear Instruments and Methods in Physics Research Section A: Accelerators, Spectrometers, Detectors and Associated Equipment* 502.1 (2003), pp. 112–116.

[59] E Albrecht et al. "Status and characterisation of COMPASS RICH-1". In: *Nuclear Instruments and Methods in Physics Research Section A: Accelerators, Spectrometers, Detectors and Associated Equipment* 553.1-2 (2005), pp. 215–219.

[60] *Russian Patent No. 2316848, 01.06.2006,http://www.zecotek.com.*

[61] C Bernet et al. "The COMPASS trigger system for muon scattering". In: *Nuclear Instruments and Methods in Physics Research Section A: Accelerators, Spectrometers, Detectors and Associated Equipment* 550.1-2 (2005), pp. 217–240.

[62] H Fischer et al. "The COMPASS data acquisition system". In: *IEEE transactions on nuclear science* 49.2 (2002), pp. 443–447.

[63] I Konorov et al. "The trigger control system for the compass". In: *2001 IEEE Nuclear Science Symposium Conference Record (Cat. No. 01CH37310)*. Vol. 1. IEEE. 2001, pp. 98–99.

[64] *https://cds.cern.ch/record/941318/files/p361.pdf*.

[65] E Nappi and J Seguinot. "Ring Imaging Cherenkov Detectors: The state of the art and perspectives". In: *Rivista del Nuovo Cimento* 28.8-9 (2005).

[66] Christian Lippmann. "Particle identification". In: *Nuclear Instruments and Methods in Physics Research Section A: Accelerators, Spectrometers, Detectors and Associated Equipment* 666 (2012), pp. 148–172.

[67] PA Čerenkov. "Visible radiation produced by electrons moving in a medium with velocities exceeding that of light". In: *Physical Review* 52.4 (1937), p. 378.

[68] IETIM Frank and Ig Tamm. "Coherent visible radiation of fast electrons passing through matter". In: *Selected Papers*. Springer, 1991, pp. 29–35.

[69] John Vernon Jelley. *Cherenkov radiation and its applications*. Pergamon, 1958.

[70] SI Vavilov. "On the possible causes of blue γ-glow of liquids". In: *CR Dokl Akad Nauk SSSR*. Vol. 2. 8. 1934, p. 457.

[71] Ig Tamm and S Frank. "CR Acad. URSS, 14, 1937". In: *I. Tamm, J. Physics (Moscou)* 1 (1939), p. 439.

[72] Arthur Roberts. "A novel mass-sensitive image-dissecting Cherenkov detector". In: *Nuclear Instruments and Methods* 99.3 (1972), pp. 589–598.

[73] E Albrecht et al. "Operation, optimisation, and performance of the DELPHI RICH detectors". In: *Nuclear Instruments and Methods in Physics Research Section A: Accelerators, Spectrometers, Detectors and Associated Equipment* 433.1-2 (1999), pp. 47–58.

[74] H-W Siebert et al. "The omega RICH". In: *Nuclear Instruments and Methods in Physics Research Section A: Accelerators, Spectrometers, Detectors and Associated Equipment* 343.1 (1994), pp. 60–67.

[75] I Arino et al. "The Hera-B Rich". In: *Nuclear Instruments and Methods in Physics Research Section A: Accelerators, Spectrometers, Detectors and Associated Equipment* 453.1-2 (2000), pp. 289–295.

[76] Dirk Ryckbosch. "The HERMES RICH detector HERMES Collaboration". In: *Nuclear Instruments and Methods in Physics Research Section A: Accelerators, Spectrometers, Detectors and Associated Equipment* 433.1-2 (1999), pp. 98–103.

[77] DIRC Group of the BABAR Collaboration et al. "The DIRC, the particle identification detector of BaBar". In: *Nuclear Physics B-Proceedings Supplements* 75.3 (1999), pp. 356–358.

[78] Andrew Powell. "Particle identification at LHCb". In: *PoS* (2010), p. 020.

[79] Roger Forty, LHCb Collaboration, et al. "RICH pattern recognition for LHCb". In: *Nuclear Instruments and Methods in Physics Research Section A: Accelerators, Spectrometers, Detectors and Associated Equipment* 433.1-2 (1999), pp. 257–261.

[80] F Garibaldi et al. "A proximity focusing RICH detector for kaon physics at Jefferson Lab Hall A". In: *Nuclear Instruments and Methods in Physics Research Section A: Accelerators, Spectrometers, Detectors and Associated Equipment* 502.1 (2003), pp. 117–122.

[81] S Nishida et al. "Aerogel RICH for the Belle II forward PID". In: *Nuclear Instruments and Methods in Physics Research Section A: Accelerators, Spectrometers, Detectors and Associated Equipment* 766 (2014), pp. 28–31.

[82] Thomas Ypsilantis and Jacques Séguinot. "Theory of ring imaging Cherenkov counters". In: *Nuclear Instruments and Methods in Physics Research Section A: Accelerators, Spectrometers, Detectors and Associated Equipment* 343.1 (1994), pp. 30–51.

[83] Jacques Séguinot and Thomas Ypsilantis. "A historical survey of ring imaging Cherenkov counters". In: *Nuclear Instruments and Methods in Physics Research Section A: Accelerators, Spectrometers, Detectors and Associated Equipment* 343.1 (1994), pp. 1–29.

[84] Eugenio Nappi. "Advances in charged particle identification techniques". In: *Nuclear Instruments and Methods in Physics Research Section A: Accelerators, Spectrometers, Detectors and Associated Equipment* 628.1 (2011), pp. 1–8.

[85] M Adinolfi et al. "Performance of the LHCb RICH detector at the LHC". In: *The European Physical Journal C* 73.5 (2013), p. 2431.

[86] Eugenio Nappi and Vladimir Peskov. *Imaging gaseous detectors and their applications*. John Wiley & Sons, 2013.

[87] Matthias Moritz et al. "Performance study of new pixel hybrid photon detector prototypes for the LHCb RICH counters". In: *IEEE Transactions on Nuclear Science* 51.3 (2004), pp. 1060–1066.

[88] H Hoedlmoser et al. "Production technique and quality evaluation of CsI photocathodes for the ALICE/HMPID detector". In: *Nuclear Instruments and Methods in Physics Research Section A: Accelerators, Spectrometers, Detectors and Associated Equipment* 566.2 (2006), pp. 338–350.

[89] H Hoedlmoser et al. "Long term performance and ageing of CsI photocathodes for the ALICE/HMPID detector". In: *Nuclear Instruments and Methods in Physics Research Section A: Accelerators, Spectrometers, Detectors and Associated Equipment* 574.1 (2007), pp. 28–38.

[90] François Piuz. "CsI-photocathode and RICH detector". In: *Nuclear Instruments and Methods in Physics Research Section A: Accelerators, Spectrometers, Detectors and Associated Equipment* 371.1-2 (1996), pp. 96–115.

[91] Jaroslav Va'vra et al. "Study of CsI photocathodes: volume resistivity and ageing". In: *Nuclear Instruments and Methods in Physics Research Section A: Accelerators, Spectrometers, Detectors and Associated Equipment* 387.1-2 (1997), pp. 154–162.

[92] André Braem et al. "Technology of photocathode production". In: *Nuclear Instruments and Methods in Physics Research Section A: Accelerators, Spectrometers, Detectors and Associated Equipment* 502.1 (2003), pp. 205–210.

[93] H Berger et al. "Recent results on the properties of CsI photocathodes". In: *Nuclear Instruments and Methods in Physics Research Section A: Accelerators, Spectrometers, Detectors and Associated Equipment* 360.1-2 (1995), pp. 411–415.

[94] L Velardi, A Valentini, and G Cicala. "Highly efficient and stable ultraviolet photocathode based on nanodiamond particles". In: *Applied Physics Letters* 108.8 (2016), p. 083503.

[95] Luciano Velardi, Antonio Valentini, and Grazia Cicala. "UV photocathodes based on nanodiamond particles: Effect of carbon hybridization on the efficiency". In: *Diamond and Related Materials* 76 (2017), pp. 1–8.

[96] C Chatterjee et al. "Nanodiamond photocathodes for MPGD-based single photon detectors at future EIC". In: *arXiv preprint arXiv:1908.05058* (2019).

[97] J Agarwala et al. "Study of MicroPattern Gaseous detectors with novel nanodiamond based photocathodes for single photon detection in EIC RICH". In: *Nuclear Instruments and Methods in Physics Research Section A: Accelerators, Spectrometers, Detectors and Associated Equipment* (2019).

[98] E Albrecht et al. "The radiator gas and the gas system of COMPASS RICH-1". In: *Nuclear Instruments and Methods in Physics Research Section A: Accelerators, Spectrometers, Detectors and Associated Equipment* 502.1 (2003), pp. 266–269.

[99] E Albrecht et al. "The mirror system of COMPASS RICH-1". In: *Nuclear Instruments and Methods in Physics Research Section A: Accelerators, Spectrometers, Detectors and Associated Equipment* 502.1 (2003), pp. 236–240.

[100] Shuddha Shankar Dasgupta. "Particle Identification with the Cherenkov imaging technique using MPGD based Photon Detectors for Physics at COMPASS Experiment at CERN". In: (2017).

[101] S Costa et al. "CLAM, a continuous line alignment and monitoring method for RICH mirrors". In: *Nuclear Instruments and Methods in Physics Research Section A: Accelerators, Spectrometers, Detectors and Associated Equipment* 553.1-2 (2005), pp. 135–139.

[102] Guenter Baum et al. "RICHONE: a software package for the analysis of COMPASS RICH-1 data". In: *Nuclear Instruments and Methods in Physics Research Section A: Accelerators, Spectrometers, Detectors and Associated Equipment* 502.1 (2003), pp. 315–317.

[103] P Schiavon. "Particle identification in COMPASS RICH-1". In: *Progress Report. September* (2001), pp. 2001–12.

[104] P Abbon et al. "The experience of building and operating COMPASS RICH-1". In: *Nuclear Instruments and Methods in Physics Research Section A: Accelerators, Spectrometers, Detectors and Associated Equipment* 639.1 (2011), pp. 15–19.

[105] P Abbon et al. "Design and construction of the fast photon detection system for COMPASS RICH-1". In: *Nuclear Instruments and Methods in Physics Research Section A: Accelerators, Spectrometers, Detectors and Associated Equipment* 616.1 (2010), pp. 21–37.

[106] P Abbon et al. "The characterisation of the multianode photomultiplier tubes for the RICH-1 upgrade project at COMPASS". In: *Nuclear Instruments and Methods in Physics Research Section A: Accelerators, Spectrometers, Detectors and Associated Equipment* 595.1 (2008), pp. 177–179.

[107] Daniel Kramer. "Optical concentrators for Cherenkov light detector". PhD thesis. Faculty of Mechatronics and Interdisciplinary Engineering Studies, TECHNICAL UNIVERSITY OF LIBEREC, 2005.

[108] *https://www.zemax.com/*.

[109] P Abbon et al. "Optical telescopes for COMPASS RICH-1 up-grade". In: *Czech. J. Phys.* 56 (2006), F315–F322.

[110] Michael Bass et al. *Handbook of optics, Volume II: Design, fabrication and testing, sources and detectors, radiometry and photometry*. McGraw-Hill, Inc., 2009.

[111] C D'Ambrosio, M Laub, and D Piedigrossi. "Optical qualification of the first COMPASS RICH mirrors". In: *COMPASS Technical Note* 4 (2000), p. 17.

[112] J Polak et al. "Hartmann test of the COMPASS RICH-1 optical telescopes". In: *Czechoslov. J. Phys.* 56 (2008), F333.

[113] P Abbon et al. "Read-out electronics for fast photon detection with COMPASS RICH-1". In: *Nuclear Instruments and Methods in Physics Research Section A: Accelerators, Spectrometers, Detectors and Associated Equipment* 587.2-3 (2008), pp. 371–387.

[114] H Fischer et al. "Implementation of the dead-time free F1 TDC in the COMPASS detector readout". In: *Nuclear Instruments and Methods in Physics Research Section A: Accelerators, Spectrometers, Detectors and Associated Equipment* 461.1-3 (2001), pp. 507–510.

[115] Michela Chiosso et al. "A fast binary front-end ASIC for the RICH detector of the COMPASS experiment at CERN". In: *2008 IEEE Nuclear Science Symposium Conference Record*. IEEE. 2008, pp. 1495–1500.

[116] F Gonnella. "M. Pegoraro A prototype front-end asic for the read-out of the drift tubes of CMS barrel muon chambers". In: *fourth workshop on electronics for LHC experiments-LEB98, Rome, 21-25 September 1988*, pp. 98–36.

[117] E Albrecht et al. "First performances of COMPASS RICH-1". In: *Nuclear Instruments and Methods in Physics Research Section A: Accelerators, Spectrometers, Detectors and Associated Equipment* 518.1-2 (2004), pp. 586–589.

[118] F Tessarotto et al. "Long term experience and performance of COMPASS RICH-1". In: *Journal of Instrumentation* 9.09 (2014), p. C09011.

[119] Maxim Alexeev et al. "THGEM-based photon detectors for the upgrade of COMPASS RICH-1". In: *Nuclear Instruments and Methods in Physics Research Section A: Accelerators, Spectrometers, Detectors and Associated Equipment* 732 (2013), pp. 264–268.

[120] M Alexeev et al. "Development of THGEM-based Photon Detectors for COMPASS RICH-1". In: *Physics Procedia* 37 (2012), pp. 781–788.

[121] M Alexeev et al. "Hybrid MPGD-based detectors of single photons for the upgrade of COMPASS RICH-1". In: *2015 IEEE Nuclear Science Symposium and Medical Imaging Conference (NSS/MIC)*. IEEE. 2015, pp. 1–5.

[122] Maxim Alexeev et al. "Status and progress of the novel photon detectors based on THGEM and hybrid MPGD architectures". In: *Nuclear Instruments and Methods in Physics Research Section A: Accelerators, Spectrometers, Detectors and Associated Equipment* 766 (2014), pp. 133–137.

[123] F Tessarotto et al. *The novel photon detectors based on MPGD technologies for the upgrade of COMPASS RICH-1*. Tech. rep. 2018.

[124] A Breskin et al. "The THGEM: A thick robust gaseous electron multiplier for radiation detectors". In: *Nuclear Instruments and Methods in Physics Research Section A: Accelerators, Spectrometers, Detectors and Associated Equipment* 623.1 (2010), pp. 132–134.

[125] Amos Breskin et al. "A concise review on THGEM detectors". In: *Nuclear Instruments and Methods in Physics Research Section A: Accelerators, Spectrometers, Detectors and Associated Equipment* 598.1 (2009), pp. 107–111.

[126] R Chechik et al. "Thick GEM-like (THGEM) detectors and their possible applications". In: *arXiv preprint physics/0606162* (2006).

[127] M Cortesi et al. "Investigations of a THGEM-based imaging detector". In: *Journal of Instrumentation* 2.09 (2007), P09002.

[128] J Agarwala et al. "The high voltage system for the novel MPGD-based photon detectors of COMPASS RICH-1". In: *arXiv preprint arXiv:1803.01667* (2018).

[129] S Dalla Torre et al. *The high voltage system for the novel MPGD-based photon detectors of COMPASS RICH-1*. Tech. rep. 2018.

[130] Maxim Alexeev et al. "Ion backflow in thick GEM-based detectors of single photons". In: *Journal of Instrumentation* 8.01 (2013), P01021.

[131] Fulvio Tessarotto. "Status and perspectives of gaseous photon detectors". In: *Nuclear Instruments and Methods in Physics Research Section A: Accelerators, Spectrometers, Detectors and Associated Equipment* 876 (2017), pp. 225–232.

[132] M Alexeev et al. "The MPGD-based photon detectors for the upgrade of COMPASS RICH-1". In: *Nuclear Instruments and Methods in Physics Research Section A: Accelerators, Spectrometers, Detectors and Associated Equipment* 876 (2017), pp. 96–100.

[133] J Agarwala et al. "The MPGD-based photon detectors for the upgrade of COMPASS RICH-1 and beyond". In: *Nuclear Instruments and Methods in Physics Research Section A: Accelerators, Spectrometers, Detectors and Associated Equipment* (2018).

[134] J Agarwala et al. "Novel MPGD based detectors of single photons in COMPASS RICH-1". In: *Nuclear Instruments and Methods in Physics Research Section A: Accelerators, Spectrometers, Detectors and Associated Equipment* (2017).

[135] Jinky Agarwala et al. "Optimized MPGD-based Photon Detectors for high momentum particle identification at the Electron-Ion Collider". In: *Nuclear Instruments and Methods in Physics Research Section A: Accelerators, Spectrometers, Detectors and Associated Equipment* 936 (2019), pp. 565–567.

[136] P Abbon et al. "Fast readout of the COMPASS RICH CsI-MWPC photon chambers". In: *Nuclear Instruments and Methods in Physics Research Section A: Accelerators, Spectrometers, Detectors and Associated Equipment* 567.1 (2006), pp. 104–106.

[137] MJ French et al. "Design and results from the APV25, a deep submicron CMOS front-end chip for the CMS tracker". In: *Nuclear Instruments and Methods in Physics Research Section A: Accelerators, Spectrometers, Detectors and Associated Equipment* 466.2 (2001), pp. 359–365.

[138] Boris Grube et al. "Architecture of the common GEM and Silicon readout for the COMPASS experiment". In: *Advanced Technology And Particle Physics*. World Scientific, 2002, pp. 264–268.

[139] *M. Alexeev et al., "Status of the Development of Large Area Photon Detectors based on THGEMs and Hybrid MPGD architectures for Cherenkov Imaging Applications", Nucl. Instrum. Meth. A824 (2016) 139; M. Alexeevet al., "The MPGD-based photon detectors for the upgrade of COMPASS RICH-1" Nuclear Instruments and Methods A876 (2017) 96; M. Alexeevet al., "Status of COMPASS RICH-1 Upgrade with MPGD-based Photon Detectors", EPJ Web of Conferences 174 (2018)01004;*

[140] P Abbon et al. "Particle identification with COMPASS RICH-1". In: *Nuclear Instruments and Methods in Physics Research Section A: Accelerators, Spectrometers, Detectors and Associated Equipment* 631.1 (2011), pp. 26–39.

[141] S Dalla Torre et al. "A study of the RICH gas refractive index". In: *Nuclear Instruments and Methods in Physics Research Section A: Accelerators, Spectrometers, Detectors and Associated Equipment* 639.1 (2011), pp. 271–273.

[142] Roger Barlow. "Extended maximum likelihood". In: *Nuclear Instruments and Methods in Physics Research Section A: Accelerators, Spectrometers, Detectors and Associated Equipment* 297.3 (1990), pp. 496–506.

[143] Malte Christian Wilfert. "Investigation of the spin structure of the nucleon at the COMPASS experiment". PhD thesis. 2017.

[144] Nicolas Pierre. "Multiplicities of hadrons in deep-inelastic scattering of muons on nucleons at COMPASS". PhD thesis. 2019.